



UNIVERSITAT DE
BARCELONA

Foetal Stem Cell conversion as a new mechanism of therapy resistance in intestinal cancer

Laura Solé Font

ADVERTIMENT. La consulta d'aquesta tesi queda condicionada a l'acceptació de les següents condicions d'ús: La difusió d'aquesta tesi per mitjà del servei TDX (www.tdx.cat) i a través del Dipòsit Digital de la UB (diposit.ub.edu) ha estat autoritzada pels titulars dels drets de propietat intel·lectual únicament per a usos privats emmarcats en activitats d'investigació i docència. No s'autoritza la seva reproducció amb finalitats de lucre ni la seva difusió i posada a disposició des d'un lloc aliè al servei TDX ni al Dipòsit Digital de la UB. No s'autoritza la presentació del seu contingut en una finestra o marc aliè a TDX o al Dipòsit Digital de la UB (framing). Aquesta reserva de drets afecta tant al resum de presentació de la tesi com als seus continguts. En la utilització o cita de parts de la tesi és obligat indicar el nom de la persona autora.

ADVERTENCIA. La consulta de esta tesis queda condicionada a la aceptación de las siguientes condiciones de uso: La difusión de esta tesis por medio del servicio TDR (www.tdx.cat) y a través del Repositorio Digital de la UB (diposit.ub.edu) ha sido autorizada por los titulares de los derechos de propiedad intelectual únicamente para usos privados enmarcados en actividades de investigación y docencia. No se autoriza su reproducción con finalidades de lucro ni su difusión y puesta a disposición desde un sitio ajeno al servicio TDR o al Repositorio Digital de la UB. No se autoriza la presentación de su contenido en una ventana o marco ajeno a TDR o al Repositorio Digital de la UB (framing). Esta reserva de derechos afecta tanto al resumen de presentación de la tesis como a sus contenidos. En la utilización o cita de partes de la tesis es obligado indicar el nombre de la persona autora.

WARNING. On having consulted this thesis you're accepting the following use conditions: Spreading this thesis by the TDX (www.tdx.cat) service and by the UB Digital Repository (diposit.ub.edu) has been authorized by the titular of the intellectual property rights only for private uses placed in investigation and teaching activities. Reproduction with lucrative aims is not authorized nor its spreading and availability from a site foreign to the TDX service or to the UB Digital Repository. Introducing its content in a window or frame foreign to the TDX service or to the UB Digital Repository is not authorized (framing). Those rights affect to the presentation summary of the thesis as well as to its contents. In the using or citation of parts of the thesis it's obliged to indicate the name of the author.

Foetal Stem Cell conversion as a new mechanism of therapy resistance in intestinal cancer

Laura Solé Font

TESI DOCTORAL UB / 2021

Programa de Doctorat en Biomedicina

Supervisor: Dr. Lluís Espinosa Blay

Tutor: Dr. Rosa Aligué Alemany

Programa d'Investigació en Càncer

Institut Hospital del Mar d'Investigacions Mèdiques (IMIM)





UNIVERSITAT DE BARCELONA

Programa de Doctorat en Biomedicina

**Foetal Stem Cell conversion as a new mechanism of
therapy resistance in intestinal cancer**

TESI DOCTORAL UB / 2021

Memòria de tesi doctoral presentada per Laura Solé Font per
optar al grau de doctora per la Universitat de Barcelona,
realitzada sota la direcció del Dr. Lluís Espinosa Blay.

Barcelona, 2021

The present thesis has been funded by grants from:

AGAUR (2018 FI_B 00088/2020 FI_B2 00150)



**Agència
de Gestió d'Ajuts
Universitaris
i de Recerca**

Instituto de Salud Carlos III FEDER (PI16/00437-PI19/00013) and CIBERONC
(CB16/12/00244-CB16/12/00241-CB16/12/00273)



Generalitat de Catalunya (2017SGR135)



**Generalitat
de Catalunya**

Agencia Estatal de Investigación and the "Xarxa de Bancs de tumors sponsored by Pla
Director d'Oncologia de Catalunya (XBTC) (PID2019-104867RB-
I00/AEI/10.13039/501100011033)

Fundación HNA in the development of orthoxenografts/PDOX

***We thank our patients for their generosity and to MARbiobank and the IdiPAZ
Biobank integrated in the Spanish Hospital Biobanks Network (RetBioH)***

IdiPAZ Biobank is supported by Instituto de Salud Carlos III, Spanish Health Ministry (Grant RD09/0076/00073) and Farmaindustria through the Cooperation Program in Clinical and Translational Research of the Community of Madrid.

“Science, my lad, is made up of mistakes, but they are mistakes which it is useful to make, because they lead little by little to the truth.”

Jules Verne – A Journey to the Center of the Earth

“[...] they beheld the old man Iolaus, known to them, but now transformed from age to youth, he seemed almost a boy, with light down on his cheeks for Juno’s daughter Hebe, had renewed his years to please her husband, Hercules.”

Ovid – Metamorphoses IX [394], The Rejuvenation of Iolaus

ACKNOWLEDGEMENTS

ACKNOWLEDGEMENTS

Tots els finals es viuen amb una mescla de tristesa i alegria de tancar una etapa i deixar enrere molts moments, lligat a l'esperança d'experimentar canvis i experiències que obrin noves portes i maneres de veure la vida. Tots aquells que han passat per una tesis estaran d'acord que es viu amb una mescla molt gran d'emocions, però en el meu cas sempre ha prevalgut més la passió per la recerca ben feta i l'emoció de seguir profunditzant en allò que encara està per conèixer, per moltes dificultats trobades pel camí. Amb tot, sense tots vosaltres no hauria pogut ser possible mantenir la il·lusió.

Qui hauria dit que després d'estudiar Genètica i començar el màster pensant en dedicar la meva vida professional a un àmbit més clínic acabaria fent la tesi. I en part va ser gràcies a vosaltres, que em vaucollir a l'IDIBELL d'una bonica manera. Olga, sempre agrairé que tinguessis la paciència d'ensenyar-me com funciona realment un laboratori d'investigació, tot i no disposar de molt temps. Així com també he d'agrair a la meva tutora, la Sònia Guil, per acceptar-me al laboratori. Laia i Louisa, recordo amb afecte els nostres dinars i totes les conversacions, entre western i western. Sobretot a tu, Louisa, que vas estar amb mi ensenyant-me tot el que sabies. Us desitjo el millor.

Arribar al BigSpin lab va ser de les millors coses que em podien passar després de no tenir clar per on encaminar la meva trajectòria. Lluís i Anna, heu aconseguit formar un molt bon equip tant acollidor com potent científicament. Lluís, sempre he admirat la teva mirada científica, capaç d'enllaçar resultats i veure clar quin és el mecanisme que hi ha darrere. Sense la teva supervisió el projecte no hauria anat pel mateix camí, i poder parlar de tu a tu sabent que donaràs bons consells i idees per tirar endavant és molt reconfortant. I Anna, sempre es pot comptar amb tu perquè aportis una segona opinió del projecte donant punts de vista diferents que sempre ajuden a millorar i també per ajudar a tocar de peus a terra en moments en què és necessari. La vostra visió combinada crec que és molt necessària per mirar des de perspectives diferents els projectes. Us dono les gràcies per tot allò que he après de vosaltres. Agrair també a la meva tutora Rosa Aligué per acceptar ser-ho en moments d'urgència.

Arribar al laboratori i tenir una brillant mestra com tu, Anna Vert, per ensenyar-me de la millor manera possible com treballar amb rigor científic em va ajudar a formar-me en qui sóc ara. Tots els moments que vam compartir, entre matrigel, esferes i molta feina, estaran sempre al meu cor. T'agraeixo molt la teva paciència ensenyant-me, t'asseguro que m'ha servit de molt i que ho aplico dia a dia. Ets una persona molt maca i amb un molt bon cor. Va ser una pena que

marxessis, però l'Èlia segur que estarà encantada de tenir-te com a mare, perquè segur que ets meravellosa. Espero que trobeu la tranquil·litat i l'entorn que buscàveu a Banyoles.

Teresa, suerte que llegaste como refuerzo después de la marcha de Anna, porque lo necesitaba. Siempre estás allí cuando lo necesito para ayudarme no solo en el laboratorio, sino también por darme apoyo moral y por nuestras conversaciones. Y no sólo a mí, sino que estás siempre dispuesta a ayudar a cualquiera y además aportas un poco de serenidad y organización al laboratorio, ¡¡que falta hace muchas veces!! El proyecto que hemos compartido no habría sido lo mismo sin ti y tu punto de vista bioinformático enriqueció muchísimo la investigación. Te admiro muchísimo, por tu fuerza, entereza y por lo trabajadora que eres. Tener una compañera con la que compartir todo el tiempo en el laboratorio hace que la tesis ha sido mucho mejor y más divertida. Muchísimas gracias, te deseo lo mejor.

I a tots els membres del laboratori, tots els companys que formeu o heu format part del Lab Crew, us trobaré molt a faltar quan sigui el moment de marxar. No he estat a gaires laboratoris per poder comparar, però està clar que el bon ambient i els riures ajuden moltíssim a viure d'una manera més positiva el doctorat. S'ha format un equip genial que espero que es mantingui, dintre del possible, al llarg del temps. He tingut molta sort de tenir-vos al costat aquests anys, sempre es pot comptar amb tots vosaltres.

Jessi i Arnau, teniu moltíssima paciència per afrontar el dia a dia al laboratori sense que la cosa es desmadi. Jessi, ets una persona amb qui sempre es pot comptar i que ajudes a tothom. Tenim una gran sort de tenir-te aquí amb nosaltres. Segur que també seràs una mare increïble, et desitjo el millor per tu i la família que esteu formant, la Júlia serà molt feliç amb vosaltres. Arnau, t'he vist aprendre i formar-te com a professional des que vas arribar i sempre m'has ajudat amb problemes varis (la pesada del matrigel, sí...). Ara hauràs de posar una mica de mà dura uns mesos... però segur que te'n sortiràs perfectament!

David, Irene, Josune, Luis i Dani, compartir les penes i glòries del que és fer un doctorat amb vosaltres durant aquests anys ha estat genial. David, sempre estàs allà per treure'ns un somriure amb les teves bromes... i també és molt divertit veure com te les tornen. Hi ha moments èpics que no se m'oblidaran mai, ni a mi ni a ningú que els veiés, segur. Ets treballador com el que més i espero que et vagi genial, tot i que m'hagis abandonat a l'últim moment... Irene, espero que te vaya genial de aquí en adelante porque te lo mereces, eres muy trabajadora y eres muy buena profesional, ¡créetelo! Tu buen humor mañanero alegra el día a todos desde que se te escucha llegar por el pasillo y haces mucho más ameno el trabajo, entre canciones y bailes. Josune, tenerte al lado todo este tiempo ha hecho mucho más divertido el rato de ordenador, que tan aburrido se puede llegar a hacer. ¡Se hace raro no tenerte en el

despacho! Admiro mucho tu constancia para conseguir tu beca, que estás demostrando que mereces totalmente. Compartir teorías y críticas varias contigo, David y todos los que hubieran visto la serie/peli en cuestión ha sido genial (¡¡como el día de Juego de Tronos!!). Y Luis, siempre afrontando todo de manera tan positiva y con tanta energía, contando todo con un brillo en la mirada y sin desanimarte, es muchísimo de admirar, ¡sigue así! La perseverancia hará que tengas magníficos resultados. Dani, acabes de començar la tesis, tot i que ja portes un temps aquí i coneixes perfectament tot. Els nostres tractes compartint feina han servit de molt. Segur que t'anirà genial, ja tens un bon projecte en marxa. ¡Ánimos a todos los que os queda poco, seguro que tendréis una súper tesis!

I les postdocs Violeta, Yolanda i Roshana. Violeta, eres muy buena profesional, muy trabajadora y se nota muchísimo que lo haces todo de la mejor manera que sabes, ¡que es mucho! Seguro que la vida te traerá cosas maravillosas. Yolanda, es nota que ets una persona molt empàtica i que et preocupes molt pels altres. Ens has ajudat a tots en allò que has pogut, ets la nostra bioinformàtica preferida (junt amb la Teresa!). Desitjo que et vagi genial a tu i a la teva família, el Gabriel segur que estarà molt ben cuidat. And Roshana, you are a great professional and you always make great comments on our research, I am sure you will obtain all you want in the future because you deserve it. No em puc oblidar de tu Joan, que sempre ens ajudes amb tot, fins i tot quan no tens temps ni per tu mateix, la teva dedicació és admirable. Quina gràcia em va fer saber que us coneixíeu amb el meu pare! Marta, tu m'has ajudat moltíssim amb totes les immunos i els teus consells, sempre tan servicial amb tots.

També vull recordar a tots els que heu passat pel laboratori en aquest temps que he estat jo aquí. Carlota, em vas ensenyar què era estar acabant un doctorat i un article a la vegada, amb tota la pressió que comporta. Erika, no et vaig conèixer mentre estaves al laboratori, però els cops que ens hem vist he pogut veure la bona professional que ets. Cristina Ruíz, verte afrontar los problemas a tu manera, hablando las cosas de frente, sin tapujos, me hizo ver la necesidad de no callarse las cosas cuando es necesario. Espero que disfrutes de tu nueva etapa, junto con tus magníficas hijas. Leonie, it was a pity that you had to leave, but I really hope you have found a great place where you can finally do your PhD and be recognised as the great researcher you are. Laura, ets una boníssima investigadora i estic segura que tindràs molt d'èxit en la teva carrera científica, ja que ens has demostrat a tots que vals molt per això. Sempre has tingut molt bones idees per intentar reconduir els projectes i has ajudat en tot allò que has pogut. Espero que quan tornis puguem celebrar tots plegats el teu èxit. Vull agrair també a la Cristina Porcheri, la Neus i tots els estudiants que han passat pel laboratori: Clàudia, Sara, Zara, Irene Hernández, Noemi, Gemma, Genís, Júlia... Tots heu estat aquí amb nosaltres compartint bons moments. Sara e Irene, fue genial estar con vosotras mientras hacíais el

máster, promoviendo el espíritu de grupo (¡¡cómo olvidar nuestra beer sesión!!) y haciendo que nos acercáramos más entre nosotros entre risas, os deseo lo mejor.

A més, vull agrair a tots els investigadors principals i integrants dels grups del programa de càncer de l'IMIM. Heu contribuït a què la qualitat de la recerca millorés amb els vostres comentaris i ajudes. També agrair al grup del Dr. Alberto Villanueva, del Dr. Alberto Muñoz i del Dr. Toni Celià i als clínics que ens han ajudat amb la part que els pertoca, Dr. Marta Guix, Dr. Mar Iglesias, Dr. Marta Salido, Dr. Beatriz Bellosillo i a tota la resta de professionals que heu ajudat a què aquest projecte es pogués dur a terme.

Per la part que us pertoca, per haver-me d'aguantar en els meus moments bons i dolents, us vull donar les gràcies a totes les persones que seguïu al meu costat després de tant de temps. A tots els amics que heu estat amb mi tot aquest temps. De tots he extret incomptables aprenentatges. Mariona, ets la meva amiga més antiga i estem molt compenetrades, espero que res ens separi i que la nostra relació no faci més que augmentar, compartint passejos (amb gossets), converses i desfogant-nos de tot. Karla i Romina, les dues sou increïbles i m'heu ajudat moltíssim a sentir-me estimada. Karla, has hagut de superar moltes coses al llarg de la teva vida però sempre estàs allà amb un somriure i amb ganes de xerrar i compartir coses. Romina, siempre con unas ganas increíbles de aprender de todo y con mil preguntas por hacer, tienes un espíritu muy curioso y con muchas ganas de mejorar día a día, preocupándote por todos. Sigue así. Cèlia, Cris, Edgar, Ivan... aquests últims temps hem compartit molt bons moments que espero que no s'acabin mai, per molts més moments així, tots junts, ajudant-me a oblidar les coses negatives i a gaudir. I també al Pablo, Berta, Ana Claudia, Nathalia, Aitor... no ens veurem tant com m'agradaria però sempre us agrairé que estigueu allà. Finalment, a totes les amigues de la universitat. Ainoa i Ana, em vau donar la vida en una etapa també bastant complicada plena d'estrès però amb moltes coses bones. I Marta, Miruna, Elena, Sara, Núria i Mireia també per tots els moments meravellosos a la universitat, però sobretot els posteriors, que encara seguim tenint i que enforteixen molt més la nostra relació.

Per últim, els més importants. Els que sempre esteu amb mi, en els dies bons i en els dolents, que són els dies en què més us necessito. La meva família m'ha donat una meravellosa vida que no canviaria per a res i que, amb la vostra educació, m'ha portat a ser la que sóc ara. Pares i Oriol, us dec moltíssim. I tu, amor, has fet que sempre segueixi endavant tot i les dificultats. Hem format una petita família increïble que m'ha fet molt feliç, junt amb els passejos amb el Kibu, que aconseguen que m'oblidi de tot en aquells moments. No us ho diré tant sovint com caldria, però no ho oblideu mai. Us estimo molt.

Moltíssimes gràcies a tots.

ABSTRACT

ABSTRACT

Current therapy against colorectal cancer (CRC) is based on DNA-damaging agents that eradicate highly proliferative malignant cells. Whether sublethal chemotherapy affects tumour cell behaviour and impacts on patient outcome is primarily unstudied. We now show that sublethal chemotherapy imposes a non-senescent quiescent-like phenotype (TQL phenotype) to *TP53* wildtype human CRC patient derived organoids (PDOs) and cell lines. CRC cells displaying this phenotype exhibit tumour-initiating activity comparable to untreated cells but superior metastatic capacity. Thus, re-entry of TQL cells into the cell cycle could be partially responsible of CRC patients' relapse and metastasis. The TQL phenotype is linked to the acquisition of foetal traits downstream of YAP1, similar to that observed in intestinal regeneration after damage. Importantly, we have uncovered from TQL cells a foetal intestinal stem cell signature (feISC signature) that is also found in untreated human CRC tumours. Notably, nuclear YAP1 accumulation or detection of this signature predict poor prognosis in untreated CRC patients carrying *TP53* wildtype tumours. Collectively, our results uncover a potential deleterious effect of chemotherapy and show that detection of nuclear YAP1 or foetal ISC signatures in tumours could be implemented in the clinical practice to inform about patient candidates for closer follow-up or specific pathway-based therapies, such as inhibition of YAP1.

RESUMEN

La terapia actual contra el cáncer colorectal (CRC) está basada en el uso de agentes que dañan el DNA, los cuales erradican específicamente las células malignas muy proliferantes. Actualmente se dispone de muy poca información sobre si el tratamiento con quimioterapia subletal afecta el comportamiento de las células tumorales y si tiene un impacto en la evolución del paciente. En el presente estudio mostramos que la quimioterapia subletal impone un fenotipo quiescente no senescente (fenotipo TQL) en organoides derivados de pacientes (PDOs) con CRC y en líneas celulares con p53 funcional. Las células de CRC que muestran este fenotipo presentan una capacidad de iniciación de nuevos tumores comparable a la de las células no tratadas y una capacidad metastática superior. Por lo tanto, la reentrada de las células TQL al ciclo celular podría parcialmente ser responsable de la recaída y la metástasis de los pacientes con CRC. El fenotipo TQL está asociado con la adquisición de rasgos fetales dependiente de YAP1, similar a lo observado en la regeneración del intestino dañado. Es importante destacar que hemos descrito a partir de las células TQL una signatura de células madre intestinales fetales (signatura feISC) que también se encuentra en tumores CRC humanos no tratados. Además, la acumulación de YAP1 al núcleo o la detección de esta signatura predice mal pronóstico en tumores con p53 funcional de pacientes con CRC no tratados. Colectivamente, nuestros resultados revelan un nuevo potencial efecto perjudicial de la quimioterapia y muestran que la detección de YAP1 nuclear o de signaturas feISC en tumores se podría implementar en la práctica clínica para informar sobre los pacientes candidatos a un seguimiento más cercano o a terapias dirigidas específicas, como la inhibición de YAP1.

RESUM

La teràpia actual contra el càncer colorectal (CRC) està basada en l'ús d'agents que danyen el DNA, els quals eradiquen específicament les cèl·lules malignes molt proliferants. Actualment es disposa de molt poca informació sobre si el tractament amb quimioteràpia subletal afecta el comportament de les cèl·lules tumorals i si té un impacte en l'evolució del pacient. En el present estudi mostrem que la quimioteràpia subletal imposa un fenotip quiescent no senescent (fenotip TQL) en organoids derivats de pacients (PDOs) amb CRC i en línies cel·lulars amb p53 funcional. Les cèl·lules de CRC que mostren aquest fenotip presenten una capacitat d'iniciació de nous tumors comparable a la de les cèl·lules no tractades i una capacitat metastàtica superior. Per tant, la reentrada de les cèl·lules TQL al cicle cel·lular podria parcialment ser responsable de la recaiguda i la metastasi dels pacients amb CRC. El fenotip TQL està associat amb l'adquisició de trets fetals depenent de YAP1, similar a l'observat en la regeneració de l'intestí danyat. És important destacar que hem descrit a partir de les cèl·lules TQL una signatura de cèl·lules mare intestinals fetals (signatura feISC) que també es troba en tumors CRC humans no tractats. A més, l'acumulació de YAP1 al nucli o la detecció d'aquesta signatura prediu mal pronòstic en tumors amb p53 funcional de pacients amb CRC no tractats. Col·lectivament, els nostres resultats revelen un nou potencial efecte perjudicial de la quimioteràpia i mostren que la detecció de YAP1 nuclear o de signatures feISC en tumors es podria implementar a la pràctica clínica per informar sobre els pacients candidats a un seguiment més proper o a teràpies dirigides específiques, com la inhibició de YAP1.

TABLE OF CONTENTS

TABLE OF CONTENTS

ACKNOWLEDGEMENTS	9
ABSTRACT	15
TABLE OF CONTENTS	23
TABLES AND FIGURES	29
ABBREVIATIONS AND ACRONYMS	35
INTRODUCTION	45
11. THE INTESTINE	47
<i>11.1. The gastrointestinal tract organisation</i>	<i>47</i>
<i>11.2. Differentiated intestinal cells</i>	<i>47</i>
<i>11.3. Intestinal stem cells</i>	<i>49</i>
<i>11.4. Regeneration of the intestine</i>	<i>51</i>
12. COLORECTAL CANCER	53
<i>12.1. General overview of colorectal cancer</i>	<i>53</i>
<i>12.2. Cancer stem cells</i>	<i>55</i>
<i>12.3. Therapy treatments in CRC</i>	<i>56</i>
13. PATIENT-DERIVED ORGANOID S	57
<i>13.1. Preclinical models</i>	<i>57</i>
<i>13.2. 3D cultures or organoids</i>	<i>58</i>
<i>13.3. Organoids for modelling the intestine and CRC</i>	<i>59</i>
14. TUMOUR DORMANCY AND RELAPSE	61
<i>14.1. Role of CSCs in tumour relapse</i>	<i>61</i>
<i>14.2. Cell cycle arrest in response to DNA damage</i>	<i>64</i>
<i>14.3. Cell quiescence and drug resistance</i>	<i>66</i>
<i>14.4. Cell cycle re-entry</i>	<i>67</i>
<i>14.5. Cell senescence: is it reversible?</i>	<i>68</i>
15. YAP1 IN INTESTINAL REGENERATION AND CANCER	70
<i>15.1. The Hippo pathway</i>	<i>70</i>
<i>15.2. YAP1 in the intestine</i>	<i>70</i>
<i>15.3. YAP1 in CRC</i>	<i>72</i>
<i>15.4. YAP1 in tumour dormancy</i>	<i>72</i>
16. STEM CELL SIGNATURES WITH CLINICAL APPLICATIONS	74
<i>16.1. Prognostic value of stem cell signatures in cancer</i>	<i>74</i>

16.2. Intestinal stem cell signatures in CRC	74
OBJECTIVES	77
MATERIALS AND METHODS	81
MM1. PDOs GENERATION	83
MM2. PDOs CULTURE AND PASSAGING	86
<i>MM2.1. Mechanical disaggregation</i>	<i>86</i>
<i>MM2.2. Disaggregation to single cells</i>	<i>86</i>
MM3. DNA ISOLATION AND SEQUENCING	87
<i>MM3.1. DNA extraction from PDOs</i>	<i>87</i>
<i>MM3.2. DNA sequencing from PDOs</i>	<i>87</i>
MM4. PDOs VIABILITY ASSAYS	88
MM5. PDOs TIC ASSAY <i>IN VITRO</i>	89
MM6. ANIMAL STUDIES	89
MM7. HUMAN SAMPLES	90
MM8. PARAFFIN EMBEDDING OF SAMPLES	91
<i>MM8.1. PDOs samples</i>	<i>91</i>
<i>MM8.2. Tissue samples</i>	<i>91</i>
MM9. HAEMATOXYLIN AND EOSIN (HE) STAINING	92
MM10. ALCIAN BLUE STAINING	92
MM11. IMMUNOHISTOCHEMISTRY AND IMMUNOFLUORESCENCES	93
MM12. CELL LINES AND REAGENTS	94
MM13. PDOs INFECTION	95
<i>MM13.1. Viral production</i>	<i>95</i>
<i>MM13.2. Viral infection</i>	<i>96</i>
MM14. FLUORESCENT IN-SITU HYBRIDISATION (FISH)	97
MM15. CELL CYCLE ANALYSIS	97
MM16. CELL SENESENCE ASSAYS	98
<i>MM16.1. Senescence β-Galactosidase Staining Kit</i>	<i>98</i>
<i>MM16.2. Cell Event Senescence Green Flow Cytometry Assay Kit</i>	<i>99</i>
MM17. ANNEXIN V BINDING ASSAY	99
MM18. COMET ASSAY	100
MM19. CELL LYSATES	101
MM20. WESTERN BLOT	101
MM21. RNA ISOLATION	103
MM22. RT-QPCR	103

MM23. RNA-SEQUENCING (RNA-SEQ) AND DATA ANALYSIS.....	104
MM24. CHROMATIN-IMMUNOPRECIPITATION (CHIP)-QPCR AND CHIP-SEQ	106
MM25. GENERATION OF FOETAL INTESTINAL STEM CELL (FEISC) SIGNATURES	109
<i>MM25.1. Description of the patient gene expression data sets.....</i>	<i>109</i>
<i>MM25.2. Signature definition.....</i>	<i>109</i>
<i>MM25.3. Association of the signatures with clinical outcome</i>	<i>109</i>
MM26. QUANTIFICATION AND STATISTICAL ANALYSIS	110
RESULTS	111
R1. ESTABLISHMENT AND CHARACTERISATION OF A CRC PDOs BIOBANK	113
<i>R1.1. Establishment of a CRC PDOs biobank.....</i>	<i>113</i>
<i>R1.2. CRC PDOs of our biobank resemble the original tumours</i>	<i>116</i>
<i>R1.3. CRC PDOs of our biobank display different drug sensitivity.....</i>	<i>118</i>
R2. CHARACTERISATION OF LOW-DOSE CHEMOTHERAPY TREATMENT EFFECTS IN CRC PDOs.....	120
<i>R2.1. Low-dose treated-PDOs acquire a non-senescent quiescent-like state</i>	<i>120</i>
<i>R2.2. Low-dose CT treatment is not associated with an increase in apoptosis or persistent DNA-damage.....</i>	<i>126</i>
<i>R2.3. TQL cells display upregulation of the p53 pathway</i>	<i>129</i>
<i>R2.4. The TQL phenotype is associated with acquisition of a foetal intestinal stem cell (feISC) signature</i>	<i>133</i>
<i>R2.5. TQL cells displaying the feISC signature retain their tumour-initiating capacity, which could be associated with increased Notch activation.....</i>	<i>134</i>
R3. DEFINITION OF A FEISC SIGNATURE WITH PROGNOSTIC VALUE	141
<i>R3.1. The feISC signature shows a coordinate expression in untreated CRC patients....</i>	<i>141</i>
<i>R3.2. The feISC signature is p53-dependent.....</i>	<i>146</i>
<i>R3.3. Tumours displaying the feISC signature are mainly classified as mesenchymal</i>	<i>150</i>
<i>R3.4. The feISC signature has prognostic value in CRC</i>	<i>151</i>
<i>R3.5. Acquisition of the feISC signature is dependent on YAP1 activation.....</i>	<i>157</i>
<i>R3.6. TQL cells are more resistant to CT treatment, but combination of CT with YAP1 or BRAF inhibitors efficiently kill them</i>	<i>164</i>
DISCUSSION	169
D1. PDOs AS A TOOL FOR CANCER RESEARCH	171
D2. REVERSIBLE GROWTH ARREST IN WT TP53 DTP CELLS.....	171
D3. TUMOURAL FOETAL CONVERSION UPON DNA DAMAGE	174
D4. CLINICAL APPLICATIONS OF THE FEISC SIGNATURE	176

D5. CONTRIBUTION OF TUMOUR STROMA TO FEISC CONVERSION.....	179
D6. IKKA IN TQL CELLS	180
CONCLUSIONS.....	181
<i>PART I: Establishment and characterisation of a CRC PDOs biobank</i>	<i>183</i>
<i>PART II: Characterisation of low-dose chemotherapy treatment effects in CRC PDOs....</i>	<i>183</i>
<i>PART III: Definition of a feISC signature with prognostic value</i>	<i>183</i>
BIBLIOGRAPHY.....	185
ANNEX.....	211
ANNEX 1	213
ANNEX 2	215

TABLES AND FIGURES

TABLES AND FIGURES

INTRODUCTION	45
FIGURE I1. SMALL INTESTINE AND COLON STRUCTURE.	49
FIGURE I2. NOTCH SIGNALLING PATHWAY.	50
FIGURE I3. THE ADENOMA-CARCINOMA SEQUENCE.	53
TABLE I1. CLASSIFICATION OF CRC ACCORDING TO TNM STAGES.	54
FIGURE I4. 3D CULTURES.....	60
FIGURE I5. TGF β SIGNALLING PATHWAY.....	62
FIGURE I6. MECHANISMS OF DRUG RESISTANCE.	63
FIGURE I7. MULTIPLE FACTORS INDUCE A GROWTH ARREST AT G1 PHASE.	65
FIGURE I8. CELL CYCLE CHECKPOINTS.	66
FIGURE I9. HIPPO PATHWAY SIGNALLING.	71
MATERIALS AND METHODS	81
TABLE MM1. LIST OF CRC PDOs IN THE BIOBANK.....	83
TABLE MM2. LIST OF DF12 ⁺⁺⁺ MEDIUM FACTORS.....	84
TABLE MM3. LIST OF COMPLETE MEDIUM FACTORS.	84
TABLE MM4. FACTORS USED FOR TUMOUR DISAGGREGATION.....	85
TABLE MM5. LIST OF CRC PDOs USED IN THIS STUDY, WITH THEIR IC ₂₀ AND IC ₃₀ INDICATED.	88
TABLE MM6. ANTIBODIES USED FOR IHC-P AND IF.....	94
TABLE MM7. SGRNA.....	95
TABLE MM8. ANTIBODIES USED FOR WB.....	102
TABLE MM9. PRIMERS USED FOR RT-QPCR.....	104
TABLE MM10. PRIMERS USED FOR CHIP-QPCR.....	108
RESULTS	111
FIGURE R1. OPTIMISATION OF CRC PDOs GENERATION.	113
FIGURE R2. CRC PDOs DISPLAY CYSTIC AND COMPACT MORPHOLOGIES.	114
FIGURE R3. CRC PDOs ARE HIGHLY PROLIFERATING AND DISPLAY ISC-LIKE TRAITS.....	115
FIGURE R4. CRC PDOs CELLS DO NOT DIFFERENTIATE TO PANETH AND GOBLET CELLS.	116
FIGURE R5. CRC PDOs RECAPITULATE ORIGINAL TUMOUR MUTATIONS.	117
FIGURE R6. EACH CRC PDO NEEDS TO BE SEEDED IN A DIFFERENT NUMBER OF CELLS PER WELL.	118
FIGURE R7. CRC PDOs DISPLAY DIFFERENT DRUG SENSITIVITY.....	119
FIGURE R8. DETERMINATION OF IC ₂₀ AND IC ₃₀ DOSES OF 5-FU+IRI.....	120

FIGURE R9. SUBLETHAL DOSES OF CT TREATMENT PRODUCE CELL GROWTH ARREST IN CRC PDOs.....	121
FIGURE R10. SUBLETHAL DOSES OF RADIATION REDUCE CELL VIABILITY IN CRC PDOs.	122
FIGURE R11. SUBLETHAL DOSES OF CT TREATMENT INHIBIT CELL PROLIFERATION.....	123
FIGURE R12. SUBLETHAL DOSES OF CT TREATMENT ALTER CELL CYCLE OF PDOs.	124
FIGURE R13. THERE IS ABSENCE OF CHROMOSOMES AND NUCLEI ALTERATIONS IN IC20 AND IC30-TREATED PDOs.	124
FIGURE R14. LOW-DOSE CT TREATMENT DOES NOT INCREASE THE PROPORTION OF SENESCENT CELLS.	125
FIGURE R15. SENOLYTIC DRUG DASATINIB DO NOT REDUCE THE CELL VIABILITY OF TREATED PDOs.....	126
FIGURE R16. SUBLETHAL DOSES OF CT TREATMENT DO NOT PRODUCE INCREASE IN APOPTOSIS AFTER 72 H.	127
FIGURE R17. SUBLETHAL DOSES OF CT TREATMENT DO NOT PRODUCE ACCUMULATION OF THE DNA-DAMAGE MARKER γ H2A.X.....	128
FIGURE R18. SUBLETHAL DOSES OF CT TREATMENT PRODUCE DNA-DAMAGE THAT CAN BE REPAIRED AFTER 72 H.	128
FIGURE R19. P53 IS THE HIGHEST ENRICHED PATHWAY IN TQL CELLS.	129
FIGURE R20. SENESCENCE IS NOT ENRICHED IN TQL CELLS.....	130
FIGURE R21. P53 PATHWAY IS UPREGULATED IN TQL CELLS, BUT NOT THE P16-DRIVEN IRREVERSIBLE SENESCENCE PATHWAY.....	131
FIGURE R22. P53 TARGET GENES ARE INDUCED AFTER SUBLETHAL DOSES OF CT TREATMENT. .	132
FIGURE R23. P53 MUTATED PDOs DISPLAY APOPTOSIS AND PERSISTENT DNA-DAMAGE UPON TREATMENT WITH SUBLETHAL DOSES OF CT.....	133
FIGURE R24. SUBLETHAL DOSES OF CT INDUCE A CONVERSION INTO A FEISC PHENOTYPE IN PDO5.....	134
FIGURE R25. TP53 WT PDO5, BUT NOT TP53 MUTANT PDOs, RETAINS ITS TIC ACTIVITY IN VITRO.....	135
FIGURE R26. RETAINED TIC CAPACITY IN VITRO IS NOT DUE TO REMAINING PROLIFERATING CELLS.	136
FIGURE R27. TREATED PDO5 CELLS DISPLAY A SLIGHTLY SUPERIOR METASTATIC CAPACITY THAN UNTREATED CELLS WHEN INJECTED INTRACARDIACALLY.	137
FIGURE R28. TREATED PDO5 CELLS DISPLAY A SIGNIFICANTLY HIGHER ABILITY TO GENERATE INTRAPERITONEAL IMPLANTS THAN UNTREATED CELLS WHEN INJECTED IN THE CECUM.....	138
FIGURE R29. ACTIVE NOTCH SIGNALLING COULD BE IMPLICATED IN THE REVERSION OF THE TQL PHENOTYPE.	139

FIGURE R30. THE FEISC SIGNATURE IS EXPRESSED IN A COORDINATE MANNER IN UNTREATED CRC PATIENTS.	141
FIGURE R31. DETERMINATION OF THE 28UP+8DOWN-FEISC SIGNATURE.	142
FIGURE R32. COORDINATED EXPRESSION OF THE 28UP+8DOWN-FEISC SIGNATURE IN TCGA DATA SET.	143
FIGURE R33. COORDINATED EXPRESSION OF THE 28UP+8DOWN-FEISC SIGNATURE IN TCGA DATA SET.	144
FIGURE R34. THE 28UP+8DOWN-FEISC SIGNATURE IS PRESENT IN TREATED TP53 WT PDOs.	145
FIGURE R35. PROTEIN LEVELS FROM THE 28UP+8DOWN-FEISC SIGNATURE ARE UPREGULATED.	146
FIGURE R36. THE 28UP+8DOWN-FEISC SIGNATURE IS NOT PRESENT IN TREATED TP53 MUTANT PDOs.	147
FIGURE R37. THE 28UP+8DOWN-FEISC SIGNATURE IS P53 DEPENDENT.	148
FIGURE R38. ADDITIONAL TRANSCRIPTION FACTORS SHOULD GOVERN THE COORDINATE EXPRESSION OF THE FEISC SIGNATURE.	149
FIGURE R39. TUMOURS DISPLAYING THE FEISC SIGNATURE ARE MAINLY CMS4 AND ASSOCIATED WITH SECRETORY AND MIGRATORY FUNCTIONS.	150
FIGURE R40. THE FEISC SIGNATURE HAS PROGNOSTIC VALUE USING CRC DATA SETS.	152
FIGURE R41. THE FEISC SIGNATURE HAS PROGNOSTIC VALUE IN STAGE II AND II+III PATIENTS.	152
FIGURE R42. THE FEISC SIGNATURE HAS PROGNOSTIC VALUE IN TP53 WT PATIENTS.	153
FIGURE R43. THE FEISC SIGNATURE HAS PROGNOSTIC VALUE IN TP53 WT PATIENTS IN TCGA DATA SET.	154
FIGURE R44. THE FEISC SIGNATURE HAS PROGNOSTIC VALUE IN PATIENTS WITH HIGH P21 LEVELS.	155
FIGURE R45. THE FEISC SIGNATURE HAS PROGNOSTIC VALUE IN CMS4 PATIENTS.	155
FIGURE R46. THE REDUCED 5UP+3DOWN-FEISC FEISC SIGNATURE HAS PROGNOSTIC VALUE.	156
FIGURE R47. THE REDUCED 5UP+3DOWN-FEISC FEISC SIGNATURE HAS PROGNOSTIC VALUE IN STAGE II AND II+III PATIENTS.	157
FIGURE R48. SUBLETHAL DOSES OF CT TREATMENT PRODUCE INCREASE IN NYAP1.	158
FIGURE R49. YAP1 INHIBITION PRECLUDES THE ACQUISITION OF THE FEISC SIGNATURE.	159
FIGURE R50. THE FEISC SIGNATURE HAS PROGNOSTIC VALUE IN PATIENTS FROM THE MARISA COHORT WITH HIGH YAP1 LEVELS.	160
FIGURE R51. A SUBGROUP OF PATIENTS DISPLAYS TQL PHENOTYPE ACQUISITION AFTER TREATMENT.	161
FIGURE R52. PATIENTS PRESENT UPREGULATION OF NYAP1 AFTER TREATMENT TOGETHER WITH FEISC GENES.	162

FIGURE R53. TREATED PATIENTS OF OUR COHORT WITH HIGHER LEVELS OF NYAP1 SHOW A TENDENCY TO POOR PROGNOSIS.	163
FIGURE R54. TREATED PATIENTS OF OUR TMA WITH HIGHER LEVELS OF NYAP1 HAVE POOR PROGNOSIS.	164
FIGURE R55. TQL CELLS DISPLAY RESISTANCE TO SUBSEQUENT CT TREATMENTS.	165
FIGURE R56. YAP1 INHIBITOR IN COMBINATION WITH CT TREATMENT EFFICIENTLY KILLS TQL CELLS.	165
FIGURE R57. BRAF INHIBITOR IN COMBINATION WITH CT TREATMENT EFFICIENTLY KILLS TQL CELLS.	166
DISCUSSION	169
FIGURE D1. WORKING MODEL.....	175
FIGURE D2. TUPDO TEST: A RT-QPCR BASED DIAGNOSIS KIT.	178

ABBREVIATIONS AND ACRONYMS

ABBREVIATIONS AND ACRONYMS

2D	Two-dimensional
3D	Three-dimensional
5-FU	5-Fluorouracil
5-FU+Iri.	5-Fluorouracil plus Irinotecan
5-FU+OX	5-Fluorouracil plus Oxaliplatin
ABHD4	Abhydrolase Domain Containing 4
ABL	Abelson Tyrosine-Protein Kinase
ACTB	Actin Beta
AEN	Apoptosis Enhancing Nuclease
AGMAT	Agmatinase
ALDH1	Aldehyde Dehydrogenase 1 Family Member
ALK	Anaplastic Lymphoma Receptor Tyrosine Kinase
ALPI	Intestinal Alkaline Phosphatase
APC	Adenomatous Polyposis Coli
ARL4C	ADP Ribosylation Factor Like GTPase 4C
aSC	Adult Stem Cell
ASCL2	Achaete-Scute Complex Homolog-Like 2
ATM	Ataxia Telangiectasia Mutated
ATOH1	Atonal BHLH Transcription Factor 1
ATP	Adenosine Triphosphate
B2M	Beta-2-Microglobulin
BAX	BCL2 Associated X
bFGF	Basic Fibroblast Growth Factor
BMI1	B Lymphoma Mo-MLV Insertion Region 1 Homolog
BMP	Bone Morphogenetic Protein
BRAF	B-Rapidly Accelerated Fibrosarcoma
BrdU	5-Bromo-2'-deoxyuridine
BSA	Bovine Serum Albumin
CAK	CDK Activating Kinase
Cas9	CRISPR-associated protein 9
CBC	Crypt Base Columnar
CD133	Cluster of Differentiation 133, or Prominin 1
CD44v6	Cluster of Differentiation 44 Variant Domain 6
CD99L2	Cluster of Differentiation 99 Molecule Like 2
CDK1/2	Cyclin Dependent Kinase 1/2
CDKN1A	Cyclin Dependent Kinase Inhibitor 1A
CDKN2A	Cyclin Dependent Kinase Inhibitor 2A

cDNA	Complement DNA
CDX	Cell Line-Derived Xenografts
CDX1	Caudal Type Homeobox 1
ChIP	Chromatin Immunoprecipitation
CIN	Chromosomal Instability
CK-18	Cytokeratin 18
CMS	Consensus Molecular Subtypes
Cnx43	Connexin 43
CoIP	Co-Immunoprecipitation
COL18A1	Collagen Type XVIII Alpha 1 Chain
CRC	Colorectal Cancer
CRIP2	Cysteine Rich Protein 2
CRISPR	Clustered Regularly Interspaced Short Palindromic Repeats
CSC	Cancer Stem Cell
CT	Chemotherapy
CTGF	Connective Tissue Growth Factor
Cyr61	Cysteine-Rich Heparin-Binding Protein 61
DAB	3,3'-Diaminobenzidine
DAPI	4',6-Diamidino-2-Phenylindone
DCLK1	Doublecortin-Like Kinase 1
DCS	Deep Crypt Secretory
DDR	DNA Damage Response
DEG	Differentially Expressed Genes
DF12 ⁺⁺⁺	Dulbecco's Modified Eagle Medium: Nutrient Mixture F-12, supplemented
DFS	Disease Free Survival
DII1/4	Delta-Like Canonical Notch Ligand 1/4
DMEM	Dulbecco's Modified Eagle Medium
DMSO	Dimethyl Sulfoxide
DNA	Deoxyribonucleic acid
DOC	2,5-Dimethoxy-4-chloroamphetamine
DPX	Dibutylphthalate Polystyrene Xylene
DSB	Double Strand Break
DSS	Dextran Sodium Sulfate
DTC	Disseminated Tumour Cell
DTP	Drug-Tolerant Persister Cell
E2F	Retinoblastoma-Associated Protein
ECL	Electrochemiluminescence
EDTA	Ethylenediaminetetraacetic acid
EGF	Epidermal Growth Factor
EGFR	Epidermal Growth Factor Receptor

EGTA	Ethylene Glycol-bis(β -aminoethyl ether)-N,N,N',N'-tetraacetic acid
EHS	Engelbreth-Holm-Swarm
EMT	Epithelial-to-Mesenchymal Transition
EPHB2	Ephrin Type-B Receptor 2
ERBB2	Erb-B2 Receptor Tyrosine Kinase 2
ES	Embryonic Stem
FAP	Familial Adenomatous Polyposis
FBS	Foetal Bovine Serum
FC	Fold Change
FDA	Food and Drug Administration
FDR	False Discovery Rate
feISC	Foetal Intestinal Stem Cell
FGFR2	Fibroblast Growth Factor Receptor 2
FISH	Fluorescence In Situ Hybridization
FOLFIRI	F olinic Acid plus 5- F luorouracil plus I rinotecan
FOLFOX	F olinic Acid plus 5- F luorouracil plus O xaliplatin
FOXO	Forkhead Box O
GEM	Genetically Engineered Mice
GEO	Gene Expression Omnibus
GFI1	Growth Factor Independent 1 Transcriptional Repressor
GFP	Green Fluorescent Protein
GI	Gastrointestinal Tract
GLIPR1	Glioma Pathogenesis-Related 1
GO	Gene Ontology
gp130	Glycoprotein 130
GPC1	Glypican 1
GRO	Growth-regulated Alpha Protein or CXCL1
GSEA	Gene Set Enrichment Analysis
H3	Histone 3
HE	Haematoxylin and eosin
HES1/2/5	Hairy and Enhancer of Split 1/2/5
HGF	Hepatocyte Growth Factor
HIF1 α	Hypoxia Inducible Factor 1 Subunit Alpha
HOPX	HOP (Homeodomain-Only Protein) Homeobox
HOXB13	Homeobox B13
HPRT1	Hypoxanthine Phosphoribosyltransferase 1
HR	Homologous Recombination
HRP	Horseradish Peroxidase
IC _{20/30/50/60}	20-30-50-60% Inhibitory Concentration
ICAM1	Intercellular Adhesion Molecule 1

ICN1	NOTCH1 Intracellular Domain
IF	Immunofluorescence
IFN γ	Interferon Gamma
IGFBP	Insulin Like Growth Factor Binding Protein
IHC-P	Immunohistochemistry in Paraffin
IL-1/6/8/25/33	Interleukin 1/6/8/25/33
IL17BR	Interleukin 17 Receptor B
iPS	Induced Pluripotent Stem
Iri.	Irinotecan
ISC	Intestinal Stem Cell
IVIS	In Vivo Imaging System
JAG	Jagged
JAK	Janus Kinase
KCNK5	Potassium Two Pore Domain Channel Subfamily K Member 5
ki67	Marker of Proliferation ki-67
KIFC3	Kinesin Family Member C3
Klf4	Kruppel Like Factor 4
KO	Knock-Out
L1CAM	L1 Cell Adhesion Molecule
LAPTM5	Lysosomal Protein Transmembrane 5
LATS1/2	Large Tumour Suppressor Kinase 1/2
LGR4/5	Leucine Rich Repeat Containing G Protein-Coupled Receptor 4/5
LKB1	Serine/Threonine Kinase 11, or STK11
LRIG1	Leucine Rich Repeats And Immunoglobulin Like Domains 1
MDM2	Mouse Double Minute 2
MET	Mesenchymal-to-epithelial transition
MEX3A	Mex-3 RNA Binding Family Member A
MIC-1	Macrophage Inhibitory Cytokine 1
miRNA	microRNA
MLH1	MutL Homolog 1
MMP-1	Metalloproteinase 1
MOB1A/B	Mps One Binder Kinase Activator-Like 1B
MSI	Microsatellite Instability
MSK1	Ribosomal protein S6 kinase alpha-5, or RPS6KA5
MST	Macrophage Stimulating
mTOR	Mechanistic Target Of Rapamycin Kinase
MUC2	Mucin 2
MYB	Avian Myeloblastosis Oncogene
MYCN	Neuroblastoma MYC (Avian Myelocytomatosis) Oncogene
N/A	Not Applicable

NF2	Neurofibromatosis 2
NFκB	Nuclear Factor Kappa B
NGN3	Neurogenin 3
NHEJ	Non-Homologous End Joining
NICD	Notch Intracellular Domain
NOTCH	Notch Receptor
NOXA	Phorbol-12-myristate-13-acetate-induced protein 1, or PMAIP1
NSG	NOD-SCID-gamma
NU/J	Athymic Nude Mice
nYAP1	Nuclear YAP1
O/N	Over-night
OLFM4	Olfactomedin 4
OS	Overall Survival
OX	Oxaliplatin
PBS	Phosphate-buffered Saline
PCA	Principal Component Analysis
PCNA	Proliferating Cell Nuclear Antigen
PCR	Polymerase Chain Reaction
PDGFRA	Platelet Derived Growth Factor Receptor Alpha
PDO	Patient-Derived Organoid
PDX	Patient-Derived Xenograft
PDZ	PDZ Domain: PSD95, Dlg1 and ZO-1
PEI	Polyethylenimine
PFA	Paraformaldehyde
PGE ₂	Prostaglandin E2
PHLDA3	Pleckstrin Homology Like Domain Family A Member 3
PI	Propidium Iodide
PIK3CA	Phosphatidylinositol-4,5-Bisphosphate 3-Kinase Catalytic Subunit Alpha
PLK2	Polo Like Kinase 2
Pou2f3	POU Class 2 Homeobox 3
PUMA	Bcl-2-binding component 3, or BBC3
Rb	Retinoblastoma Protein
PS	Phosphatidylserine
PVDF	Polyvinylidene Fluoride
RAS	Rat Sarcoma Oncogene
RASSF1A	Ras Association Domain Family Member 1A
revSC	Revival Stem Cell
RIPA	Radioimmunoprecipitation Assay
RNA	Ribonucleic Acid
RNA-seq	RNA sequencing

ROCK	Rho-associated Protein Kinase
RT	Room Temperature
RT-qPCR	Reverse Transcription PCR
RUNX	Runt-related transcription factor 1
S100A4	S100 Calcium Binding Protein A4
SAHF	Senescence-Associated Heterochromatin Foci
SASP	Senescence Associated-Secretory Phenotype
SAV1	Salvador Family WW Domain Containing Protein 1
SA- β -gal	Senescence-Associated β -Galactosidase
SCA-1/LY6A	Stem Cell Antigen 1/Lymphocyte Antigen 6A
SCRIB	Scribble
scRNA-seq	Single Cell RNA-seq
SDS	Sodium Dodecyl Sulphate
SDS-PAGE	SDS-polyacrylamide gel electrophoresis
SERPINH1	Serpin Family H Member 1
SESN1	Sestrin 1
sgRNA	Single Guide RNA
SMAD2/4	Small Mothers Against Decapentaplegic Family Member 2/4
SOX9	SRY (Sex Determining Region Y)-Box 9
SPDEF	SAM Pointed Domain Containing ETS Transcription Factor
SPIB	Spi-B Transcription Factor
SRC	Avian Sarcoma (Schmidt-Ruppin A-2)
SSB	Single Strand Break
STAT	Signal Transducer and Activator of Transcription
TA	Transient amplifying
TAZ	Transcriptional co-activator with PDZ-binding motif
TBP	TATA-Box binding Protein
TBS-T	Tris-Buffered Saline with Tween-20
TCGA	The Cancer Genome Atlas
TCGA-COAD	The Cancer Genome Atlas Colon Adenocarcinoma
TCGA-READ	The Cancer Genome Atlas Rectum Adenocarcinoma
TEAD	Transcription Enhancer Factor Domain
TERT	Telomerase Reverse Transcriptase
TGF α / β	Transforming Growth Factor Alpha/Beta
TIC	Tumour Initiating Capacity
TIMP2	Metalloproteinase Inhibitor 2
TMA	Tissue Microarray
TP53	Tumour Protein 53
TQL	Therapy-Induced Quiescent Like
TROP2	Tumour Associated Calcium Signal Transducer 2, or TACTSTD2

TSA	Tyramide Signal Amplification
TSPAN4	Tetraspanin 4
TUBB6	Tubulin Beta 6 Class V
VAMP5	Vesicle Associated Membrane Protein 5
VEGF	Vascular Endothelial Growth Factor A
WB	Western Blot
Wnt3	Wnt Family Member 3
WT	Wildtype
YAP	Yes-Associated Protein
YES	Yes Proto-Oncogene 1
ZMAT3	Zinc Finger Matrin-Type 3
β -ME	β -Mercaptoethanol
γ H2A.X	Phospho-Histone H2A family member X

INTRODUCTION

11. THE INTESTINE

11.1. The gastrointestinal tract organisation

The **gastrointestinal (GI) tract** is part of the digestive system, beginning in the oral cavity and ending in the anus. Its main functions are digestion and absorption of the nutrients that come from ingested food. Specifically, the intestine is divided into the small and large part, being the **small intestine** subdivided in duodenum, jejunum and ileum; and the **large intestine** in the cecum, colon (ascending, transverse, descending and sigmoid colon), rectum and anus ¹.

The small intestine consists of four layers. The **mucosa** is located in the inner part of the intestine, where the digestion process is carried out, and presents a very particular distribution to accomplish its function. It is formed by projections of the layer into the lumen, the villi, along with interspersed invaginations, the crypts. Then, there are the **submucosa**, where lymphatic and blood vessels are located; the **muscularis externa**, a muscular layer which permits the movements necessary for digestion; and the **serosa**, which recovers most of the GI tract for protection ¹.

The small intestine is responsible of performing the major part of the absorption, thanks to mucosal folds, villi and microvilli shapes that produce a huge absorptive surface area. In contrast, the large intestine lacks of these structures, because, unlike the small intestine, it primarily absorbs water and electrolyte still left in the digested food and is where the faeces are formed. For this, the **crypts** in the colon are deeper but they are not folded forming **villi** (FIGURE I1). However, the rest of the layers of the large intestine are similar to the small intestine ².

11.2. Differentiated intestinal cells

In the villi resides the main proportion of the fully differentiated cells, which are cells specialised to carry out specific functions in the intestine. Progenitor cells can acquire two different cell fates: the **absorptive** fate, which is controlled by the Notch pathway target *Hes1* ³, or the **secretory** fate, when *Atoh1* and *Dll1* are expressed ⁴. The main cell types in the small intestine are ^{1,5}:

- **Enterocytes:** they are the major cell type in the villi and are responsible of nutrient absorption. Enterocytes can be detected by alkaline phosphatase (*Alpi*) high expression ⁶.

- **M cells:** they are lymphoid follicle-associated epithelium cells, which permit antigenic presentation to immune cells. *Spi-B* expressing cells differentiate towards M cells ⁵.
- **Goblet cells:** they are the main secretory cells, which produce mucus (mainly Muc2) to produce a barrier for intestine protection against possible damage by innate immunity ⁷⁻⁹. Progenitor cells need expression of *Klf4* to differentiate into Goblet cells. To note, there are several types of Goblet cells depending on their location and function ¹⁰.
- **Enteroendocrine cells:** they are secretory cells that have chemosensory function and secrete different hormones with regulatory functions of the GI tract ^{11,12}. Specific hormone secretion has been demonstrated to be regulated by a BMP signalling gradient, which is higher in the villi, and also depends on cell location in the proximo-distal axis of the intestine ¹³. There are multiple subtypes of enteroendocrine cells, but all express *Ngn3* ¹⁴ and participate in the brain-gut axis bidirectional communication ¹⁵.
- **Paneth cells:** in contrast to the other differentiated cells, Paneth cells are located in the crypts ¹⁶. Their main function is to act as a support for intestinal stem cells (ISC), by secreting factors such as Wnt3, Dll4, TGF α and EGF ¹⁷. Moreover, they also secrete antimicrobial peptides, such as defensins, for intestine protection and for regulation of commensal microbiota ^{18,19}. Paneth cells need Sox9 for their differentiation and can be identified by using lysozyme as a marker ²⁰.
- **Tuft cells:** they are rare secretory cells, which are commonly associated to type 2 immune responses to helminth infections by secreting IL-25 ^{5,21,22}. Tuft cells also display a chemosensory function of factors present in the lumen and express *Dclk1*, CK-18, neurofilaments ²³ and *Pou2f3* ²⁴.

Importantly, *Gfi1* expression has been found to be required for cell differentiation to Goblet and Paneth cells, by inhibiting *Ngn3* expression ²⁵, being *Spdef* also required for correct differentiation of both cell types ²⁶. In contrast, for tuft differentiation, *Atoh1* is necessary but *Ngn3*, *Sox9*, *Gfi1* and *Spdef* are dispensable ²⁷.

In contrast to the small intestine, the **colon** is mainly composed of Goblet cells, colonocytes (absorptive cells) and enteroendocrine cells, presenting a really few number of Paneth cells, sometimes located in the ascending colon ² (FIGURE I1). In contrast, the colonic mucosa contains **deep crypt secretory (DCS) cells** that are functionally similar to Paneth cells and have been demonstrated to be required for colon homeostasis ²⁸.

I1.3. Intestinal stem cells

The intestine is a tissue very exposed to damage, which is compensated with the highly proliferative rate of ISC and linked to the high **plasticity** of intestinal cells upon injury. **ISCs** are located at the bottom of the crypts and are able to divide giving rise to **transit-amplifying (TA) cells** or new ISCs (a process known as self-renewal). TA cells, in turn, rapidly proliferate and migrate towards the villi while differentiating into all the epithelial subtypes. The only exception are Paneth cells that migrate towards the crypt bottom^{29–31} (FIGURE I1). Whereas ISCs has been thought to divide asymmetrically, there are evidences that the rate of ISCs replacement is comparable to the cell division pointing out to symmetric division and neutral drift dynamics^{32,33}. However, asymmetrical division may regulate the excessive proliferation induced upon inflammation³⁴.

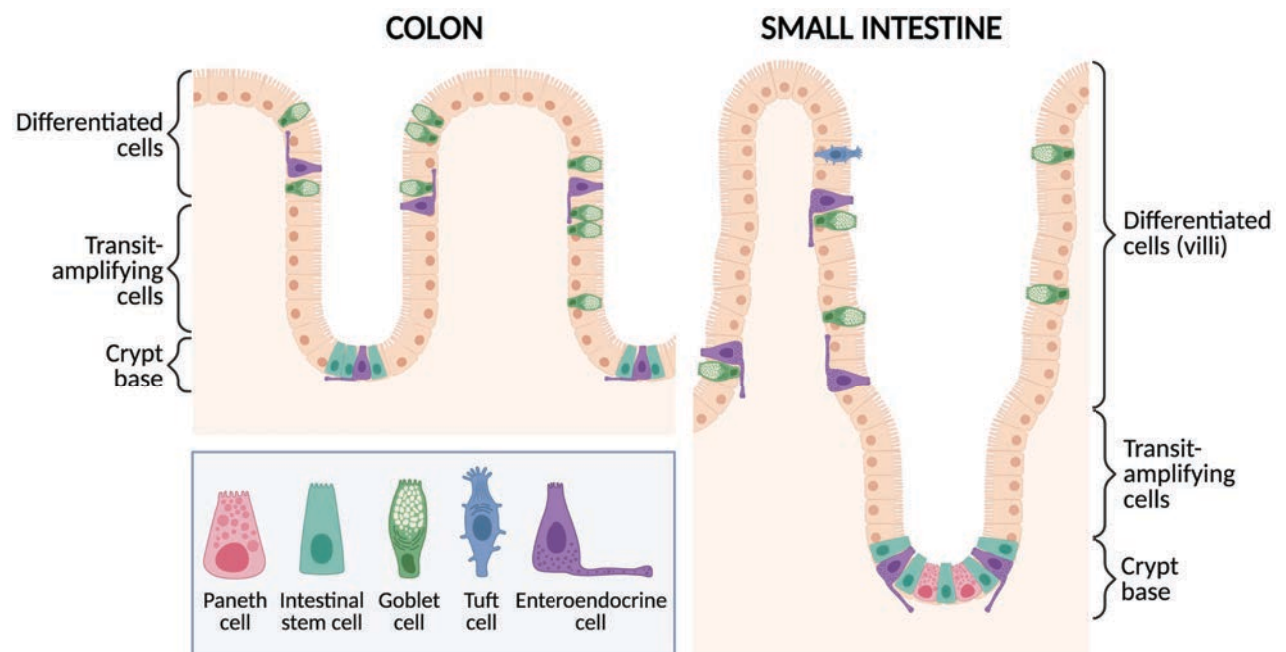


Figure I1. Small intestine and colon structure. Differentiated cells located in small intestine and colon and their compartments are indicated. Paneth cells are only found in the small intestine at the crypt base, where ISCs reside. Created with BioRender.com.

Two main ISC subtypes have been identified, displaying specific characteristics and expression profiles^{35–37}. **Crypt base columnar (CBC) cells** are found at the base of the crypts and are the main cell subtype responsible of intestine renewal and homeostasis. *Lgr5*, a coactivator of the Wnt pathway³⁸, has been traditionally used as the main marker for CBC cells³⁹, although other genes are also highly expressed⁴⁰, such as *Ascl2*⁴¹, *Olfm4* or *CD133*. *Lgr5*⁺ cells are not a

homogenous group, as seen by the discovery of $Lgr5^+$ $Mex3a^+$ cells that are slow cycling and can revert to a high cycling state to maintain homeostasis ⁴².

On the other hand, **quiescent “+4” cells**, located around +4 position in the crypts, are ISCs arrested in the G_0 phase of the cell cycle. These cells are commonly considered as reserve ISCs, as they are able to survive after irradiation and to regenerate CBC cells to maintain the intestinal integrity ^{43,44}. Elimination of +4 ISC cells challenges intestinal homeostasis, although there are some controversial reports that question it ⁴⁵. Some markers used for their identification ⁴⁶ are *Bmi1* ⁴⁷, *Tert* ⁴⁸, *Hopx* ⁴⁹ and *Lrig1* ⁵⁰. However, these markers are also expressed in CBC cells and are not useful for differentiating between ISC populations ^{51,52}.

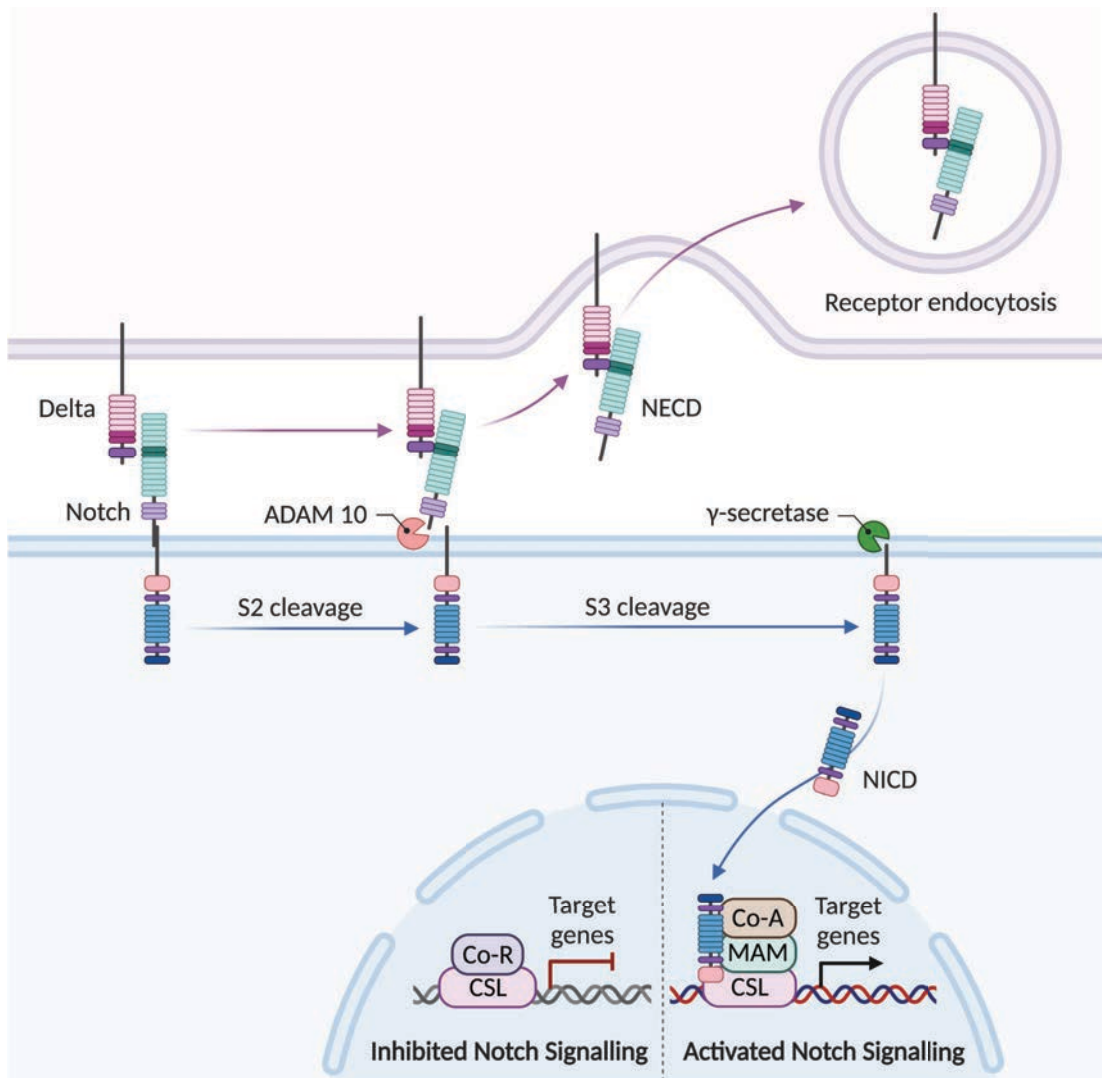


Figure I2. Notch signalling pathway. Upon Notch receptor-ligand interaction, the Notch receptor is cleaved by ADAM and γ -secretase and NICD is released. NICD is translocated into the nucleus to regulate gene expression. Created with BioRender.com.

There are many pathways involved in the homeostasis and regeneration of the intestine, with many similarities between small intestine and colon⁵³. Specifically, the **Wnt/ β -catenin pathway** is of huge importance in intestinal homeostasis maintenance. Briefly, Wnt3 is mainly produced by Paneth cells at the bottom of the crypts and the binding to its receptors produces translocation of β -catenin into the nucleus, inducing ISC proliferation⁵⁴. At this point, β -catenin induces the expression of EphB receptors and ephrin ligands. Gradients of specific EphB receptors and ligands along the crypt-villus axis generate attractive and repulsive forces that regulate compartmentalisation of the proliferative compartment and cell migration^{55–58}. Another important regulator of intestinal homeostasis is **BMP signalling** that inhibits Wnt/ β -catenin signalling, producing a negative regulation of the self-renewal of ISCs^{59,60}.

Notch and Jak/Stat signalling also participate in regulating proliferation and differentiation of intestinal cells^{61,62}. Specifically, the Notch pathway is activated when Notch ligands (Dll1-4 and Jag1-2) interact with their receptors (Notch1-4) producing the cleavage of the receptor, which releases its intracellular domain (NICD) in the cytoplasm. Then, NICD is translocated into the nucleus and, in association with CSL, induces gene transcription (i.e. *Hes1* and *Gata2*)⁶³ (FIGURE I2). Our group has uncovered that the Notch pathway is required for the homeostasis of ISCs and is specifically activated by Notch ligands Dll1 and Dll4⁶⁴. Moreover, *Bmi1* is also expressed in ISCs and the TA compartment regulating cell proliferation, being co-regulated by Notch and β -catenin signalling driven by Paneth cells⁶⁵.

I1.4. Regeneration of the intestine

Apart from the classical view of ISCs as the main source of cells in intestinal regeneration, other intestinal more differentiated cells can contribute to this process. Dll1⁺/Atoh1⁺ secretory^{66–69} or Alpi⁺ absorptive progenitors⁷⁰ are able to revert to ISCs in response to damage. In fact, a recent study shows that a vast majority of ISC restoration originates in *Ascl2*-driven **dedifferentiation of absorptive and secretory progenitors**⁷¹. Not only progenitors but mature intestinal cells can dedifferentiate into ISCs such as enteroendocrine cells⁷², tuft cells⁷³ and Paneth cells^{74,75}, revealing the huge plasticity of the intestine.

Another important process involved in intestinal regeneration has been recently uncovered: the **foetal-like reversion** of intestinal cells⁷⁶. After intestinal damage induced either by infection with the parasitic helminths, irradiation or direct ablation of Lgr5⁺ ISCs, murine ISCs lose ISC markers associated with an enrichment of the interferon-gamma (IFN γ) pathway, linked to *Ly6a* expression (encoding for Sca-1). This transcriptional switch is associated to the acquisition of a foetal-like signature^{77,78}, also observed upon transplantation of foetal spheroids in a damaged

colon, which were able to reconstitute crypts and produce mature cells ⁷⁹. **Foetal ISCs** have been shown to express a completely different transcriptional signature than adult ISCs, characterised by low levels of *Lgr5* but high expression of *Lgr4*, *Trop2* and *Cnx43*, and by the ability to grow in an undifferentiated state *in vitro* and, upon exposure to Wnt3a, differentiate ⁸⁰. However, the conversion of foetal ISCs to adult ISCs, necessary to also understand the regeneration process, associated with a huge intestinal remodelling and fission of villi, is not completely known ⁸¹.

12. COLORECTAL CANCER

12.1. General overview of colorectal cancer

Colorectal cancer (CRC) is the third most common cancer in men and the second in women, strongly increasing its incidence with age, but more importantly is still the third leading cause of cancer-related death in both genders. According to World Health Organization statistics, there were 1,931,590 cases of CRC worldwide that caused 935,173 deaths in 2020 (Globocan 2020). Multiple factors, such as inflammatory intestinal diseases, obesity and high fat diet⁸², increase the risk of developing CRC. Although having an important **heritable component** (about a 35% of the total risk), only a 5% of CRC cases are directly hereditary, as familial adenomatous polyposis (FAP) and hereditary non-polyposis colon cancer (Lynch syndrome)⁸³.

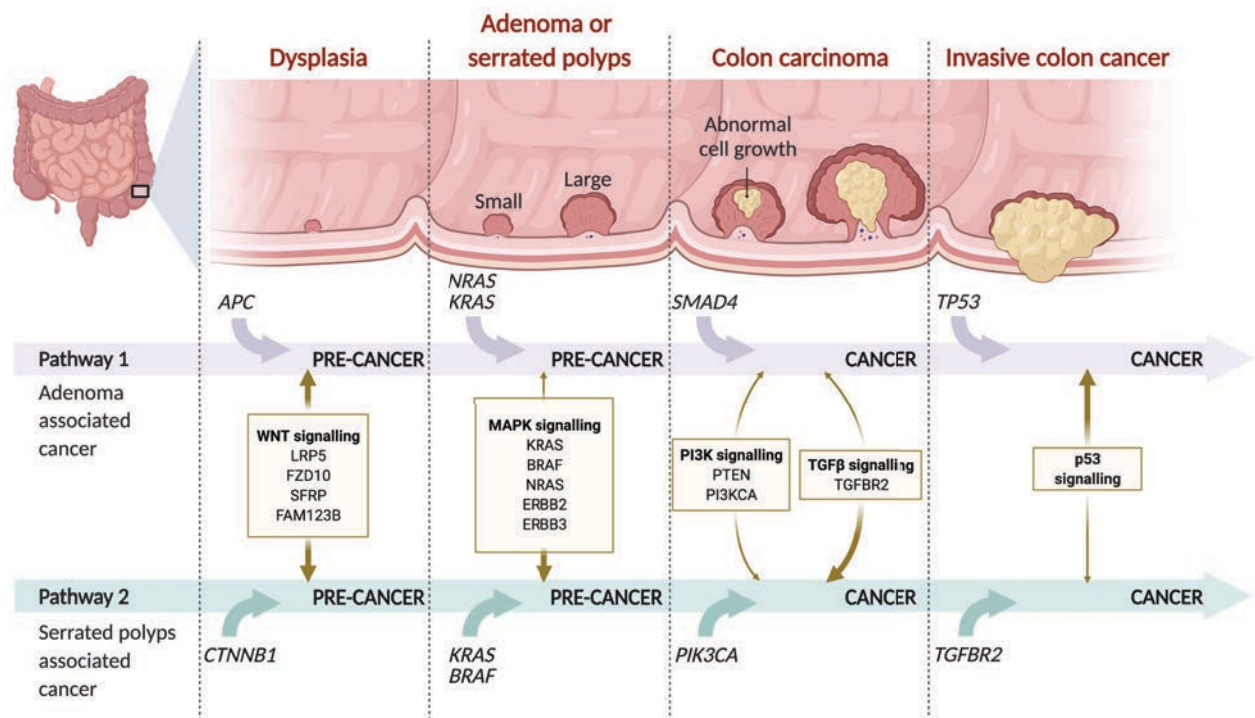


Figure I3. The adenoma-carcinoma sequence. CRC can be initiated by adenomas or serrated polyps, which acquire different mutations sequentially that permits the progression into colon carcinoma and, as the final step, invasive carcinomas. Mutations associated to each step are indicated. Created with BioRender.com.

CRC development has traditionally been explained by the **adenoma-carcinoma sequence**. The main premalignant lesions are dysplastic adenomas, which very often display Wnt-activating *APC* mutations as the main cancer driver^{84,85}. Further accumulation of activating mutations in *KRAS* or *BRAF* and inactivating mutations in *TP53* or *SMAD2/4*, along with other mutations such as chromosomal gain/loss^{86,87} or microsatellite instability (CIN and MSI, respectively), permit the progression from early adenomas to late adenomas, and finally into invasive carcinomas that can acquire the ability to produce metastasis⁸⁸ (FIGURE I3).

The **histological classification** of CRC takes into account local invasion depth (T stage), lymph node involvement (N stage) and the presence of metastases to distant sites (M stage), which permits the overall cancer stage classification, as described in TABLE I1⁸⁹.

T stages	Definition
Tx	No information about local tumour infiltration available
Tis	Tumour restricted to mucosa
T1	Infiltration through mucosa into submucosa
T2	Infiltration into, but not beyond, muscularis externa
T3	Infiltration into subserosa or non-peritonealised pericolic or perirectal tissue, or both
T4a	Infiltration of the serosa
T4b	Infiltration of neighbouring tissues or organs

N stages	Definition
Nx	No information about lymph node involvement available
N0	No lymph node involvement
N1a	Cancer cells detectable in 1 regional lymph node
N1b	Cancer cells detectable in 2–3 regional lymph nodes
N1c	Tumour satellites in subserosa or pericolic or perirectal fat tissue, regional lymph nodes not involved
N2a	Cancer cells detectable in 4–6 regional lymph nodes
N2b	Cancer cells detectable in 7 or greater regional lymph nodes

M stages	Definition
Mx	No information about distant metastases available
M0	No distant metastases detectable
M1a	Metastasis to 1 distant organ or distant lymph nodes
M1b	Metastasis to more than 1 distant organ or set of distant lymph nodes or peritoneal metastasis

	T	N	M
Stage 0	Tis	N0	M0
Stage I	T1/T2	N0	M0
Stage II	T3/T4	N0	M0
IIA	T3	N0	M0
IIB	T4a	N0	M0
IIC	T4b	N0	M0
Stage III	Any	N+	M0
IIIA	T1/T2	N1	M0
	T1	N2a	M0
IIIB	T3/T4a	N1	M0
	T2/T3	N2a	M0
	T1/T2	N2b	M0
IIIC	T4a	N2a	M0
	T3/T4a	N2b	M0
	T4b	N1/N2	M0
Stage IV	Any	Any	M+
IVA	Any	Any	M1a
IVB	Any	Any	M1b

Table I1. Classification of CRC according to TNM stages. Histological classification of T, N and M stages and overall classification, with characteristics of each stage indicated. Adapted from⁸⁹.

Different molecular classifications of CRC tumours have emerged based on gene expression, but they present some inconsistencies when comparing them, likely due to differences in how data is obtained, processed or normalised and which other tumour characteristics are considered^{90,91}. For instance, although previous classifications also subdivided CRC tumours

based on their transcriptomic profile, recent published data from **Lee and collaborators** ⁹² showed a classification of CRC cells from untreated patients into nine different epithelial subtypes (in comparison to previous five-six subtypes ^{91,93}), obtained by single cell RNA-seq (scRNA-seq) and specifically selecting tumour epithelial cells.

To overcome these problems, the classification done by **Guinney and collaborators** ⁹⁰ integrated not only expression data from all published cohorts, but also taking into account other biological features, like genomic aberrations and mutations, in order to confirm if there was a good genomic-phenotypic correlation. They divided the CRC tumours into four different groups: the called **consensus molecular subtypes (CMS)**. CMS1 tumours present MSI and strong immune infiltration and activation; CMS2 tumours are canonical tumours characterised by Wnt/ β -catenin signalling activation; CMS3 tumours carry *KRAS* mutations with metabolic deregulation and CMS4 tumours present stromal infiltration and TGF β signalling activation (associated with **epithelial-to-mesenchymal transition (EMT)** gene signatures). Both CMS2 and CMS3 tumours are poorly immunogenic, in contrast to CMS1 tumours. Importantly, CMS4 tumours have the worst disease free (DFS) and overall survival (OS).

12.2. Cancer stem cells

Heterogeneity inter- and intra-tumours has been consistently demonstrated, but the mechanisms driving this heterogeneity are not completely understood. One explanation could be that identical cells subjected to different intrinsic and extrinsic factors (which might come from the microenvironment) may adopt heterogeneous changes (stochastic model), although another explanation could be that tumours retain the hierarchical organisation from the original intestine (hierarchical model) ^{94,95}.

The identification of **cancer stem cells (CSCs)**, cells with stem cell-like properties that have self-renewal capacity and are able to re-establish the tumour heterogeneity, provides a proof of concept of the hierarchical model of tumours ⁹⁶. Some **markers** used to identify CSCs are *CD44* ⁹⁷, *CD133* ^{98,99}, *Lgr5* ^{100,101}, *ALDH1* ¹⁰², *CD166*, *CD29* and *CD24* expression or presence of nuclear β -catenin ¹⁰³, being some of them shared by ISCs. However, *Lgr5* has been demonstrated to be dispensable for tumour growth ¹⁰⁴, in particular for a subset of CRC tumours characterised by their high biosynthetic state ¹⁰⁵.

CSCs vary enormously among patients and tumour regions both in number or properties, making difficult to define a common CSC profile ^{106–108}. In fact, some undifferentiated tumour types do not present a specific CSC population, as all cells present some degree of stemness

traits. Moreover, it has been demonstrated that deletion of *APC* in ISCs initiates their tumoural transformation¹⁰⁹ and that upon aberrant Wnt signalling in CD133⁺ ISCs produced neoplastic expansion^{110,111}, being the source of the tumour growth while remaining at the bottom of the crypts. In addition, other studies have shown that Wnt activation in differentiated intestinal cells also induces the acquisition of CSC properties¹¹². All this data indicates that the process of tumour initiation and acquisition of CSC activity highly resembles the **plasticity** of the normal intestine¹¹³.

12.3. Therapy treatments in CRC

The standard guidelines for CRC treatment are **surgery** for complete resection of the rectum in the case of rectal cancer and resection of the colonic area containing the tumour and lymph vessels in the case of colon cancer. Surgery is normally combined with **radiotherapy** and/or **chemotherapy (CT)** to reduce relapse probability in invasive tumours. Neoadjuvant therapy, which refers to therapy administered before surgery, is normally indicated for stage III rectal tumours; adjuvant therapy is administered after surgery in stage III colon tumours. The first-line CT agents used in CRC are 5-fluorouracil (5-FU) with leucovorin together with irinotecan (Iri.) (FOLFIRI) or oxaliplatin (OX) (FOLFOX)⁸⁹.

In the case of CRC patients with metastasis, resectable tumours are treated with surgery along with CT. If not resectable, palliative CT is administered. The use of antiangiogenic drugs that inhibit VEGF, like bevacizumab and ramucirumab, or inhibitors of proteins acting as immune checkpoints, like ipilimumab and pembrolizumab, increases CT efficacy. CT in combination with monoclonal antibodies against EGFR, like cetuximab and panitumumab, in metastatic non-mutant *KRAS* tumours is also useful^{89,114}. Nowadays, targeted therapies for *KRAS* mutant tumours, which are resistant to antibodies against EGFR^{115,116}, are currently being explored^{117,118}.

13. PATIENT-DERIVED ORGANOID

13.1. Preclinical models

Traditionally, **two-dimensional (2D) cell cultures** have been widely used for modelling normal and cancerous tissues *in vitro*. 2D cultures are easy to handle and allow performing a great variety of experiments and studies. However, this type of cultures does not recapitulate certain features of the original tumour tissue, such as the structural organisation, the microenvironment or the hierarchical process of cell differentiation. Moreover, 2D cell cultures are frequently derived from immortalised cell lines, because, otherwise, they are not able to grow indefinitely. This implies genetic modifications and a high degree of selection that make cell lines very different from the original tumour cells. To overcome these limitations, **three-dimensional (3D) cultures** generated from primary tumours or metastasis (known as organoids) have recently been developed, as described in I3.2.¹¹⁹.

In addition, ***in vivo* models** are normally used to validate findings based on the *in vitro* models. First, cell lines injected into mice (cell line-derived xenografts (CDX)) models were used, but similar to 2D cultures, they do not recapitulate the original tissue characteristics. Therefore, new strategies have been developed. Specifically, two animal models have been used for studying cancer: genetically engineered mice (GEM) and patient-derived xenografts (PDX)¹²⁰.

In **GEM models**, cancer develops as a consequence of mutations present or generated in mice, which (in some models) allows studying the complete process of cancer development: initiation, progression and metastasis^{121,122}. In **PDX models**, fragments of tumours obtained from patients are directly transplanted into immunocompromised mice. In this case, the resulting tumour carries most of the characteristics of the original tumour. For this reason, although GEM models can permit to study multiple cancer stages, PDX are becoming the most common animal model for cancer studies. PDX tumours can be transplanted into secondary recipient mice to expand them. Organoids can also be injected to mice to directly translate the *in vitro* findings in an *in vivo* model¹²³. When cells are injected in the same localisation than the original tumours, we refer to orthotopic PDX tumours, which is the most close-to-the-patient method to produce PDX^{124,125}.

Nowadays, 3D cultures are normally the preferred option of preclinical cancer model, as they are reliable and less expensive models that permit studies under more controlled conditions than in the animal *in vivo* models, although further validation in PDX is most of the times required¹²⁶.

13.2. 3D cultures or organoids

3D cultures or organoids have their origin on stem cells, which are able to self-renew and produce cells that differentiate into the cell types present in the original tissue, forming in these conditions organ-like structures. Organoids have been derived from all types of stem cells, commonly from mice and humans, in order to reproduce the original characteristics of the tissue and to be able to study them more accurately than in 2D cultures. Organoids can be maintained at long-term without substantial modifications of the genetic background ¹¹⁹. However, genetic engineering of organoids is possible and already set up, making them a really powerful research tool. For example, it is useful for modelling specific diseases, studying functions, tagging specific genes or performing CRISPR screenings ^{127–129}.

Organoids can derive from pluripotent, embryonic or induced-pluripotent stem cells (**ES** or **IPS** cells, respectively), which can produce differentiated cells upon exposure to the appropriate factors. Organoids can also be generated from adult stem cells (**aSCs**), which are restricted to produce specific cell subtypes. By adjusting culture conditions to that present in the original stem cell niche, aSCs can reproduce the homeostasis of the tissue ^{130–132}.

Originally, 3D cultures were performed as *ex vivo* tissue explants/slices, displaying a very limited lifespan. Since then, 3D cultures have rapidly evolved. Nowadays, organoids can be grown in different culture conditions, such as cell suspension in non-adherent surfaces, embedded or on top of hydrogels, extracellular matrices, alginates, as well as mechanical supports and scaffolds. In general, different stages of organoid formation and organoids derived from different sources require different culture conditions ¹³³. Embedding cells in a laminin-rich extracellular matrix called **Matrigel**, which is secreted by the mouse sarcoma cell line Engelbreth-Holm-Swarm (EHS), is the most used 3D culture strategy ¹²⁶. Microfluidic organs-on-chip is another type of 3D culture, which is formed by continuously perfused chambers where cells are grown, allowing a more accurate reproduction of physiological conditions. These culture conditions also permit to co-culture organoids with other cell types, like commensal microbes or immune cells to mimic the process of intestinal infections or the immune-response ¹³⁴.

Importantly, organoids can recapitulate tissue development, hereditary diseases and infectious processes or mimic most cancer types when derived from cells with tumour initiating capacity (TIC) ^{135–137}. When tumours are the source of the organoids, they are normally called **tumouroids or spheres**. Moreover, using tumours and other affected tissues directly from patients permits approaches that mimic better the real behaviour of these cells. Cultures from patients' samples are referred to **patient-derived organoids (PDOs)**. PDOs are powerful tools

for drug screening and drug discovery, allowing personalised medicine ¹³⁰. For this reason, biobanks of PDOs from different cancer types have been developed to perform large-scale studies and for other applications. These biobanks represent the genetic and phenotypic characteristics of the original tumours while maintaining the heterogeneity of the tumours, thus allowing establishing correlations between drug response and tumour phenotype ^{138–142}. Although some discrepancies in drug response between organoids and the original tumours have been identified, tumours that respond *in vitro* normally respond *in vivo*. In contrast, tumours that are refractory to a particular drug *in vitro* can still respond *in vivo* due to the effect of the tumour microenvironment and the immune system ¹⁴³. Therefore, some improvement of the PDO cultures is still required to include the different elements of the tumour stroma.

I3.3. Organoids for modelling the intestine and CRC

The first protocol of reproducible organoid cultures was described by **Sato and collaborators**, by seeding single sorted *Lgr5*⁺ stem cells from mouse small intestinal crypts ¹⁴⁴. With the exception of whether Sato was seeding single cells or doublets containing one stem cell and its neighbouring Paneth cell, the authors demonstrated that *Lgr5*⁺ stem cells were able to generate full organoids displaying an organisation comparable to that found in the intestine, distributed in crypts and villi (FIGURE I4). After 2 or 3 days of culture, the first crypt-like structures appeared, containing ISCs and Paneth cells. These 3D cultures are grown in Matrigel with the addition of a medium containing EGF (to enhance proliferation), R-spondin1 (Wnt agonist, ligand for *Lgr5*), Noggin (inhibitor of BMP pathway, to prevent differentiation), and Y-27632 (Rho kinase inhibitor, to prevent anoikis) ^{144,145}.

Later on, culturing conditions for generation and expansion of organoids from different origins have been greatly set up. Specifically, optimisation of **mouse and human colon cultures** revealed the importance of adding Wnt3a (initially for increasing crypt culture efficiency), gastrin, nicotinamide, prostaglandin E₂ (PGE₂, to also prevent anoikis), A 83-01 (Alk inhibitor) and SB202190 (p38 inhibitor) ^{123,146}. Importantly, withdrawal of Wnt3a, SB202190 and nicotinamide is necessary for correct differentiation of normal organoids. These culture conditions have also permitted the production of organoid cultures from **adenomas, adenocarcinoma and Barrett's epithelium**, with particular variations on the medium composition ^{147–149}.

Other types of 3D cultures are now arising. For instance, intestinal organoids cultured in floating collagen gel rings are able to self-organise and form tubes that are macroscopically visible. These tubes display a lumen-like region inside the tube where villi are localised, in

structures more similar to the intestine than the organoids¹⁵⁰. Specific techniques for generating intestinal organoids^{151–154} and CRC organoids¹⁵⁵ from ES or iPS cells have successfully been developed. Notably, CRISPR/Cas9 technology has allowed deriving CRC organoids from normal organoids as a useful tool for studying possible tumour drivers^{156,157}.

In general, the establishment of intestinal organoid cultures has allowed the emergence of a plethora of studies focused on intestinal development and organisation^{158,159}, differentiation and plasticity of the different cell types¹⁶⁰ and the mechanisms of regeneration upon damage¹⁶¹. On the other hand, CRC organoids have emerged as a really potent tool for **cancer research**. CRC organoids recapitulate the original mutations of the tumour and, in contrast to normal intestinal organoids, grow forming a spherical structure composed mostly by undifferentiated cells (FIGURE I4). In this scenario, multiple living biobanks of CRC PDOs have already been generated¹⁶² that are demonstrating to be important for the identification of cells with TIC potential¹⁶³, study the accumulation of mutations in the initiation and progression of CRC^{164–166} or to analyse the mechanisms of therapy responses/resistance^{167–169}.

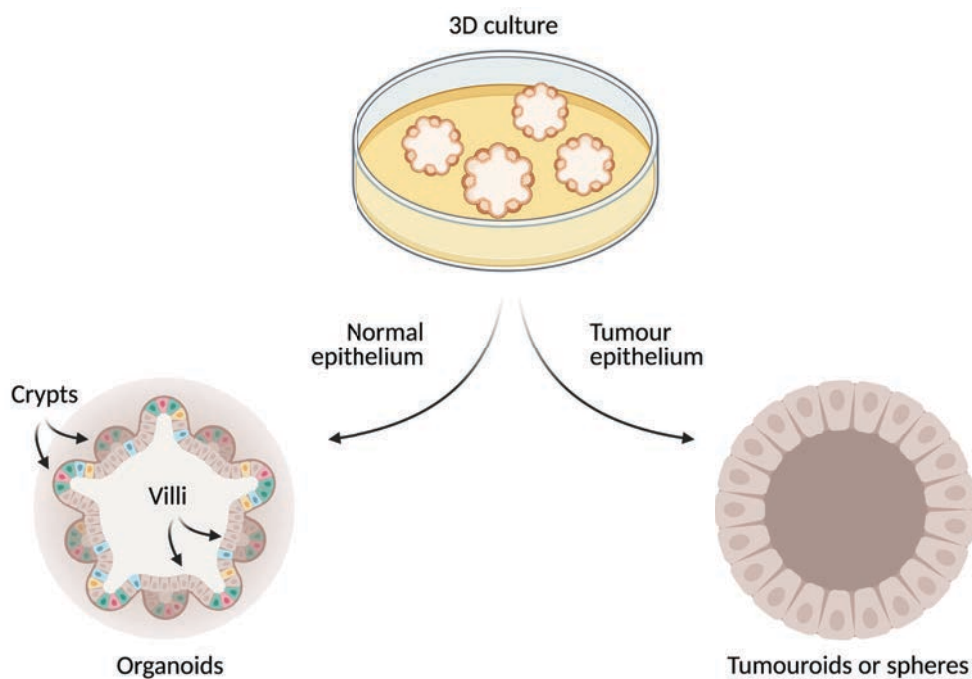


Figure I4. 3D cultures. 3D cultures can be produced from normal and tumour epitheliums, producing organoids resembling the intestinal structure or tumouroids/spheres formed by undifferentiated cells, respectively. Created with BioRender.com.

14. TUMOUR DORMANCY AND RELAPSE

14.1. Role of CSCs in tumour relapse

Despite the advances in cancer treatment, 30 to 50% of CRC patients **relapse** after adequate treatment and ultimately die, normally due to regrowth of primary tumour or to **metastasis** (the process of colonisation of cancer cells to distant organs), associated to acquisition of tumour **resistance** to treatments (data from American Cancer Society).

Since the seminal investigations of Antonio Garcia de Herreros' and Amparo Cano's groups in 2000^{170,171}, it is believed that **disseminated tumour cells (DTCs)**, by undergoing the **EMT process**, acquire the ability to migrate and invade ultimately producing metastasis. Indeed, it has been demonstrated that this process increases the TIC potential and the stem-like properties of cancer cells¹⁷². However, EMT is a transient process that need to be reverted, in a process called **mesenchymal-to-epithelial transition (MET)**, once DTCs have colonised their target organ and under adequate metastatic niche conditions (FIGURE I5)^{107,173}. It has been shown that **CSCs** and metastatic cells share EMT traits, but whether CSCs are directly responsible of metastasis remains to be elucidated¹⁷⁴. Indeed, it was recently demonstrated that metastatic cells are initially Lgr5⁻, but acquire the stem cell marker Lgr5 when they grow in the metastatic site¹⁷⁵. The metastatic process is enhanced by the expression of *L1CAM*¹⁷⁶ and *CD44v6*¹⁷⁷.

The **TGFβ pathway** is a widely demonstrated tumour suppressor pathway in epithelial cells that is commonly inactivated in the CRC adenoma to carcinoma progression (see FIGURE I3). Physiologically, TGFβ binds to its receptor that phosphorylates SMAD2/3 transcription factors. In association with SMAD4, the complex is translocated into the nucleus to inhibit cell proliferation and induce differentiation (FIGURE I5 and I7). However, the TGFβ pathway was found to facilitate the metastasis process, facilitating the extravasation of breast cancer cells to the lungs and the formation of cancer bone metastasis¹⁷⁸⁻¹⁸². Upregulation of the TGFβ and Wnt signalling pathways in tumoural cells facilitate the EMT process¹⁸³, as well as the release of TGFβ by stromal cells¹⁸⁴ facilitates immune evasion of metastatic cells by inducing T-cell exclusion¹⁸⁵ and TGFβ-mediated neutrophil infiltration dependent on Notch1 also enhances metastases¹⁸⁶.

On the other hand, both primary and metastatic tumours can acquire therapeutic resistance, which has a major impact on patient survival. Tumour cells can adopt multiple **resistance mechanisms** against CT, commonly related with activation of pro-survival pathways and

increased expression of anti-apoptotic genes. As explained, CT drugs commonly used for treating CRC patients are 5-FU, which targets thymidilate synthase and therefore DNA synthesis; Iri., a topoisomerase I inhibitor; and OX, a platinum compound which directly binds DNA ¹⁸⁷. Notable, most adopted resistance mechanisms are treatment specific. For example, resistance to 5-FU can be acquired by increased thymidylate synthase expression or *MLH1* hypermethylation. Iri.-resistance is achieved by increased rates of drug efflux or topoisomerase I mutations. Finally, OX-resistance can be provided by increased drug efflux, reduced cellular uptake, increased DNA repair or *MLH1* hypermethylation ^{187,188}.

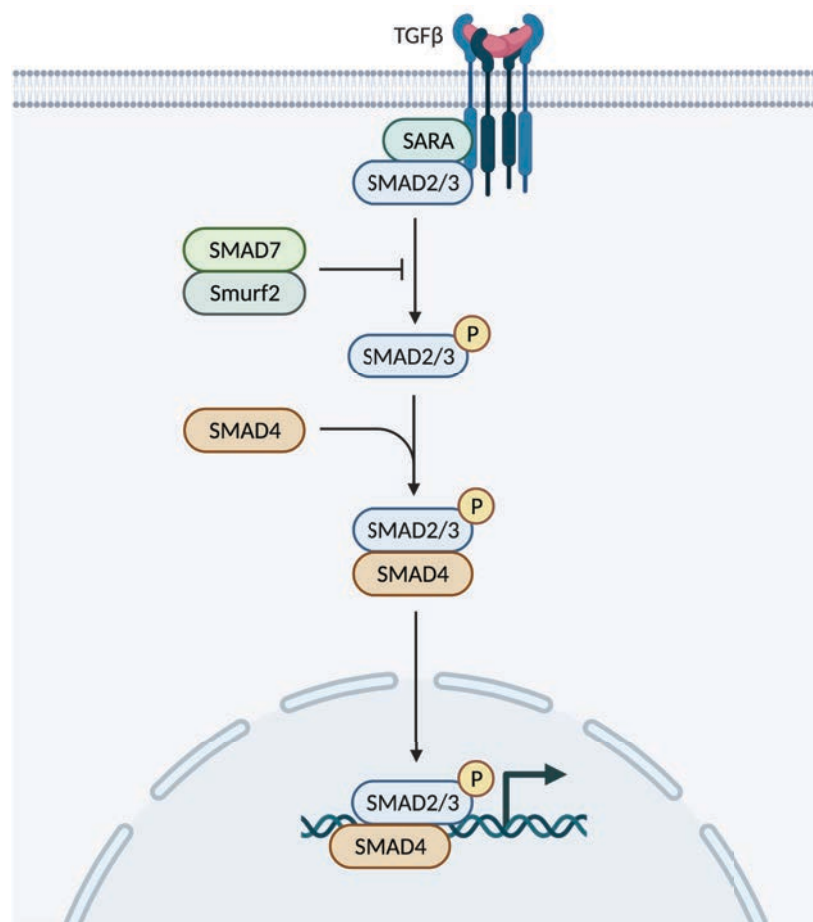


Figure 15. TGFβ signalling pathway. When TGFβ binds to its receptor, the TGFβ cascade is activated and induces the regulation of multiple cell functions. Created with BioRender.com.

How cells acquire drug resistance is still under investigation but one of the mechanisms involved is the selection of drug-resistant mutant cells already present before the initiation of treatment. Alternatively, specific mutations can also arise during therapy (FIGURE I6) ^{189,190}.

Cancer cells that remain after therapy and are the main source of relapse are called **drug-tolerant persister (DTP) cells** ¹⁹¹.

Because common DNA-damaging agents used for cancer treatment directly target highly proliferating cells, DTP cells are mostly **slow-cycling cells** that in some cases display EMT or stem-like properties ¹⁹². Consequently, ISCs and CSCs displaying slow-cycling (or quiescent) features that escape from treatment are postulated as the main source of cancer relapse and metastasis ^{193,194}. Interestingly, tumour relapse and metastasis can occur several years after the initial diagnosis, suggesting that there is a period of **tumour dormancy**, in which the cells stay in a slow-cycling state or at low numbers due to compensation of cell proliferation by tumour cell death ¹⁹⁵. In primary tumours, dormancy can be driven by the equilibrium imposed by treatment or the immune system. In the metastatic sites, the difficulty of cancer cells to adapt to the new microenvironment can also contribute. Re-entering of cells into the cell cycle or escape from immune system may explain tumour relapse and metastatic outgrowth ^{196,197}.

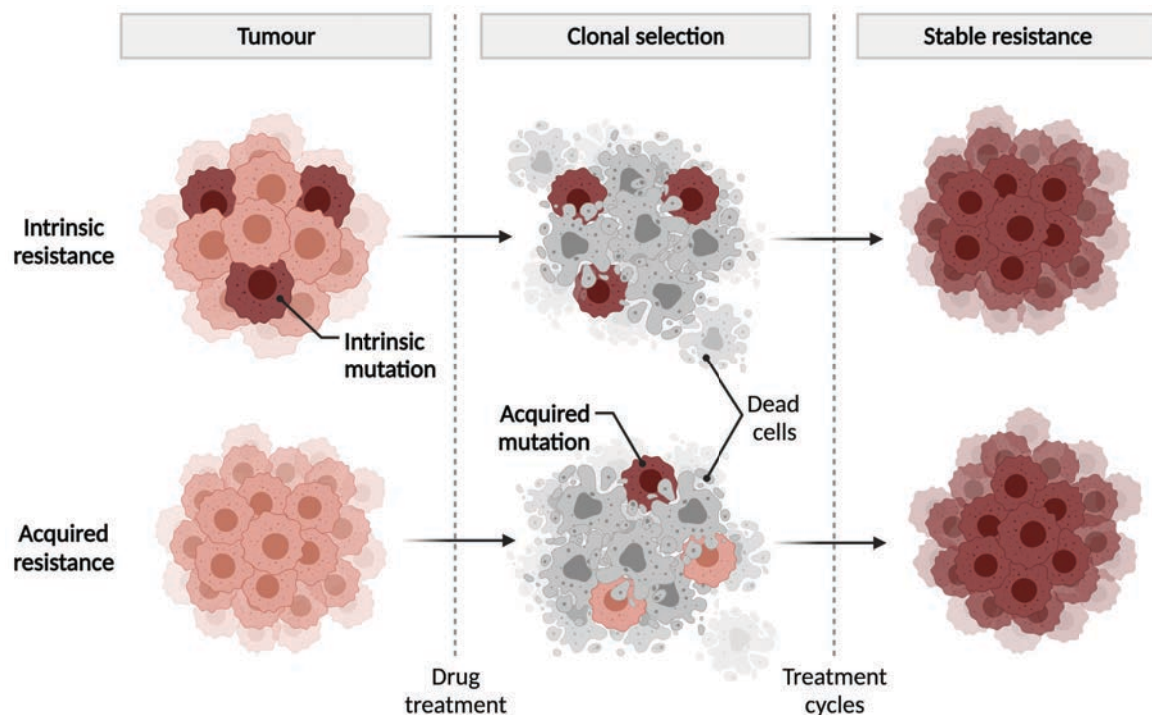


Figure 16. Mechanisms of drug resistance. Upon drug treatment, DTP cells are able to survive, either by intrinsic or acquired mutations that permit drug resistance. DTP cells can drive tumour resistance and be the source of the tumour regrowth. Created with BioRender.com.

Whether CSCs are more resistant to therapy is not clear, as it is primarily tumour dependent^{106,174}. Considering the likely role of CSCs in metastasis and resistance, at least in a proportion of tumours, therapeutic strategies **targeting CSCs** might be a good strategy. However, strategies targeting CSC features could similarly affect ISCs¹⁹⁸, and inhibitors of Hedgehog, Notch, Wnt or TGF β pathways are currently being tested for their differential requirement in CSCs and ISCs^{199–201}.

14.2. Cell cycle arrest in response to DNA damage

Activation of the **DNA damage response (DDR)** as a result of anti-cancer treatments can impose a cell cycle arrest that facilitates DNA repair and cell survival (FIGURE 17), or induce cell death in case of irreparable damage²⁰². Different types of DNA damage are produced by anti-cancer treatments including single-strand and double-strand breaks (SSBs and DSBs). DSBs are particularly difficult to repair and can cause severe damage to cells, which are basically repaired by **homologous recombination (HR)** or **non-homologous end joining (NHEJ) DDR pathways**. Briefly, DDR cascade starts when DNA damage is detected leading to ATM recruitment and H2A.X phosphorylation (γ H2A.X), which is generally used as a marker for DNA damage. The phase of the cell cycle of the cell experiencing DNA damage mainly define the type of DDR pathway that is selected for repair: HR for cells in S/G₂/M cell cycle phases and NHEJ for cells in G₀/G₁ phases²⁰³, the latter including quiescent CSCs.

DDR signalling involves multiple proteins, with **p53** and its downstream effector **p21^{CIP}** (CDKN1A, hereafter referred as p21) playing an important role in regulating the cell cycle progression in damage conditions and also under physiological conditions. p53 levels are regulated by the E3 ubiquitin ligase MDM2, which is a negative regulator of p53 that bounds to its N-terminal domain and leads to its ubiquitination and subsequent proteasomal degradation. In turn, p53 induce increased levels of MDM2, producing a negative feedback loop. Under DNA damage, p53 is released and then stabilised and activated by post-translational modifications. p53 is then translocated into the nucleus where binds to promoter regions of the DNA inducing the expression of its downstream transcriptional targets, such as p21 (FIGURE 17). In G₁ phase, p21 prevents cell cycle progression by inhibiting the activity of the complex formed by cyclin E and CDK2, impeding Rb phosphorylation (pRb), which is sequestering E2F; but also by directly blocking DNA synthesis, bound to PCNA. In contrast, in G₂/M phase p21 inactivates the complex formed by CDK1 and cyclin B by inhibiting CAK^{204–206} (FIGURE 18).

In addition, *CDKN2A* encodes for **p16^{INK4a}** (hereafter referred as p16) and **p14^{ARF}**, which are also involved in the cell cycle arrest. p14^{ARF} acts as an inhibitor of MDM2 and therefore

activating p53. p16, in turn, inhibits the complex formed by the cyclin D and CDK4/6 that also impedes Rb phosphorylation in G₁ phase. Multiple other proteins, such as p27 and p15, have also a role in regulating the cell cycle²⁰⁷ (FIGURE I7).

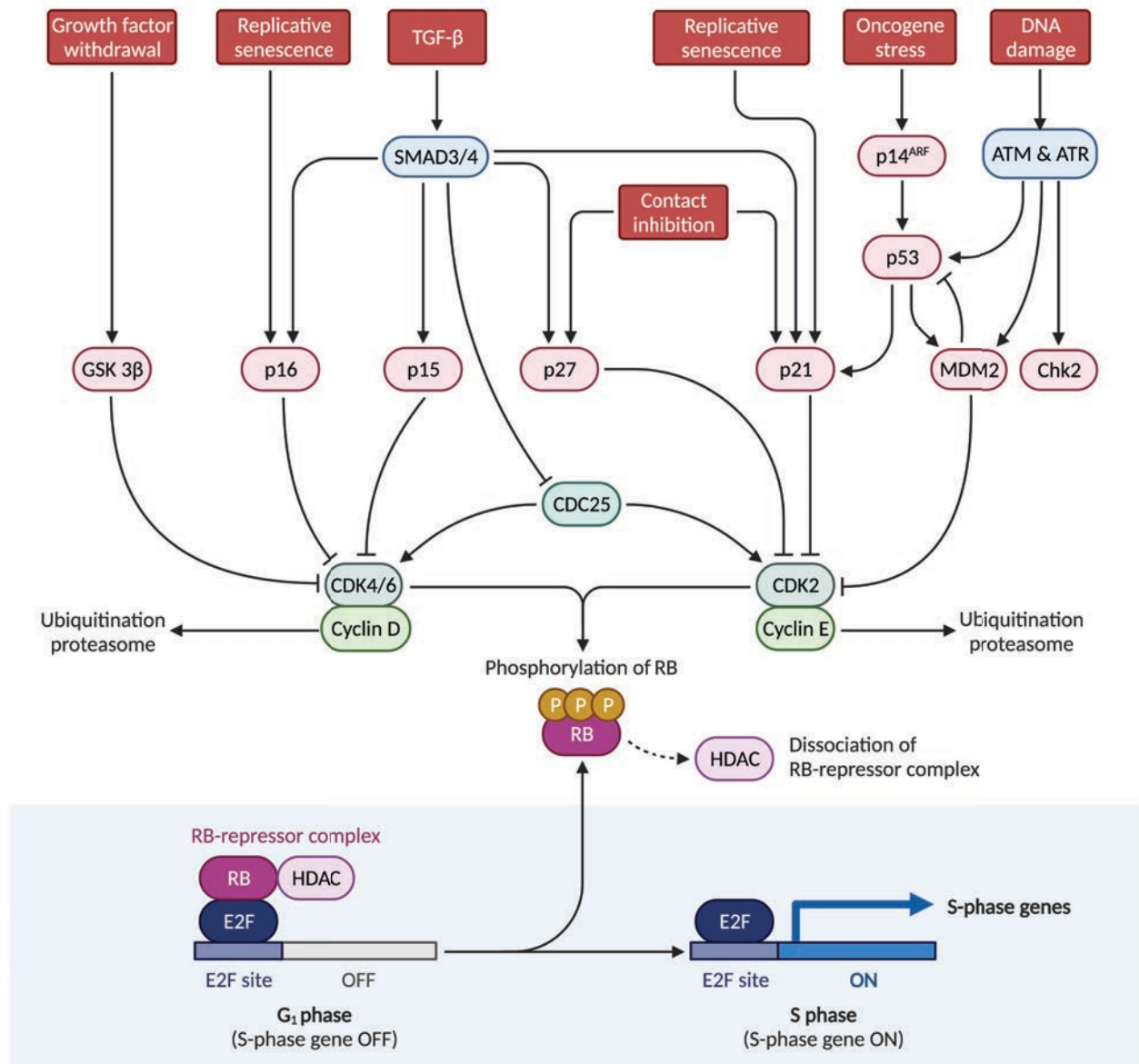


Figure I7. Multiple factors induce a growth arrest at G₁ phase. DNA damage (ATM/ATR and p53), oncogene stress (p14^{ARF}/p53), TGFβ (SMAD3/4) or replicative senescence (p16 or p21) can drive growth arrest at G₁ phase of the cell cycle. These factors inhibit CD4/6-cyclin D or CDK2-cyclin E, not enabling the phosphorylation of Rb, which is sequestering E2F and impeding cell cycle progression. Created with BioRender.com.

Importantly, when DNA damage is not repaired, p53/p21 and p16 signalling produce a **persistent growth arrest** that can lead to entering into a **senescent** state or directly into

apoptosis. p53 is involved in inhibiting apoptosis by directly binding to BAX, NOXA and PUMA, which increases the permeability of the mitochondrial membrane and therefore the release of pro-apoptotic factors in the cytoplasm, like cytochrome C. p53 also controls the DNA repair and the replication processes ²⁰⁴, and is required to stop cells into G₀ phase or **quiescence**, indicating that p53 pathway is involved in multiple processes ²⁰⁸.

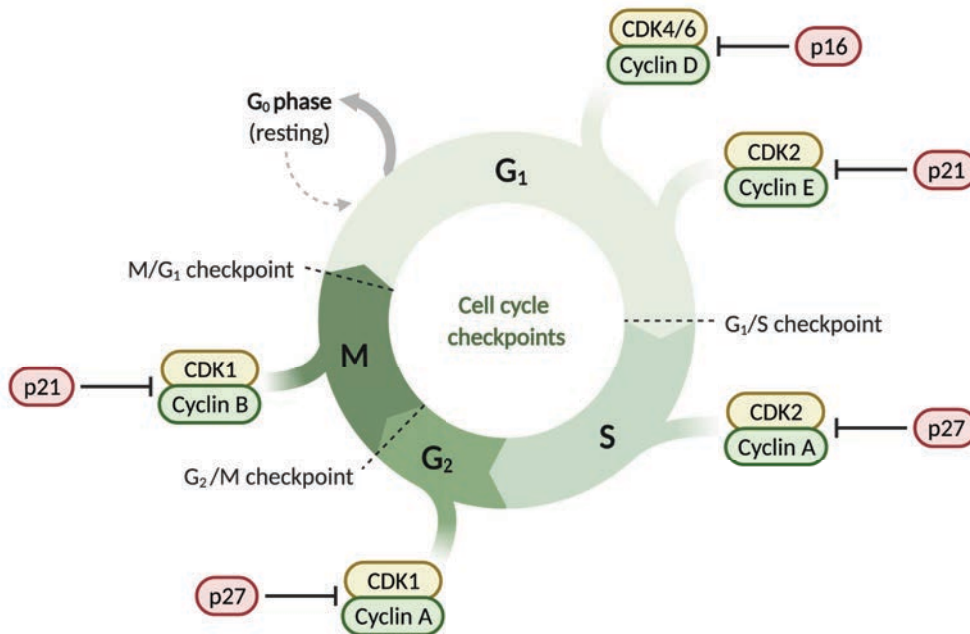


Figure 18. Cell cycle checkpoints. Cell cycle checkpoints impede the progression into the cell cycle when any insult is detected. p21, p16 and p27, among other regulators, inhibit CDK/cyclin complexes producing a growth arrest. Created with BioRender.com.

14.3. Cell quiescence and drug resistance

Quiescence is a reversible non-cycling state, in which cells enter into the G₀ phase of the cell cycle. Quiescence is normally associated to specific stem cell populations, which have been identified by label-retaining experiments, indicative of their non-proliferating trait ^{209,210}. In the intestine, ISCs located at the bottom of the crypts are proliferative, but other cells, such as the quiescent +4 ISCs, act as a reservoir of ISCs ²¹¹. As described above, p53, p21 and pRb regulate the entrance and escape from quiescence ^{212–214}.

Apart from quiescent stem cells, other cells may undergo quiescence due to certain factors that disrupt the normal functioning of tissues, like nutrient deprivation, oxidative stress or for immune evasion. All quiescent cells show a **common gene signature** that involves genes linked to cell

cycle regulation, DNA replication, mitochondrial function and RNA processing, among other functions. In addition, they present a metabolism based on glucose consumption and mitochondrial oxidative respiration ²¹¹. Paradoxically, quiescent stem cell mainly displays a glycolytic metabolism, similar to that observed in proliferating cells, despite their quiescent state ²¹⁵.

Quiescent cells are more able to survive to environmental stress than proliferating cells, by expressing FOXO, HIF1 α and LKB1, along with autophagy, which permits the removal of damaged internal cellular components. Upon **DNA damage**, they activate preferentially the NHEJ pathway of the DDR, which is prone to accumulate mutations, rather than HR that is used by proliferating cells ^{211,216}. In addition, it has been shown that when damaged DNA is transferred to a daughter cell it can trigger quiescence in the receiving cell ²¹⁷.

In tumours, **DTP cells** are in a quiescent state characterised by enrichment in stem cells markers with no acquired mutations in comparison to non-DTP tumour cells. Normally, they resume proliferation after drug withdrawal and display epigenetic modifications that facilitate drug resistance. DTP cells can be eliminated by directly targeting them or by forcing them to re-enter the cell cycle. Not only DTP cells, but also **DTCs** may display a quiescent state in disseminated organs, before being able to re-enter the cell cycle and contribute to form metastasis ¹⁹⁷.

To note, in cancer and in CRC in particular, *TP53* is frequently mutated and its loss has been associated to more aggressive tumours in patients ²¹⁸. Paradoxically, it has recently been demonstrated that ***TP53* knock-out (KO)** cells are unable to acquire a dormant state and are more sensitive to external stresses, supporting the concept that quiescence acquisition might be linked with cell drug resistance ²¹⁶. Indeed, p53 can promote cancer stemness upon 5-FU treatment by direct activation of the Wnt pathway ²¹⁹.

I4.4. Cell cycle re-entry

Besides the p53/p21 pathway, other important pathways were found to regulate quiescence and reanimation (re-entry into cell cycle of quiescent cells) in the tumour dormancy context. The **Notch pathway** (see FIGURE I2), which is required for normal ISC homeostasis, is essential in the reversibility of quiescence. In fact, the main downstream target of the Notch pathway, *HES1*, allows quiescence reversibility by inhibiting the entrance to premature senescence or differentiation in quiescent fibroblasts ²²⁰. In breast cancer cells, tenascin C activates Notch and **Wnt signalling** to facilitate DTCs colonisation to the lung ²²¹. In turn, autocrine Wnt inhibition

permits the maintenance of DTCs' dormancy, which facilitates DTCs' immune evasion, in metastatic lung and breast carcinoma cells ²²². The **TGFβ pathway** (see FIGURE 15) also contributes to impose a quiescent state to DTCs independent of p21 in squamous cell carcinoma, contributing to tumour dormancy. These DTCs display higher tumourigenic potential and CT resistance that was reversed by inhibiting TGFβ ²²³. Metastatic dormancy is also reverted by downregulation of *MSK1* expression, which impairs differentiation of tumoural cells and enhances DTCs' capacity to metastasise in breast cancer tumours ²²⁴. In addition, Coco has been demonstrated to reanimate breast cancer cells to permit lung metastasis grow, acting as a BMP inhibitor ²²⁵.

14.5. Cell senescence: is it reversible?

Replicative **senescence** is a type of cell cycle arrest that physiologically limits the proliferation of normal cells after multiple cell divisions. Other mechanisms of cellular control are specifically dedicated to prevent proliferation of damaged cells, as is the case of apoptosis or autophagy, which directly induce cell death ²²⁶. Senescence has also a role in arresting cells displaying persistent DDR activation, oncogenic signals such as mutant RAS, and to prevent expansion of cells carrying damaged DNA ^{227–230}. Thus, cell senescence is highly induced after treatment with sublethal doses of **DNA-damaging agents** (therapy-induced senescence) ¹⁹¹. Although anticancer therapies are intended to totally eradicate cancer cells (lethal doses), the total amount of drug that effectively reaches different regions of the tumour depends on the pharmacokinetics of the administered drugs and the localisation of the tumours in the body. In addition, the phases of liberation, absorption, distribution, metabolism and excretion can vary enormously between patients, producing variability in the amount of drug tumour cells are finally exposed to. Moreover, drug doses are limited but their general toxicity and the characteristics of the patient. Thus, the final result is that, in a high proportion of cases, tumour cells can be finally exposed to sublethal CT doses ^{231,232}.

Senescence is characterised by morphological changes (enlarged and irregular shape), enlarged nuclei with loss of LaminB1, shortening of telomeres and abnormalities in the DNA content (polyploidies or aneuploidies) ^{208,233}. Senescent cells are metabolically active, as seen by their increased secretion of pro-inflammatory cytokines, often referred as a **senescence associated-secretory phenotype (SASP)**, high expression of the **senescence-associated β-galactosidase** (SA-β-gal, indicates increased lysosomal content) and activation of anti-proliferative and inflammatory (like NF-κB) pathways. Common SASP factors are interleukins (IL-1, IL-6), chemokines (IL-8, GRO), growth factors (bFGF, HGF) or proteases (MMP-1) ²³⁴.

The main drivers of cell cycle arrest in senescent cells are **p16^{INK4a}** and **p53/p21**, driven by DDR upon DNA damage or other stimuli ²³⁵. In parallel, senescence-associated heterochromatin foci (SAHF) are formed in sites with persistent DNA damage through recruitment of pRb, associated to increased H3K9me3 and γ H2A.X levels ^{236,237}. Besides p53/p21 regulation, low levels of **MYCN** at the time of CT treatment were found to induce senescence in cells, whereas high MYC levels are permissive of cell cycle arrest followed by proliferation or apoptosis, depending on DNA damage resolution or persistence ²³⁸.

Whether senescence is **an irreversible or a reversible program** is under study. It was elegantly demonstrated by Beauséjour et al. that senescence induced by the p53 pathway is reversible in the absence of high p16 levels, whereas high p16 levels makes the senescent phenotype irreversible ²³⁹. Levels of **p21 can also** impact in cell fate and induction of growth arrest, but not in its maintenance ²⁴⁰. However, when p21 response is delayed or very acute, senescence is the chosen fate with intermediate p21 responses favouring proliferation, thus indicating the complex regulation of this process ²⁴¹. In addition, **p53 dynamics** after drug exposure differs from cell to cell thus leading to either proliferating or senescent phenotypes. When p53 levels are sustained, growth arrest is maintained and cells derive to senescence, whereas cells with transient damage and temporary p53 activation can re-enter cell cycle after damage resolution, Importantly, *TP53* mutant cells can proceed into mitosis in the presence of damage, but they become multinucleated and finally succumb by apoptosis ²⁴².

Cellular senescence in tumours can be seen as a good prognostic marker, due to the associated reduction in tumour growth ²⁴³ and because senescent cells can also induce immune surveillance against pre-malignant cells, as a mechanism for suppressing tumour growth ^{244,245}. However, although senescent cells are less proliferative compared to non-senescent tumour cells, they are metabolically active and are characterised by the expression of a SASP that can contribute to either **suppress** (by IGFBP, Maspin or MIC-1 secreted suppressor factors) or **promote** (by TGF α , Cyr61, CTGF secreted promoting factors) tumour growth by directly affecting neighbouring (non-senescent) tumour cells, or facilitating the remodeling of the extracellular matrix ²⁴⁶⁻²⁴⁹. In addition, senescent cells that re-enter cell cycle were shown to display increased tumorigenic capacity compared to cells without senescent record linked to expression of adult stem cell markers, higher proliferation rates and increased TIC. This **senescence-associated stemness phenotype** is also detected after tumour relapse, suggesting that senescent cells may be the source of tumour regrowth in patients ^{250,251}. For this reason, drugs that selectively kill therapy-induced senescent cells, called **senolytic drugs**, are being investigated for their use in anti-cancer therapies ²⁵²⁻²⁵⁴. However, there is limited data indicating their efficacy in improving current treatment strategies ^{255,256}.

15. YAP1 IN INTESTINAL REGENERATION AND CANCER

15.1. The Hippo pathway

The **Hippo pathway** has been involved in development, tissue homeostasis and regeneration, and in cancer processes. Their main effectors are the Yes-Associated Protein (YAP) and the transcriptional co-activator with PDZ-binding motif (TAZ). MST1/2 bound to SAV1 phosphorylates LATS1/2 kinases activating them and their regulatory subunits MOB1A/B. LATS1/2 inactivate **YAP and TAZ** proteins by phosphorylating them in serine residues, producing its retention into the cytoplasm and its proteasomal degradation. In addition, other kinases like Yes/Src and c-Abl has been described to phosphorylate YAP1 in tyrosine residues²⁵⁷. There are different **upstream regulators** of the Hippo pathway. NF2 acts inhibiting YAP/TAZ proteins by inducing LATS1/2 activity. Scribble (SCRIB) is localised in the membrane and permits the formation of the MST/LATS/TAZ complex. In addition, E-cadherin and α -catenin also has been demonstrated to increase YAP phosphorylation (FIGURE I9)²⁵⁸.

Nuclear YAP1 associated with transcription factors like TEADs, SMADs or RUNX proteins binds to promoter of genes to induce specific gene transcription²⁵⁷. Overall, when YAP and TAZ are localised in the cytoplasm, apoptosis and growth arrest are induced along with adipocyte differentiation. Their nuclear localisation induces proliferation or epithelial cells and osteoblasts differentiation. They also contribute to the extracellular matrix remodelling and adhesion processes (FIGURE I9)²⁵⁸.

15.2. YAP1 in the intestine

Loss of YAP1 produces intestinal growth defects, probably by impairment in glucose transport and nucleotide biosynthesis as shown in the liver²⁵⁹, and increases Goblet and absorptive cell differentiation in cell lines²⁶⁰. In addition, it has recently been shown that LATS1/2 kinases are necessary for Wnt pathway activation in the intestinal crypts and for ISCs self-renewal, dependent on YAP/TAZ but independent on TEAD²⁶¹. However, the main effect of the deregulation of the Hippo signalling is observed in **intestinal regeneration**.

Upon dextran sodium sulfate (DSS) treatment in mice, there is an induction of intestinal damage and an activation of its regeneration. In this context, **Cai and colleagues** found that increased YAP1 levels were necessary for this process, as there is impairment in regeneration after inactivation of YAP1²⁶². In addition, in Taniguchi et al. intestinal regeneration is shown to be induced by gp130, a co-receptor for IL-6, which produces YAP and Notch activation²⁶³.

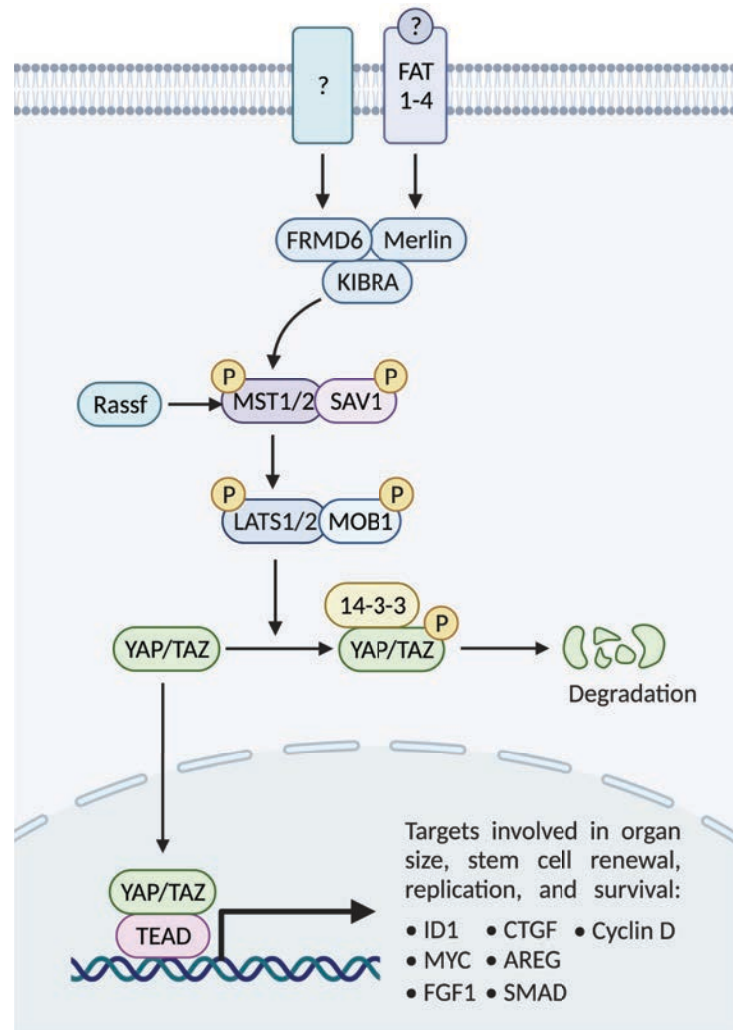


Figure 19. Hippo pathway signalling. It is not completely known which factors activate the Hippo pathway. Upon activation of the pathway, YAP and TAZ are phosphorylated and degraded. Therefore, when Hippo pathway is active, the gene expression is not induced. Created with BioRender.com.

It has been uncovered that YAP1 has a role in restricting **Wnt signalling** to crypts, regulating cell proliferation. Indeed, when YAP1 is up- or downregulated, the regeneration process is altered, leading to loss of proliferation or hyperplasia, respectively ²⁶⁴. Particularly, the Lgr5⁺ ISCs reprogramming has been directly associated to YAP1 driven suppression of Wnt signalling and Paneth cell differentiation, as shown in YAP1 KO organoids and *in vivo* ²⁶⁵. Moreover, the Hippo pathway also regulates the **Notch pathway**, which is involved in ISCs regulation. It has been demonstrated that inhibition of Notch when there is upregulation of YAP1 abrogates its negative effects in uncontrolled proliferation ²⁶⁶.

The regeneration process has been linked to an acquisition of **foetal-like properties**, as discussed in I1.4, and, remarkably, YAP/TAZ activation has been found to be required for this

reprogramming⁷⁸. Moreover, by scRNA-seq in the regenerating mouse intestine, Ayyaz and colleagues showed an emerging new ISCs subtype, called revival stem cells (revSCs), which are quiescent cells really expanded upon intestinal damage in a YAP1-dependent manner²⁶⁷. Overall, these studies indicate that in the regeneration of the intestine cells undergo important transcriptional changes, dependent on Hippo pathway^{268,269}.

15.3. YAP1 in CRC

Given the important roles of Hippo pathway in the regeneration of the intestine, it is straightforward linking its deregulation with **CRC initiation and progression**. Indeed, previous studies have already shown that active YAP/TAZ is required for maintaining the TIC and self-renewal of CSCs and TAZ levels have prognosis value in breast cancer²⁷⁰. As previously described, Wnt/ β -catenin pathway has an important role in ISCs regulation and its hyperactivation induces CRC initiation²⁷¹. As YAP1 regulates Wnt pathway in the regenerating intestine, its activation could also contribute to CRC initiation downstream of APC^{265,272}. APC has demonstrated to bind directly SAV1 and LATS1/2, which promotes LATS1/2 phosphorylation and therefore YAP1 degradation²⁷².

One mechanism leading to YAP1 activation is through TGF β . Specifically, **TGF β promotes** RASSF1A degradation leading to YAP1 and SMAD2 interaction, imposing YAP1/SMAD2 nuclear localisation and oncogenic signalling²⁷³. Another mechanism, involving the Zyxin-Siah2-LATS2 axis, has been also proposed as a mediator of Hippo and TGF β pathway²⁷⁴. To note, in the EMT process, which is induced by TGF β , there is inactivation of the Hippo pathway by delocalisation of SCRIB, which has been also linked to KRAS action^{258,275}.

Not only Wnt and TGF β pathway, but also other canonical oncogenic pathways have been associated with YAP1. Hedgehog, Notch, insulin and mTOR pathways are commonly mutated in cancer and have been found to interact with the Hippo pathway²⁷⁶. In addition, YAP/TAZ are involved not only in tumour initiation but in other cancer processes such as metastasis, drug resistance or angiogenesis, making it a potential therapeutic target^{277–279}.

15.4. YAP1 in tumour dormancy

Many crosslinks between the Hippo pathway and **tumour dormancy** have been recently identified, including that associating p53 and the Hippo pathway in the process of quiescence entrance^{280,281}. Indeed, **Touil and colleagues** proposed that YAP1 could be a potential target to eliminate quiescent cancer cells after CT treatment, as its expression levels are predictive of

tumour relapse ²⁸². In general, activation of the Hippo pathway leading to YAP1 inactivation has tumour suppressor functions in several systems. For example, tetraploid cells, commonly found in many tumours, undergo p53-dependent growth arrest, by LATS2-induced stabilisation of p53 and inhibition of YAP/TAZ ²⁸³. In addition, **functional p53** has been found to promote Hippo signalling, thus inactivating YAP/TAZ and enhancing tumour suppression ²⁸⁴. In contrast, YAP1 activation has been demonstrated to induce tumour survival by inducing dormancy and suppressing apoptosis in lung cancer cells ²⁸⁵. Contrary to Kurppa et al. results, Cheung and collaborators demonstrated that YAP1 activation induced by LATS deletion reprogrammed Lgr5⁺ ISCs into a **foetal-like state** similar to that observed in the regenerating intestine leading to tumour growth and metastasis suppression in CRC, whereas YAP1 deletion promotes tumour growth ²⁸⁶. One explanation for these opposite results could be found in the different models used by these authors. For example, Cheung et al. tumour models are mainly **TP53 deficient**, whereas Kurppa et al. are likely using *TP53* proficient cells, although it is not clearly mentioned. Since functional p53 is essential for inducing tumour dormancy, *TP53* deficient could be unable to induce quiescence in response to YAP1 activation thus leading to cell death. More studies are needed to clarify the actual relation between Hippo and p53 pathway in tumour dormancy.

16. STEM CELL SIGNATURES WITH CLINICAL APPLICATIONS

16.1. Prognostic value of stem cell signatures in cancer

Multiple studies have demonstrated that activation of normal stem cell pathways in cancer cells contributes to increase tumourigenesis. Thus, identifying specific **stem cell genes**²⁸⁷ or **signatures**^{288–291} that are specifically overexpressed in CSCs can be useful for predicting prognosis or therapy responses in patients. For instance, a *BMI1*-related 11-gene signature in primary tumours, obtained from microarray analysis, has been demonstrated to be predictor of distant metastases, in 11 different types of cancer²⁹². Another study highlighted the capacity of microarray analysis as a diagnostic test for identification of previously established prognostic signatures²⁹³.

In order to facilitate the clinical implementation of gene signatures in patient prognosis, some **gene expression ratios** have been established. Commonly, they are ratios between the expression of a subset of genes that predicts poor prognosis when highly expressed and a subset of genes predicting poor prognosis when having low expression. These expression ratios have been demonstrated to have clinical applications, both in general and at certain tumour stages^{294,295}. In particular, the ratio between HOXB13 and IL17BR predicts disease-free survival in breast cancer patients and has been widely used for identifying patients that will respond to tamoxifen treatment^{294,296}, specifically in early-stage tumours^{297,298}. Another expression ratio derived from genes of the Yin and Yang pathways demonstrated its value in lung cancer prognosis, independently on the sequencing platform used^{295,299}.

16.2. Intestinal stem cell signatures in CRC

Gene expression profiling has been widely used to improve the knowledge in cancer progression^{300,301}, tumour classification^{302,303} and risk stratification of **CRC patients**^{304–307}, specifically relevant in early stage tumours^{308–312}. Moreover, it has been used to explore the link between the presence of certain gene signatures with **treatment response** to specific drugs^{313–315}. For example, p53 mild expression has been associated with poor prognosis in CRC patients treated with adjuvant FOLFOX at stage II and III³¹⁶.

As mentioned, around 25-30% of CRC patients with stage II tumours and up to 30-50% in stage III still relapse, even after adequate treatment (data from American Cancer Society). Thus, generating tools for **predicting disease relapse** is of major importance. Merlos-Suárez and colleagues in 2011 demonstrated that the presence of an **adult ISC signature** in CRC tumours

predicts high risk of relapse. Briefly, they defined an ISC signature specifically expressed in EphB2-high murine crypt cells, which was also present in metastatic and poorly differentiated CRC tumours and predicted disease relapse. Further experimental validation demonstrated that EphB2-high cancer cells showed superior TIC *in vivo* and self-renewal capacity, consistent with the higher malignancy of this signature in patients ³¹⁷.

Another gene signature derived from colorectal CSCs displaying high levels of Wnt signalling predicted poor prognosis in patients. However, a more detailed analysis of Wnt target genes in this signature demonstrated that they become silenced by promoter methylation upon tumour progression and re-expression of these genes was associated to decreased tumour growth. Thus, high levels of promoter methylation of Wnt target genes were predictive of CRC recurrence ³¹⁸. In line with this study, a signature based on epigenomic modifications at enhancer elements has been identified to promote tumourigenesis ³¹⁹.

OBJECTIVES

OBJECTIVES

Taking into account all the previous published data, our general objective is to study the effects of low-dose CT treatment and its implications in the progression and relapse of CRC patients, in order to explore new therapeutic strategies for cancer treatment.

This main goal is subdivided in particular sub-objectives:

1. To expand and characterise a CRC PDOs biobank.
2. To characterise the effect of low-dose CT treatment in our CRC PDOs.
3. To analyse the pathways and signatures associated with low-dose CT treated-PDOs and explore their possible clinical applications.
4. To study the TIC activity of low-dose CT treated-PDOs *in vitro* and *in vivo*.
5. To test the resistance of these cells to subsequent treatments and analyse possible treatment strategies.

MATERIALS AND METHODS

MM1. PDOs GENERATION

PDOs have been recently used as a cancer model, which have the capacity to resemble the original human tumour. In this study, fragments of primary or xenograft human CRC tumours were obtained from Parc de Salut MAR Biobank (MARbiobanc; <https://marbiobanc.imim.es>) with the informed consent of patients and following all recommendations of Hospital del Mar' Ethics Committee, the Spanish regulations, and the Helsinki declaration's Guide.

PDO	Tumour subtype	PDO mutations	Original tumour mutations
PDO3	CRC	N/A	<i>BRAF</i> (N/A)
PDO4	CRC metastasis in the liver	<i>TP53</i> I254T (100%) <i>EGFR</i> S464L (97.21%)	<i>TP53</i> I254T (77.96%) <i>EGFR</i> S464L (97.18%)
PDO5	CRC	<i>KRAS</i> G12D (66.43%)	<i>KRAS</i> G12D (15.52%) <i>PDGFRA</i> R293H (14.79%) <i>TP53</i> H179R (12.51%)
PDO6	CRC metastasis in the liver	<i>NRAS</i> Q61K (38%) <i>TP53</i> R175H (99.04%) <i>EGFR</i> E928K (48.45%)	<i>NRAS</i> Q61K (26.70%) <i>TP53</i> R175H (61.92%) <i>EGFR</i> E928K (37.57%)
PDO7	CRC	<i>TP53</i> deletion53pb STOP (79.01%) <i>PIK3CA</i> D939G (50.98%) <i>ALK</i> R1060H (47.96%)	<i>PIK3CA</i> D939G (39.02%) <i>TP53</i> K120R (4.42%)
PDO8	CRC	<i>TP53</i> Q192stop (98.46%) <i>KRAS</i> G13C (67.27%)	<i>TP53</i> Q192stop (44.72%) <i>KRAS</i> G13C (44.26%)
PDO9	MSI	N/A	<i>APC</i> (N/A) <i>BRAF</i> (N/A) <i>TP53</i> (N/A)
PDO10	MSI	<i>TP53</i> R282W (99.82%) <i>FGFR2</i> C809W (62.72%) <i>KRAS</i> A146V (80.25%)	N/A
PDO11	MSI	<i>TP53</i> H168R (46.54%) <i>FGFR2</i> N194stop (45.87%) <i>KRAS</i> G12D (49.58%) <i>ERBB2</i> A87T (4.76%) <i>PIK3CA</i> S874N (41.93%) <i>PDGFRA</i> R293H (5.97%) <i>EGFR</i> K960R (46.3%) <i>BRAF</i> E71D (42.08%)	N/A
PDO12	CRC	N/A	<i>KRAS</i> G12D
PDO15	CRC metastasis in the ovary	<i>TP53</i> G262V (98.82%)	wt for <i>KRAS</i> , <i>BRAF</i> , <i>NRAS</i>
PDO20*	CRC	<i>APC</i> Q1123X (60.38%) <i>KRAS</i> G12V (26.42%) <i>PI3KCA</i> H1047L (49.94%)	N/A
PDO53*	CRC	<i>KRAS</i> G12D (42.98 %)	N/A
PDO66*	CRC	<i>NRAS</i> (G12S) (99.05%) <i>APC</i> (S1110stop) (99.80%)	N/A

Table MM1. List of CRC PDOs in the biobank. Mutations of PDOs and the original tumour they come from are indicated. * PDOs not in the biobank, provided by Alberto Muñoz group.

PDO20, PDO53 and PDO66 were kindly provided by IdiPAZ Biobank, integrated in the Spanish Hospital Biobanks Network (RetBioH; www.redbiobancos.es). The PDOs used in this thesis are listed in TABLE MM1, with their corresponding genotypes indicated and also the mutations from the original tumour. Normally, PDOs carry the same mutations as the original tumour, although percentage of cells carrying them can vary.

Factors	Stock Concentration	Final Concentration	Volume
DMEM-F12 [GIBCO Ref. 12634028]	1X	1X	50 mL
Penicillin/Streptomycin (P/S) [Thermo Scientific Ref. 15140122]	100 U/mL	1U/mL	500 µL
L-Glutamine [Thermo Scientific Ref. A2916801]	100X	1X	500 µL
Primocin [Invitrogen Ref. ant-pm-1]	100 µg/mL	200 ng/mL	100 µL

Table MM2. List of DF12⁺⁺⁺ medium factors.

Factors	Stock Concentration	Final Concentration	Volume
DF12 ⁺⁺⁺ medium	1X	1X	40 mL
B-27 Supplement [GIBCO Ref. 17504044]	50X	1X	800 µL
N-2 Supplement [GIBCO Ref. 17502048]	100X	1X	400 µL
Nicotinamide [Sigma-Aldrich Ref. N3376]	1 M	10 mM	400 µL
N-Acetyl-L-cysteine [Sigma-Aldrich Ref. A7250]	0.5 M	1.25 mM	100 µL
Recombinant Human Noggin [PeproTech Ref. 120-10C]	100 µg/mL	100 ng/mL	40 µL
Recombinant Human R-Spondin-1 [PeproTech Ref. 120-38]	100 µg/mL	100 ng/mL	40 µL
Y-27632 dihydrochloride (ROCK inhibitor) [Sigma-Aldrich Ref. Y0503]	40 mM	10 µM	10 µL
Prostaglandin E2 [Tocris Ref. 2296]	50 µM	10 nM	8 µL
SB 202190 [Sigma-Aldrich Ref. S7067]	15 mM	3 µM	8 µL
A 83-01 (ALK inhibitor) [Sigma-Aldrich Ref. SML0788]	10 mM	0.5 µM	2 µL
hEGF [Sigma-Aldrich Ref. E9644]	1 mg/mL	50 ng/mL	2 µL
Gastrin I [Tocris Ref. 3006]	500 µM	10 nM	0.8 µL
Ciprofloxacin [Sigma-Aldrich Ref. 17850]	2 mg/mL	8 µg/mL	200 µL

Table MM3. List of complete medium factors.

For PDO generation and culture, DF12⁺⁺⁺ and complete medium is needed. The preparation of these mediums is performed using the factors listed in TABLES MM2 and MM3. Complete medium can be kept a maximum of 2 weeks at 4°C. The protocol used for human tumour cell isolation was adapted from ¹⁷, as follows:

1. For every human sample, perform everything for duplicate. Cut the tumour samples with a scalpel to 1-2 mm².
2. Transfer the samples with a plastic Pasteur pipette into previously prepared falcons containing the factors listed in TABLE MM4.
3. Incubate at 37°C for 40 min in agitation, in horizontal position, for disaggregation of the tumours.
4. Add 1 mL of FBS.
5. Filter with a 100 µm cell strainer.
6. Centrifuge at 100 rcf for 3 min.
7. Aspirate the supernatant. Resuspend the pellet with 1 mL of DF12⁺⁺⁺ medium and transfer it to an eppendorf.
8. Centrifuge at 600 rcf for 5 min.
9. Aspirate the supernatant. Resuspend the pellet with 1 mL of DF12⁺⁺⁺ medium.
10. Prepare adequate dilutions of cell suspension depending on the cell pellet, for example 1/2, 1/10 and 1/100. Make 2 wells per dilution.
11. Centrifuge the eppendorfs again and leave 50 µL of medium.
12. Resuspend the pellet and add 100 µL of Matrigel Basement Membrane Matrix [Corning Ref. 354234] (50 µL per well). Maintain the matrigel with the cells always in ice. Seed 50 µL of the mix in the middle of the well of a 24-well plate, avoiding bubble formation.
13. Incubate 10 min at 37°C.
14. Add 450 µL of complete medium, slowly against the well.

Factors	Stock Concentration	Final Concentration	Volume
PBS + 5% P/S	1X	85%	8.5 mL
Collagenase II [Sigma-Aldrich Ref. C6885]	10 mg/mL	1.5 mg/mL	1.5 mL
Hyaluronidase [Sigma-Aldrich Ref. H3506]	10 mg/mL	20 µg/mL	20 µL
Y-27632 dihydrochloride (ROCK inhibitor) [Sigma-Aldrich Ref. Y0503]	40 mM	10 µM	2.5 µL

Table MM4. Factors used for tumour disaggregation.

MM2. PDOs CULTURE AND PASSAGING

PDOs normally have to be passaged every 1-2 weeks and complete medium has to be changed at least once a week. Depending on the PDO, you should disaggregate them mechanically or produce single cells. PDOs were expanded by serial passaging and kept frozen in liquid Nitrogen for being used in subsequent experiments.

MM2.1. Mechanical disaggregation

1. Resuspend the matrigel: with 1 mL filter tips, pipetting up and down the matrigel with the medium. Avoid bubble formation. Transfer it to an eppendorf.
2. Pass the cell suspension 8 times through a 21 G needle.
3. Centrifuge at 1100 rcf for 5 min. Eliminate the supernatant, leaving 50 μ L.
4. Perform the right dilutions, normally 1 well to 2-4 wells. Add the right amount of matrigel (50 μ L per well) and seed them as explained before in a 24-well plate.
5. Incubate at 10 min at 37°C.
6. Add 450 μ L of complete medium, slowly against the wall.

MM2.2. Disaggregation to single cells

Used for passaging (24-well plate) but also for seeding PDOs to perform experiments (in 24- or 96-well plate).

1. Slowly, remove the medium and add 400 μ L of PBS. Resuspend the matrigel.
2. Centrifuge at 1100 rcf for 5 min. Eliminate the maximum of supernatant you can and resuspend the pellet with trypsin, the same volume as medium you left.
3. Incubate a 37°C for 15 min.
4. Add the double amount of trypsin of DF12⁺⁺⁺ medium + 10% FBS.
5. Pass the cell suspension 8 times through a 21G needle.
6. Count the cells with trypan blue.
7. Depending on the PDO, you will need to seed a different amount of cells per well. You should have 85% of matrigel and a mix of cells+DF12⁺⁺⁺ medium up to the final volume. If you need to add more than 15% of cells, then centrifuge and count again, reducing the cell suspension volume. You should seed 50 μ L per well of a 24-well plate or 10 μ L per well of a 96-well plate (if seeding for an experiment).
8. Incubate 10 min at 37°C and add the complete medium: 450 μ L/well in a 24-well plate and 100 μ L/well in a 96-well plate. If you have seed it in a 96-well plate for an

experiment, add 100 μL of water in the wells next to your seeded wells, for avoiding medium evaporation.

MM3. DNA ISOLATION AND SEQUENCING

In order to be able to determinate if variability in response to treatments are due to the presence of different mutations in the PDOs, total DNA was extracted using the QIAamp DNA Mini kit [Qiagen Ref. 51306] and sequenced for a selected number of genes.

MM3.1. DNA extraction from PDOs

1. Use 2-4 wells (24-wells plate) full of spheres.
2. Resuspend wells with 400 μL of PBS, 2 wells per eppendorf.
3. Pass the cell suspension 8 times through a 21G needle.
4. Centrifuge at full speed 1 min.
5. Resuspend cell pellet in 200 μL of PBS in total.
6. Add 20 μL Qiagen Protease and then add 200 μL of Buffer AL to the sample.
7. Incubate at 56°C for 10 min and centrifuge to remove drops.
8. Add 200 μL ethanol 100% and vortex.
9. Transfer the sample to the QIAamp Mini spin column and centrifuge at 6000 rcf for 1 min. Discard the filtrate.
10. Add 500 μL of Buffer AW1 and centrifuge at 6000 rcf for 1 min. Discard the filtrate.
11. Add 500 μL of Buffer AW2 and centrifuge at full speed for 3 min. Discard the filtrate and repeat the step centrifuging for 1 min.
12. For elution, incubate the QIAamp Mini spin column loaded with 50 μL of Buffer AE at room temperature for 5 min and then centrifuge at 6000 rcf for 1 min. Repeat this step.
13. Samples were quantified with a NanoDrop spectrophotometer [Thermo Scientific].

MM3.2. DNA sequencing from PDOs

MARGenomics, using next generation sequencing, performed DNA sequencing. A panel of genes (including *BRAF*, *EGFR*, *ERBB2*, *FGFR2*, *HRAS*, *KRAS*, *NRAS*, *PIK3CA* and *TP53*) was used. Some of these genes are commonly assessed in the clinics for selecting the adequate treatment of patients and assess their prognosis. Mutations identified in this step are detailed in TABLE MM1.

MM4. PDOs VIABILITY ASSAYS

Viability assays have been used in this study for analysing the response to drugs of the different PDOs. The number of viable cells has been measured by analysing the ATP present in the medium, which allows identifying the quantity of metabolically active cells in culture. 600 single PDO cells were plated in 96-well plates in 10 μ L matrigel with 100 μ L of complete medium. After 6 days in culture, growing PDOs were treated with combinations of 5-FU [Accord Ref. 606544.3] and Irinotecan [Fresenius Kabi Ref. 687014.3] for 72 hours at the concentrations that reduce a 20 and 30% of the cell growth (IC_{20} and IC_{30} , respectively), which are specific for each PDO as described in TABLE MM5. After 72 hours of treatment, we changed to fresh medium and measured the cell viability after 3 days, 1 week and 2 weeks using the CellTiter-Glo 3D Cell Viability Assay [Promega Ref. G7571], all steps done in the dark:

1. Equilibrate the plate and CellTiter Glo Reagent at room temperature for approximately 40 min.
2. Add 15 μ L of CellTiter-Glo Reagent to every well.
3. Mix contents for 5 min on an orbital shaker to induce cell lysis.
4. Allow the plate to incubate at room temperature for 25 min.
5. Record luminescence (measurement of 1 second per well) in an Orion II multiplate luminometer.
6. Images in each experiment were obtained with an Olympus BX61 microscope at the indicated time points and the diameter of at least 70 PDOs per condition was determined using Adobe Photoshop.

PDO	IC_{20} (μ g/mL)	IC_{30} (μ g/mL)
PDO4	5-FU 1.25 Iri. 0.50	5-FU 2.00 Iri. 0.80
PDO5	5-FU 0.14 Iri.] 0.06	5-FU 0.25 Iri. 0.10
PDO8	5-FU 0.78 Iri. 0.31	5-FU 1.56 Iri. 0.63
PDO10	5-FU 6.25 Iri. 2.50	5-FU 12.50 Iri. 5.00
PDO11	5-FU 0.78 Iri. 0.31	5-FU 1.56 Iri. 0.63
PDO15	5-FU 1.56 Iri. 0.63	5-FU 3.13 Iri. 1.25
PDO20	5-FU 0.25 Iri. 0.10	5-FU 0.50 Iri. 0.20
PDO53	5-FU 0.33 Iri. 0.10	5-FU 0.50 Iri. 0.20
PDO66	5-FU 0.63 Iri. 0.30	5-FU 2.50 Iri. 1.00

Table MM5. List of CRC PDOs used in this study, with their IC_{20} and IC_{30} indicated.

For dose-response curves, PDOs were plated in 96-well plates in matrigel and after 6 days in culture were treated with combinations of 5-FU and Irinotecan. Following 72 hours of treatment, we changed to fresh medium and treated with increasing concentrations of either 5-FU, Iri., dasatinib [Selleckchem Ref. S1021] (senolytic drug), verteporfin [Selleckchem Ref. S1786] (YAP1 inhibitor), vemurafenib (BRAF inhibitor) or combinations for 72 hours at the indicated concentrations. Cell viability was determined as described above.

MM5. PDOs TIC ASSAY *IN VITRO*

TIC assay assessed *in vitro* was performed to analyse the capacity of PDOs, after treatment with sublethal doses of chemotherapy for 72h, to produce new organoids when seeded as single cells.

1. Use 2 wells (24-wells plate) per condition of previously treated PDOs for 72h.
2. Produce single cells as described in MM2.
3. Seed 300 single cells in 96-well plates with 10 μ L matrigel.
4. After 11 days in culture, the number of PDOs in each well was counted, photographs were taken for PDO diameter determination with Photoshop and cell viability was measured as described in MM4.

MM6. ANIMAL STUDIES

In all our procedures, animals were kept under pathogen-free conditions, and animal work was conducted according to the guidelines from the Animal Care Committee at the Generalitat de Catalunya. The Committee for Animal Experimentation at the Institute of Biomedical Research of Bellvitge (Barcelona) approved these studies. In all the experiments, mice were sacrificed using exposure to CO₂. Fragments of human CRC tumours obtained from Parc de Salut MAR Biobank (MARbiobanc) were transplanted and expanded as orthoxenografts in the cecum of nude mice, NU/J (*Foxn1^{nu}*) from the Jackson Laboratory [JAX Red. 002019]. The expanded human tumours obtained with this procedure can be seeded as described in MM1 in order to obtain PDOs, increasing the efficiency of the technique.

To perform TIC assays *in vivo*, two approaches were used. Firstly, intracardiac injection of 40.000 Untreated (n=8) and IC₂₀ (n=7) or IC₃₀ (n=6) -treated PDO5 cells carrying a luciferase

reporter to NSG mice was performed. For checking that the injection was performed correctly, after injection animals were anaesthetised with isoflurane and were given 100µl of substrate D-luciferin [Goldbio Ref. LUCK] at 15 mg/mL by intraorbital injection. Bioluminescent imaging was performed placing the animals into the IVIS Lumina III In Vivo Imaging System [PerkinElmer]. Images were recorded with an exposure time of 2 minutes and were taken every week. Quantification was done using Living Image® software [PerkinElmer], taking into account the number of animals which developed metastasis. Secondly, equivalent amounts of disaggregated PDOs, previously treated for 72h with IC₂₀ and IC₃₀ of 5FU+Iri., were implanted as orthoxenografts. Follow-up of the growing tumours was done by palpation and animals were sacrificed when controls developed tumours of around 2 cm of diameter. Number of tumours and intraperitoneal implants formed were counted and weighted.

Tumours were expanded orthotopically to perform *in vivo* drug testing. When tumours were detectable by palpation (4-5 weeks), animals were randomly ascribed to the different groups of treatment. vemurafenib [LC Laboratories Ref. V-2800] (50 mg/kg) was administered orally every day, and 5-FU+Iri. (50 mg/kg each) intravenously every 4 days. After 21 days of treatment, mice were euthanised and tumours collected, photographed, measured and processed for IHC-P examination.

MM7. HUMAN SAMPLES

Formalin-fixed, paraffin-embedded tissue blocks of gastrointestinal tumour samples (from patients at diagnosis (biopsy) and after neoadjuvant therapy at the time of surgery) and tissue microarrays from CRC patients were obtained from Parc de Salut Mar Biobanc. Samples were retrieved under informed consent and approval of the Tumour Bank Committees according to Spanish ethical regulations and the guidelines of the Declaration of Helsinki. Patient identity for pathological specimens remained anonymous in the context of this study. Patient data was collected (ANNEX 1) and used for disease-free survival and overall survival calculation. IHC analyses were performed as described below and ki67 and YAP1 protein levels evaluated.

MM8. PARAFFIN EMBEDDING OF SAMPLES

For long-term conservation of samples and to perform immunohistochemistry and immunofluorescence analysis, samples have to be paraffin embedded. Depending on the origin of the sample, the protocol to embed with paraffin is slightly different, having to increase the times of each dehydration step when the using tissues.

MM8.1. PDOs samples

1. Use 2 wells (24 well-plate) for every paraffin block.
2. Resuspend the well with 400 μ L of PBS.
3. Centrifuge at 600 rcf for 5 min. Eliminate the supernatant very carefully.
4. Add 1 mL of paraformaldehyde (PFA) without resuspending the pellet.
5. Centrifuge at 600 rcf for 5 min.
6. Incubate 4 h at RT (maximum of 5 h).
7. Eliminate the supernatant, and wash adding 1 mL of the corresponding ethanol (25%-50%-75%-90% ethanol), centrifuge at 600 rcf for 5 min and incubate 30 min. Repeat the step for each alcohol. Leave it O/N with 90% ethanol.
8. Eliminate the supernatant, add 1 mL of the corresponding alcohol (x3 absolute ethanol and xylene), centrifuge at 600 rcf for 5 min and incubate 30 min. Repeat the step for each alcohol. Eliminate the supernatant.
9. Transfer the pellet to an adequate mould, with the help of a pipette. The pellet may be difficult to identify because is transparent at this step, so watch out not to lose it in the process.
10. Add paraffin very slowly and leave it O/N at 60°C.
11. Change the paraffin. Place the pellet correctly.
12. Cool down at -20°C for 30 min.
13. Unmould the block and store it at 4°C.

MM8.2. Tissue samples

1. Collect the tissues from the organs of interest in ice-cold PBS and place them in a cassette.
2. Fix in 4% PFA rocking O/N at RT. Wash x2 in PBS 15 min rocking at RT.
3. Wash in 25% and 50% ethanol rocking 15 min each at RT.
4. Wash in 75% ethanol rocking O/N at 4°C.
5. Wash in 90% ethanol rocking 30 min at RT.
6. Wash x3 in absolute ethanol and xylene rocking 1 h each at RT.

7. Place tissue in embedding moulds and incubate in paraffin 1 h at 65°C.
8. Change paraffin and incubate O/N at 65°C.
9. Change paraffin and cool down at -20°C.
10. Unmould the block and store it at 4°C.

MM9. HAEMATOXYLIN AND EOSIN (HE) STAINING

HE staining is widely used for correct visualisation of cell structures. Cell nucleus is stained by haematoxylin (dark-purple) and cytoplasm by eosin (pink), although other cell structures can also be stained, such as components from the extracellular matrix. With this objective, PDOs and tissue paraffin embedded samples were sectioned appropriately and stained with HE.

1. Dewax the slides heating them at 65°C, for 2 h or O/N if they have been re-paraffined, to melt all the paraffin.
2. Rehydration battery: xylene I and II 15 min each, absolute ethanol I and II, 96%, 70% and 50% ethanol 10 min each and distilled water for 10min.
3. Staining with haematoxylin for 30 sec [Merck Ref. 1092530500]. Wash with tap water for 5 min.
4. 80% ethanol 0.15% HCl for 30 sec. Wash with distilled water for 30 sec.
5. Ammonia water [NH₃(aq)] 0.3% for 30 sec. Wash with distilled water for 30 sec.
6. 96% ethanol for 5 min.
7. Counterstaining with eosin for 3 sec [Bio-Optica Ref. 05-10003/L].
8. Wash x3 with absolute ethanol 1 min each.
9. Dehydration battery: absolute ethanol I and II 5 min each and xylene I and II 5 min each.
10. Mount in DPX [Merck Ref. 1.01979.0500].
11. Images were obtained with an Olympus BX61 microscope.

MM10. ALCIAN BLUE STAINING

Alcian Blue staining is commonly used for Goblet cells identification, because stains acid mucopolysaccharides and glycosaminoglycans, which are produced by them. The staining is blue.

1. Dewax and rehydrate paraffin samples (see MM9).

2. Immerse in 3% of acetic acid in H₂O for 3 min at RT.
3. Immerse in Alcian Blue (10 mg/mL pH 2.5) [Merck Ref. 101647] for 2-10 min at RT.
4. Wash x1 with running water and x1 with distilled water.
5. Counterstain with Nuclear Fast Red solution [Sigma Ref.6409-77-4] for 10 min at RT.
6. Wash x1 with running water and x1 with distilled water.
7. De-hydration battery: ethanol 50%, ethanol 70%, ethanol 96%, ethanol 100% and xylene 100%, 2 min each.
8. Mount in DPX. Images were obtained with an Olympus BX61 microscope.

MM11. IMMUNOHISTOCHEMISTRY AND IMMUNOFLUORESCENCE

Immunohistochemistry (IHC-P) and immunofluorescence (IF) with paraffin embedded samples are commonly performed for direct visualisation of protein localisation and expression. However, proteins in IHC-P are stained with a coloured chromogen and in IF with a fluorochrome. PDOs and tissue paraffin embedded samples were sectioned appropriately (2.5- for PDOs or 4-micrometer sections for tissues) and stained by IHC-P or IF, only the final steps involved in developing the staining differ between them.

1. Dewax the slides heating them at 65°C, for 2 h or O/N if they have been re-paraffined, to melt all the paraffin.
2. Rehydration battery: xylene I and II 15 min each, absolute ethanol I and II, 96%, 70% and 50% ethanol 10 min each and distilled water for 10min.
3. Antigen retrieval: citrate-based antigen retrieval (sodium citrate pH 6.0) was used, at 100°C for 20 min without pressure.
4. Quenching of endogenous peroxidase activity with 1.5% H₂O₂ for 20 min.
5. Wash x3 with PBS rocking 5 min at RT.
6. Permeabilisation and blockage with 0.3% Triton X-100, 1% BSA in PBS for 1 h.
7. Incubate the appropriate dilutions of the primary antibodies in PBS containing 0.05% BSA, O/N at 4 °C (TABLE MM6).
8. Wash x3 with PBS 5 min at RT.
9. Incubate with the secondary antibodies, using the Envision+ System HRP Labelled Polymer anti-Rabbit [Dako Ref. K4003] or anti-Mouse [Dako Ref. K4001] for 90 min at RT.
10. Wash x5 with PBS 5 min at RT.
11. Develop the samples with the corresponding method, 3,3'-diaminobenzidine (DAB)

[Dako Ref. K3468] for IHC-P and Tyramide Signal Amplification System (TSA) [PerkinElmer Ref. NEL753001KT] for IF, as follows:

- a. **DAB:** develop with DAB for the appropriate time, wash x5 in PBS 5 min at RT and counterstain with haematoxylin and mount with DPX as explained in MM8. Images were obtained with an Olympus BX61 microscope.
- b. **TSA:** develop with TSA for the appropriate time, wash x5 in PBS 5 min at RT and mount with 4,6-diamino-2-phenylindole (DAPI) Fluoromount-G [Southern Biotech Ref. 0100-20], which counterstains nuclei with DAPI. Images were taken in an SP5 upright confocal microscope [Leica].

Antibody	Company	Reference	Specie	Dilution
ki67 (MM1)	Novocastra	NCL-Ki67-MM1	Mouse	1:500
Lysozyme	Dako	A0099	Rabbit	1:4000
γ H2A.X (pS139)	BD Biosciences	564719	Mouse	1:500
Cleaved caspase 3 (Asp175)	Cell Signaling	9661	Rabbit	1:100
Notch1 Cleaved (ICN1) (Val 1744)	Cell Signaling	2421	Rabbit	1:100
Hes1	Santa Cruz	13844	Goat	1:200
p53 DO-1	Abcam	ab1101	Mouse	1:500
p21 [EPR362]	Abcam	ab109520	Rabbit	1:500
CKN2A/p16 ^{INKa4} [EPR1473]	Abcam	ab108349	Rabbit	1:500
EphB2	RD Systems	AF467	Goat	1:250
YAP1	Abcam	ab52771	Rabbit	1:500
SERPINH1	Abcam	ab109117	Rabbit	1:200
S100A4	Sigma-Aldrich	AMAb90599	Mouse	1:200
TUBB6	Invitrogen	PA-598948	Rabbit	1:100
CD99L2	Abcam	ab224164	Rabbit	1:50

Table MM6. Antibodies used for IHC-P and IF.

MM12. CELL LINES AND REAGENTS

CRC cell lines HCT116 [ATCC Ref. CCL-247] and Ls174T [ATCC Ref. CCL-188] (*KRAS* mutated and *TP53* WT), SW480 [ATCC Ref. CCL-228] (*KRAS* and *TP53* mutated), HT29 [ATCC Ref. HTB-38D] (*BRAF* and *TP53* mutated) and HEK293T [ATCC Ref. CRL-11268] (for viral production) were obtained from the American Type Culture Collection [ATCC, USA]. All cells were grown in Dulbecco's modified Eagle's medium (DMEM) [Invitrogen] plus 10% FBS [Biological Industries], 4.5 g/L glucose [Life Technologies], 2 mM L-glutamine [Biological

Industries], 56 U/mL penicillin and 56µg/mL streptomycin [Biological Industries] and were maintained in a 5% CO₂ incubator at 37°C. Cell lines were used for Western blot (WB) analysis after 72 h of 5-FU+Iri. treatment, alone or in combination with verteporfin. 5-FU and irinotecan concentrations that reduced 30% of each cell growth were as follows: HCT116, 0.01 µg/mL 5-FU and 0.004 µg/mL Iri.; Ls174T, 0.025 µg/mL 5-FU and 0.01 µg/mL Iri.; SW480, 0.28 µg/mL 5-FU and 0.11 µg/mL Iri.; HT29, 0.33 µg/mL 5-FU and 0.13 µg/mL Iri.

MM13. PDOs INFECTION

PDOs were infected with lentiviruses carrying the appropriate plasmids. pLEX-hFLiG plasmid ¹⁷³ (for luciferase expression) was used for *in vivo* detection of metastasis, pLTPC-H2BeGFP plasmid (Gift from Héctor G. Palmer Lab, unpublished) was used for flow cytometry experiments and lentiCRISPR v2 plasmid [Addgene Ref. 52961] was used for knock-out experiments. Three sgRNA against *TP53* gene were designed using Benchling [RRID: SCR_013955] (TABLE MM7).

Target	sgRNA sequence
<i>TP53</i> – Exon 2	TCGACGCTAGGATCTGACTG
<i>TP53</i> – Exon 4	ACCAGCAGCTCCTACACCGG
<i>TP53</i> – Exon 4	CCATTGTTCAATATCGTCCG

Table MM7. sgRNA.

MM13.1. Viral production

Cell transfection is the non-viral process that permits exogenous nucleic acids enter into mammalian cells, without using viral infection. Polyethylenimine (PEI)-mediated [Polysciences Inc. Ref. 23996] transient transfection method was used to produce lentiviral particles, using HEK293T cells, as follows:

1. Seed 2.5M cells/plate of HEK293T cell line. Let them grow O/N.
2. Perform cell transfection with PEI.
 - a. Per plate, you will need:
 - i. 10 µg of the DNA of interest (non-common DNA)
 - ii. 7.5 µg pCMV-dR8.2 [Addgene Ref. 8455]
 - iii. 3 µg pMD2.G [Addgene Ref. 12259]
 - iv. 1 µg pCS2EA (GFP)

- v. PEI: 4 $\mu\text{L}/\mu\text{g}$ DNA
 - vi. 1 mL serum-free DMEM
- b. Mix the serum-free DMEM and PEI and incubate for 5 min.
 - c. Add the common plasmids. Then add 1 mL of the mix to previously prepared eppendorfs containing the non-common DNA.
 - d. Incubate for 20 min.
 - e. Add 1 mL to every plate, drop by drop.
3. After one day, change the medium with fresh DMEM+10% FBS.
 4. After 24 h more, concentrate the viruses using Lenti-X Concentrator [Clontech Ref. 631232].
 - a. Filtrate the medium of every plate using a 0.45 μm filter and transfer it to 15 mL Falcon.
 - b. Add 1 volume of Lenti-X Concentrator per 3 volumes of supernatant. Mix per inversion.
 - c. Incubate at 4°C for 30 min.
 - d. Centrifuge at 1500 rcf for 45 min at 4°C. Eliminate the supernatant.
 - e. Resuspend with 700 μL of cold PBS.
 - f. Store at -80°C.

MM13.2. Viral infection

PDOs infection with viruses carrying plasmids described above was performed as follows:

1. Use 2-4 wells (24 wells plate) full of spheres.
2. Produce single cells as described in MM2.
3. Wash with DF12⁺⁺⁺ and centrifuge at 800 rcf for 5 min. Eliminate the supernatant.
4. Resuspend in an adequate volume of complete medium.
5. Count the cells and prepare the mix, for every well: 15.000 cells + complete medium up to 150 μL + 100 μL of PBS (negative control) or viruses + 0.25 μL polybrene.
6. Transfer 250 μL of the mix to a well of a 24 well-plate.
7. Seal the plate with parafilm and centrifuge it at 600 rcf for 1 h at 32°C.
8. Incubate the plate at 37°C for 5 h.
9. Transfer the content of every well to an eppendorf. Centrifuge at 800 rcf for 5 min.
10. Eliminate the supernatant, add 50 μL of matrigel and seed every eppendorf in a different well.
11. Incubate at 10 min at 37°C.
12. Add 450 μL of complete medium, slowly against the wall.

13. If the construct carries antibiotic resistance, put the antibiotic 3 days later and leave it at least for 1 week.

MM14. FLUORESCENT IN-SITU HYBRIDISATION (FISH)

FISH technique is commonly performed to identify numerical and structural chromosomal abnormalities. Specifically, centromeric or locus-specific probes can be useful for detecting aneuploidies or polyploidies, a common feature of tumoural cells. FISH analyses from control and IC₃₀-treated PDOs were performed using commercial probes [Abbott Molecular Inc.], one including the centromeric alpha-satellite region specific for chromosome 8, and a second one containing locus-specific probes from the long arm of chromosome 13 and 21.

1. Use 2 wells (24-wells plate) per condition.
2. Resuspend wells with 400 µL of PBS, 2 wells per eppendorf.
3. Concentrate the cells in the FISH slide by performing a cytopspin.
4. Pre-treatment with pepsin for 5 min at 37°C.
5. Co-denaturation at 80°C for 5 min.
6. Hybridisation at 37°C O/N in a hot plate [Hybrite chamber, Abbot Molecular Inc.].
7. Post-hybridisation washes at 73°C in x2 sodium salt citrate buffer and at room temperature in x2 SSC, 0.1% NP-40 solution.
8. Counterstaining with DAPI [Abbott Molecular Inc.].
9. Analysis of the results in a fluorescence microscope (Olympus, BX51) using the Cytovision software [Applied Imaging, Santa Clara, CA]. A minimum of 50 nuclei per case was analysed.

MM15. CELL CYCLE ANALYSIS

The study of cell cycle distribution permits to quantify the percentage of cells undergoing cell division. With this objective, bromodeoxyuridine (BrdU) incorporation has been used, which allows identifying cells that are newly synthesising DNA (cells entering in S phase will incorporate BrdU). Together with total DNA staining (for example with DAPI), cells can be classified in G_{0/1} (BrdU negative, DAPI staining), S (BrdU positive) and G_{2/M} (BrdU negative, double DNA content than G_{0/1}) cell cycle phases. Cell cycle was analysed by flow cytometry using a standard APC BrdU Flow Kit [BD Pharmigen Ref. 552598].

1. Add 10 μL of BrdU solution (1 mM BrdU in 1X PBS) to each mL of culture medium. Incubate the cells for 24h. Use at least 5 wells (24-wells plate) full of PDOs for each condition.
2. Produce single cells as described in MM2.
3. Wash with 1 mL of PBS.
4. Fixation and permeabilisation with 100 μL of BD Cytofix/Cytoperm Buffer. Incubate 30 min at RT.
5. Wash with 1 mL of 1X BD Perm/Wash Buffer. Centrifuge at 300 rcf for 5 min.
6. Add 100 μL of BD Cytoperm Buffer Plus. Incubate 10 min on ice and wash.
7. Re-fix with 100 μL of BD Cytofix/Cytoperm Buffer. Incubate 5 min at RT and wash.
8. Add 100 μL of 300 $\mu\text{g}/\text{mL}$ DNase. Incubate 1 h at 37°C and wash.
9. Add 50 μL of BD Perm/Wash Buffer with anti-BrdU antibody 1:50. Incubate 20 min at RT and wash.
10. Stain total DNA with DAPI.
11. Analyse the cells with the LSR II analyser and process the results with FlowJo software [BD Biosciences].

MM16. CELL SENESCENCE ASSAYS

Cell senescence is mainly characterised by cell cycle arrest, increase in the expression of certain proteins and the release of SASP factors. One of the most used biomarkers used to classify cells as senescent is the presence of SA- β -gal activity, which is a hydrolase enzyme only acting in senescent cells. In this study, SA- β -gal has been detected using two different approaches.

MM16.1. Senescence β -Galactosidase Staining Kit

Direct staining of SA- β -gal in cultured cells was carried out using the Senescence β -Galactosidase Staining Kit [Cell Signaling Ref. 9860]. PDOs were seeded in 24-well plates (3000 cells per well). After 6 days, PDOs were treated with combinations of 5-FU and Iri. for 72 hours and were subsequent stained as follows:

1. Use 2 wells (24-wells plate) per condition.
2. Resuspend wells with 400 μL of PBS, 2 wells per eppendorf.
3. Fix cells for 15 min with 1 mL of the fixative solution.
4. Wash x2 with PBS, centrifuging cells at 600 rcf for 5 min each wash.

5. Incubate the cells with 1 mL of the β -galactosidase staining solution for 2 h at 37°C, without CO₂.
6. After checking that cells have been stained, proceed to embed them in paraffin, as explained in MM8.
7. Counterstain paraffin sections with Fast Red for nuclei visualisation.
8. Images were obtained with an Olympus BX61 microscope.

MM16.2. Cell Event Senescence Green Flow Cytometry Assay Kit

SA- β -gal activity was addressed by flow cytometry using the Cell Event Senescence Green Flow Cytometry Assay Kit [Invitrogen Ref. C10840] and analysed in the LSR II analyser.

1. Use 5 wells (24-wells plate) per condition.
2. Produce single cells as described in MM2.
3. Wash with 1 mL of PBS. Centrifuge at 600 rcf for 5 min.
4. Resuspend cells in 100 μ L of Fixation Solution. Incubate for 10 min at RT.
5. Wash with 1% BSA in PBS.
6. Resuspend cells in 100 μ L of Working Solution (Green Probe 1:500 in CellEvent Senescence Buffer). Incubate for 2 h at 37°C without CO₂.
7. Wash with 1% BSA in PBS.
8. Resuspend cells in 300 μ L of 1% BSA in PBS.
9. Analyse the cells with the LSR II analyser and process the results with FlowJo software [BD Biosciences].

MM17. ANNEXIN V BINDING ASSAY

An early marker of apoptosis is phosphatidylserine (PS), which is transported from the inner to the outer part of the plasma membrane when pro-apoptotic signals are released. It has been demonstrated that annexin V can specifically bind to PS. For this reason, for analysing increase of apoptosis in cells under certain conditions the annexin V binding assay can be used. Apoptosis in treated PDOs was determined by flow cytometry using the standard Annexin V Apoptosis Detection Kit APC [Thermo Fisher Ref. 88-8007].

1. Use 2-4 wells (24-wells plate) per condition.
2. Produce single cells as described in MM2 and wash x1 with PBS and x1 with 1X Binding Buffer.

3. Incubate 15 min 100 μL of cells with 5 μl of fluorochrome-conjugated Annexin V, in the dark.
4. Wash cells in 1 mL of 1X Binding Buffer.
5. Resuspend in 300 μL of 1X Binding Buffer and add 7.5 μL of Propidium Iodide, for staining the DNA content.
6. Incubate 10 min at RT in the dark.
7. Analysis of the cells in the Fortessa analyser.

MM18. COMET ASSAY

One method to analyse DNA-damage is by comet assay, or single cell gel electrophoresis assay, which is based on the capacity of denatured and damaged DNA fragments to migrate when performing an electrophoresis. Conversely, intact DNA migrates slower and stays inside the nucleus. Analysis of the size and shape of the DNA “tail” reflects the quantity of DNA-damage in the cells. Comet assays were performed using the Comet Assay Kit [Trevigen Ref. 4250-050-K]. The alkaline assay was used because is more sensitive and is able to detect both single and double-stranded breaks and other types of DNA-damage, like DNA adducts.

1. Use 2-3 wells (24-wells plate) per condition.
2. Produce single cells as described in MM2.
3. Wash with 1 mL of PBS and resuspend in 100 μL of PBS.
4. Combine 35 μL of 12.500 cells diluted in PBS with 250 μL molten LMAgarose at 37°C and pipette 60 μL onto CometSlide.
5. Keep the slides at 4°C for 30 min.
6. Immerse slides in 4°C Lysis Solution O/N.
7. Immerse slides in Alkaline Unwinding Solution for 1 h at 4°C.
8. Perform electrophoresis at 21 V for 30 min immersing slides in 4°C Alkaline Electrophoresis Solution.
9. Wash with dH₂O twice end with 70% ethanol, 5 min each.
10. Dry samples at 37°C for 45 min.
11. Stain DNA with 100 μL of diluted SYBR Safe for 30 min.
12. Wash with dH₂O.
13. Allow slides to dry at 37°C.

14. At least 15 pictures of every replicate were taken using a Nikon Eclipse Ni-E epifluorescence microscope and tail moment was calculated using the OPENCOMET plugin for Fiji.

MM19. CELL LYSATES

Cell lysates from cultured PDOs were obtained for posterior WB analyses. CoIP buffer, used for this purpose, allows us to obtain the soluble fraction of cells separately from the insoluble fraction.

1. Use at least 2-4 wells (24-wells plate) full of spheres.
2. Resuspend the wells with 400 μ L of PBS, 2 wells per eppendorf.
3. Centrifuge at 1100 rcf 5 min.
4. Resuspend the cell pellet with 150 μ L of cold CoIP (PBS plus 0.5% Triton X-100, 1 mM EDTA, 100 mM NA-orthovanadate, 0.2 mM phenyl-methylsulfonylfluoride and protease and phosphatase inhibitor cocktails (1 tablet /0.5 L PBS) [Roche Ref.11836153001 and PHOSS-RO]).
5. Incubate 20 min on ice.
6. Centrifuge at maximum speed for 10 min at 4°C.
7. Recover the supernatant (soluble fraction), sonicate for 10 min (10 cycles 30 sec ON, 30 sec OFF), keep 5 μ L for Bradford and add the adequate volume of 6X Loading Buffer (50 mM Tris-HCl pH 6.8, 1.4 M β -mercaptoethanol (β -ME), 2% SDS, 0.1% bromophenol blue, 10% glycerol, in H₂O).
8. Resuspend the pellet with 100 μ L of 1X Loading Buffer and sonicate for 10 min (10 cycles 30 sec ON, 30 sec OFF) (insoluble fraction).
9. Boil at 95°C for 10 min.

MM20. WESTERN BLOT

WB is a common method to detect and quantify proteins from cell lysates. Briefly, denatured proteins are separated by gel electrophoresis based on their molecular weight and transferred to a membrane where they will be detected using specific antibodies. For protein visualisation, membranes are incubated with secondary antibodies conjugated to HRP that catalyse the

reaction to generate a light signal.

1. Carry out protein separation using standard SDS-polyacrylamide gel electrophoresis (SDS-PAGE) at 120 V. Load 25 µg of cell lysate.
2. Transfer the proteins to a Polyvinylidene difluoride (PVDF) membrane [Millipore Ref. IPVH00010] at 400 mA for 1 h.
3. Block the membrane with 5% non-fat milk in Tris buffered saline plus Tween-20 (TBS-T) buffer (50 mM Tris-HCl pH 8.0, 150 mM NaCl, 0.05% Tween-20 [VWR, Ref. 8.22184], in H₂O) rocking 1 h at RT.
4. Incubate the membranes with the adequate dilution of primary antibody in blocking solution (TABLE MM8) rocking O/N at 4°C.

Antibody	Company	Reference	Specie	Dilution
γH2A.X (pS139)	Cell Signaling	2577	Rabbit	1:1000
p53 DO-1	Abcam	ab1101	Mouse	1:1000
p21 [EPR362]	Abcam	ab109520	Rabbit	1:1000
CKN2A/p16 ^{INKa4} [EPR1473]	Abcam	ab108349	Rabbit	1:1000
ICAM1	Abcam	ab109361	Rabbit	1:1000
TIMP2	Abcam	ab1828	Mouse	1:1000
MRAS	Abcam	ab26303	Rabbit	1:2500
SERPINH1	Abcam	ab109117	Rabbit	1:1000
TUBB6	Invitrogen	PA-598948	Rabbit	1:6000
CD99L2	Abcam	ab224164	Rabbit	1:600
TSPAN4	Invitrogen	PA5-69344	Rabbit	1:1000
S100A4	Sigma-Aldrich	AMab90599	Mouse	1:1000
YAP1	Abcam	ab52771	Rabbit	1:1000
Tubulin-α	Sigma-Aldrich	T6074	Mouse	1:10000
Histone H3	Abcam	ab1791	Rabbit	1:5000
Polyclonal Goat anti-Rabbit Immunoglobulins/HRP	Dako	P0448	Goat anti-rabbit	1:2000
Polyclonal Rabbit anti-Mouse Immunoglobulins/HRP	Dako	P0260	Rabbit anti-mouse	1:2000

Table MM8. Antibodies used for WB.

5. Wash x6 in TBS-T buffer rocking 5 min at RT.
6. Incubate the membranes with the secondary antibody (HRP-conjugated) in blocking solution (TABLE MM8) rocking 2 h at RT.
7. Wash x6 in TBS-T buffer rocking 5 min at RT.
8. Peroxidase activity was visualised incubating them with the appropriate ECL solution

[Biological Industries Ref. 20-500-120] or [GE Healthcare RPN2232], which contains a chemiluminescent HRP substrate, and developing the signal in an autoradiography film [GE Healthcare Ref. 28906835].

MM21. RNA ISOLATION

Total RNA from treated PDOs was extracted with the RNeasy Micro Kit [Qiagen Ref. 74004], in order to be able to perform RT-qPCR or RNA-seq analyses afterwards.

1. Use 2-4 wells (24-wells plate) full of spheres
2. Resuspend wells with 400 μ L of PBS, 2 wells per eppendorf.
3. Produce single cells as described in MM2.
4. Centrifuge at 600 rcf for 5 min and discard supernatant.
5. Prepare 1 mL of RLT buffer plus 10 μ L of β -ME and add 350 μ L to PDOs.
6. Homogenise with a 21 G needle.
7. Add 1 volume of 70% ethanol and transfer it to a RNeasy MinElute spin column.
8. Centrifuge at 8000 rcf for 20 sec.
9. Add 350 μ L of RW1 Buffer. Centrifuge at 8000 rcf for 20 sec.
10. Add 10 μ L of diluted DNase I. Incubate for 15 min at RT.
11. Add 350 μ L of RW1 Buffer. Centrifuge at 8000 rcf for 20 sec.
12. Add 500 μ L of RPE Buffer. Centrifuge at 8000 rcf for 20 sec.
13. Add 500 μ L of 80% ethanol. Centrifuge at 8000 rcf for 2 min.
14. Centrifuge at 20.000 rcf for 5 min and discard supernatant.
15. For elution, add 15 μ L of H₂O. Centrifuge at 20.000 rcf for 1 min.

MM22. RT-qPCR

Reverse transcription quantitative real-time polymerase chain reaction (RT-qPCR) is a technique used to both amplify and quantify specific RNA sequences. First, complementary DNA (cDNA) has to be synthesised from total RNA by retrotranscription, using in this study the Transcriptor First Strand cDNA Synthesis Kit [Roche Ref. 04897030001].

Target	Forward	Reverse
<i>TP53</i>	CTTTGAGGTGCGTGTGTTGTG	GGGCAGTGCTCGCTTAGT
<i>CDKN1A</i>	CCGAAGTCAGTTCCTTGTGGA	TGGTGTCTCGGTGACAAAGT
<i>MDM2</i>	GCCATTGAACCTTGTGTGATT	GGCAGGGCTTATTCCCTTTTC
<i>PHLDA3</i>	CAGCTGTGGAAGCGGAAG	GCGAAGCTGAGCTCCTTG
<i>PLK2</i>	AATAACAAAGTCTACGCCGCA	TCTTTGTCAATCTTTCCCTTTG
<i>ZMAT3</i>	CTAGGGCAAAGCGCAAATAG	GACCAGCCACTCCAAAAGAG
<i>SESN1</i>	TGACCTGATGCCTTTCCTTC	CCTGGGGCTTAGTACCTTCC
<i>LAPTM5</i>	TCTTTTCCATCGCCTTCATC	CCTTCTGGAGCATCTTGGAG
<i>TIMP2</i>	TTCCCTCCCTCAAAGACTGA	CAAAGCCACCTACCTCCAAA
<i>CRIP2</i>	CGGTGGGCAGCTACATCTAT	CTGAGCACTCTCCAGCAGA
<i>KIFC3</i>	TGCCATGTACGAGTCAGAGC	CGGTTCTTGTCTCTTCCAG
<i>MRAS</i>	ACCGAGTTTTCCCATCAGTG	TCTCTTCCCTCCCAGGTTT
<i>SERPINH1</i>	CTTCATGGTGACTCGGTCCT	CGATTTGCAGCTTTTCCCTTC
<i>CD99L2</i>	CGGGTTGACATGAGAAAGGT	ATTCTGGCTTTGATGCTCGT
<i>TUBB6</i>	TGAGGGGCCACAAAATAAAC	TATAAGGCAACACGGCACAA
<i>TPM2</i>	GGACAGAGGATGAGGTGGAA	GCATCAGTGGCCTTCTTCTC
<i>GLIPR1</i>	CGCCATCACAACTGGTATG	ATCTGCCCAAACAACCTGAG
<i>TSPAN4</i>	TGCCTCCTGCTCACTTTCTT	GTCTTGCTGGGCATACCTGT
<i>ICAM1</i>	GAAGTGGCCCTCCATAGACA	TCAAGGGTTGGGGTCAGTAG
<i>ARL4C</i>	TGAGTCCCTGCCTATTGTCC	CAGATGGGCTGCTAGGTTTC
<i>VAMP5</i>	CCTGAAGGAGAAGCCAAATG	GTCAAGGGAGAGCAAACACC
<i>GPC1</i>	CCCTACGCTCATCTCTGGAA	GACCTTGTGGAGGAAGGACA
<i>COL18A1</i>	GAGGGACAAGTGGACTCAGG	TTGGCTTCACATCACACACA
<i>AGMAT</i>	TCTTTCTGGGAACACAGCCC	CGGTTGTCACTTTGGGGAGA
<i>KCNK5</i>	GAGGTGTGAGTCTGCGGAAG	GCCCTCGATGTAGTTCCACC
<i>CDX1</i>	ACCTCCTCTCCAATGCCTGT	AGACTCGGACCAGACCTCCT
<i>NOTCH3</i>	CTCATCCGAAACCGCTCTAC	TCTTCCACCATGCCCTCTAC
<i>HES1</i>	TCAACAGGACACCGGATAAA	CCGCGAGTATCTTTCTTCA
<i>HES2</i>	ACCCTGTAATGAGCCTTGGA	CCACACCTCCCCAGTATTTG
<i>HES5</i>	CCCTGCCGTTTTAGGACAATC	CATCCACCCACACAGAGGAATC
<i>ACTB</i>	GCACCACACCTTCTACAATGAGC	TAGCACAGCCTGGATAGCAACG
<i>B2M</i>	CCCCTGAAAAAGATGAG	CCTCCATGATGCTGCTT
<i>HPRT1</i>	ATAAGCCAGACTTTGTTGG	ATAGGACTCCAGATGTTTCC
<i>TBP</i>	GGAAGTGACATTATCAACGC	CCAAGAAACAGTGATGCTG

Table MM9. Primers used for RT-qPCR.

1. Measure RNA concentration with Nanodrop.
2. Mix 2 µg of RNA with H₂O up to 11 µL.
3. Add 2 µL of anchored-oligo(dT)18 primer.

4. Denature the template-primer mixture by heating the tube for 10 min at 65°C in a block cycler with a heated lid. This step ensures denaturation of RNA secondary structures.
5. Cool the tube on ice immediately.
6. Add 7 µL of a mix containing (X1 reaction): 4 µL of buffer, 2 µL of dNTPs, 0.5 µL RNase inhibitor and 0.5 µL Transcriptor Reverse Transcriptase.
7. Incubate at 30 min at 55°C in the block cycler.
8. Inactivate Transcriptor Reverse Transcriptase by heating to 85°C for 5 min and keep at 4°C.
9. Dilute the sample 1:10 with H₂O and store at -20°C.

After producing cDNA, RT-qPCR was performed in LightCycler 480 system using the SYBR Green I Master Kit [Roche Ref. 04887352001]. Samples were normalised to the mean expression of the housekeeping genes *TBP*, *HPRT1*, *B2M* and *ACTB*. Primers used for qPCR are listed in TABLE MM9.

1. Prepare a mix containing (X1 reaction): 5 µL of SYBR Green I Master Kit, 2 µL of H₂O, 0.5 µL of forward primer and 0.5 µL of reverse primer.
2. Add 8 µL of the mix to a 384-wells plate.
3. Add 2 µL of the diluted RNA.
4. Seal the plate and centrifuge at 150 rcf for 1 min.
5. Perform the RT-qPCR in a LightCycler 480 machine [Roche].

MM23. RNA-SEQUENCING (RNA-seq) AND DATA ANALYSIS

Total RNA from untreated and treated PDOs was extracted as described in MM20. The RNA concentration and integrity were determined using Agilent Bioanalyzer [Agilent Technologies]. Libraries were prepared at the Genomics Unit of PRBB (Barcelona, Spain) using standard protocols, and cDNA was sequenced using Illumina HiSeq platform, obtaining ~ 45-64 million 50-bp paired-end reads per sample. Adapter sequences were trimmed with Trim Galore. Sequences were filtered by quality ($Q > 30$) and length (> 20 bp). Filtered reads were mapped against the latest release of the human reference genome (hg38) using default parameters of TopHat (v.2.1.1)³²⁰ and expressed transcripts were then assembled. High-quality alignments were fed to HTSeq (v.0.9.1)³²¹ to estimate the normalised counts of each expressed gene.

Differentially expressed genes between different conditions were explored using DESeq2 R package (v.1.24.0)³²² and adjusted p-values for multiple comparisons were calculated applying the Benjamini-Hochberg correction (FDR). Plots were done in R. Expression heatmaps were generating using the heatmaply and pheatmap packages in R³²³. Gene Set Enrichment Analysis (GSEA) was performed with described gene sets using gene set permutations (n = 1000) for the assessment of significance and signal-to-noise metric for ranking genes. RNA-seq data are deposited at the GEO database with accession number GSE155354.

MM24. CHROMATIN-IMMUNOPRECIPITATION (ChIP)-qPCR AND ChIP-seq

ChIP is an assay used for studying the interaction of proteins to specific regions of the chromatin. Control and IC₂₀-treated PDOs were subjected to ChIP following standard procedures and ChIP-qPCR and ChIP-seq was performed, as follows:

1. Cross-linking reaction

- a) Use 30 wells (24-wells plate) full of spheres.
- b) Resuspend wells with 400 μ L of PBS, 2 wells per eppendorf.
- c) Produce single cells as described in MM2 and wash with PBS.
- d) Add 100 μ L (1/10) of cross-link solution (50 mM HEPES pH 8.0, 10 mM NaCl, 1 mM EDTA, 0.5 mM EGTA, 5.55% formaldehyde, in H₂O) to the samples to a final concentration of 0.5% formaldehyde [Sigma Ref.252549] and incubate 10 min gently rocking at RT.
- e) Add 100 μ L (1/10) of stop solution (1.25 M Glycine, 10 mM Tris-HCl pH 8.0, in H₂O) and incubate 5 min gently rocking at RT.
- f) Centrifuge 5 min at 600 rcf, discard supernatant and wash x2 with cold PBS supplemented with 0.5 mM EDTA and protease inhibitor cocktail.
- g) Centrifuge 5 min at 600 rcf. Discard supernatant.

2. Cell lysis

- a) Add 1 mL of lysis buffer (10 mM Tris-HCl pH 8.0, 0.25% Triton X-100, 10 mM EDTA, 0.5 mM EGTA, 10 mM Na-butyrate, 20 mM β -glycerol-phosphate, 0.1 mM Naorthovanadate, protease inhibitor cocktail, in H₂O) and incubate 20 min on ice.
- b) Centrifuge at 1000 rcf 4°C for 4 min. Discard supernatant.

- c) Add 1.5 mL ice-cold washing buffer, which contains sonication buffer (10 mM Tris-HCl pH 8.0, 0.1 M NaCl, 1 mM EDTA, 0.5 mM EGTA, 10 mM Na-butyrate, 20 mM β -glycerol-phosphate, 0.1 mM Naorthovanadate, protease inhibitor cocktail, in H₂O) plus 0.1 M NaCl.
 - d) Centrifuge at 1000 rcf 4°C for 4 min. Discard supernatant.
3. Sonication
- a) Add 800 μ L sonication buffer and 80 μ L of 10% SDS.
 - b) Sonicate cells at medium power with a 0.5 interval for 10 min using a Bioruptor Sonicator [Diagenode] and 200 μ L of beads
 - c) Check with a 2% agarose gel if 500 to 1500 bp DNA fragments have been generated.
 - d) Centrifuge at maximum speed for 30 min at 20°C. Collect the supernatant (soluble chromatin).
4. SDS wash
- a) Dilute the supernatant 10-fold with sonication buffer to reduce the concentration of SDS to 0.1%.
 - b) Concentrate the samples using a Vivaspin column [Sartorius Ref. VS2032], centrifuging at 1200 rcf at 20°C for 20 min.
 - c) Adjust the concentrated chromatin solution to RIPA buffer by adding (for 800 μ L of sample) 9 μ L of 10% deoxycholate (DOC), 25 μ L of 5 M NaCl and 80 μ L of 10% Triton X-100.
 - d) Collect 100 μ L, it will be the input sample.
5. Pre-clearing
- a) Pre-clear the chromatins by adding 1% BSA, 1 μ g salmon sperm DNA, unspecific pre-immune IgG (volume and species according to the used antibodies) and 60 μ L of 50:50 protein A/G-sepharose beads [GE Healthcare, Refs. 17-0618-01 and 17-0780-01]. Incubate rotating 2 h at 4°C.
 - b) Centrifuge at 240 rcf for 2 min and recover supernatant.
6. Immunoprecipitation
- a) Add 5 μ g of target antibody (anti-TP53 antibody, see TABLE MM8) to 800 μ L of the chromatin.
 - b) Incubate rotating O/N at 4°C.
 - c) Pull down the IgG-chromatin complexes by adding 60 μ L 50:50 protein A/G-sepharose beads. Incubate rotating 2 h at 4°C.
 - d) Centrifuge at 100 rcf for 2 min at 4°C. Discard the unbound fraction.

7. Washes: Rotate the samples at 4°C for 1 min, centrifuge at 100 rcf for 1 min and discard the supernatant after each washing step:
 - a) 2x with ice-cold RIPA buffer.
 - b) 2x with ice-cold RIPA-sodium buffer (RIPA buffer plus 1 M NaCl).
 - c) 1x with LiCl buffer (0.25 M LiCl, 1% Nonidet P-40, 1% DOC, 10 mM Tris-HCl pH 8.0, 1 mM EDTA, 1 mM EGTA, 10 mM Na-butyrate, 0.1 mM Na-orthovanadate, in H₂O).
 - d) 1x with TE buffer (10 mM Tris- HCl pH 8.0, 1 mM EDTA, in H₂O).
8. Elution and purification of DNA
 - a) Resuspend the complexes in 100 µL of Elution buffer (10 mM Tris-HCl pH 7.5, 1% SDS, 30 mM NaCl, 80 mM β-Glycerolphosphate, 10 mM NaButyrate). Incubate rocking 1 h at RT.
 - b) Centrifuge at 240 rcf for 2 min and recover supernatants.
 - c) Incubate the obtained DNA and inputs O/N at 65°C, for cross-link reversion.
 - d) Add 0.5 µg/µL Proteinase K [Roche Ref. 03115828001] and incubate 2 h at 55°C.
 - e) Purify the DNA using the MinElute PCR purification Kit [Qiagen Ref. 28006], following the manufacturer's instructions, eluting in 50 µL of H₂O.

ChIP-qPCR was performed as the qPCR described in MM22 with primers listed in TABLE MM10. Inputs were used to normalise the ChIP-qPCR and samples were compared to control IgGs.

Target	Forward	Reverse
<i>MDM2</i>	GGGCAGGTTGACTCAGCTTTT	AGCTGGGAAAATGCATGGTTTA
<i>CDKN1A</i>	AGCAGGCTGTGGCTCTGATT	CAAATAGCCACCAGCCTCTTCT
<i>ZMAT3</i>	CAAATTGCCACAAACATTCTGC	CTGGGGGAGACACATGCTAGA

Table MM10. Primers used for ChIP-qPCR.

ChIP-seq was directly sequenced in the genomics facility of Parc de Recerca Biomèdica de Barcelona (PRBB) using Illumina® HiSeq platform. Raw single-end 50-bp sequences were filtered by quality (Q>30) and length (length>20 bp) with Trim Galore³²⁴. Filtered sequences were aligned against the reference genome (hg38) with Bowtie2³²⁵. MACS2 software³²⁶ was run first for each replicate using unique alignments (q-value<0.1). Peak annotation was performed with ChIPseeker package³²⁷ and peak visualisation was done with Integrative Genomics Viewer (IGV). ChIP-sequencing data are deposited at the GEO database with accession number GSE164161.

MM25. GENERATION OF FOETAL INTESTINAL STEM CELL (feISC) SIGNATURES

MM25.1. Description of the patient gene expression data sets

Transcriptomic and available clinical data data sets from CRC were downloaded from the open-access resource CANCERTOOL. We used three different data sets: the Marisa (GSE39582) data set, which includes expression and clinical data for 566 patients with CRC and 19 non-tumoural colorectal mucosa, the Jorissen (GSE14333) data set of 226 patients and the TCGA data set of 329 patients.

MM25.2. Signature definition

To generate the feISC signatures, we selected genes with \log^2 Fold Change (FC) $TreatedvsControl > 0$ and $FoetalvsAdult^{80} > 0$ in the case of the 28up-feISC and \log^2FC $TreatedvsControl < 0$ and $FoetalvsAdult < 0$ in the case of the 8down-feISC. Next, we used the Marisa data set to perform expression correlation matrices for the selected expression gene pairs using the corrplot package (v.0.84). To obtain the simplified signature (5up+3down), genes were scored by their coordinate expression taking into account the three CRC data sets analysed. Then, genes from the 28up+8down signature were sequentially added, starting from the highest scored 28up plus the highest scored 8down-feISC genes and progressing with the next highest scored genes. The process ended when adding a gene did not improved the prognosis value. Correlations were considered as statistically significant when the Pearson correlation coefficient corresponded to a $p\text{-value} < 0.05$. Clusters of genes were selected when the absolute value for the Pearson correlation coefficient was above 0.1.

MM25.3. Association of the signatures with clinical outcome

Association of the signatures expression with relapse was assessed in the cancer transcriptomic data sets using a Kaplan-Meier estimates and Cox proportional hazard models. A standard log-rank test was applied to assess significance between groups. This test was selected because it assumes the randomness of the possible censorship. All the survival analyses and graphs were performed with R using the survival (v.3.2-3) and survimer (v.0.4.8) packages and a $p\text{-value} < 0.05$ was considered statistically significant.

MM26. QUANTIFICATION AND STATISTICAL ANALYSIS

Statistical parameters, including number of events quantified, standard deviation and statistical significance, are reported in the figures and in the figure legends. Statistical analysis has been performed using GraphPad Prism 6 software, and p -value <0.05 is considered significant. Two-sided Student's t -test was used to compare differences between two groups. Each experiment shown in the manuscript has been repeated at least twice. Combinations of 5-FU and Iri. treatment has been checked for an appropriate IC_{20} and IC_{30} effect in every experiment, by cell viability assay. Bioinformatics analyses were performed as indicated above.

RESULTS

Solé L, Lobo-Jarne T, Villanueva A, Vert A, Guillén Y, Sangrador I, Barbachano A, Lop J, Guix M, Salido M, Bellosillo B, García-Romero R, Garrido M, González J, Martínez-Iniesta M, Lopez-Arribillaga E, Salazar R, Montagut C, Torres F, Iglesias M, Celià-Terrassa T, Muñoz A, Bigas A and Espinosa L. Chemotherapy imposes a fetal phenotype to p53 wild type cancer cells predictive of poor prognosis. Recently submitted.

R1. ESTABLISHMENT AND CHARACTERISATION OF A CRC PDOs BIOBANK

R1.1. Establishment of a CRC PDOs biobank

In our laboratory, we have recently generated a CRC PDOs living biobank, which is available for any research group in the context of a research project. Our biobank is part of the Parc de Salut MAR Biobank (MARbiobanc) and the tumour samples come from patients at Hospital del Mar. The generation of the PDOs has been optimised as described in MM1, seeding them in a 3D culture using Matrigel. Once PDOs are generated, they are expanded and the PDO material (a minimum of 10 vials per PDO) is kept frozen and incorporated in the biobank (FIGURE R1A). We are able to expand the PDOs multiple passages, and we have set up all kind of techniques for their characterisation and drug screening.

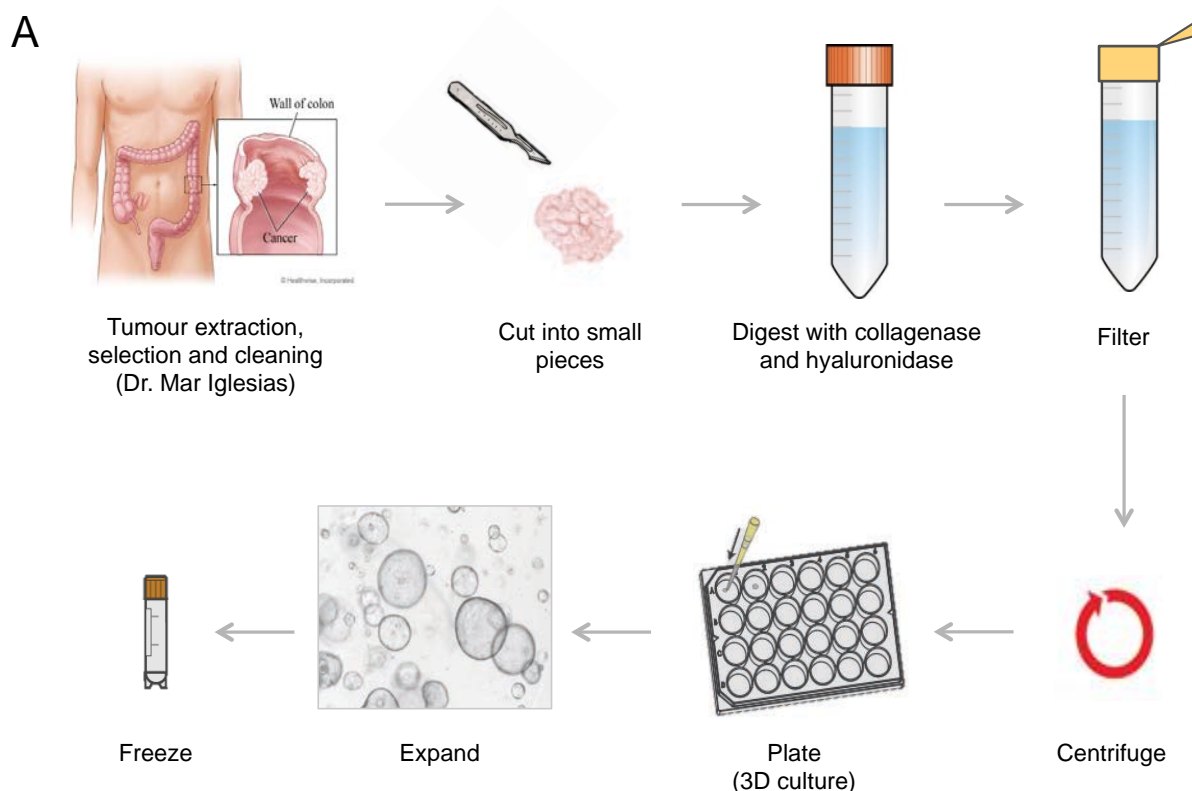


Figure R1. Optimisation of CRC PDOs generation. (A) Tumour extraction, selection and cleaning is done in the Hospital del Mar, by Dr. Mar Iglesias. In our laboratory, the tumour is cut into small pieces, digested with collagenase and hyaluronidase, filtered, centrifuged and plated in a 3D culture. When the PDO can be passaged, is then expanded until it can be frozen.

By now, the biobank is composed of 11 different PDOs (TABLE MM1). In the near future we will also try to generate “in parallel” samples including the PDOs and the normal organoid from their corresponding healthy tissue. The PDOs can be classified by their appearance into cystic (adenoma-like, formed by an epithelial monolayer) or compact (multilayer spheres) PDOs, although there are heterogeneous PDOs composed of both types of structures. Examples of these different morphologies can be identified in Figure R2A and the histology of PDOs can be observed with HE staining (FIGURE R3A, left panel).

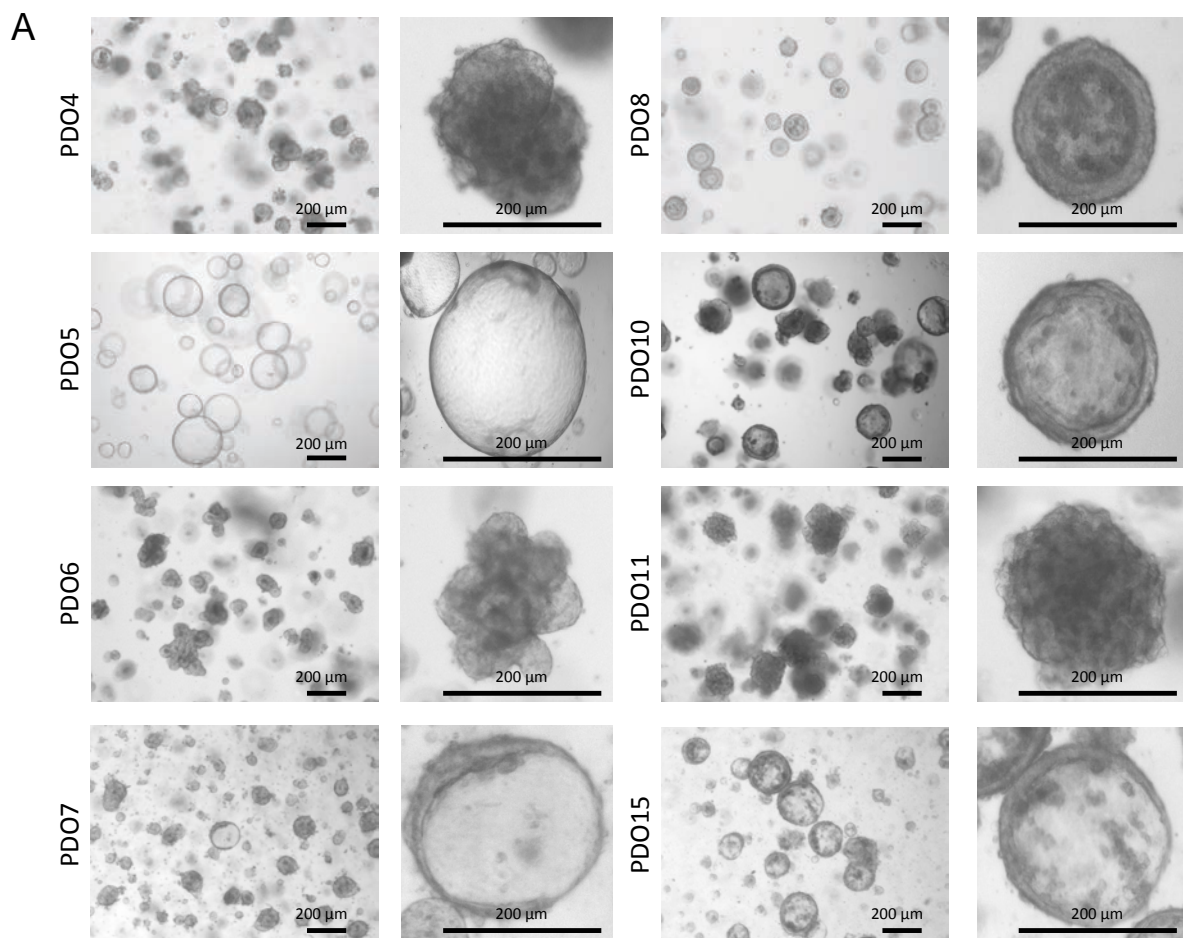


Figure R2. CRC PDOs display cystic and compact morphologies. (A) Photographs of PDOs in our biobank, displaying cystic (PDO5 and PDO15), compact (PDO6 and PDO11) and mixed (PDO4, PDO7, PDO8 and PDO10) morphologies.

Under PDOs culture conditions (including the matrix, medium and factors) stem cells growth is favoured. In culture conditions for normal intestine, stem cells proliferate and then differentiate

into the different cell types of the intestine. In contrast, tumour PDO cells are mainly maintained in an undifferentiated state and keep proliferating as tumour tissue. In order to characterise the cell types that are present in our PDO collection, some IHC-P were performed. First, ki67 staining demonstrated that our PDOs are highly proliferating, with some differences inter- and intra-PDOs (FIGURE R3A, middle panel). Staining with EphB2, a marker of ISCs, demonstrated that almost all cells composing the PDOs display ISC-like traits (FIGURE R3A, right panel).

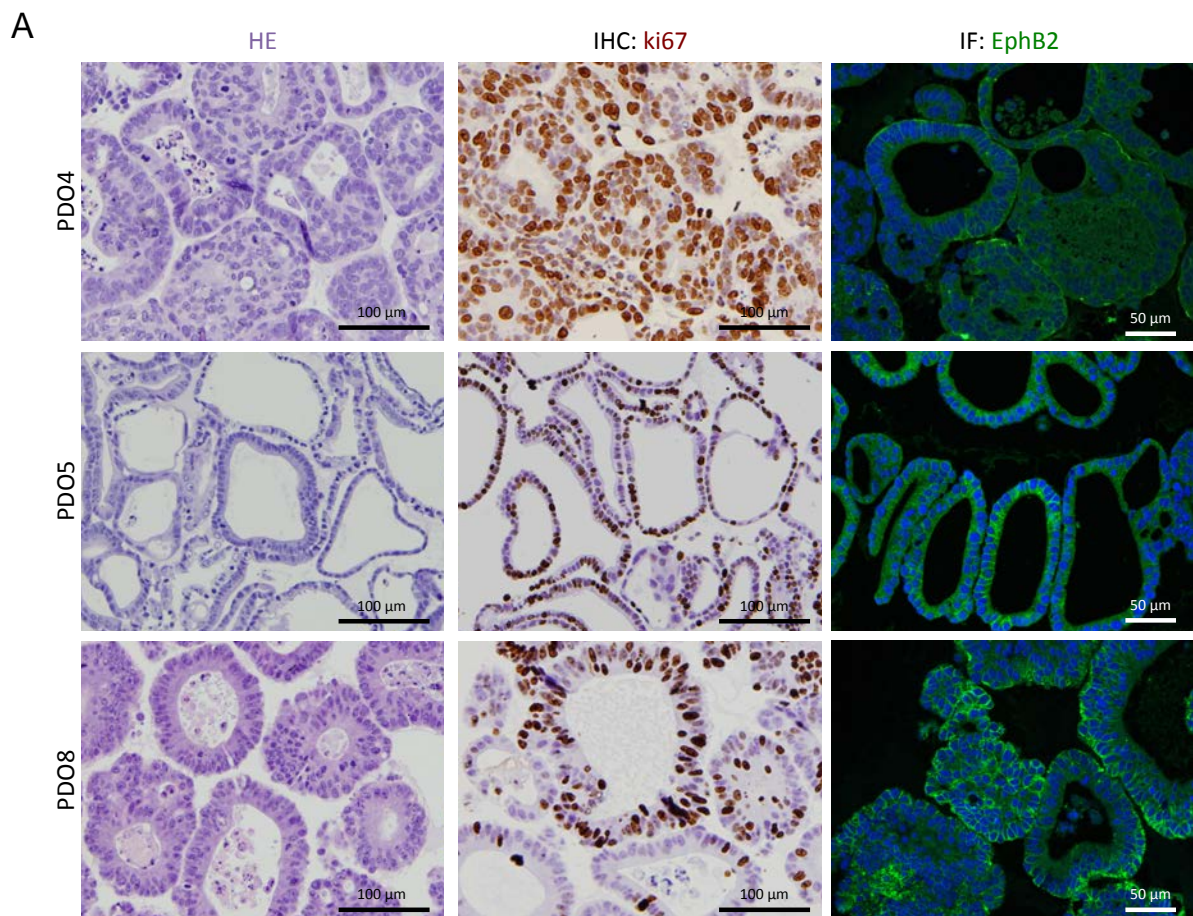


Figure R3. CRC PDOs are highly proliferating and display ISC-like traits. (A) Photographs of HE staining (left panel), IHC-P of ki67 staining counterstained with haematoxylin (middle panel), IF of EphB2 staining counterstained with DAPI (right panel).

Differentiated cells can be identified by specific stainings, such as Paneth cells (by lysozyme IHC-P staining) or Goblet cells (by Alcian Blue staining). In contrast with organoids from normal intestine, which present a high number of differentiated cells (FIGURE R4A), PDOs are mainly

composed of undifferentiated cells, as they lack Paneth and Goblet cells as determined by the absence of lysozyme and Alcian Blue stainings (FIGURE R4B).

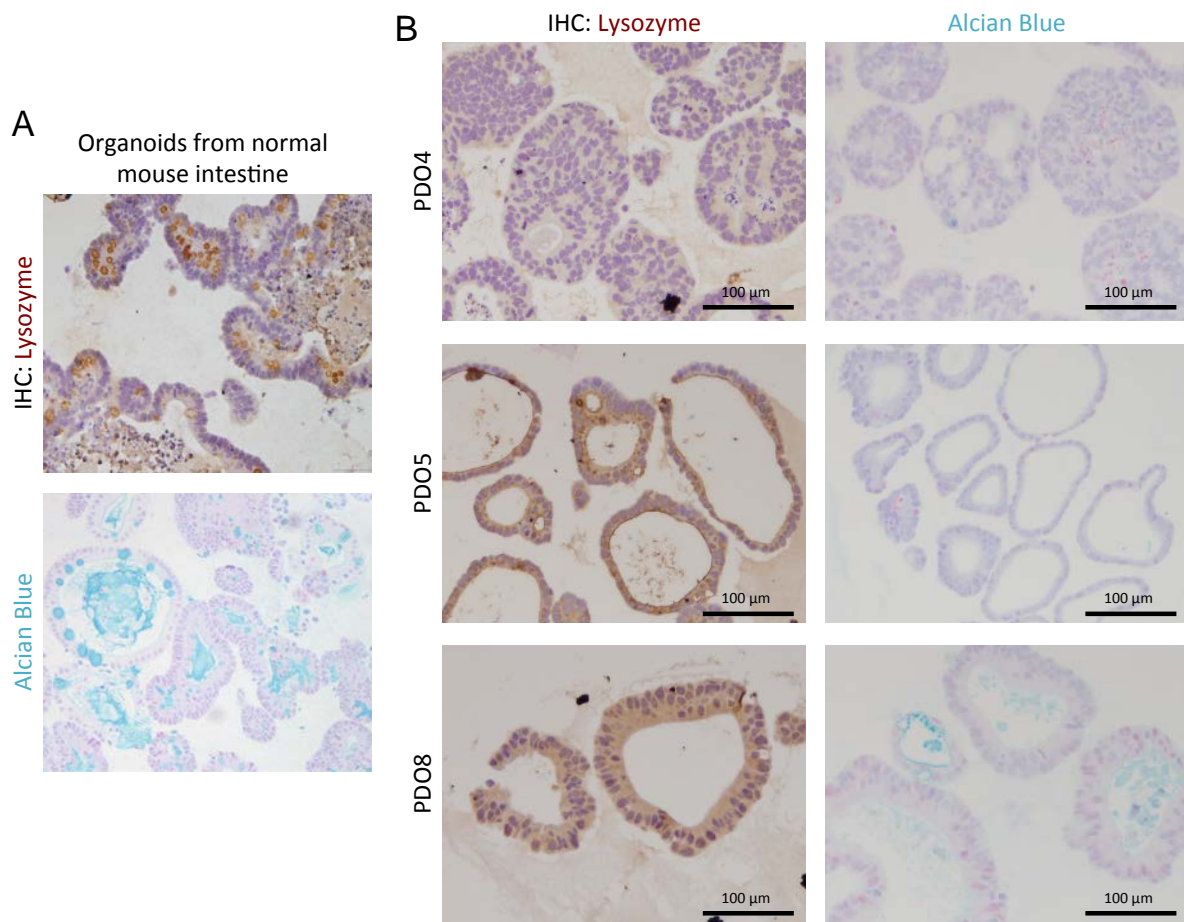


Figure R4. CRC PDOs cells do not differentiate to Paneth and Goblet cells. (A and B) IHC-P of lysozyme and Alcian Blue staining of **(A)** organoids from normal mouse intestine and **(B)** of CRC PDOs.

R1.2. CRC PDOs of our biobank resemble the original tumours

To analyse in more detail the generated PDOs, we classified them in three different subgroups, according to the subtype of the tumour they come from. 45.45% of the PDOs come from primary CRC tumours (PDO3, PDO5, PDO8, PDO7 and PDO12), 27.27% from CRC metastasis (PDO4, PDO6 and PDO15) and 27.27% from CRC patients presenting MSI (PDO9, PDO10 and PDO11) (TABLE MM1).

Moreover, we compared the mutational landscape of our PDOs by new-generation sequencing (NGS) of a panel of genes that are normally mutated in CRC (including *BRAF*, *EGFR*, *ERBB2*, *FGFR2*, *HRAS*, *KRAS*, *NRAS*, *PIK3CA* and *TP53*) in comparison with the mutations of the original tumours obtained from Hospital del Mar (TABLE MM1). Although we do not know the

mutations of all the cases yet, we studied if mutations in PDOs and in the tumours were similar together with the percentage of cells carrying each specific mutation. We found that the majority of the mutations in the tumours were also present in PDOs, although their percentage was frequently higher in PDOs (FIGURE R5A). In some cases there were some variations in the mutations. For example, the mutation in *ALK* in PDO7 was newly detected in the PDO. This result suggests that this mutation is poorly represented in the tumour and was positively selected in the PDO culture. On the other hand, mutations in *TP53* and *PDGFRA* that are present in the tumour that originated PDO5 is lost in the PDO, leading to a partial loss of heterogeneity.

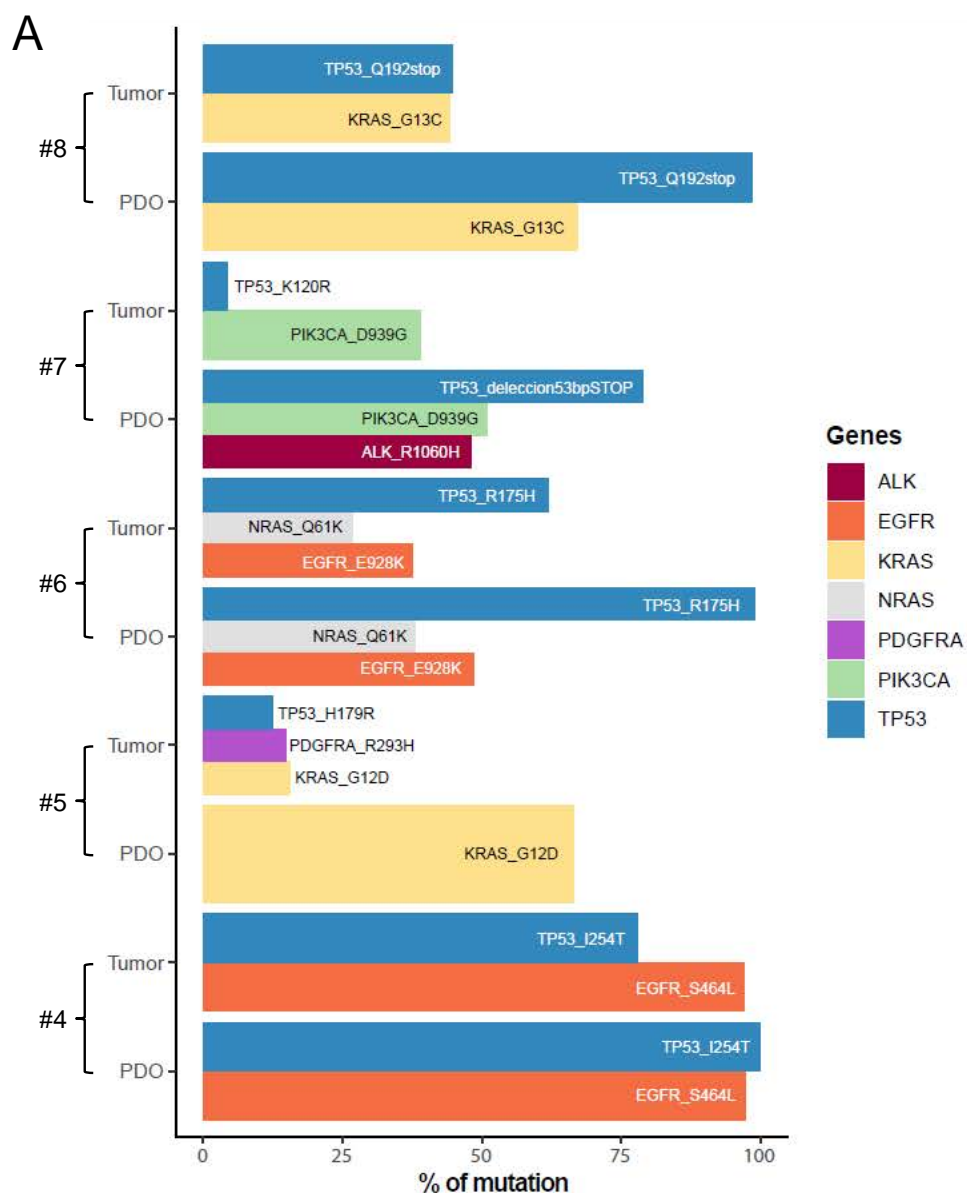


Figure R5. CRC PDOs recapitulate original tumour mutations. (A) Comparative graphical representation of percentage of gene mutations found in CRC tumours and their corresponding PDOs. Colours indicate genes and specific mutations are depicted in the barplots.

R1.3. CRC PDOs of our biobank display different drug sensitivity

PDOs are widely used for drug screening analysis since results obtained in these models can be reliably extrapolated to patients¹⁶². To determine CT sensitivity of our PDOs in a more accurate manner, we first seeded different number of cells per well in 96-well plates, and after 9 days we determined the amount of cells to obtain 50% of the saturated cultures. This data is specific for each PDO (FIGURE R6A, B, C and D).

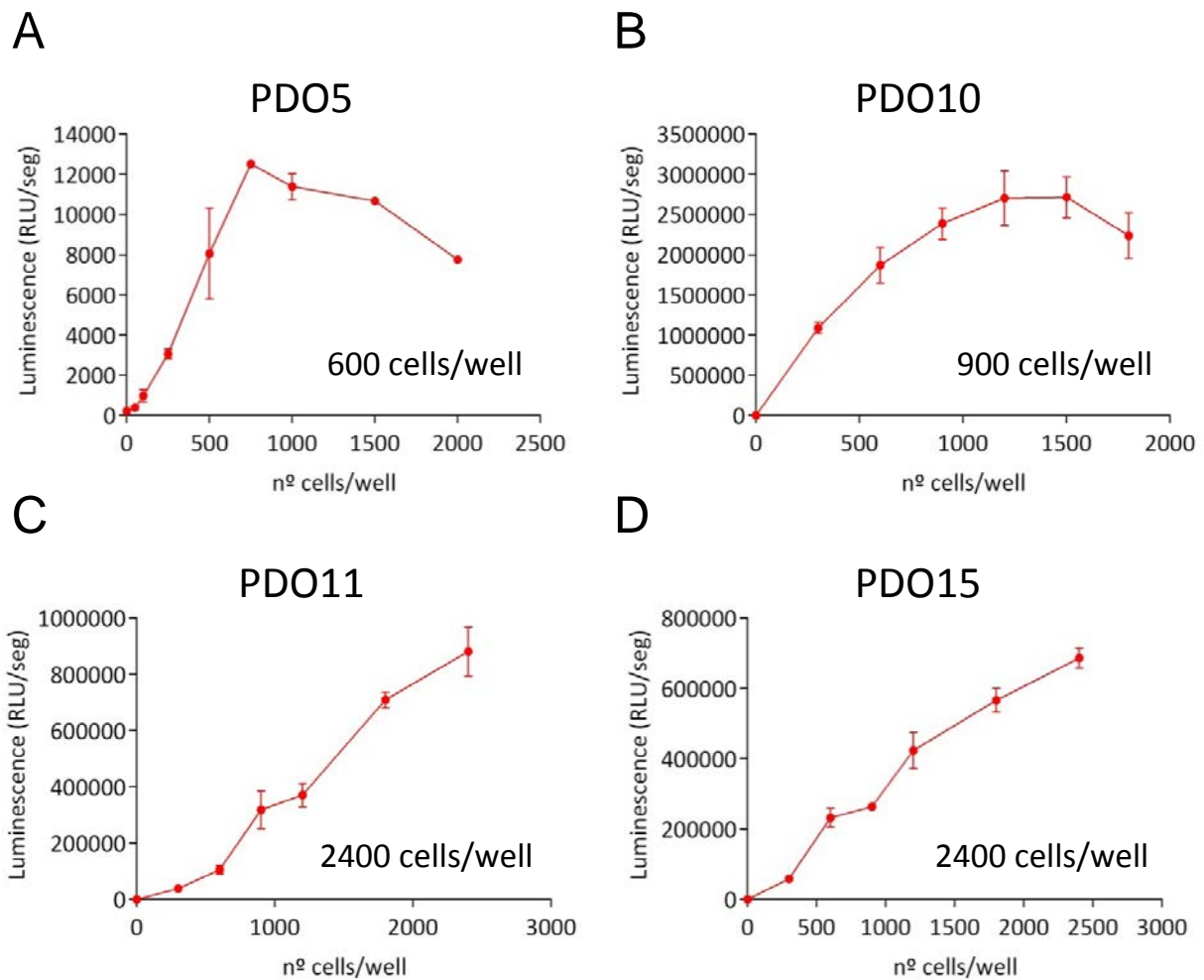


Figure R6. Each CRC PDO needs to be seeded in a different number of cells per well. (A, B, C and D) Cell growth analysis by luminescence measure of cells after seeding different number of cells per well of (A) PDO5, (B) PDO10, (C) PDO11 and (D) PDO15. Adequate amount of cells per well to be seeded for each PDO is indicated.

For drug screening, we used a library composed by anti-cancer drugs, which have been approved by the Food and Drug Administration (FDA) for treating CRC or are currently being tested for that use. Drugs were administered at 100 μ M for 72h and we analysed cell growth in comparison to untreated cells (FIGURE R7A). It can be observed that PDOs have different drug

sensitivities and therefore different Inhibitory Concentrations 50 (IC_{50}), being PDO4 particularly sensitive to most tested drugs. These results indicate that the appropriate doses for drug treatment must be assessed for each PDO and compound.

A

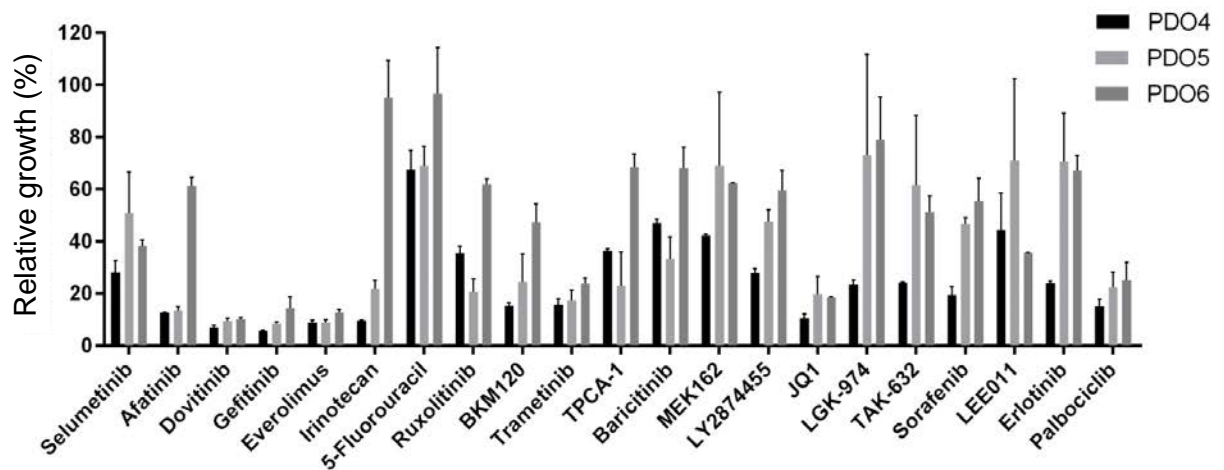


Figure R7. CRC PDOs display different drug sensitivity. (A) Cell growth analysis of PDO4, PDO5 and PDO6 by luminescence measure after treatment with the indicated drugs at 100 μ M for 72 h, relative to control cells. Data from 2 independent experiments is shown.

R2. CHARACTERISATION OF LOW-DOSE CHEMOTHERAPY TREATMENT EFFECTS IN CRC PDOs

R2.1. Low-dose treated-PDOs acquire a non-senescent quiescent-like state

Previous results from our laboratory ³²⁸ demonstrated that BRAF inhibitors synergise with CT agents in producing (or accumulating) DNA-damage in cancer cells. Thus, combination treatments were particularly effective for eradicating PDO cells in dose-response assays. Importantly, further analysis of γ H2A.X and Caspase-3 IF indicated that low CT doses precluded PDO proliferation but produced minor effects in PDOs viability, with little or no presence of DNA-damage and apoptosis after 72 h of treatment ³²⁸. These observations indicated that sublethal doses of CT might induce growth arrest to cancer cells, which could be translated to tumours in patients that are receiving sublethal doses of CT (as discussed in the introduction section).

To further investigate the effects of sublethal CT treatment, we first treated CRC PDOs with serial dilutions of the first-line CT agents 5-FU, Iri. and OX to explore the effects of each chemotherapeutic agents separately. OX alone did not have a significant impact in PDO cells viability, having to use really high concentrations to observe an effect. In contrast, both 5-FU and Iri. alone affected cell growth significantly (FIGURE R8A). Since the combinations of 5-FU+Iri. or 5-FU+OX are the most used in clinics, and OX did not have a huge impact in cell viability, we selected 5-FU+Iri. as the DNA-damaging treatment used in our experiments.

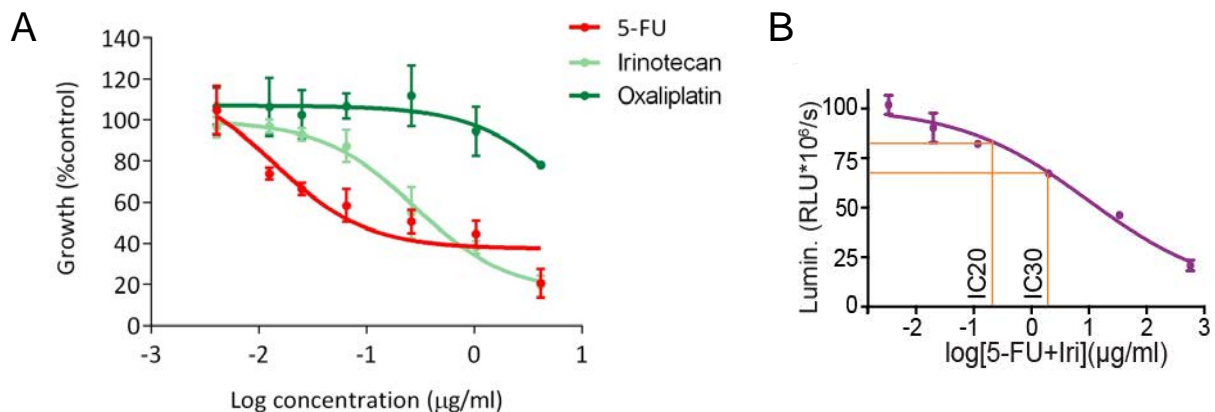


Figure R8. Determination of IC₂₀ and IC₃₀ doses of 5-FU+Iri. (A) Dose-response assay of PDO5 treated with 5-FU, Iri. and OX for 72 h. (B) Dose-response assay of PDO5 treated with the combination 5-FU+Iri. for 72 h, indicating the IC₂₀ and IC₃₀ doses.

As expected, high 5-FU+Iri. concentrations led to eradication of most PDO cells. However, we were able to define the 5-FU+Iri. doses that reduced cell viability by 20 and 30% after 72 h of treatment (hereafter referred as IC₂₀ and IC₃₀) (FIGURE R8B). IC₂₀ and IC₃₀ doses were specific for each PDO, as seen in TABLE MM5 for PDO4, PDO5, PDO8, PDO10, PDO11, PDO15, PDO20, PDO53 and PDO66.

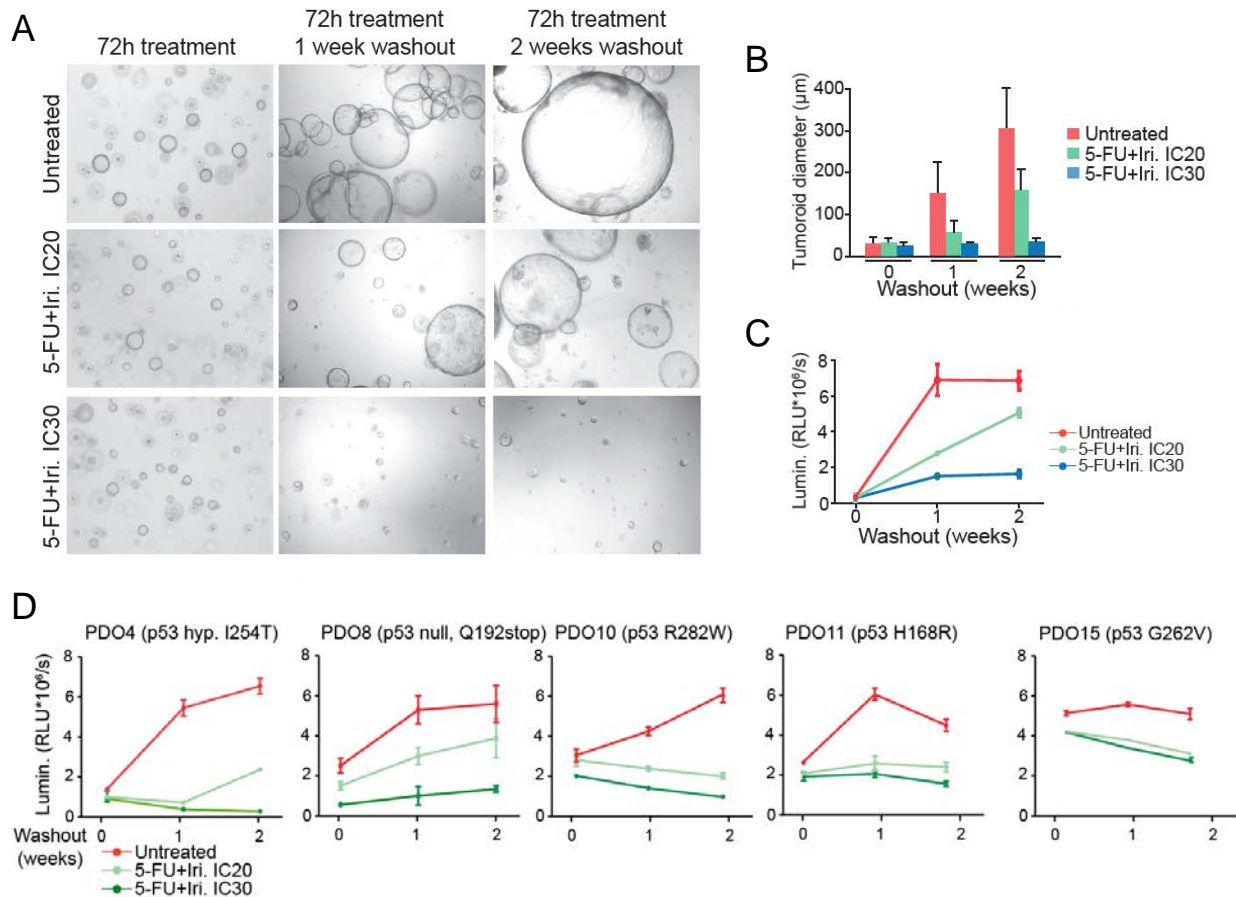


Figure R9. Sublethal doses of CT treatment produce cell growth arrest in CRC PDOs. (A) Representative photographs, (B) diameter measurement and (C and D) viability quantification of (C) PDO5 and (D) other PDOs after 72 h of 5-FU+Iri. treatment and subsequent washout and culture in fresh medium for 1 and 2 weeks. Representative data from 4 independent experiments is shown.

Microscopic analysis of PDO5 (*TP53* WT, *KRAS* G12D) treated at IC₂₀ and IC₃₀ did not reveal obvious signs of cell death, but we noticed a dose-dependent growth arrest in treated PDOs, quantified by reduced PDO diameters, that persisted for at least 2 weeks after drug washout (FIGURES R9A and B). Measurement of cell viability, by a luminescence-based strategy, at 72 h of treatment and after 1 and 2 weeks of washout supported our observations (FIGURE R9C). This growth arrest was also identified in PDO4, PDO8, PDO10, PDO11 and PDO15 (all presenting mutated *TP53* together with other mutations, TABLE MM1) at 72 h after treatment.

However, most *TP53* mutated PDOs showed reduced their cell viability after drug washout in comparison to the measures at 72 h, especially in IC₃₀-treated conditions (FIGURE R9D).

Radiotherapy is also used to treat CRC patients, therefore we analysed whether gamma radiation produced cell growth arrest in PDOs. We first determined the maximum sublethal doses of gamma radiation (in Gy) after 7 and 14 days post-treatment. For PDO5 we selected 8 Gy and 12 Gy and for PDO4, 4 Gy and 8 Gy (FIGURE R10A). We confirmed that sublethal gamma radiation produced growth patterns comparable to CT, but we observed more heterogeneity between spheres and replicates (FIGURE R10B). Thus, all subsequent experiments were performed with 5-Fu+Iri. treatment, as results were more consistent and easier to perform.

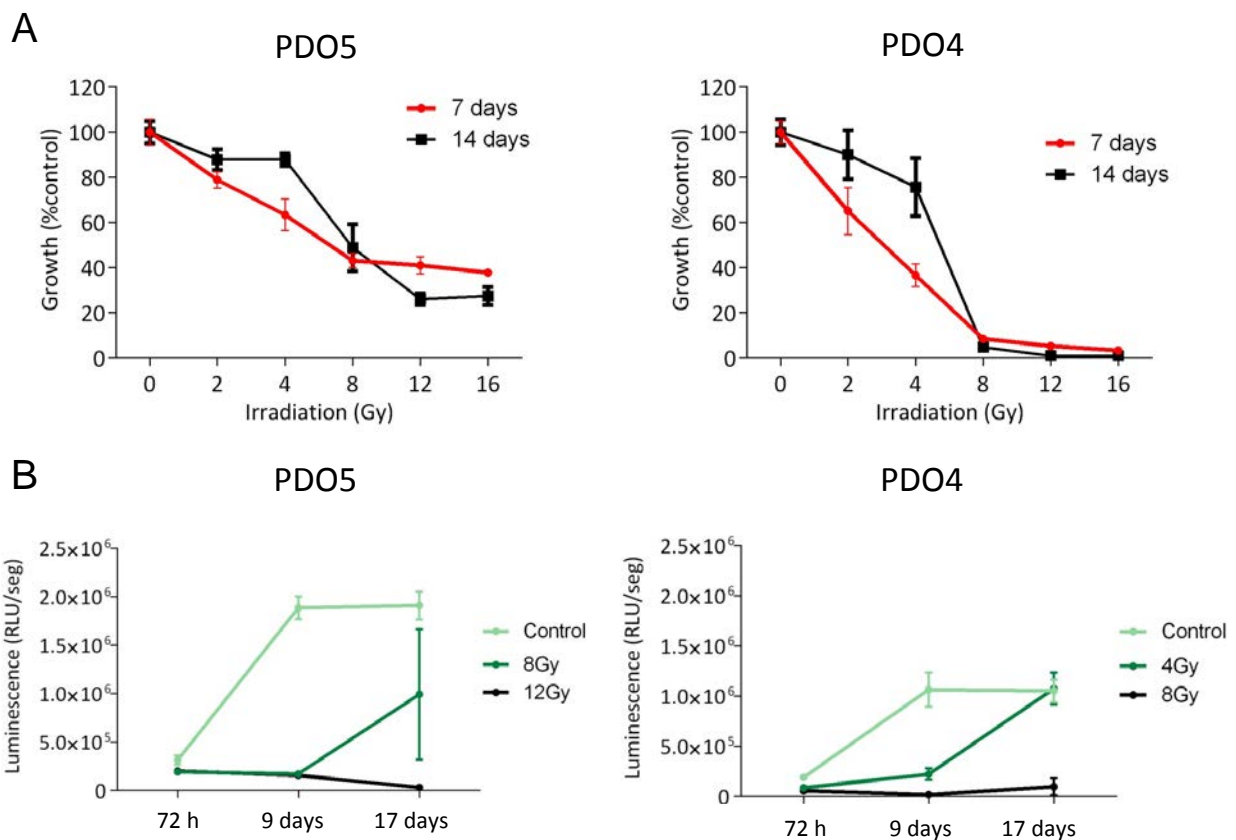


Figure R10. Sublethal doses of radiation reduce cell viability in CRC PDOs. (A) Quantification of cell viability of PDO5 and PDO4 untreated or treated with different Gy of gamma radiation after 7 and 14 days. **(B)** Quantification of cell viability of PDO5 and PDO4 untreated or treated as indicated after 7, 9 and 17 days.

As PDO5 was the organoid showing the clearer results in terms of growth arrest after sublethal CT treatment, we selected PDO5 for subsequent assays. We first analysed whether growth

arrest after CT and washout was maintained in time. Low-dose CT treatment was associated with inhibition of cell proliferation as determined by IF analysis of ki67 after 72 h of treatment (FIGURE R11A). In untreated PDOs, the proportion of positive ki67 cells is almost 80%, but this percentage is reduced to 30% in IC₂₀- and to 10% in IC₃₀-treated cells (FIGURE R11B). Moreover, this reduction in proliferation is maintained after drug withdrawal, as expected for the results in cell viability, after 1 week of washout (FIGURE R11C).

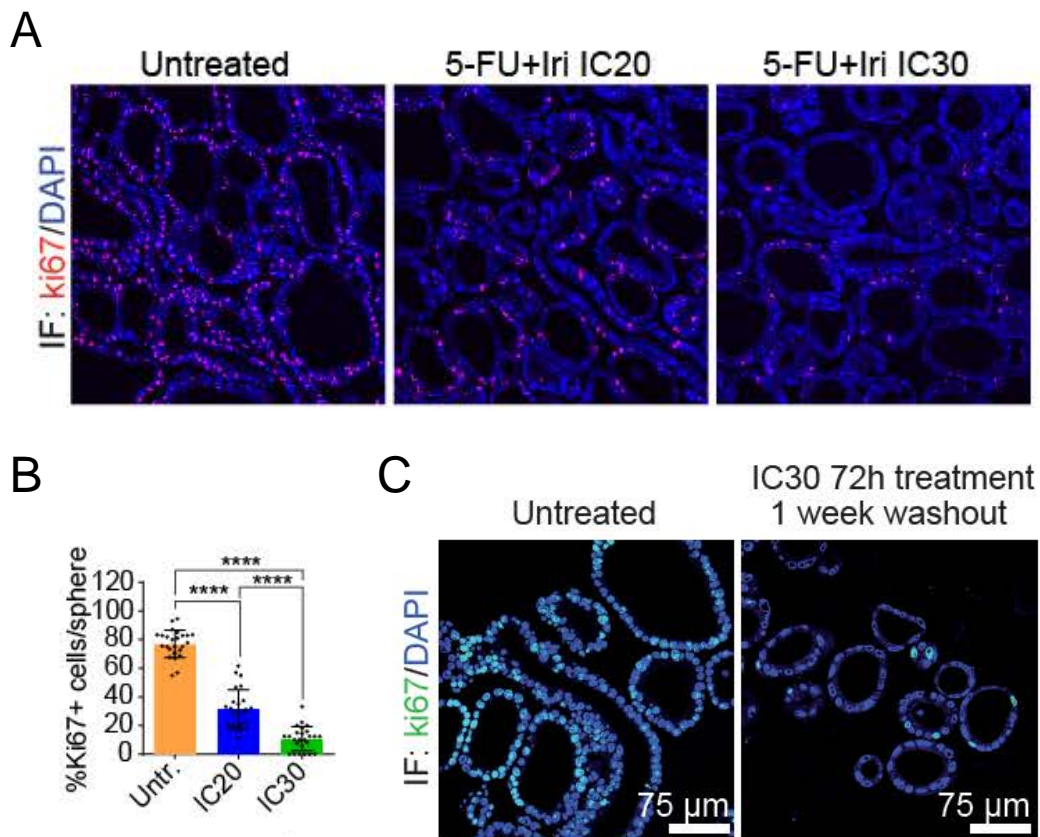


Figure R11. Sublethal doses of CT treatment inhibit cell proliferation. (A, B and C) Representative images of ki67 staining by IF in PDO5 untreated or treated with 5-FU+Iri. at IC₂₀ and IC₃₀ for (A) 72 h and (C) after 1 week of washout, and (B) quantification of the percentage of ki67⁺ cells/sphere in each condition. Counterstained with DAPI.

Cell cycle distribution could be altered because of the CT treatment and cells could be accumulating in specific phases, such as G₀, where quiescent cells stay. We found by flow cytometry analysis of BrdU incorporation a reduced number of cells in S phase in treated PDO5 (61.5% in untreated compared to 32.7% in IC₂₀-treated cells). In addition, IC₂₀ and IC₃₀ treatment imposed a partial accumulation of cells in G₀/G₁ and G₂/M (15.1%/16.8% in untreated compared to 26%/30.9% in IC₂₀-treated cells, respectively) (FIGURE R12A).

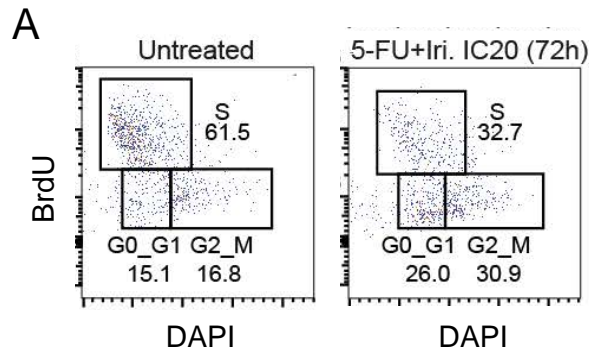


Figure R12. Sublethal doses of CT treatment alter cell cycle of PDOs. (A) Flow cytometry analysis showing BrdU incorporation of PDO5 after 72 h of 5-FU+Iri. treatment, compared with the control. Three boxes are shown, representing cells in G₀/G₁, S and G₂/M cell cycle, respectively.

Cells in G₂/M may correspond to cells not undergoing cytokinesis, which could produce the generation of polyploid or multinucleated cells ^{208,242}327</sup>³²⁷. By FISH and DAPI staining, we demonstrated the absence of polyploid nuclei or with other chromosome number alterations in IC₃₀-treated PDOs (FIGURE R13A and B). Staining of PDOs with DAPI and the membrane marker EphB2, that is found in almost all cells of our PDOs (see FIGURE R3), allowed us to confirm the absence of multinucleated cells in both untreated and CT-treated conditions (FIGURE R13C).

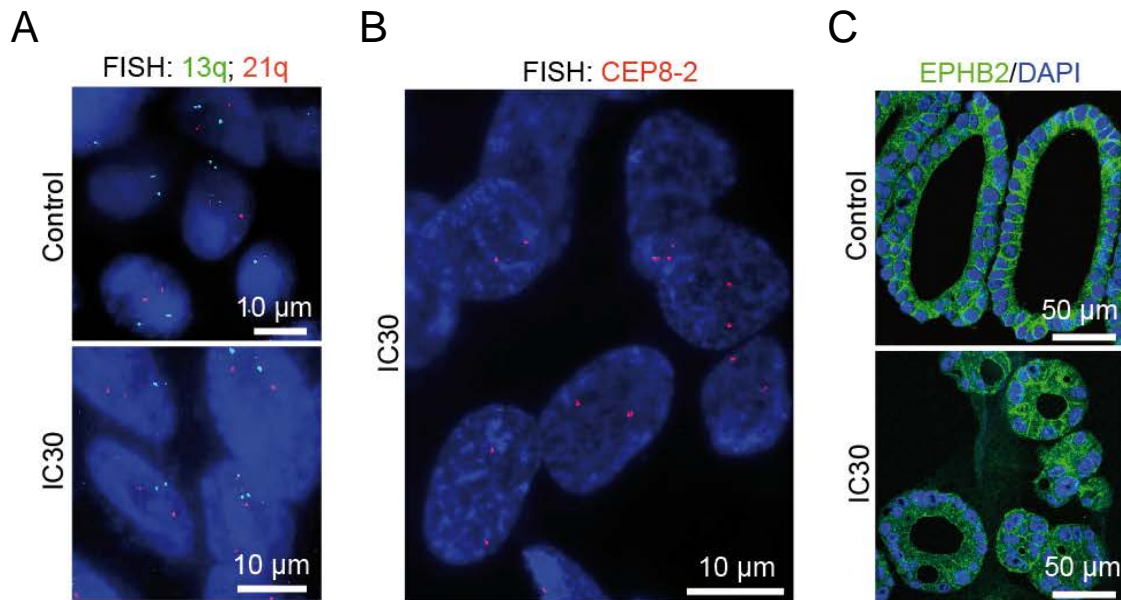


Figure R13. There is absence of chromosomes and nuclei alterations in IC20 and IC30-treated PDOs. (A and B) Representative images of fluorescent in-situ hybridisation (FISH) analysis from control and IC₃₀-treated PDO5 using probes for **(A)** 13q (green) and 21q (red) and **(B)** the centromeric probe CEP8-2 (red). **(C)** Representative images of IF analysis using the surface marker EphB2 in control and IC₃₀-treated PDO5. DAPI is used as a nuclear marker.

On the other hand, cells accumulated in G_0/G_1 may correspond to senescent cells, a state of growth arrest associated with other changes, such as specific protein expression and secretion of SASP factors. To determine if IC_{20} and IC_{30} treatments inflicted a senescent phenotype to PDO5 cells, we first evaluated the SA- β -gal activity by flow cytometry (FIGURE R14A) and direct staining (FIGURE R14B). Cells treated at IC_{20} or IC_{30} did not display a consistent senescent phenotype, although some levels of SA- β -gal were detected. In contrast, in IC_{60} treated cells at 72 h SA- β -gal was consistently detected, indicating the presence of senescent cell at high CT doses. To note, it was observed some unspecific staining in untreated cells after direct staining.

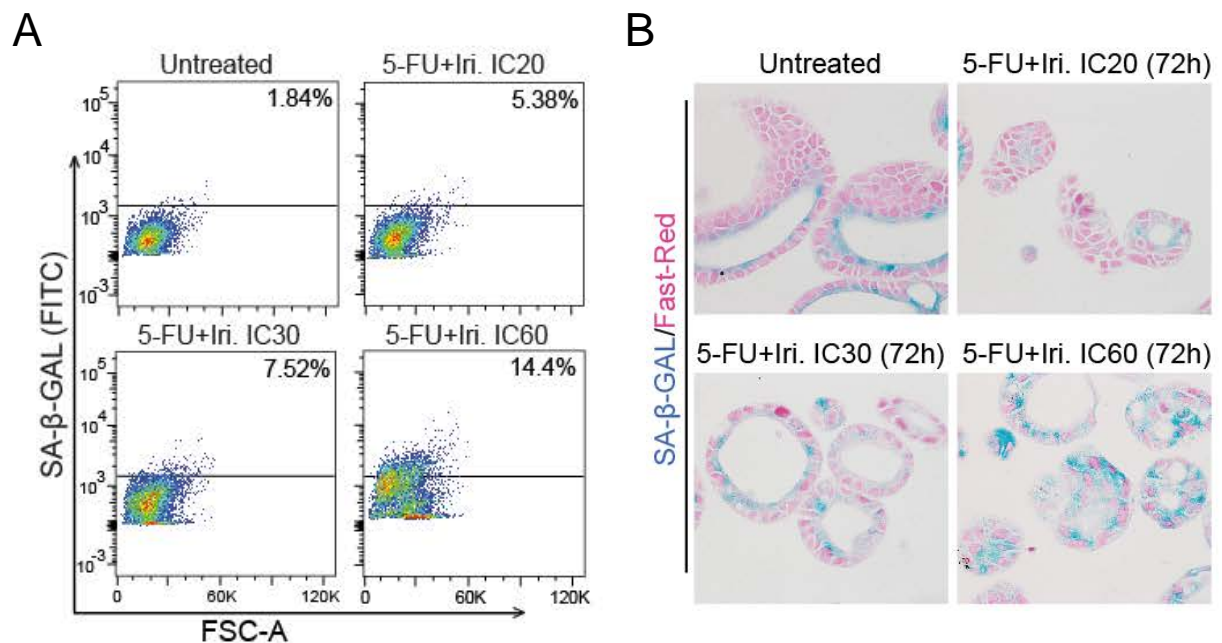


Figure R14. Low-dose CT treatment does not increase the proportion of senescent cells. (A and B) Quantification of SA- β -gal activity detected by (A) flow cytometry or (B) by direct staining in untreated or treated PDO5 with 5-FU+Iri. as indicated for 72 h. Representative images in B were obtained with Olympus BX61.

Senolytic drugs are able to selectively target senescent cells and induce their apoptosis. Dasatinib is a tyrosine kinase receptor inhibitor approved by FDA and one of the first senolytic drugs ever used²⁵⁵. To further demonstrate that our treated PDOs do not display a consistent senescent phenotype, we performed dose-response assays using dasatinib plus IC_{20} and IC_{30} 5-FU+Iri. Dasatinib did not potentiate the growth inhibition imposed by IC_{20} and IC_{30} 5-FU+Iri. (indicative of the absence of senescent cells) but enhanced the deleterious effect of IC_{60} 5-FU+Iri. treatment (FIGURE R15A). In order to validate that dasatinib specifically eliminated senescent cells, we analysed SA- β -gal by flow cytometry after dasatinib treatment. In untreated

PDOs, dasatinib did not kill almost any cell (4.96%, untreated cells, to 4.46% with dasatinib). However, in IC₆₀-treated cells, addition of dasatinib increased the number of cells positive for SA-β-gal from 13.6% in the single IC₆₀-treated cells to 4.55% with Dasatinib (indicative of specific lose of SA-β-gal⁺ cells). Together, these results indicate that sublethal doses of CT treatment in PDOs produce a quiescent-like state not associated with the acquisition of a senescent phenotype.

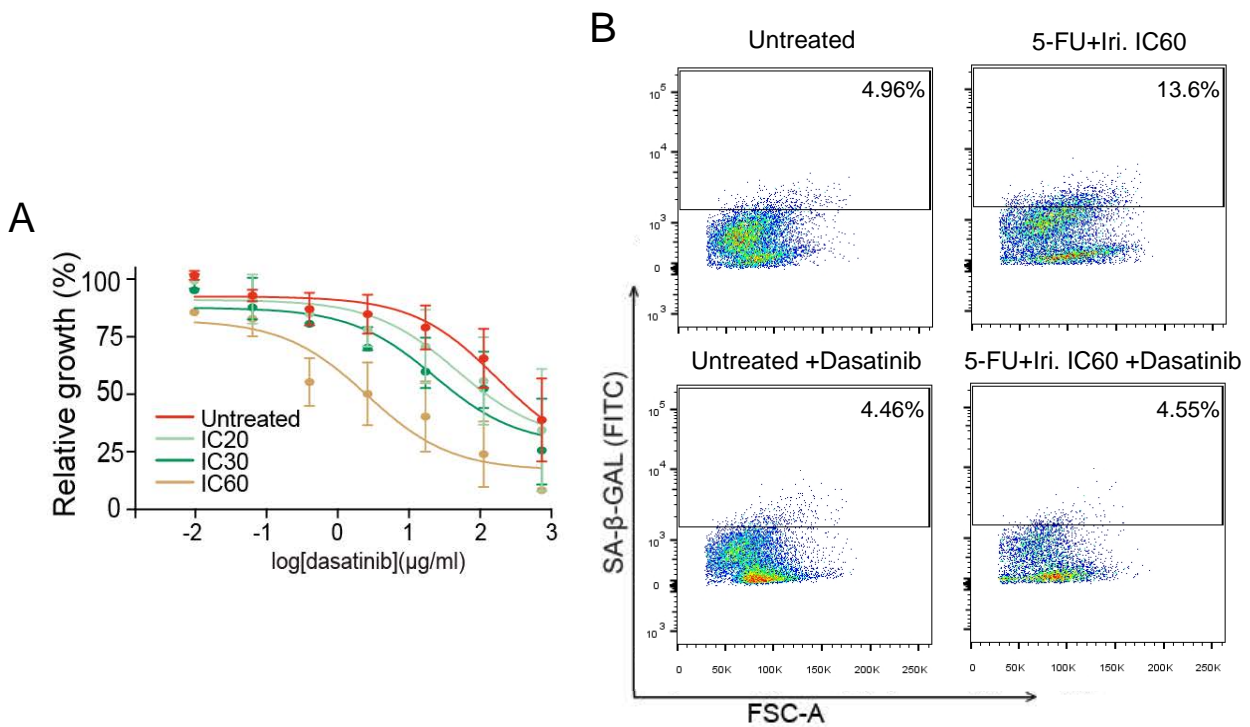


Figure R15. Senolytic drug dasatinib do not reduce the cell viability of treated PDOs. (A) Dose-response curves of PDO5 treated with dasatinib for 3 days after pre-treatment with 5-FU+Iri. at the indicated doses for 72 h. **(B)** Quantification of SA-β-gal activity detected by flow cytometry in untreated or treated PDO5 with 5-FU+Iri. as indicated for 72 h.

R2.2. Low-dose CT treatment is not associated with an increase in apoptosis or persistent DNA-damage

To investigate other possible effects produced the low-dose CT treatment of PDOs, we analysed if apoptosis increased after the treatment. We did not detect apoptotic cells after IC₃₀ treatment of PDO5 as determined by IF of cleaved-caspase 3 staining, which were detected in the IC₈₀-treated cells, used as a positive control (FIGURE R16A). We also studied apoptosis by flow cytometry analysis of Annexin V binding and Propidium Iodide (PI) incorporation, considering double Annexin V (apoptosis) and PI (cell death) positive cells as late apoptotic or necrotic cells.

In our analysis, the proportion of double positive cells did not increase with low-dose CT treatment (16%, untreated cells, to 13.2%, IC₂₀-treated cells) (FIGURE R16B).

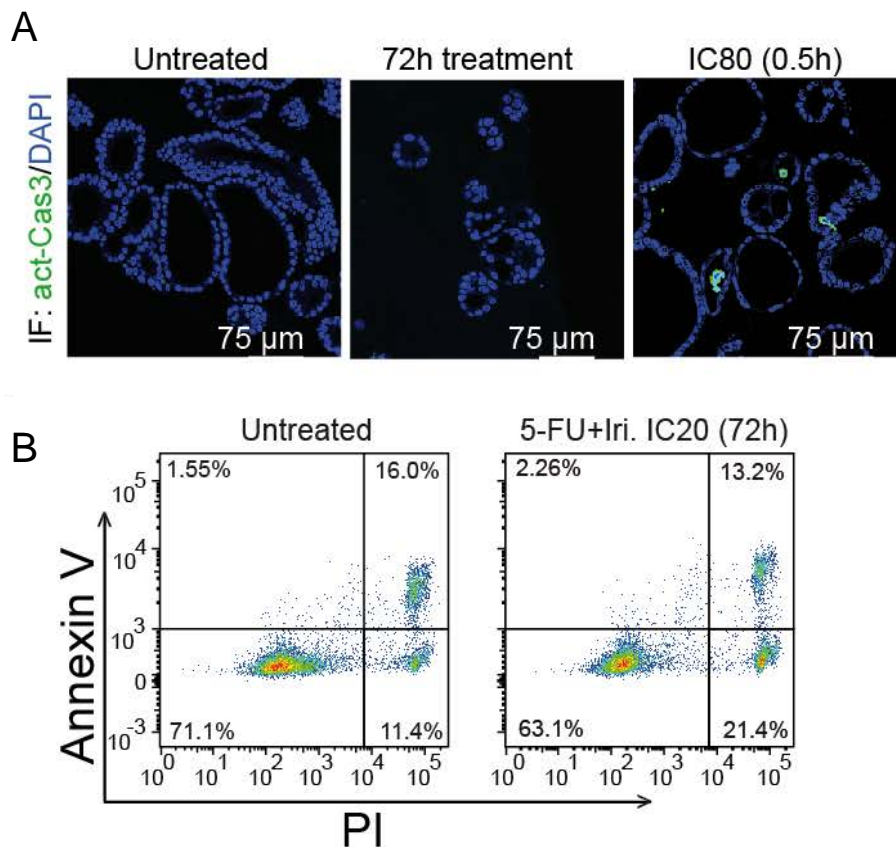


Figure R16. Sublethal doses of CT treatment do not produce increase in apoptosis after 72 h. (A) Representative IF images of cleaved-caspase 3 staining in PDO5 treated with 5-FU+Iri. at IC₂₀ at the indicated time points and with IC₈₀ as a positive control. **(B)** Cytometry analysis of Annexin V binding in PDO5 untreated or treated as indicated.

We next studied the possibility that cell cycle arrest imposed by IC₂₀ and IC₃₀ treatment was due to persistent DNA-damage. IF staining of the DNA-damage marker γ H2A.X demonstrated that there is no accumulation of damage after 72 h of IC₂₀ treatment and after 1 week of washout (FIGURE R17A). Moreover, WB analysis of γ H2A.X of PDO5 cells revealed a dose-dependent increase in DNA-damage levels starting at 1-3 h and showing a maximum around 24 h. Importantly, we noticed the absence of DNA-damage at 72 h after IC₂₀ treatment, being the levels of γ H2A.X comparable to untreated cells (FIGURE R17B). A more direct method to assess DNA-damage caused by CT treatment is by quantifying DNA-strand breaks. Comet assay allows an easy visualisation of both single and double strand breaks and other types of DNA-damage. At 3 h after treatment we observed DNA-damage in all treated conditions (FIGURE R18A), which was not detected after 72 h, in the IC₂₀ and IC₃₀-treated PDOs. This was

in contrast with IC₆₀-treated PDOs that showed persistent DNA damage after 72h (FIGURE R18B). These results indicate that low-doses of CT impose a non-senescent and non-proliferating phenotype to PDO (hereafter called therapy-induced quiescent-like, TQL) cells, in the absence of apoptosis or persistent DNA-damage.

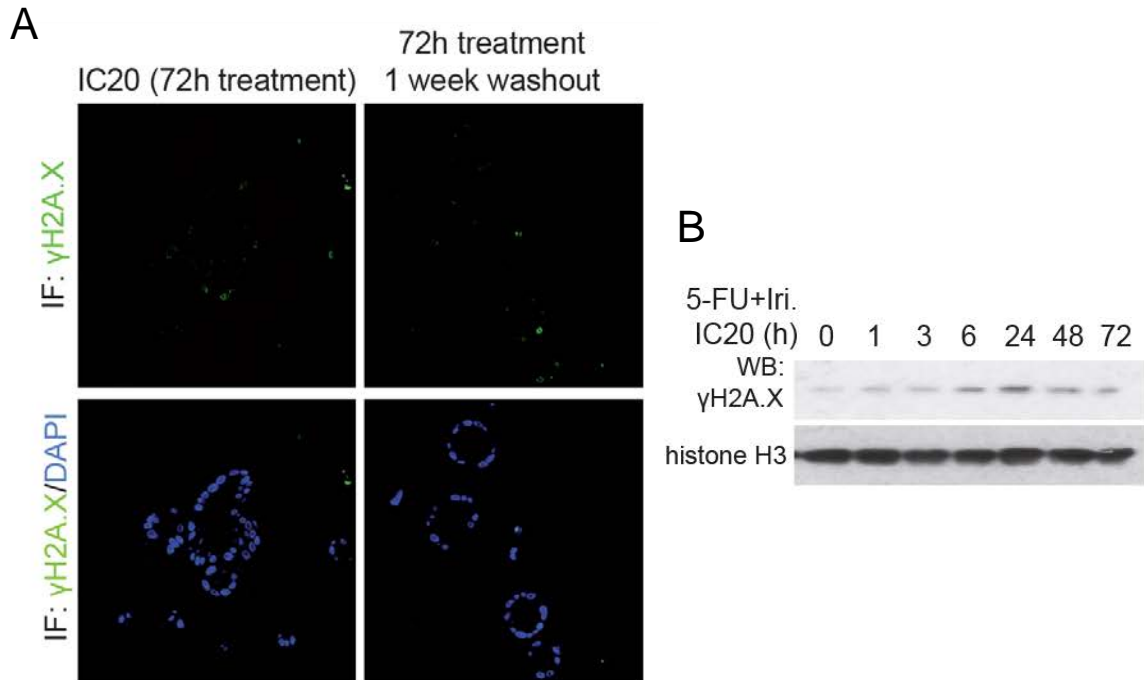


Figure R17. Sublethal doses of CT treatment do not produce accumulation of the DNA-damage marker γ H2A.X. (A) Representative images of γ H2A.X staining by IF in PDO5 treated with 5-FU+Iri. at IC₂₀ for 72 h and after being maintained in fresh medium for 1 week. (B) WB analysis of γ H2A.X in control and 5-FU+Iri.-treated PDO5 cells collected at the indicated time points after treatment.

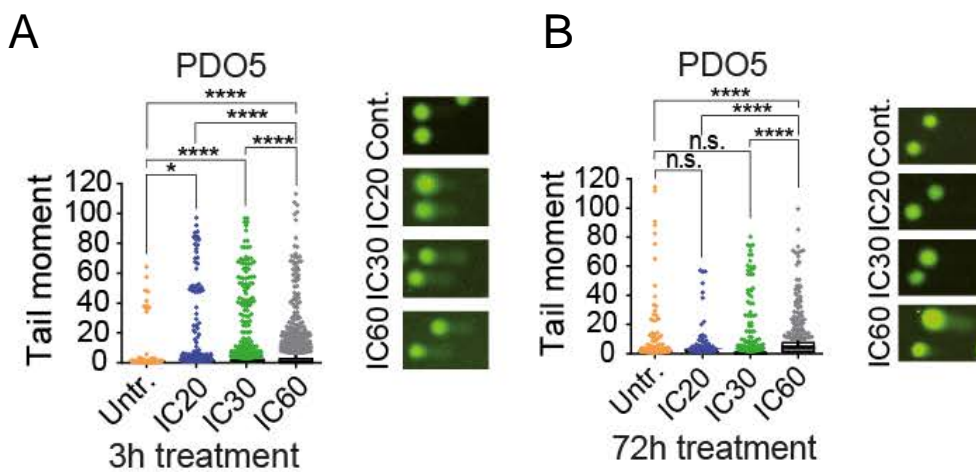


Figure R18. Sublethal doses of CT treatment produce DNA-damage that can be repaired after 72 h. (A and B) Comet assay to measure levels of DNA-damage in PDO5 at (A) 3 h and (B) 72 h after the indicated treatments. Representative images of the produced comets are shown in the right panel of A and B.

R2.3. TQL cells display upregulation of the p53 pathway

To study the transcriptional changes associated with the TQL phenotype, we performed RNA sequencing (RNA-seq) analysis of control, IC₂₀- and IC₃₀-treated PDO5 cells, including two samples per condition (FIGURE R19A). Principal Component Analysis (PCA) demonstrated that all the samples replicated correctly (FIGURE R19B). Moreover, bioinformatics examinations of differentially expressed genes (DEGs) showed an almost perfect correlation of gene expression changes between pairwise comparisons (IC₂₀ vs. untreated and IC₃₀ vs. untreated) ($p < 2.2 \times 10^{-16}$, $R = 0.974$) (FIGURE R19C). For these reasons, all posterior RNA-seq analyses were performed considering IC₂₀ and IC₃₀ samples together as the “treated” group.

Gene Set Enrichment Analysis (GSEA) uncovered p53 as the highest enriched pathway in treated cells, which is not surprising as growth arrest is often linked to this pathway. DEGs genes also clustered in the NF- κ B, EMT and IFN γ pathways that have been associated with inflammatory response and acquisition of ISC characteristics^{77,172,329–331} (FIGURE R19D).

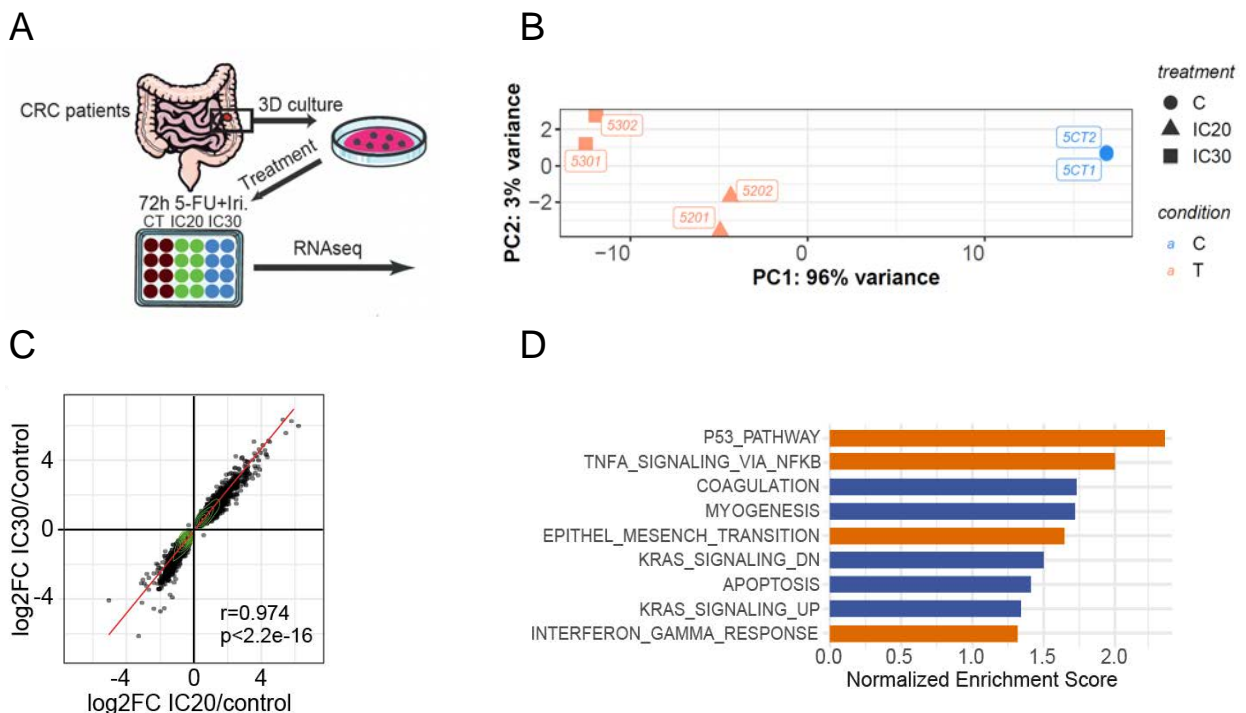


Figure R19. p53 is the highest enriched pathway in TQL cells. (A) Scheme of how the RNA-seq was performed. **(B)** PCA score plot analysis of the samples used for the RNA-seq. **(C)** Linear association of the genes differentially expressed in treated PDO5 compared with the control. Dots represent the log₂ fold change values of genes for IC₂₀ compared with control (x-axis) and IC₃₀ compared with control (y-axis). The Pearson correlation and p-value are shown. **(D)** Barplot depicting the normalised enrichment score of the statistically significant enriched pathways obtained by GSEA analysis with the Hallmark gene set for treated samples (NOM p-val < 0.05).

To corroborate our findings that TQL cells show non-senescent quiescent phenotype, we used a list of senescence-related genes previously described as either inhibitors or promoters³³². We observed that inhibitor or promoter genes were equally distributed in the CT-induced and repressed groups of genes (FIGURE R20A). In addition, DEG genes negatively correlated with the senescent signature, showing no evident correlation between senescence and the TQL phenotype (not depicted).

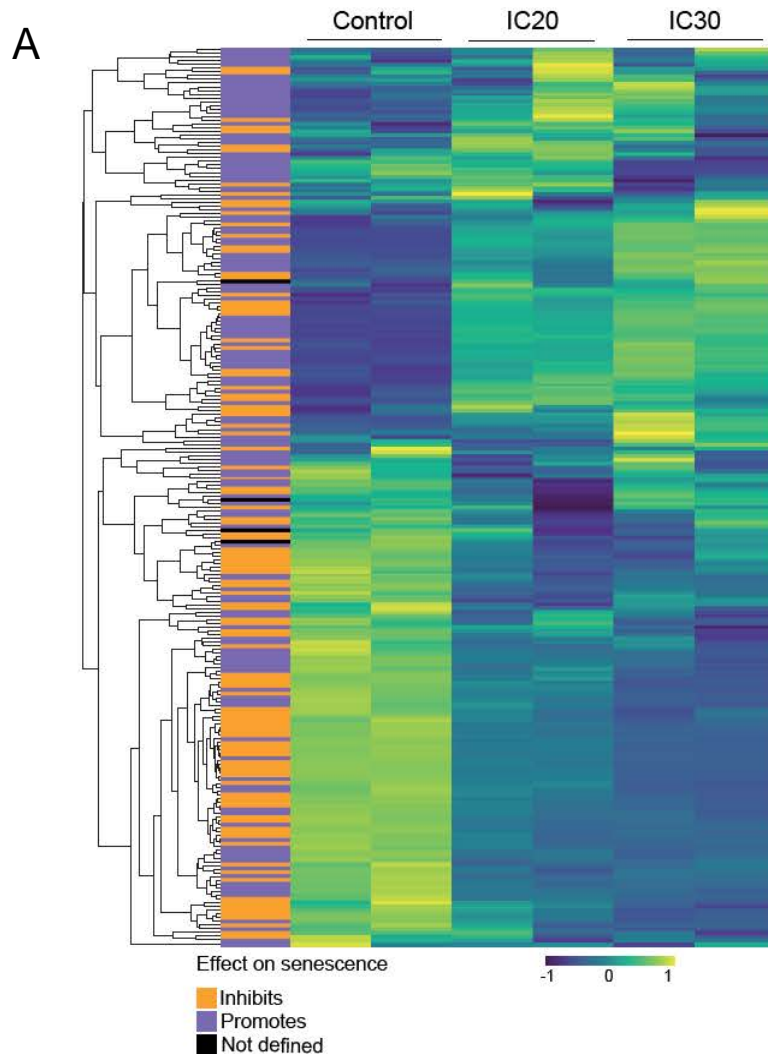


Figure R20. Senescence is not enriched in TQL cells. (A) Heat map showing the expression levels of the previously described senescence genes in each condition. The effect of senescence lane represents the classified effect in senescence that corresponds to each gene. Name of genes are not depicted, as their effect on senescence is sufficient for visualising if there is a correlation. Data represent normalised, centred and scaled Illumina probe intensities on a \log_2 scale.

To confirm that p53 pathway is upregulated in CT-treated PDO5 cells (see FIGURE R19D), we performed IHC-P and WB analyses of p53 and its downstream target p21 (FIGURE R21A, B

and D). We found a consistent upregulation of these proteins after CT treatment, starting at 1-3 h and maintained after 72 h. Levels of p16, a protein associated to irreversible senescence, did not increase with sublethal doses of CT, but was induced at higher CT doses IC₆₀ treatment (FIGURE R21C and D). These data are consistent with the concept that TQL cells do not enter into an irreversible senescent state, opening the possibility that cells could recover from the growth arrest under certain stimuli.

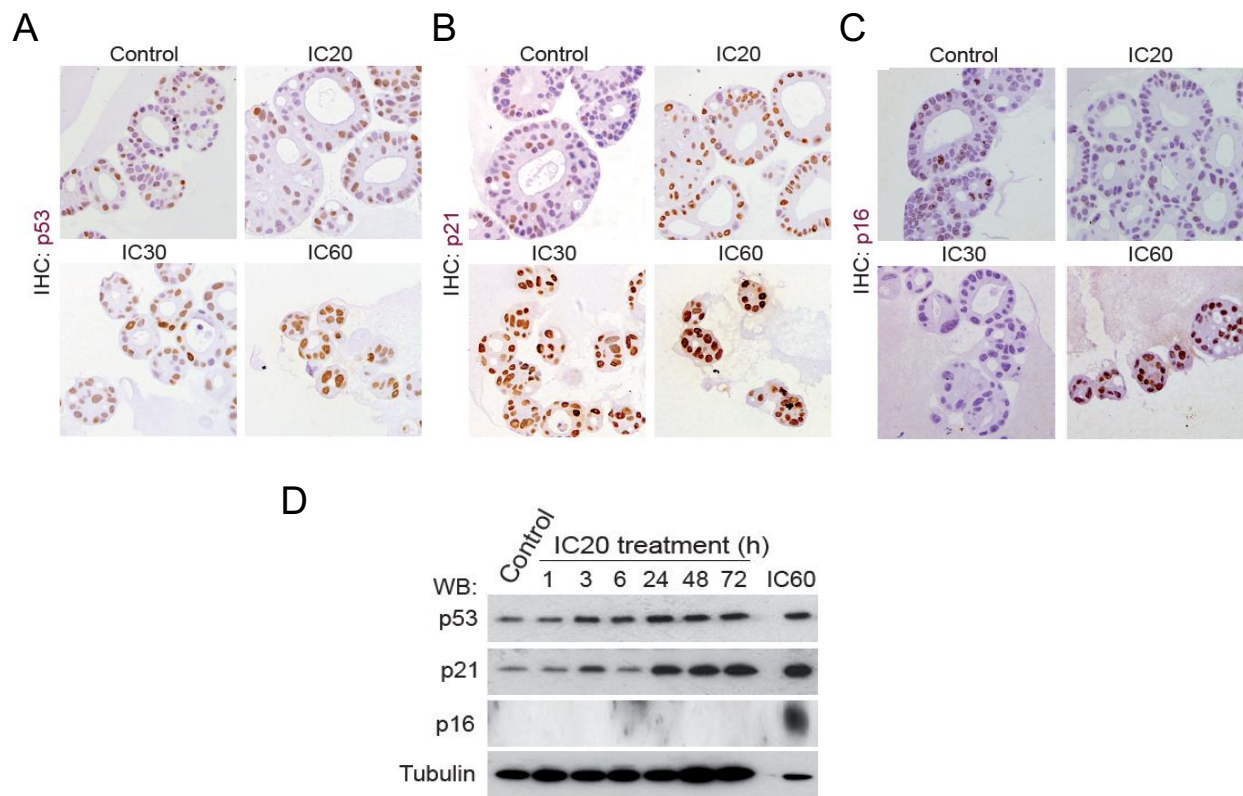


Figure R21. p53 pathway is upregulated in TQL cells, but not the p16-driven irreversible senescence pathway. (A, B and C) IHC-P analysis of (A) p53, (B) p21 and (C) p16 proteins in PDO5 after 72 h of culture with the indicated 5FU+Iri treatment. (D) WB analysis of control and treated PDO5 collected at the indicated time points after 5FU+Iri treatment. (E) GSEA of a p53 pathway related gene set in untreated versus treated PDO5 condition.

We used the list of p53 target genes collected by Fischer³³³ to investigate whether genes induced by low-doses of CT in PDO5 were direct p53 targets. By crossing the IC₂₀-IC₃₀ hallmark signature with the top-120 p53 target genes from Fischer, we uncovered a subset of common hits, which are likely CT-induced transcriptional p53 targets (FIGURE R22A). We confirmed CT-induced activation of candidate p53 targets by RT-qPCR (FIGURE R22B). Moreover, ChIP-qPCR assay demonstrated direct association of p53 to the promoter regions of *CDKN1A*, *MDM2* and *ZMAT3*, canonical p53 target genes, which were massively induced following CT treatment (FIGURE R22C).

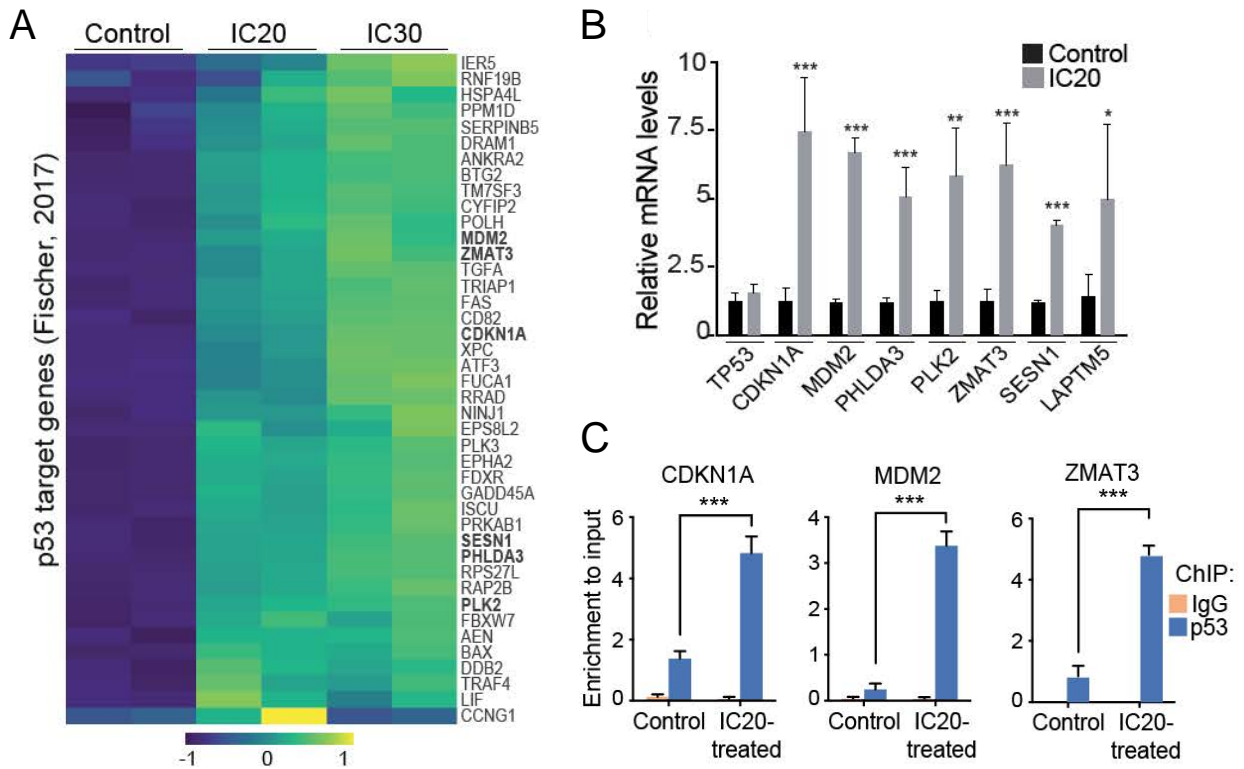


Figure R22. p53 target genes are induced after sublethal doses of CT treatment. (A) Heat map showing the expression levels of the 42 common genes resulted by crossing the p53-associated IC₂₀ and IC₃₀ hallmark signature with the top 116 previously identified p53 targets³³³ (two replicates per condition analysed). Data represent normalised, centred and scaled Illumina probe intensities on a log₂ scale. **(B)** RT-qPCR analysis of selected p53 target genes (depicted in bold in A) from control and IC₂₀-treated PDO5 cells. **(C)** ChIP-qPCR analysis of p53 binding in untreated and IC₂₀-treated PDO5 in a subset of putative p53 target genes expressed as relative enrichment normalised to the input.

Some PDOs carrying *TP53* mutations presented reduced cell viability when treated with low-dose CT for 72 h and after washout, as previously demonstrated (see FIGURE R10A). Moreover, since we have just demonstrated that p53 pathway is upregulated in TQL cells, we speculated that having functional p53 could be essential for the induction of this phenotype. Examination of PDO4 and PDO8 cells (carrying mutant *TP53*) treated at IC₂₀ and IC₃₀ 5-FU+Iri. demonstrated a significant increase in apoptosis in these PDOs after CT (12.3% to 38% in PDO4 and 18.6% to 32.1% in PDO8), in comparison to PDO5 that presented no increase in apoptosis (FIGURE R23B). Additionally, PDO4 and PDO8 CT-treated cells also exhibited high amounts of DNA that persisted for at least 72 h, a time point when PDO5 cells had already repaired the damage (FIGURE R23C). These observations suggest that functional p53 is indeed necessary for the acquisition of the TQL phenotype.

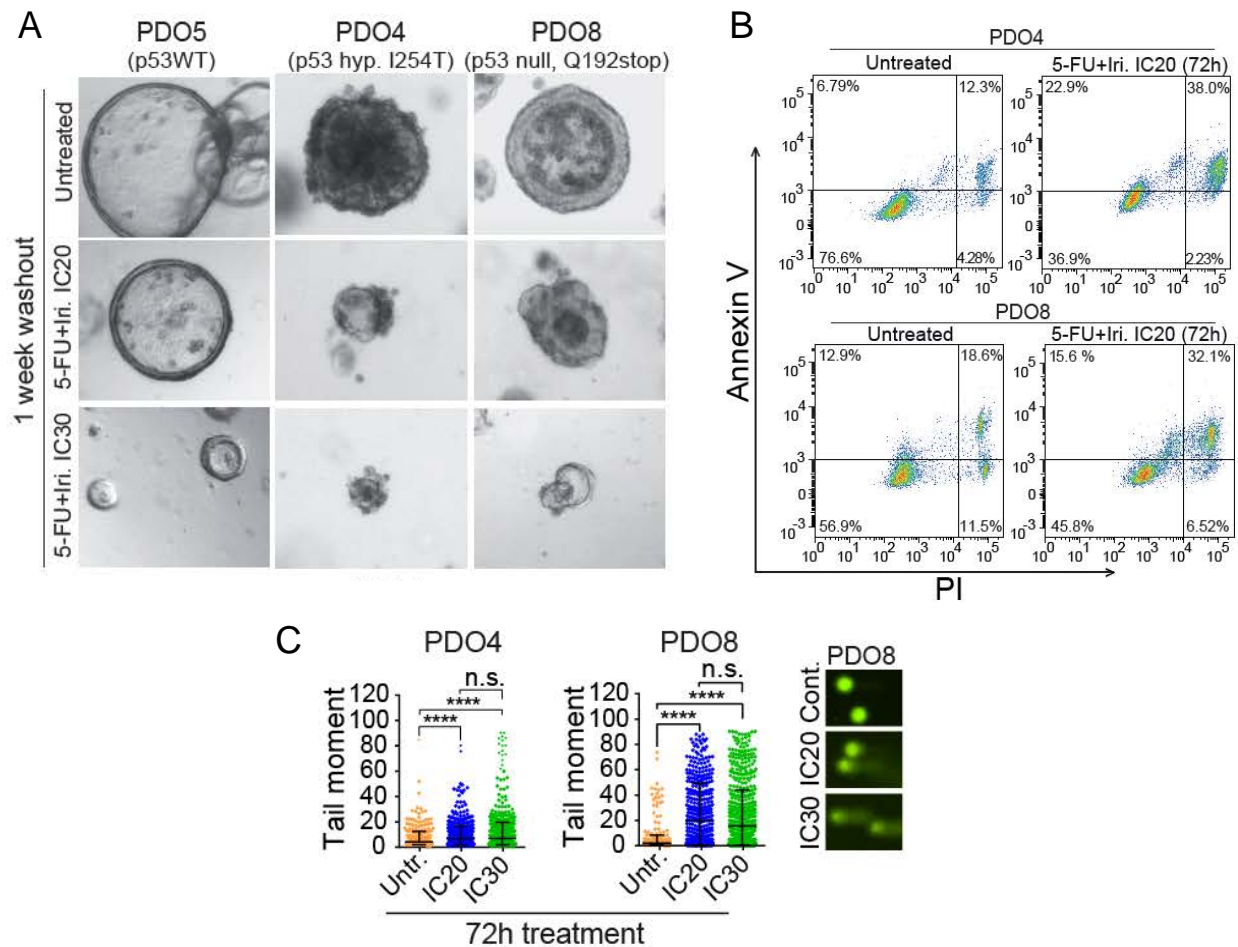


Figure R23. p53 mutated PDOs display apoptosis and persistent DNA-damage upon treatment with sublethal doses of CT. (A) Representative photographs of PDO5, PDO4 and PDO8 after 72 h of 5-FU+Iri. treatment and washout for 1 week. **(B)** Cytometry analysis of Annexin V binding in PDO4 and PDO8 untreated or treated as indicated. **(C)** Comet assay to measure levels of DNA-damage in p53 mutants PDO4 and PDO8, treated for 72 h as indicated. Representative images of the produced comets are shown in the right panel of **C**.

R2.4. The TQL phenotype is associated with acquisition of a foetal intestinal stem cell (feISC) signature

Sublethal CT treatment has been linked to the acquisition of tissue stem cell signatures in B-cell lymphoma²⁵⁰ and intestinal cancer²¹⁹ previously. To investigate if our TQL cells presented alterations in the expression of stem cells related genes, we crossed the DEG genes in our treated PDOs with the canonical ISC signature, obtained from adult mouse ISCs⁵¹. Unexpectedly, we found a negative correlation between TQL DEG genes and this ISC signature (FIGURE R24A). Further analysis of data showed a mixed pattern of up- and downregulated ISC genes after IC₂₀ and IC₃₀ treatment (FIGURE R24B).

Prominently, genes upregulated following CT included *LY6D* and *YAP1*, which are instrumental in the conversion of adult to foetal ISC (feISC) after intestinal injury^{77,78,80,286}, with the canonical adult ISC markers *LGR5* and *EPHB2* severely downregulated (FIGURE R24B). After crossing our DEG genes with a previously described foetal mouse ISC signature⁸⁰, we found a significant direct correlation between genes transcriptionally modified by CT treatment and ISC genes up- or downregulated in foetal intestine-derived organoids compared with adult-derived ones (FIGURE R24C and D). Thus, sublethal doses of CT induce a conversion into a feISC phenotype, at least in PDO5.

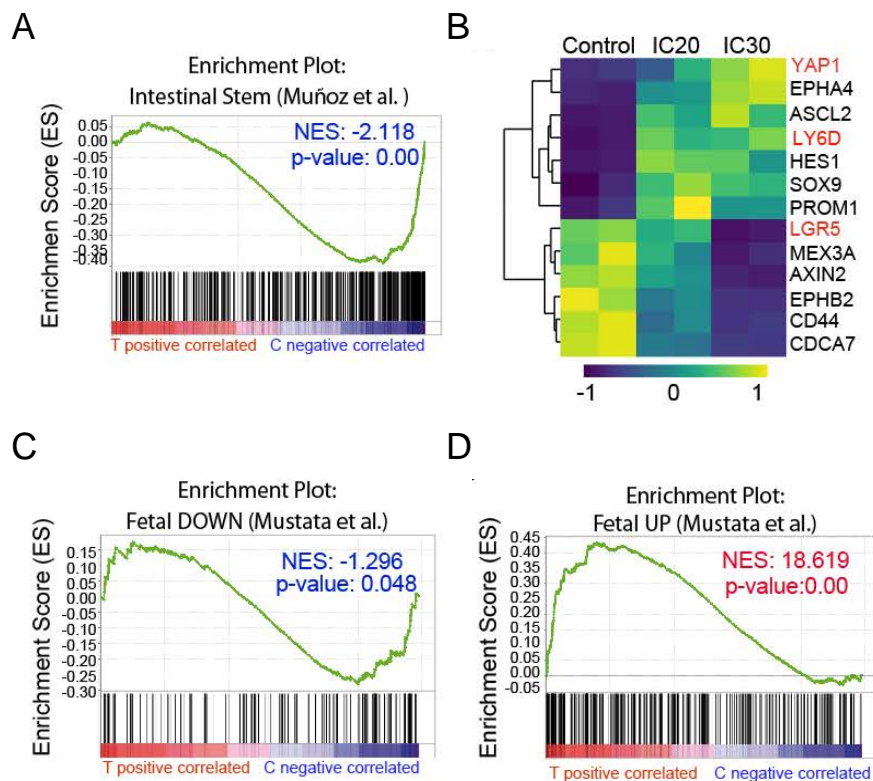


Figure R24. Sublethal doses of CT induce a conversion into a feISC phenotype in PDO5. (A) GSEA of an intestinal stem cell (ISC) gene set, according to Muñoz et al, in treated versus IC₂₀-treated PDO5 condition. **(B)** Heat map showing the expression levels of the indicated ISC genes in untreated, IC₂₀ and IC₃₀-treated PDO5 cells. **(C and D)** GSEA of **(C)** a foetal down and **(D)** a foetal up stem cell gene set, according to Mustata et al., in control (C) versus treated (T) PDO5 condition.

R2.5. TQL cells displaying the feISC signature retain their tumour-initiating capacity, which could be associated with increased Notch activation

It was recently shown that foetal ISC conversion results in tumour and metastasis suppression²⁸⁶. However, the study from Cheung et al used as a model the *Apc*^{-/-}; *Kras*^{G12D}; *p53*^{-/-} murine intestinal tumour cells. Since we identified functional p53 as a requirement for the acquisition of

Considering that TIC activity in PDO5 could be driven by the fraction of cells which still undergo replication after IC₂₀ and IC₃₀ treatment (FIGURE R11 AND R12), we next compared the TIC *in vitro* of the general population with the TIC of specifically quiescent cells found in our treated PDOs. For this, we generated TP53 WT PDO5 carrying a doxycycline-inducible histone-GFP reporter that is specifically retained by the quiescent tumour population after doxycycline withdrawal (but sequentially diluted in each cell cycle)²¹⁰. Upon 6 days of doxycycline treatment, PDO5 cells were treated with 5-FU+Iri. for 72 h and, after 2 weeks of doxycycline washout, analysed by flow cytometry and GFP_{high} and GFP_{low} were sorted (FIGURE R26A and B). We found that sorted GFP_{high}, which represents the quiescent population present at the time of CT-treatment, displayed identical capacity for PDO generation as GFP_{high} plus GFP_{low} cells indicating that TIC activity does not reside in the remaining proliferating population but is retained in the TQL population (FIGURE R26C). We can conclude that retained TIC activity in treated PDO5 is not due to the presence of proliferating cells, but to the TIC capacity of TQL cells.

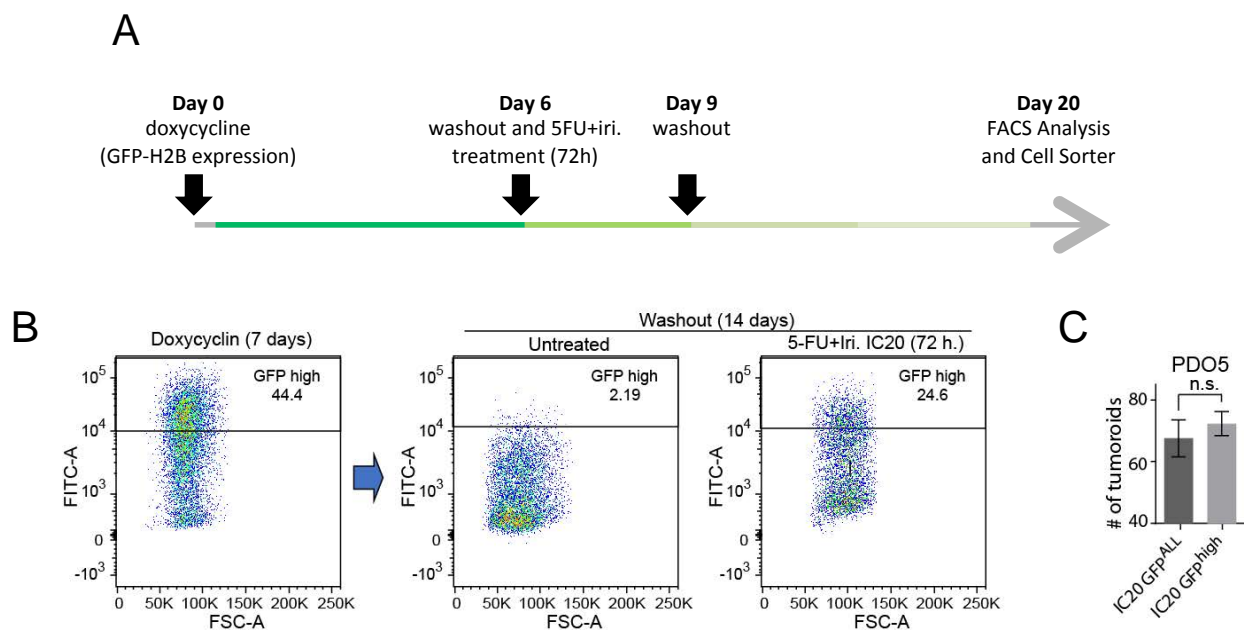


Figure R26. Retained TIC capacity in vitro is not due to remaining proliferating cells. (A and B) (A) Scheme of how experiment was conducted and (B) analysis of GFP distribution by flow cytometry of PDO5 cells carrying a doxycycline-inducible GFP-H2B construct. Cells were treated for 6 days with doxycycline to induce GFP-H2B expression and then left untreated or treated with 5-FU+Iri. IC₃₀ for 72 h and maintained in fresh medium for 2 additional weeks. Quiescent cells that retained high or low GFP levels were purified by cell sorting. (B) Number of PDOs generated from seeding 300 GFP^{high+low} and GFP^{high} sorted cells after 2 weeks with fresh medium.

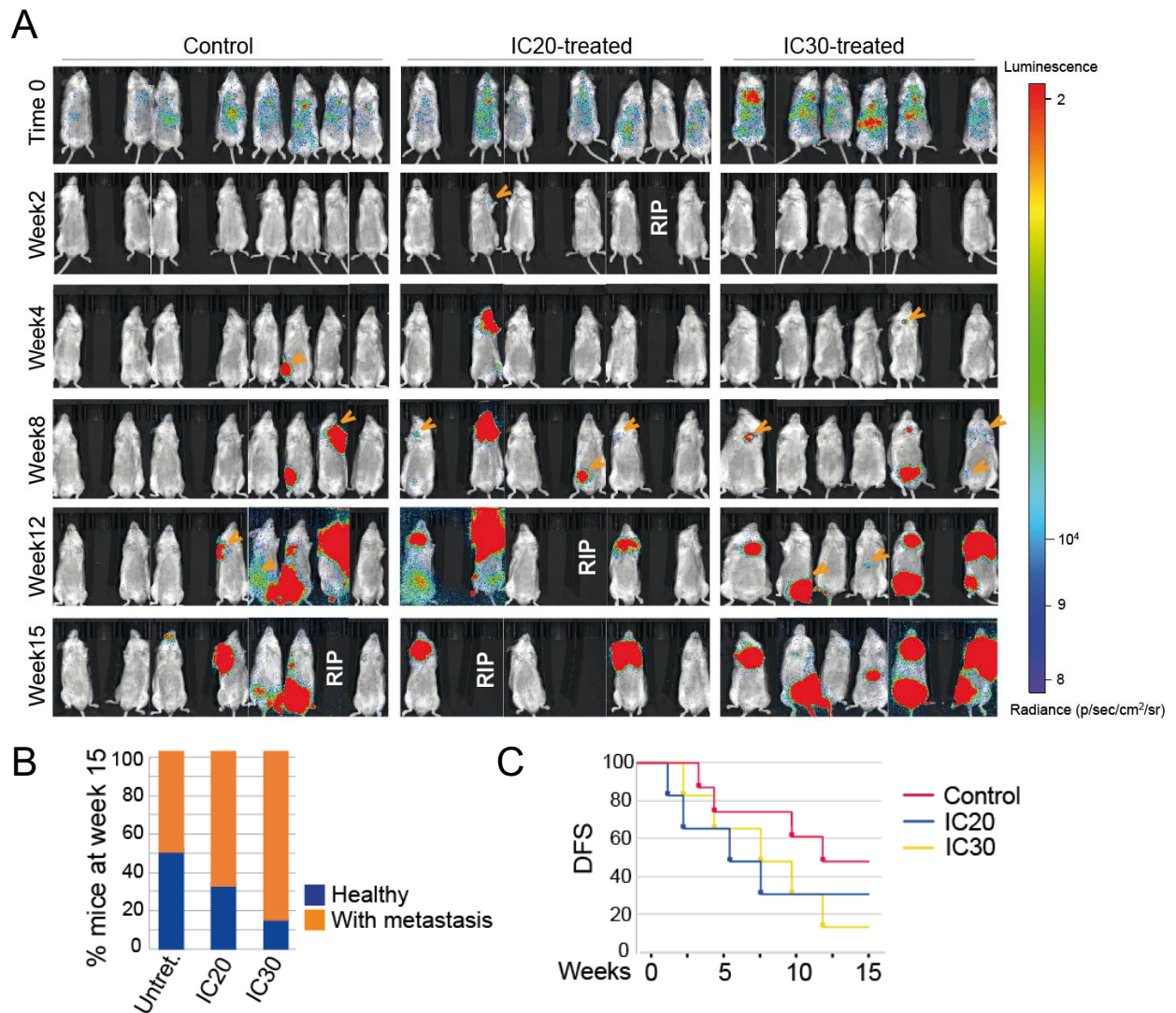


Figure R27. Treated PDO5 cells display a slightly superior metastatic capacity than untreated cells when injected intracardiacally. (A) In vivo bioluminescence representative images of mice administered intracardiac injection of 40,000 luciferase-PDO5 CT and IC₂₀ or IC₃₀-treated cells in NSG mice. Orange arrows indicate the first time tumours can be detected. **(B)** Percentage of healthy and with metastasis mice at week 15. **(C)** Kaplan-Meier representation of DFS probability over time for untreated, IC₂₀ and IC₃₀-treated PDO inoculated intracardiacally in mice.

We next studied the *in vivo* tumourigenic capacity of IC₂₀ and IC₃₀ pretreated PDO5 cells using two complementary strategies. Firstly, we performed intracardiac injection of 40,000 single PDO5 cells (untreated, IC₂₀ or IC₃₀ pretreated) labelled with firefly luciferase into NOD-SCID-gamma (NSG) immunocompromised mice. Mice were analysed weekly using bioluminescence (BLI) to monitor metastatic growth using the IVIS animal imaging system (FIGURE R27A). We found that PDO5 treated with 5-FU+Iri. displayed a superior metastatic capacity than untreated cells. Specifically, 4 of 8 mice transplanted with untreated PDO5 cells contained metastatic

lesions at week 15 after transplantation. Importantly, 4 of 6 mice transplanted with IC₂₀-treated cells and 5 of 6 mice with IC₃₀-treated cells showed visible metastasis 15 weeks after injection (FIGURE R27B and C). To note, one mouse from the IC₂₀ condition died due to problems in the intracardiac injection and it was not considered for the analyses. Observable tumours were collected, paraffin embedded and HE staining for morphology visualisation. Tumours from untreated and IC₂₀/IC₃₀ conditions had similar morphologies.

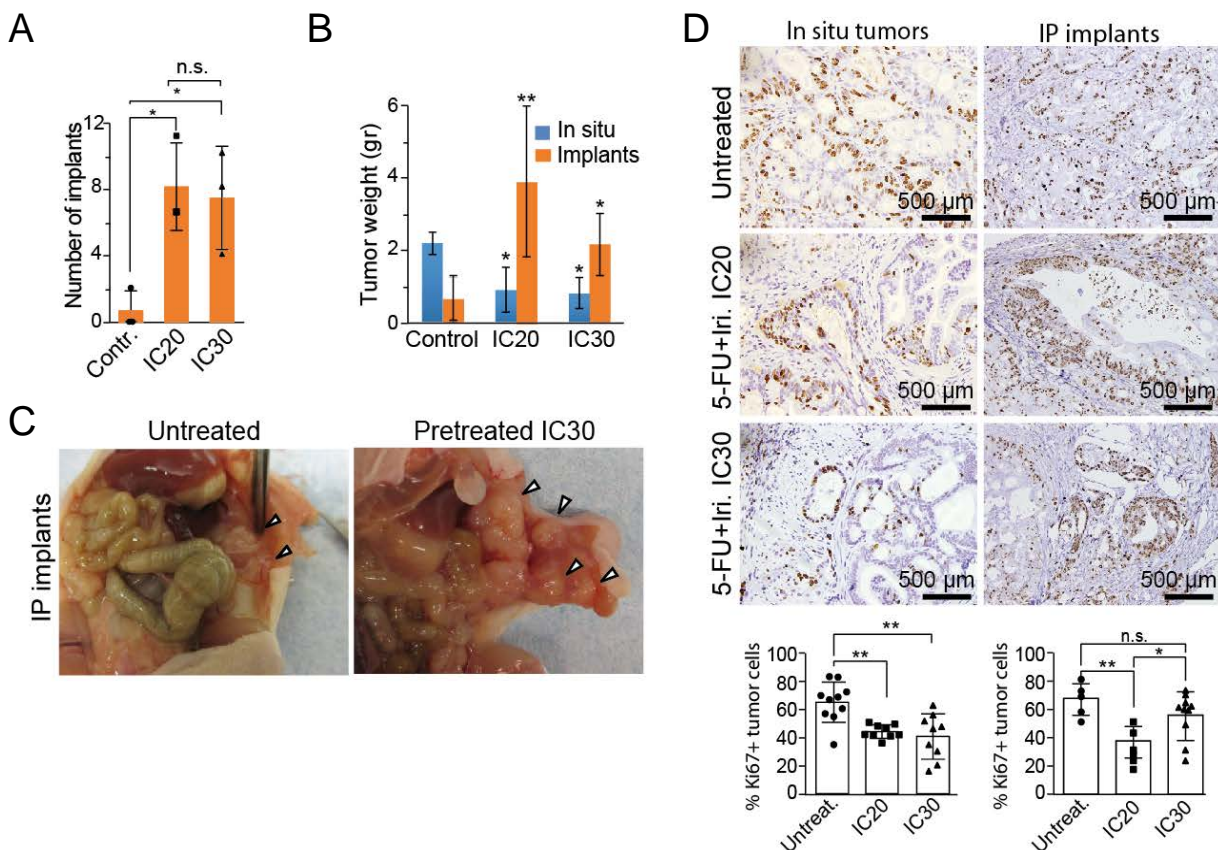


Figure R28. Treated PDO5 cells display a significantly higher ability to generate intraperitoneal implants than untreated cells when injected in the cecum. (A, B and C) (A) Number of intraperitoneal implants, **(B)** tumour weight of *in situ* growing tumours and intraperitoneal implants and **(C)** representative photographs of the tumours after injecting untreated or treated PDO5 cells in the cecum of mice. **(D)** IHC-P analysis of ki67 in PDO-derived *in situ* tumours and implants with the quantification of the percentage of ki67⁺ tumour cells in the indicated conditions.

Secondly, we inoculated equivalent numbers of untreated, IC₂₀ and IC₃₀ pretreated PDO5 cells in the cecum of nude mice. Tumour growth was assessed by palpation weekly and animals sacrificed synchronously 70 days after transplantation. We found that untreated, IC₂₀ and IC₃₀-treated PDOs all generated tumours in the site of inoculation, being IC₂₀ and IC₃₀-treated derived tumours being much smaller than those arising from untreated controls (FIGURE R28B), as expected. Importantly IC₂₀ and IC₃₀-treated PDO cells displayed a significantly higher

ability to generate intraperitoneal implants when compared with untreated tumour cells (FIGURE R28A and C). By IHC-P analysis of the proliferation marker ki67, we detected a reduction in the proliferation capacity of CT-treated PDO5 cells in comparison with untreated cells, but this difference was not as pronounced as in the *in vitro* culture conditions after treatment. This data could point to a partial reversion of the cell cycle arrest in the treated cells in the *in vivo* conditions. These results indicate that *TP53* WT PDO cells treated with low-doses of 5-FU+Iri. show reduced capacity to proliferate *in vitro* and in the primary tumours, but display comparable TIC as untreated cells *in vitro* and higher metastatic activity *in vivo*.

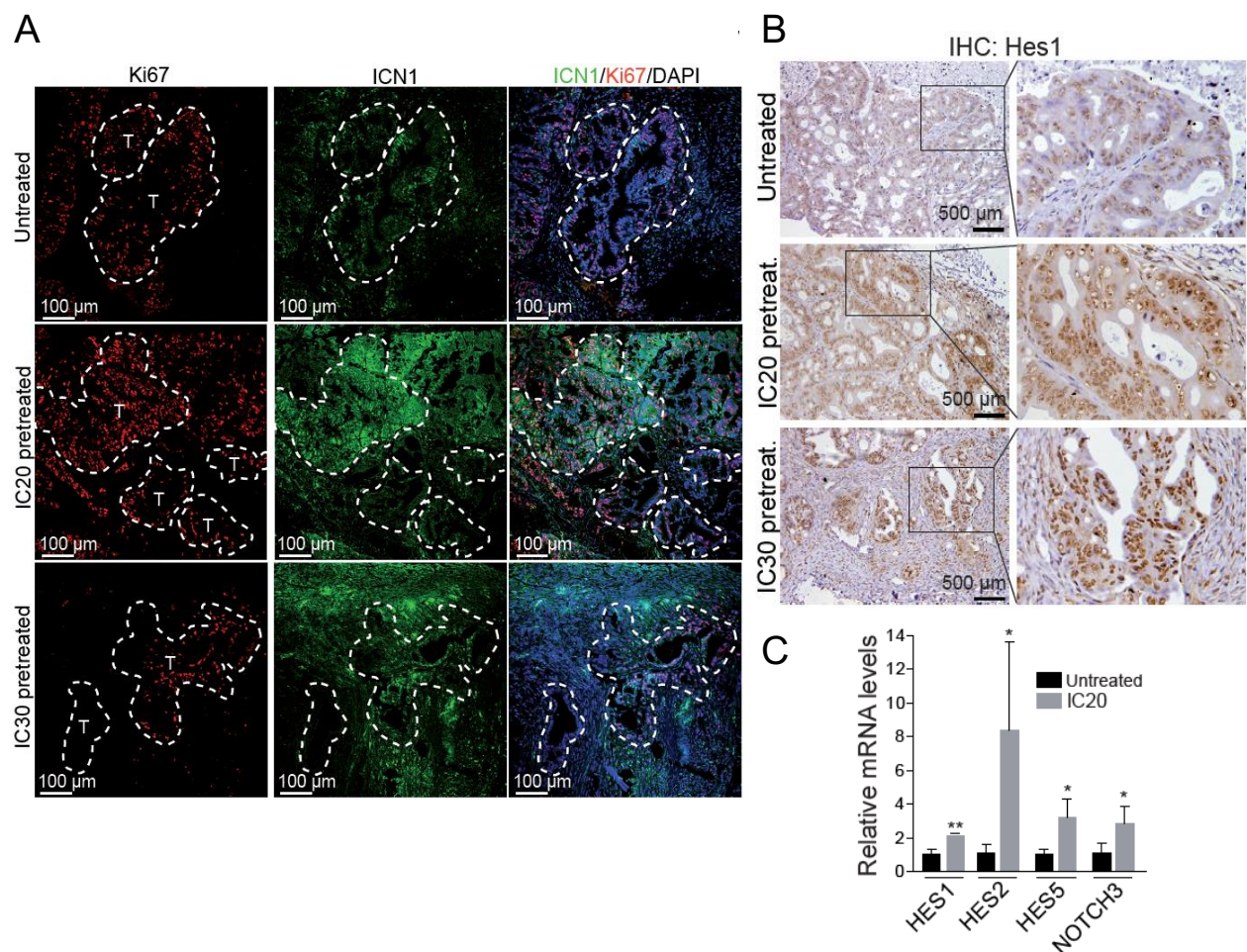


Figure R29. Active Notch signalling could be implicated in the reversion of the TQL phenotype. (A) Representative images of double IF analysis of ki67 and ICN1 of PDO-derived tumours (T) *in vivo*, indicated by dashed lines. **(B)** IHC-P analysis of Hes1 in PDO-derived tumours. **(C)** RT-qPCR analysis of Notch target genes in PDO5 treated as indicated.

To further explore which mechanisms could be involved in the reversion of the cell growth arrest *in vivo*, we searched in the bibliography for previously described genes or pathways related with that process. Activation of Notch signalling has already been demonstrated as essential for quiescence reversibility²²⁰ and scape from dormancy at metastatic niches²²¹.

We determined levels of activated Notch1 (ICN1) by IHC-P of control and CT-treated *in vivo* growing tumours. IC₂₀ and IC₃₀ treated tumours displayed a consistent ICN1 staining compared with control tumours (FIGURE R29A) that was associated with high levels of the canonical Notch target HES1 (FIGURE R29B). Importantly, high levels of ICN1 were found in highly proliferating areas, pointing to a direct correlation with active ICN1 and tumour growth. Then, we tested the expression levels of several Notch target genes in control and CT-treated PDOs. IC₂₀ and IC₃₀ treatments imposed a significant upregulation of *Hes1*, *Hes2*, *Hes5* and *Notch3* as determined by RT-qPCR analysis (FIGURE R29C). Further studies should be performed to further demonstrate the impact of Notch activation in reverting the TQL phenotype and starting proliferation, including the use of Notch inhibitors or genetic Notch mutant mouse models.

R3. DEFINITION OF A feISC SIGNATURE WITH PROGNOSTIC VALUE

R3.1. The feISC signature shows a coordinate expression in untreated CRC patients

Low-doses of CT treatment induce the acquisition of a feISC signature, as demonstrated previously in PDO5 (*TP53* WT). After the characterisation of this phenomenon, we wondered if the phenotype could be present in untreated CRC cancer patients and had prognostic value. With this objective, we used CANCEERTOOL³³⁴, which is a freely accessible web-based interface which contains public transcriptomic data sets from cancer patients. Importantly, this tool already provides a normalisation of all expression data.

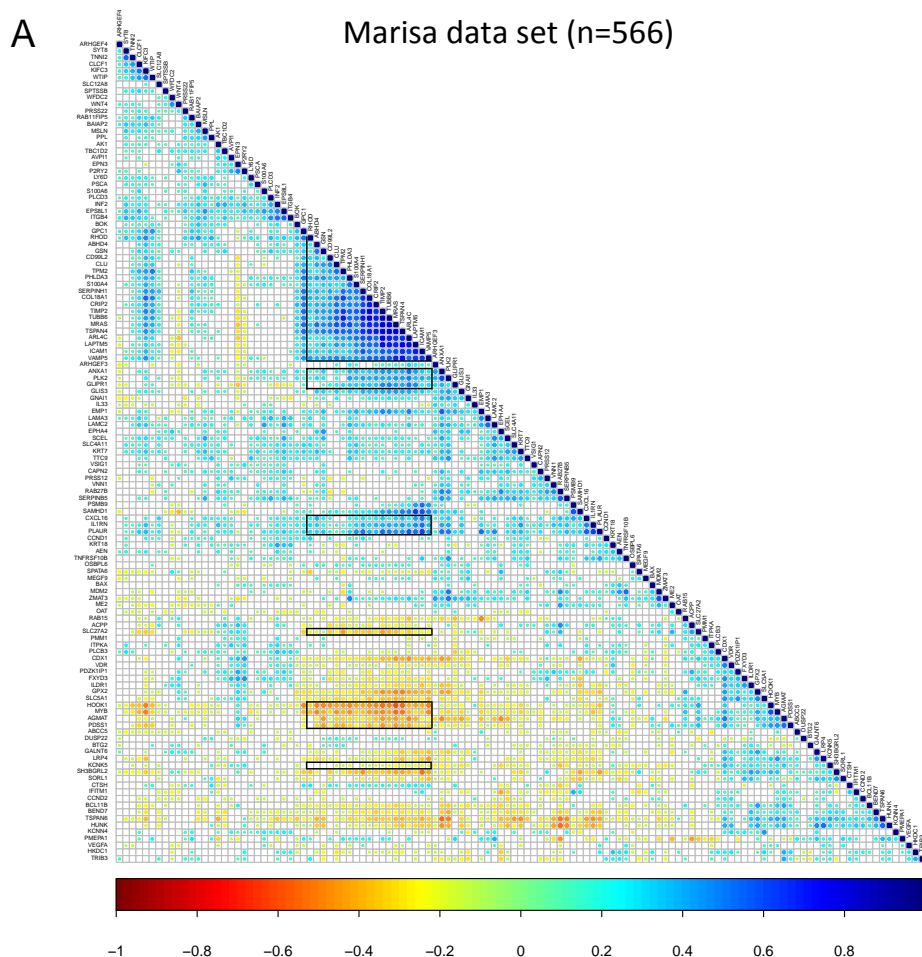


Figure R30. The feISC signature is expressed in a coordinate manner in untreated CRC patients. (A) Expression correlation matrix from all feISC signature genes, differentially expressed in treated PDOs, using the Marisa database. The size of circles and colour intensity are proportional to the Pearson correlation coefficient found for each gene pair. Name of the genes are not readable, but what is important is visualising the correlation between genes. Squares indicate the selected genes for defining the feISC signature.

We found seven CRC data sets in CANCERTOOL, but only four of them had disease-free survival (DFS) data, necessary for analysing the prognostic value (not selected: ^{311,314} and Colonomics Portal). As Kemper data set only contained 90 samples ³³⁵ (GSE33113), we decided to use the other remaining three data sets. The selected data sets were: Marisa, which contained 566 number of patients ⁹³ (GSE39582); Jorissen, with 226 patients ³³⁶ (GSE14333); and TCGA, with 329 patients (TCGA Portal). Marisa and Jorissen data were obtained from microarray affymetrix and TCGA data from RNA-seq techniques. Moreover, TCGA is a mix of two studies: TCGA-COAD (from colon cancer samples) and TCGA-READ (rectum), which we have used as a unique data set. Another consideration is that not all the patients of the three data sets had DFS data, so we have performed all the analyses only with the patients with this data available.

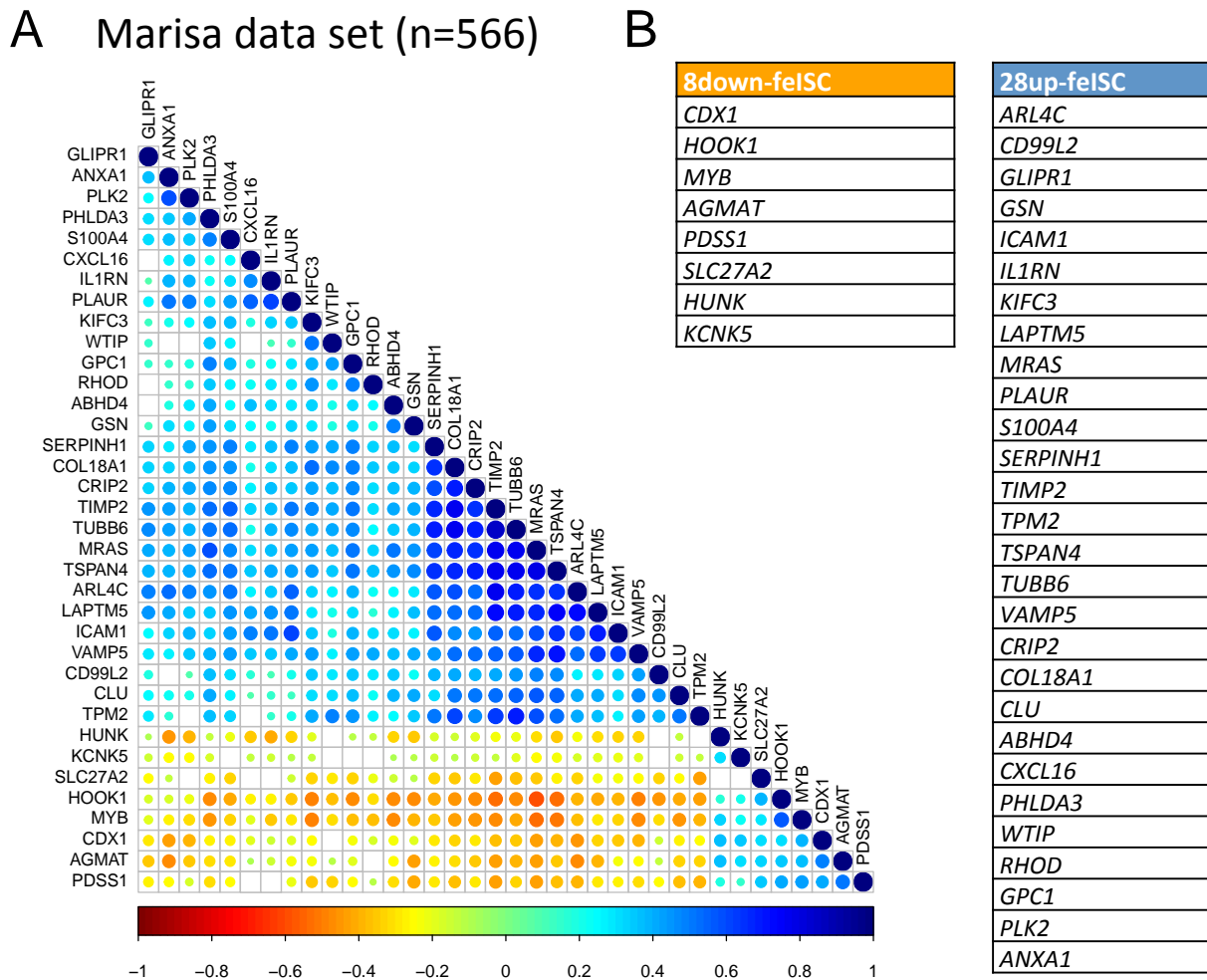


Figure R31. Determination of the 28up+8down-feISC signature. (A) Expression correlation matrix from the 28up+8down-feISC gene signature using the Marisa database ($n=566$). The size of circles and colour intensity are proportional to the Pearson correlation coefficient found for each gene pair. **(B)** List of the 8 down- and 28 up-regulated genes from the feISC signature.

Computational analysis of these three CRC data sets demonstrated that many genes in the TQL-associated felSC signature were expressed in untreated tumours and distributed in clusters of coordinate expression with either positive or negative correlation (FIGURE R30, only shown for Marisa). These results indicate that stimuli other than sublethal CT could induce the acquisition of the felSC signature in untreated patients.

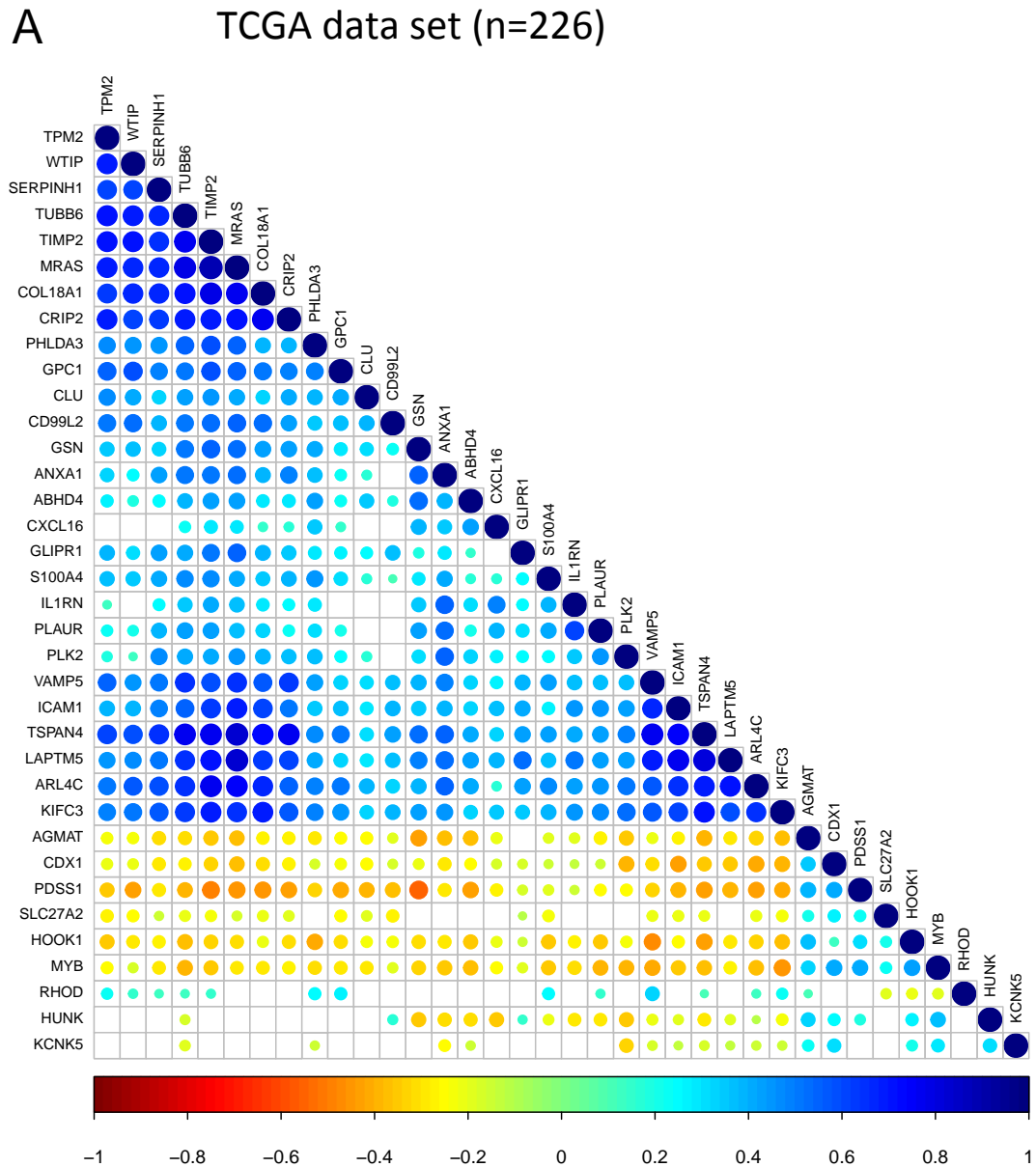


Figure R32. Coordinated expression of the 28up+8down-felSC signature in TCGA data set. (A) Expression correlation matrix from the 28up+8down-felSC gene signature using the TCGA ($n=226$) data set. The size of circles and colour intensity are proportional to the Pearson correlation coefficient found for each gene pair.

Since we were interested in genes with prognosis potential, we selected the genes with prognostic value in at least one of the three cohorts and the highest positive or negative correlative expression (we speculated that genes with poor correlation might impose a poorer clustering of patients). For simplicity, we integrated these genes in a new cluster, containing 28 upregulated and 8 downregulated genes in CT-treated PDOs and feISCs (FIGURE R31A and B). The 28up+8down-feISC cluster of genes was present in Marisa (FIGURE R31A), Jorissen and TCGA CRC cohorts (FIGURE R32A and R33A).

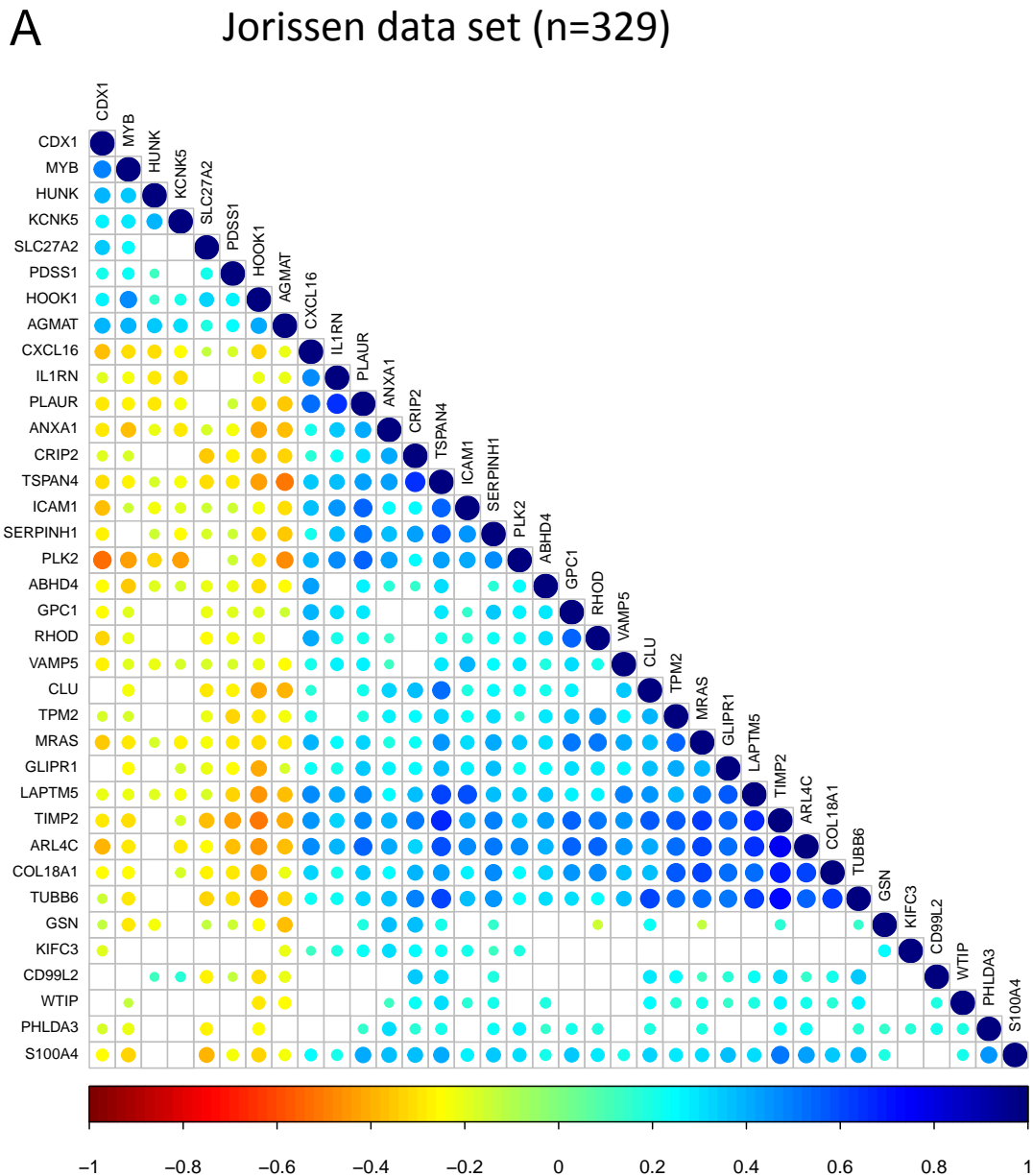


Figure R33. Coordinated expression of the 28up+8down-feISC signature in TCGA data set. (A) Expression correlation matrix from the 28up+8down-feISC gene signature using the Jorissen ($n=329$) data set. The size of circles and colour intensity are proportional to the Pearson correlation coefficient found for each gene pair.

To further establish the levels of up- or down-regulation of this simplified feISC signature, we performed RT-qPCR (FIGURE R34A) of randomly selected 28up+8down-feISC genes from RNA obtained of PDO5 untreated and IC₂₀ 5-FU+Iri.-treated at 72 h. We also analysed the expression of these genes in additional *TP53* WT PDOs (PDO66, PDO20 and PDO53, provided by Alberto Muñoz lab), and other *TP53* mutated PDOs from our biobank (FIGURE R34B, C and D). Although the levels of gene expression are not homogeneous, we observed the same tendency in all *TP53* WT PDOs. To note, RT-qPCR of PDO53 should be repeated for better results with less deviation of the samples. Results from *TP53* mutated PDOs are included in section R3.2.

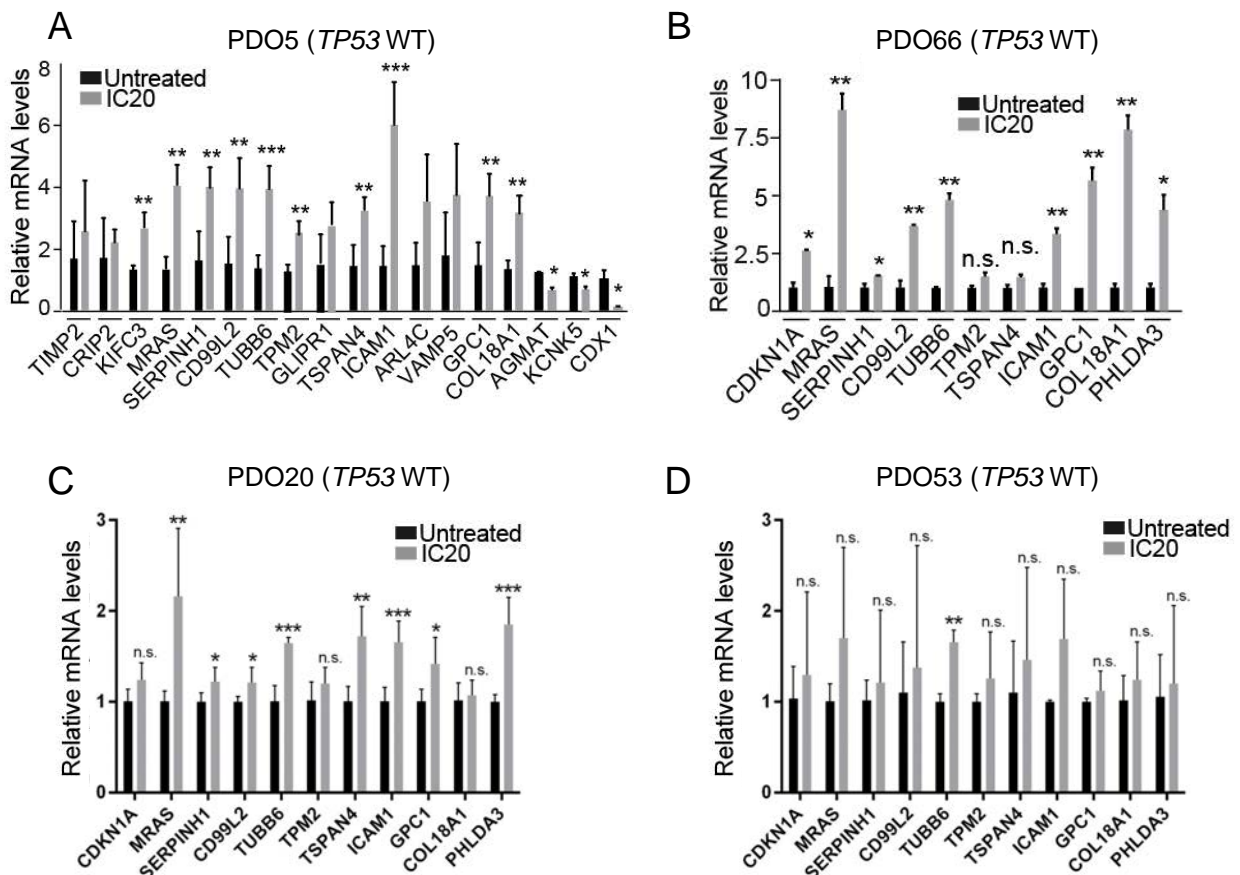


Figure R34. The 28up+8down-feISC signature is present in treated *TP53* WT PDOs. (A, B, C and D) RT-qPCR analysis of normalised relative expression of selected 28up+8down-feISC signature genes in control and treated *TP53* WT (A) PDO5, (B) PDO66, (C) PDO20 and (D) PDO53, as indicated.

We next setup the evaluation of protein levels of genes from the 28up+8down-feISC signature by IHC-P, since this is the preferred diagnosis tool used in most Pathological Anatomy departments. We first did this analysis in control and CT-treated PDO5. From the different biomarkers tested, TUBB6 and CD99L2 were the ones showing more reproducible results. We

detected increased levels of CD99L2 in CT-treated PDO5, with TUBB6 showing little differences between untreated and treated conditions (FIGURE R35A). Using antibodies against other proteins from the 28up+8down-felSC signature, we also observed less consistent but similar behaviour (not depicted). This could indicate that the increase expression in CT-treated PDOs is not sufficient to be detected in the less-quantitative IHC-P method. Thus, IHC-P may not be the better tool in clinics for felSC signature determination.

We also carried out WB analyses of PDO5 after IC₂₀ 5-FU+Iri. treatment in time course assays. Most of the analysed proteins showed variable levels of increase at 72 h after treatment, but displayed different kinetics. For instance, CD99L2 levels did not significantly increase along time and TIMP2 showed increased levels at 1-24 h but then the levels decreased, although at 72 h the levels were still higher than in the untreated condition (FIGURE R35B).

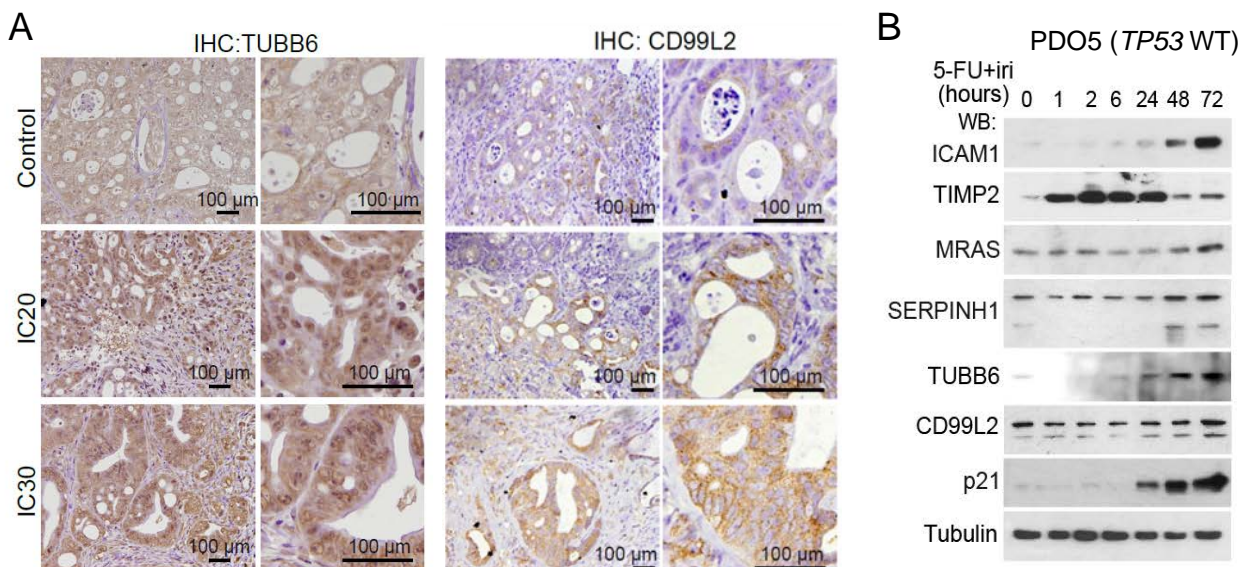


Figure R35. Protein levels from the 28up+8down-felSC signature are upregulated. (A) IHC-P analysis of selected genes from the felSC signature (TUBB6 and CD99L2) in control and IC₂₀ or IC₃₀ treated PDO5. **(B)** WB analysis of the indicated antibodies in control and treated PDO5 cells collected at the indicated time points after 5-FU+Iri. treatment.

R3.2. The felSC signature is p53-dependent

Previous experiments suggested that functional p53 signalling is necessary for the acquisition of the TQL phenotype (SEE FIGURE R10 and R23). Thus, we analysed levels of felSC genes following CT treatments in the *TP53* mutant PDO4 and PDO8 (FIGURE R36A and B). Activation of all tested felSC genes by CT was diminished in comparison to *TP53* WT PDOs. However, we

still detected some degree of activation in the hypomorphic *TP53* mutation in PDO4, which did not produce a completely loss of functional p53 protein. To further study the p53 dependency for feISC activation by CT, we followed a CRISPR-Cas9 strategy to generate PDO5 KO pools, which showed variable degree of p53 depletion (FIGURE R36C). RT-qPCR analysis revealed that PDO5 KO#3 showing the lowest p53 levels displayed significantly lower activation of all tested 28up-feISC genes after 5-FU+iri. IC₂₀ treatment, compared with p53 WT PDO5 (FIGURE R36D).

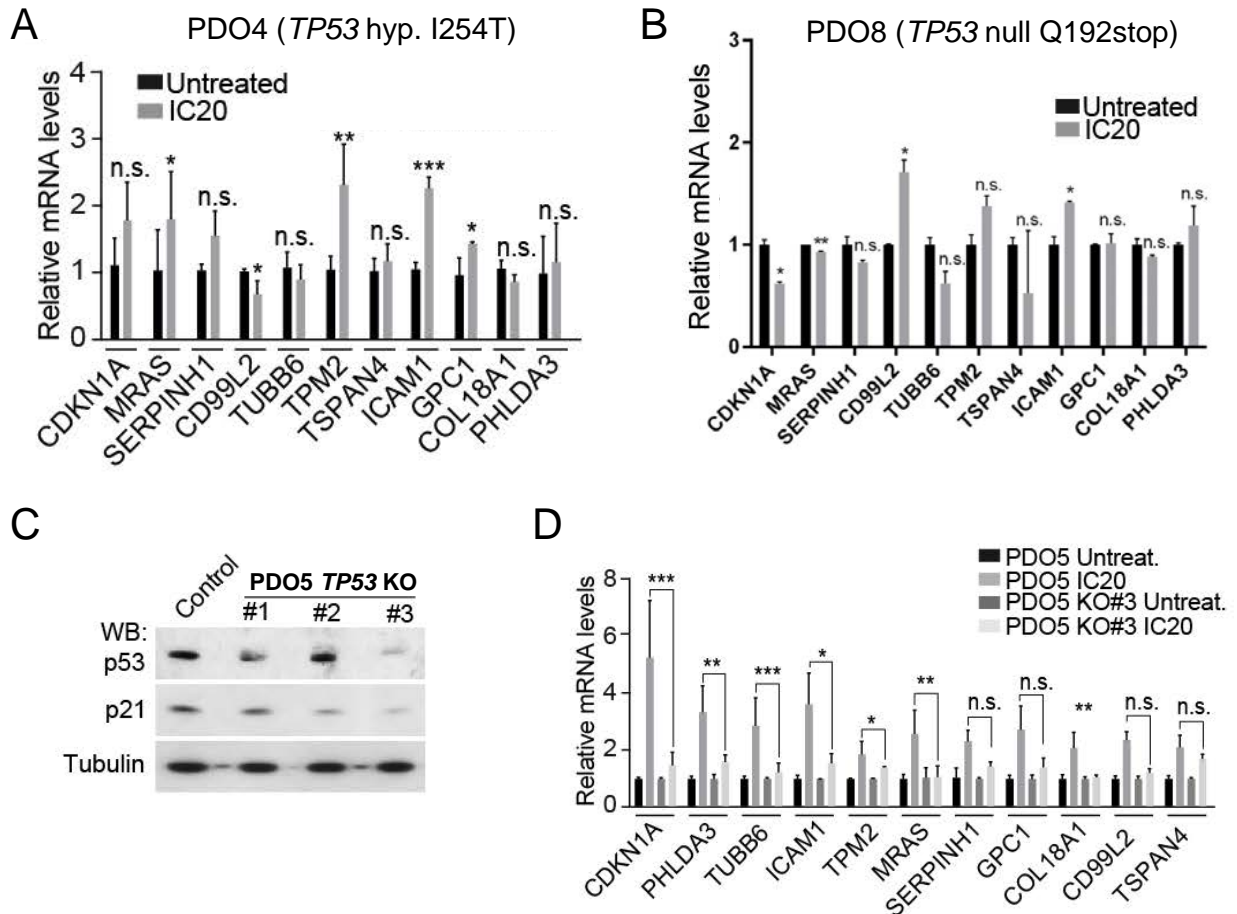


Figure R36. The 28up+8down-feISC signature is not present in treated TP53 mutant PDOs. (A, B and D) RT-qPCR analysis of normalised relative expression of selected 28up-feISC signature genes plus *CDKN1A* gene in control and CT-treated **(A)** *TP53* hypomorphic PDO4, **(B)** *TP53* mutant PDO8 and **(D)** PDO5 *TP53* KO #3. **(C)** WB analysis of p53 levels and its downstream target p21 in CRISPR-Cas9-engineered p53 KO pools.

Although PDOs are considered the best *in vitro* model for studying cancer cell behaviour, we wanted to use a different model for investigating feISC signature induction after sublethal CT treatment. Specifically, we used a panel of CRC cell lines either *TP53* WT (HCT116 and Ls174T) or *TP53* mutant (HT29 and SW480). We detected an increase in the levels of feISC

proteins after CT treatment that was slightly higher in cells carrying functional p53 (FIGURE R37A). Remarkably, the DNA-damage marker γ H2A.X was massively increased after CT treatment specifically in *TP53* mutant CRC cell lines, similar to that seen in *TP53* mutant PDOs by comet assay (see FIGURE R23C).

In addition, analysis of the Marisa data set demonstrated that 28up-feISC and 8down-feISC signatures were upregulated and downregulated, respectively (FIGURE R37B) in CRC tumours compared with colonic normal tissue, with higher significance in *TP53* WT tumours.

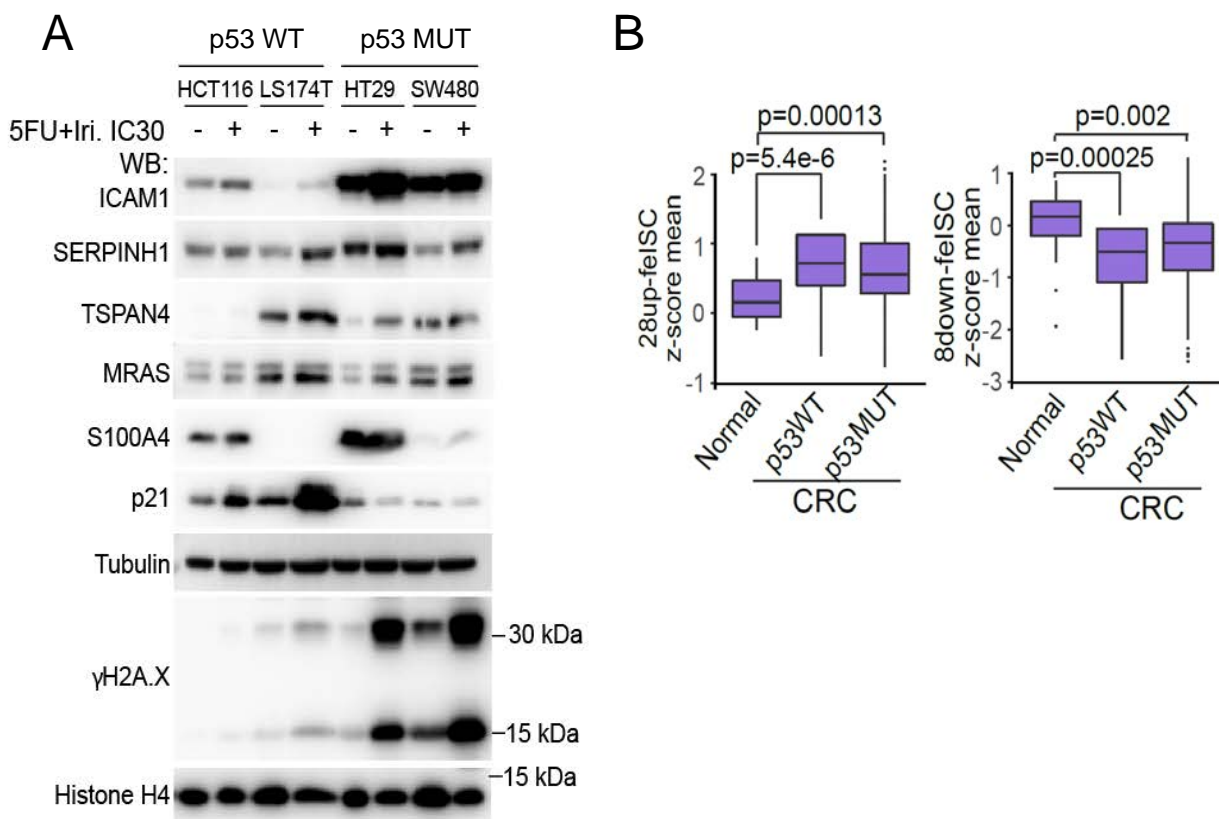


Figure R37. The 28up+8down-feISC signature is p53 dependent. (A) WB analysis of various CRC cell lines untreated or collected after 72 h of 5-FU+Iri. treatment. Membranes were incubated with the indicated antibodies. **(B)** Box plots of the 28up-feISC and 8down-feISC gene signature scaled expression means for normal and CRC patients in Marisa database. Statistical p-value from Anova test is shown.

We next performed CHIP-seq assay of 5-FU+Iri. IC₂₀-treated PDO5 cells, to determine if there is a direct association between p53 signalling and the genes from our signature. CHIP peaks were equally distributed in the two replicates performed, with a majority of peaks corresponding to distal intergenic regions (FIGURE R38A). Comparison between the two replicates uncovered 111 common p53 peaks (212 peaks in the first and 135 in the second replicate). GO pathway

analysis of genes associated to p53 peaks uncovered signal transduction by p53, regulation of cell cycle G1/S phase transition and DNA-damage checkpoints (not depicted).

Only five of the 28up-feISC genes (*PLK2*, *PHLDA3*, *LAPTM5*, *ABHD4* and *GPC1*) had been previously identified as p53 targets³³³ (FIGURE R38B), and we only detected p53 binding at the promoter of *PLK2*, *PHLDA3* and *GSN* genes (FIGURE R38C) included in the 28up-feISC signature. These results suggest that additional transcription factor/s govern the coordinate expression of the signature likely associated with p53.

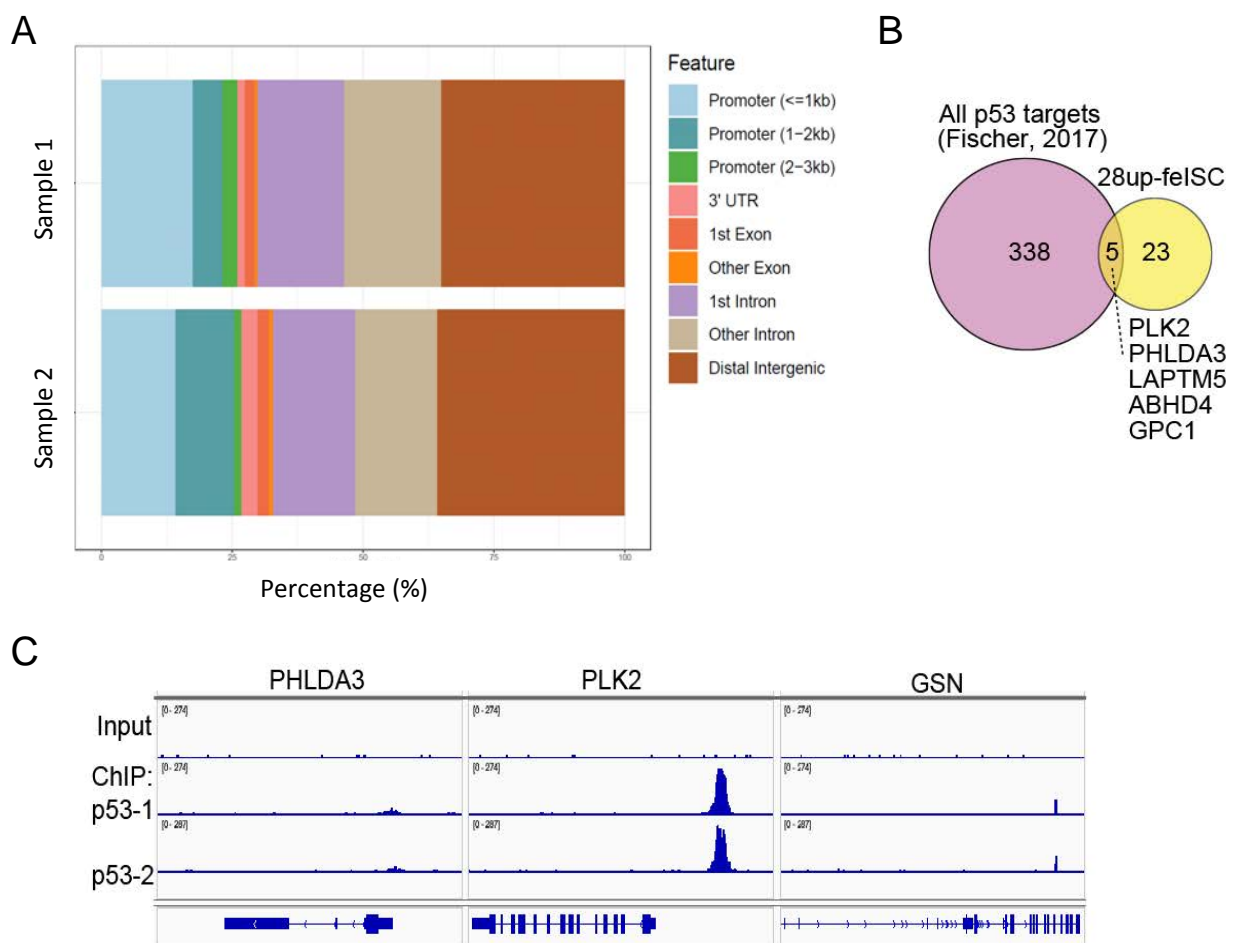


Figure R38. Additional transcription factors should govern the coordinate expression of the feISC signature.

(A) Representation of the ChIP peak annotation profile obtained from ChIP-seq analysis in IC₂₀-treated PDO5 (n=2).

(B) Venn diagram representing the distribution of 28up-feISC genes across genes identified as p53 targets.

(C) Representation of some 28up-feISC genes distribution in the indicated genomic regions from ChIP-seq analysis.

R3.3. Tumours displaying the feISC signature are mainly classified as mesenchymal

We next determined whether tumours carrying the 28up+8down-feISC signature were restricted to a specific molecular cancer subtype. Using the classification done by Guinney and collaborators (explained in I2.1)⁹⁰, we found that 74% of tumours with the 28up+8down-feISC signature were categorised as CSM4 (FIGURE R39A) and 21% as CMS1. In contrast, a 64% of the 28up-low+8down-high tumours were primarily ascribed to CMS2 subtype and a 34% to CMS3. This classification indicates that our 28up+8down-feISC signature is present in more immunogenic tumours.

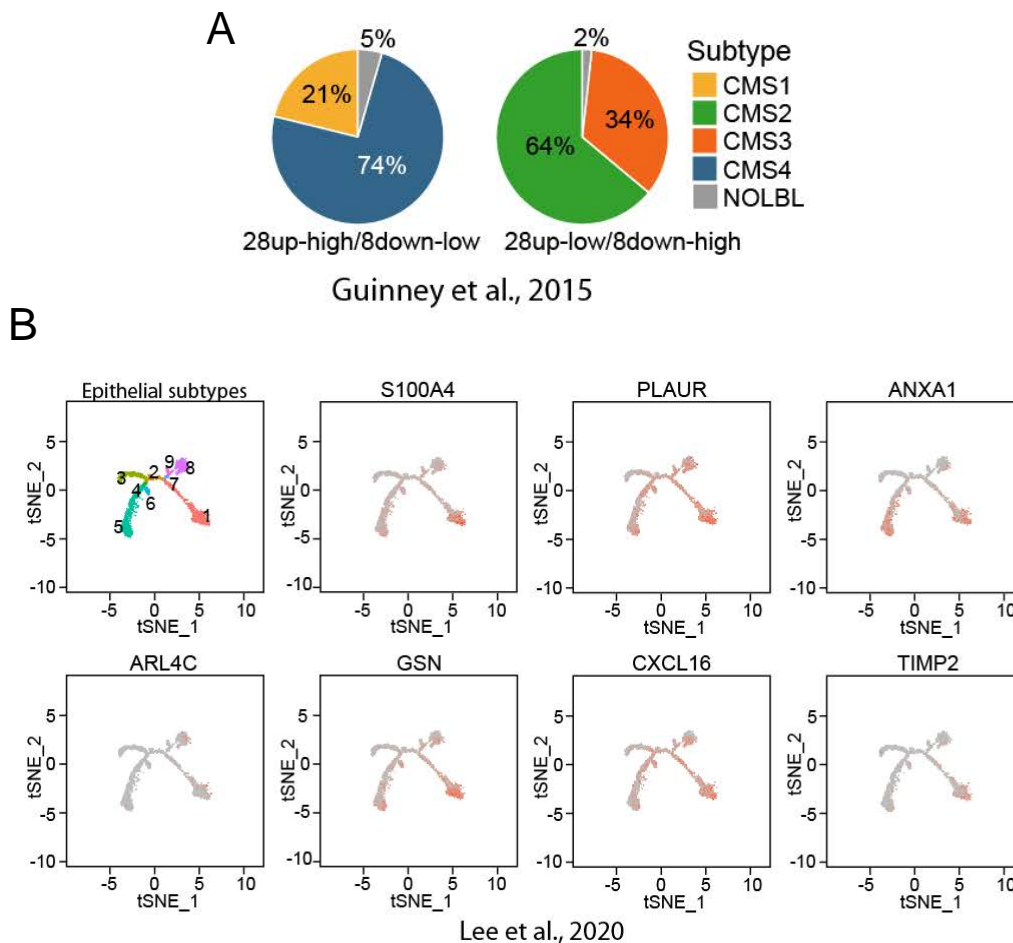


Figure R39. Tumours displaying the feISC signature are mainly CMS4 and associated with secretory and migratory functions. (A) Pie charts showing the molecular subtype distribution, according to Guinney et al, in patients within the feISC signature groups as indicated. **(B)** Localisation of several 28up-foetal-ISC genes in epithelial subtypes cell states 1-9 previously classified in Lee et al 2020. The *t*-SNE plots were obtained using the web-based tool URECA. Cell states 1, 5 and 6 correspond to a transcriptional group enriched for secretory and migratory gene expression, whereas cell states 2, 3, 4, 7, 8 and 9 correspond to transport and Wnt signalling gene expression.

We next studied whether the feISC signature identified in untreated tumours was expressed in the epithelial cancer cells or primarily contributed by the stromal component of tumours, since CMS4 tumours have high stromal infiltration. Therefore, we analysed some of our feISC genes in the data from the CRC scRNA-seq data from Lee and collaborators, where they identify epithelial cells and classify them according to the transcriptomic data ⁹². We were able to demonstrate that the genes are expressed in the epithelial component of untreated tumours, particularly in states 1, 5 and 6, which are associated with secretory and migratory pathways (FIGURE R39B). The other states are associated with transport and Wnt signalling gene expression.

R3.4. The feISC signature has prognostic value in CRC

We studied the possibility that the presence of the feISC signature in untreated CRC tumours was associated with patients' outcome. To this aim, we analysed the predictive capacity of the 28up+8down-feISC gene signature in the Marisa, Jorissen and TCGA CRC data sets. The global 28up+8down-feISC signature was sufficient to demarcate at least 2 subsets of patients in either data set (not depicted), with the group with highest 28up and lowest 8down-feISC levels displaying the poorest DFS (FIGURE R40A, B and C). It is worth mentioning that in Marisa and TCGA data sets an unclassified group was defined that contained a mixed distribution in the expression of the feISC genes. Thus, the number of patients included in the analysis may not coincide with the total number of patients in the cohorts.

A more detailed analysis of the Marisa data set demonstrated that the feISC signature was significantly associated with tumour relapse in patients at stages II (n=264) (p=0.041) (FIGURE R41A) and II+III (n=469) (p=0.0033) (FIGURE R41B), and imposed a trend towards poor prognosis at stage IV (n=60) (FIGURE R41C). These findings are important, since patient prognosis at stages II and III are nowadays uncertain due to the absence of adequate markers. Instead, stage IV patients normally have poor prognosis, being of less importance this classification. TCGA data set have not assigned tumour stage for all patients, which made difficult obtaining significant results (not depicted). We did not perform this analysis in the Jorissen data set since the stage classification was annotated differently than the other cohorts.

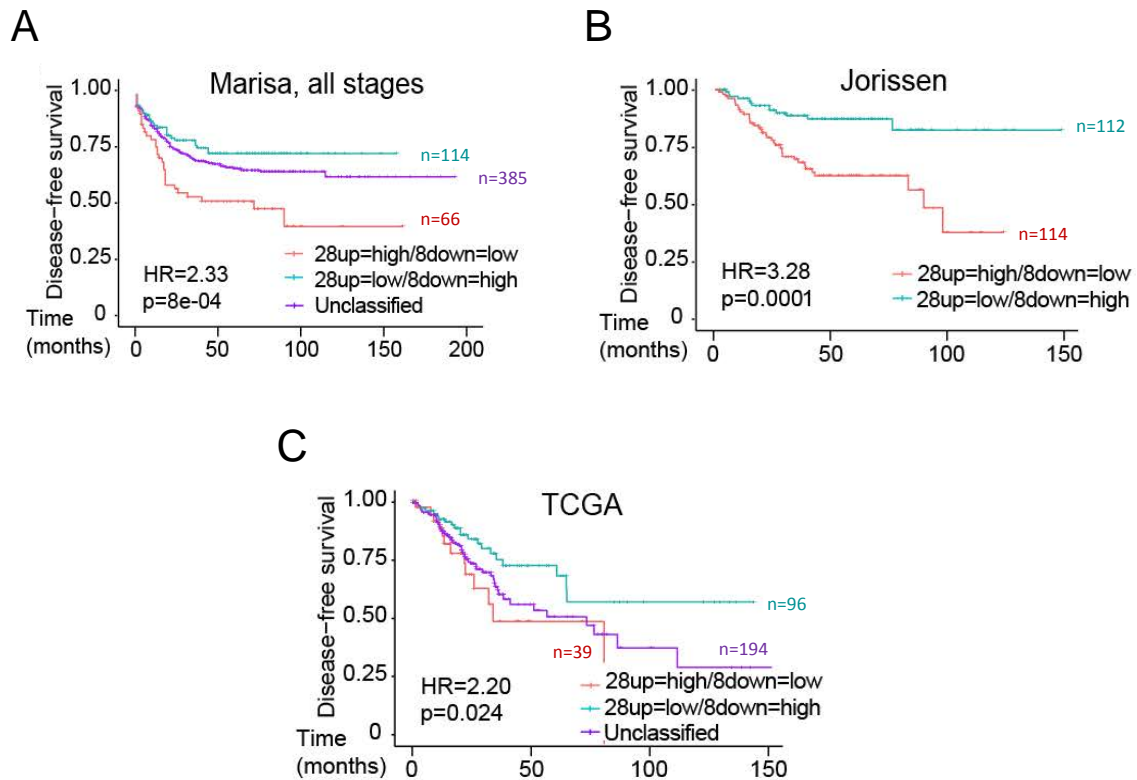


Figure R40. The feISC signature has prognostic value using CRC data sets. (A, B and C) Kaplan-Meier representation of DFS probability over time for patients unclassified and with high or low expression of the 28up+8down-feISC signature in **(A)** Marisa, **(B)** Jorissen and **(C)** TCGA CRC databases.

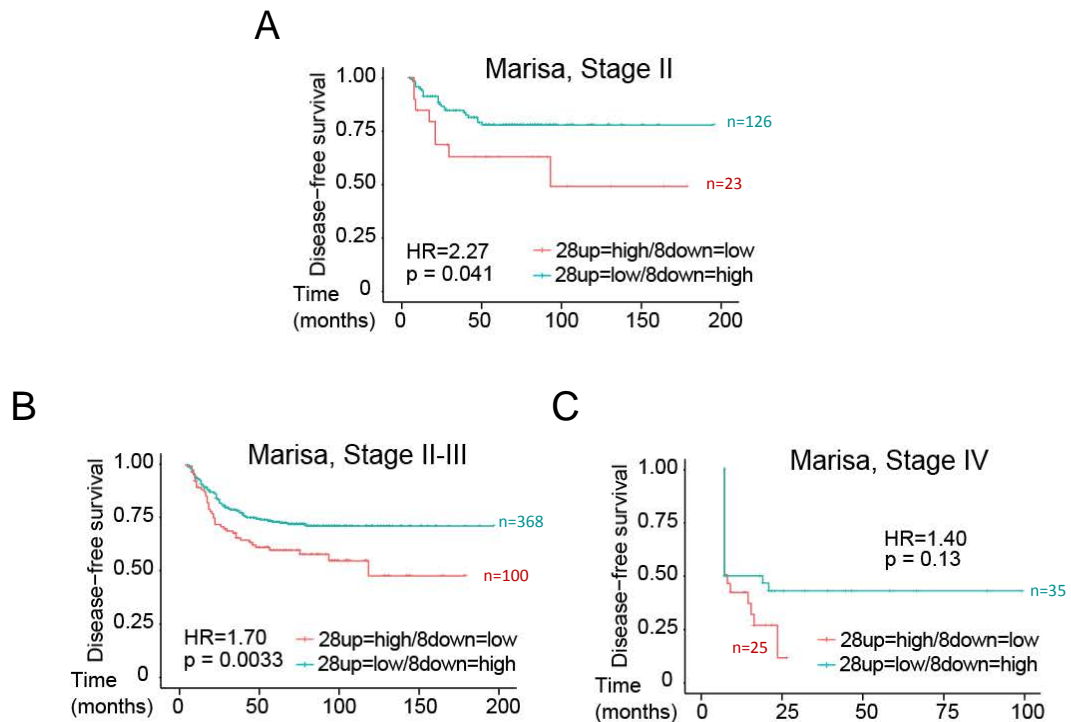


Figure R41. The feISC signature has prognostic value in stage II and II+III patients. (A, B and C) Kaplan-Meier representation of DFS probability over time for patients classified according to the 28up+8down-feISC signature of patient groups from **(A)** stage II, **(B)** stage II and III and **(C)** stage IV, from Marisa CRC database.

Since we have previously demonstrated that feISC conversion is dependent on p53, (SEE FIGURES R36 and R37), we explored the possibility that *TP53* status determined the prognosis value of 28up+8down-feISC signature in CRC patients. First, we analysed the DFS probability when stratifying patients according to their *TP53* status, which by itself did not have prognosis value (FIGURE R42A). However, classifying *TP53* WT patients according to the 28up+8down-feISC signature stratified patients according to their DFS, which was not the case for *TP53* mutant patients (FIGURES R42B and C). These results indicate that the feISC signature has prognostic value specifically in *TP53* WT patients. Using TCGA data set we found the same results as using Marisa's data (FIGURE R43A, B and C). We did not perform this analysis in Jorissen data set that lacks data about *TP53* mutations.

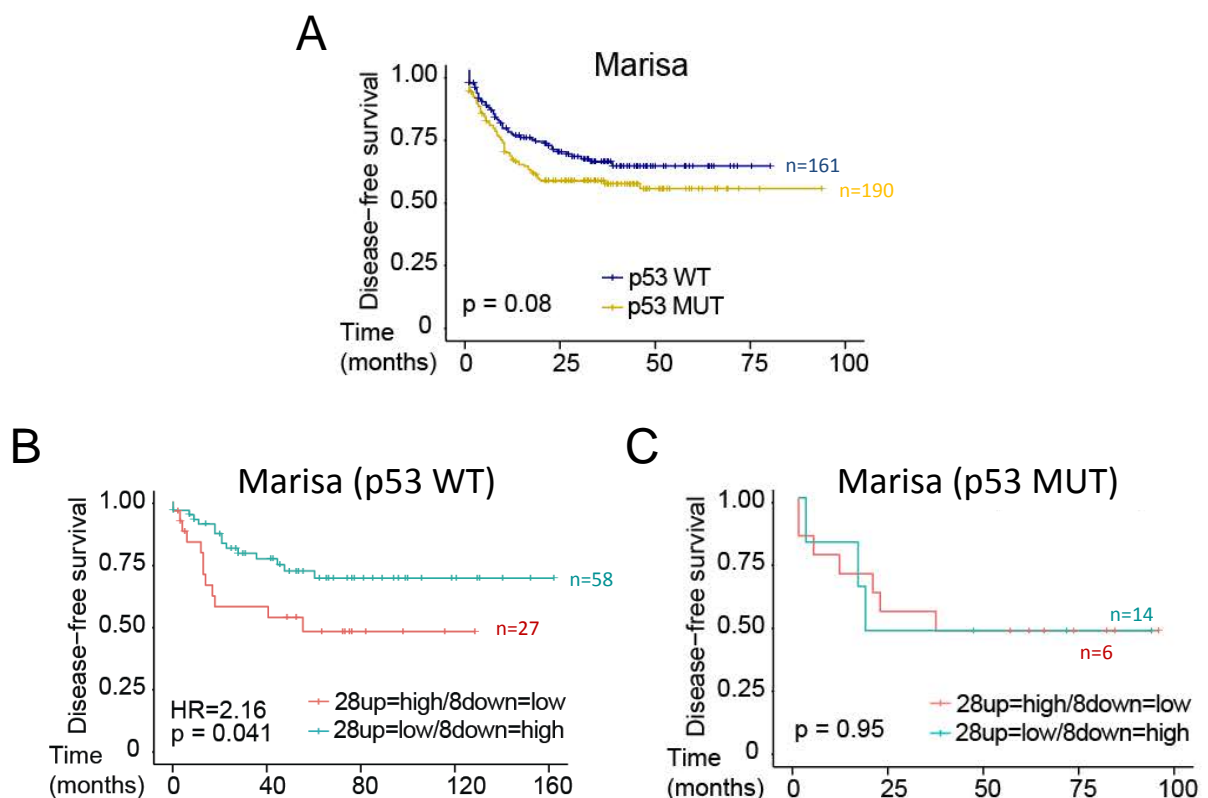


Figure R42. The feISC signature has prognostic value in *TP53* WT patients. (A) Kaplan-Meier representation of DFS probability over time of patients classified according to their *TP53* status in the Marisa CRC data set (*TP53* WT and *TP53* MUT). (B and C) Kaplan-Meier representation of DFS probability over time of patients, from the Marisa data set, for (B) *TP53* WT and (C) *TP53* mutant patients.

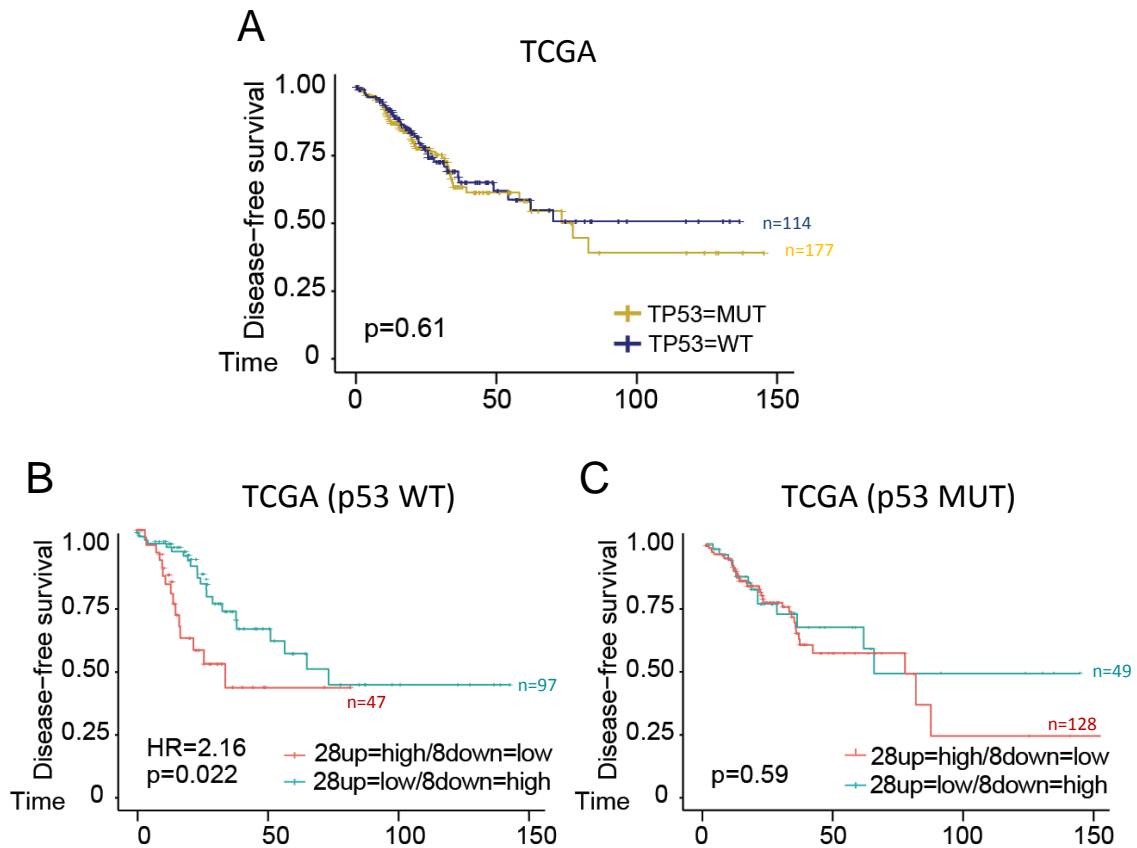


Figure R43. The felSC signature has prognostic value in TP53 WT patients in TCGA data set. (A) Kaplan-Meier representation of DFS probability over time of patients classified according to their *TP53* status in the TCGA CRC data set (*TP53* WT and *TP53* MUT). (B and C) Kaplan-Meier representation of DFS probability over time of patients, from the TCGA data set, for (B) *TP53* WT and (C) *TP53* mutant patients.

To overcome the problem that mutational status of p53 is not available from all tumour samples, we stratified patients according to p21 levels, as readout of p53 activity. We first determined whether p21 levels correlated with existing p53 information. Tumours with high p21 expression levels were mainly found in the group carrying *TP53* WT (a 76%); further indicating that high p21 levels are commonly associated to functional p53 in tumours (FIGURE R44A). Stratification of Marisa patients according to p21 levels did not have prognosis value by itself (FIGURE R44B), as it also happened with p53 levels (see FIGURE R42A). Importantly, prognosis value of the 28up/8down-felSC signature was restricted to tumours carrying p21 high levels (FIGURES R44C and D).

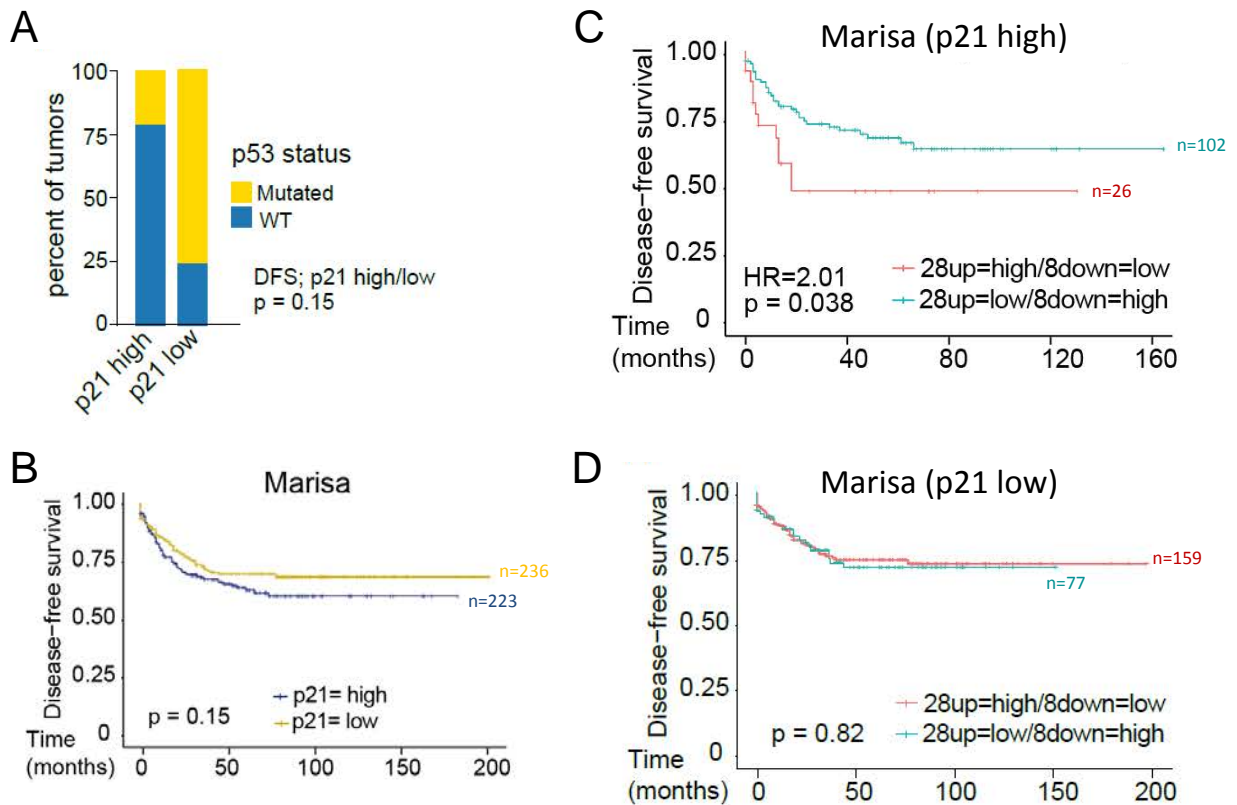


Figure R44. The feISC signature has prognostic value in patients with high p21 levels. (A) Percentage of tumours in the Marisa database with *TP53* WT or *TP53* mutant alleles according to p21 levels. (B) Kaplan-Meier representation of DFS probability over time of patients classified according to their p21 levels. (C and D) Kaplan-Meier representation of DFS probability over time for patients with high or low expression of the 28up/8down-feISC signature inside the group of tumours with (C) high and (D) low levels of p21.

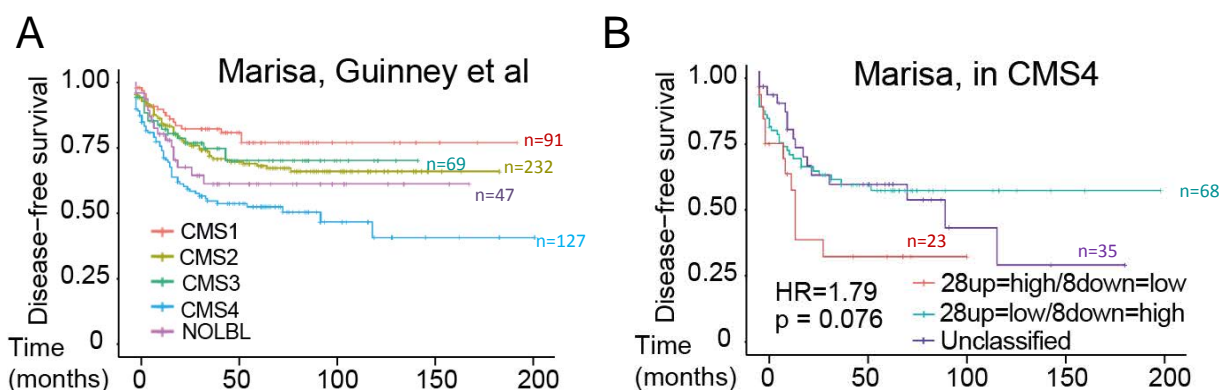
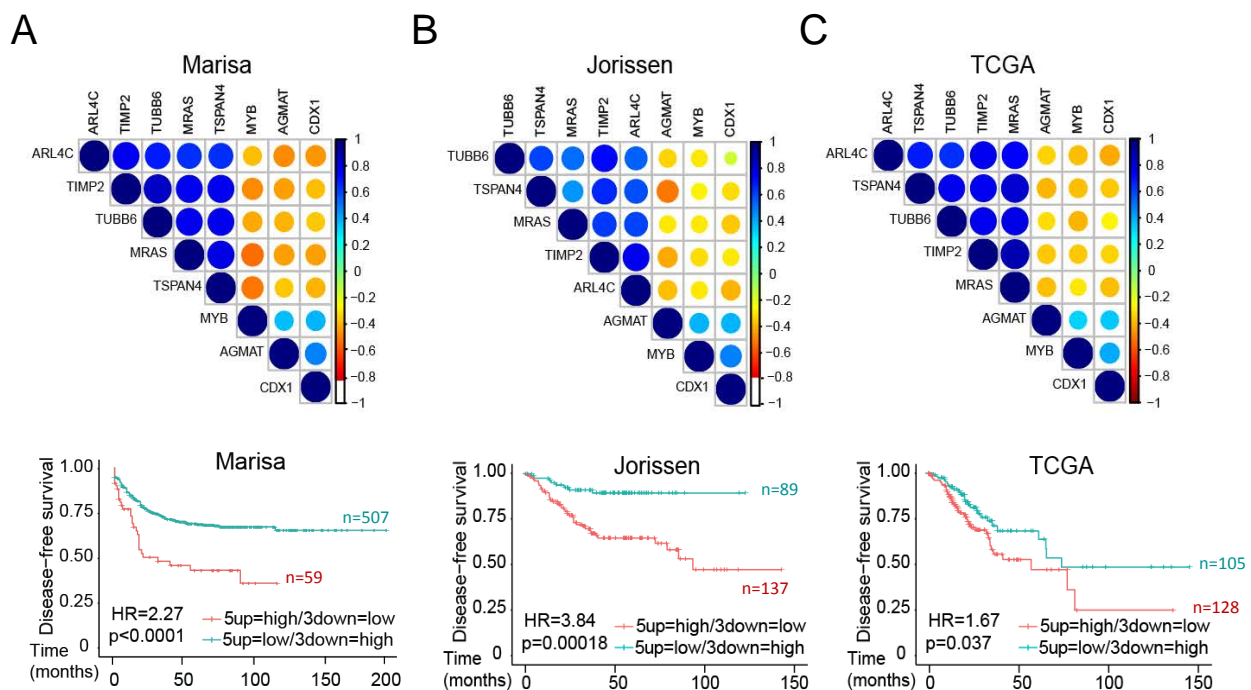


Figure R45. The feISC signature has prognostic value in CMS4 patients. (A and B) Kaplan-Meier representation of DFS probability over time of Marisa patient's tumours (A) classified by their CMS subtype or (B) tumours previously categorised as CMS4⁹⁰, and classified according to their cluster analysis of the 28up+8down-feISC signature.

As indicated, 28up+8down-feISC tumours are mainly included in the CMS4 subtype (see FIGURE R39A), which is the worst prognosis subtype (FIGURE R45A). We tested whether the prognosis value of the feISC signature was due to its association with the CMS4 subtype or it represents an independent prognosis factor. Our results indicate that the 28up+8down-feISC signature represents an independent prognosis factor within the CMS4 group (FIGURE R45B). Comparable results were obtained using the Jorissen and TCGA cohorts, although they were not statistically significant likely due to the low number of CMS4 patients (not depicted).

Overall, our results indicate that the 28up+8down-feISC signature has prognostic value in CRC patients without further classification. As there is a lack of good prognostic markers, in particular for II and III stage CRC tumours, we propose that our signature could be used in the clinical practice. To facilitate its clinical implantation, we explored the possibility of reducing the number of genes in the signature. First, we scored genes by their coordinate expression in the 3 CRC data sets analysed. Then, we evaluated the added value of single genes to the simplest signature composed by the highest scored 28up plus the highest scored 8down-feISC genes, as explained in MM25.



Using this strategy, we uncovered a minimal signature composed by 5-up genes (*ARL4C*, *TIMP2*, *TUBB6*, *MRAS* and *TSPAN4*) and 3-down genes (*MYB*, *AGMAT* and *CDX1*) that shared coordinate expression in tumours (FIGURE R46A, B and C, upper panels). This 5up+3down-felSC signature stratifies patients with poor prognosis in all tested CRC cohorts (FIGURE R46A, B and C, bottom panels). Remarkably, the 5up+3down-felSC signature also stratifies patients carrying tumours at stage II and II-III according to their prognosis (FIGURE R47A and B). These data indicate that the reduced signature could be used in clinics as a prognosis marker. It is of note that using the TCGA data set, the results were less clear, since the number of tumours in specific stages is very low. Only analysing stage III tumours DFS curves were statistically significant (not depicted).

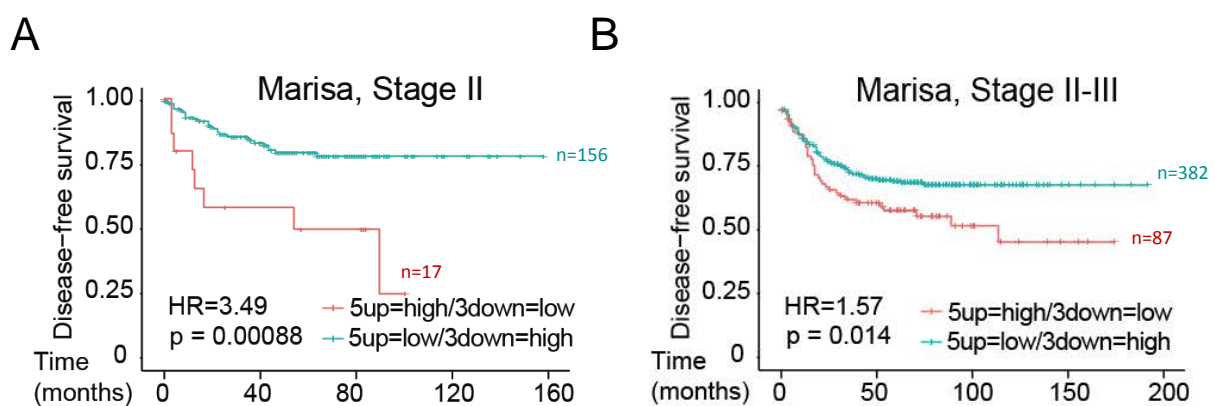


Figure R47. The reduced 5up+3down-felSC signature has prognostic value in stage II and II+III patients.

(A and B) Kaplan-Meier representation of DFS probability over time for patients with high or low expression of the 5up+3down-felSC signature of (A) stage II and (B) stage II and III Marisa database, selected according to their unsupervised hierarchical cluster analysis.

R3.5. Acquisition of the felSC signature is dependent on YAP1 activation

We previously suggested that factors other than p53 might regulate felSC gene expression (see FIGURE R38). *YAP1*, shown to be involved in the process of adult to foetal ISC conversion after intestinal injury^{78,286}, was found upregulated following sublethal CT treatment in the RNA-seq data (see FIGURE R24B). Thus, we speculated that YAP1 activation might be involved in the acquisition of the felSC signature.

We first studied whether YAP1 protein was upregulated in CT-treated PDO5 cells. By WB analysis we observed increased YAP1 expression after 5-FU+Iri. treatment, which was restricted to cells carrying WT *TP53* (FIGURE R48A). Similar behaviour was found in various CRC cell lines (FIGURE R48B). We also detected a dose-dependent accumulation of nuclear

(active) YAP1 (nYAP1) in IC₂₀ and IC₃₀-derived PDO5 tumours at 2 months after implantation in mice (FIGURE R48C) that was present, but not exclusively, in ki67⁺ regions.

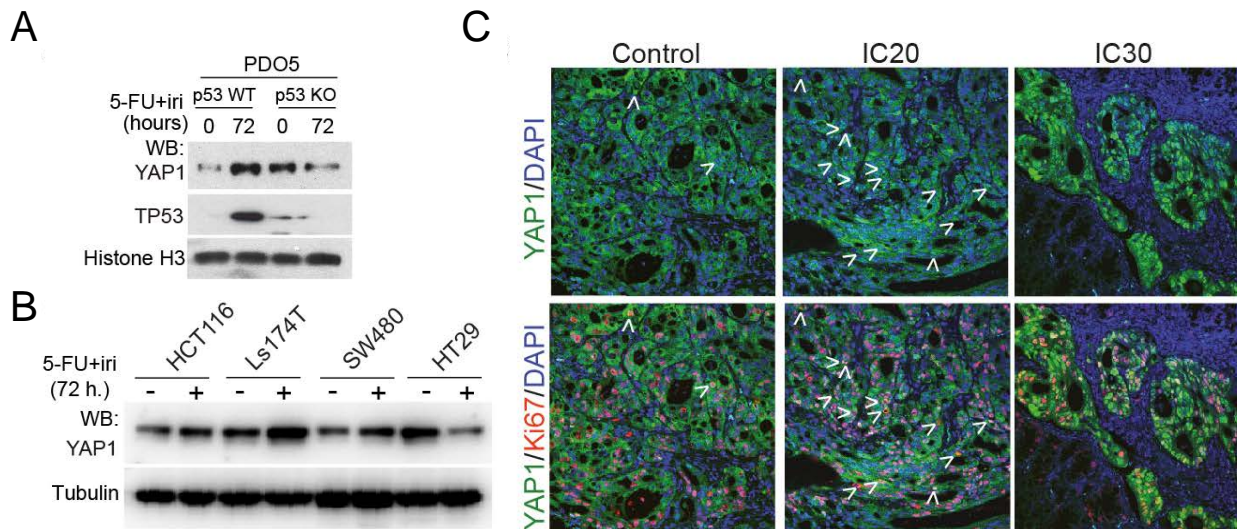


Figure R48. Sublethal doses of CT treatment produce increase in nYAP1. (A) WB analysis of the indicated antibodies of control and *TP53*-depleted PDO5 KO# 3 cells collected after 72 h of 5-FU+iri. treatment. (B) WB analysis of *TP53* WT (HCT116 and Ls174T) and *TP53* mutant (SW480 and HT29-M6) CRC cell lines untreated and collected after 72 h of 5-FU+iri. treatment. (C) Representative images of YAP1 and ki67 staining by IF in tumours derived from orthotopically implanted CT, IC₂₀ and IC₃₀-pretreated PDOs in nude mice. White arrows indicate nuclear translocation of YAP1. Counterstained, DAPI.

Next, we studied whether YAP1 activity was required for transcriptional induction of feISC genes by CT. For this, we used the YAP1 inhibitor verteporfin, which impedes the interaction between YAP1 and TEAD. To note, verteporfin is approved by the FDA for the treatment of macular degeneration due to its photosensitizer capacity, and it is currently involved in clinical trials for cancer treatment.

Treatment of Ls174T CRC cells with CT led to an increase in YAP1, SERPINH1 and TSPAN4 protein levels, which was abrogated by verteporfin (FIGURE R49A). In PDO5 cells, the YAP1 inhibitor verteporfin precluded induction of all tested feISC genes by RT-qPCR, after IC₂₀ 5-FU+iri. treatment (FIGURE R49B). Verteporfin treatment not only prevented the feISC acquisition, but also produced tumour cell death in both *TP53* WT and *TP53* mutant PDO cells, especially when treated in combination with IC₂₀ 5-FU+iri. treatment (FIGURE R49C).

We next analysed whether YAP1 was a transcriptional target of p53. By analysis of ChIP-seq data, we did not find binding of p53 to the promoter of YAP1.

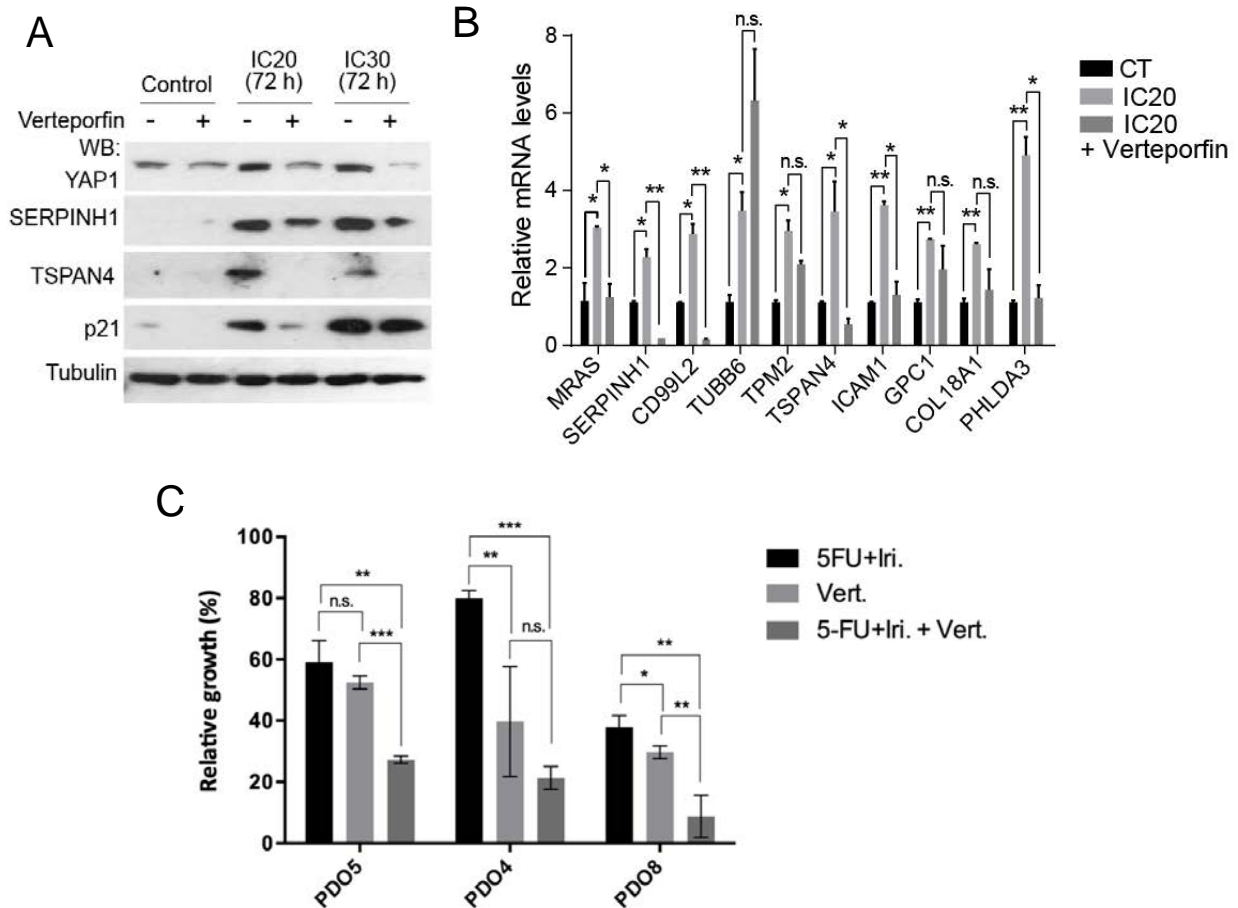


Figure R49. YAP1 inhibition precludes the acquisition of the felSC signature. (A) WB analysis of control and treated *TP53* WT Ls174T CRC cells collected after 72 h of 5-FU+Iri. treatment alone or in combination with the YAP1 inhibitor verteporfin at a final concentration of 5 μ M. **(B)** RT-qPCR analysis of normalised relative expression of selected 28up-felSC signature genes in control and treated PDO5 with 5-FU+Iri. alone or in combination with verteporfin at 0.2 μ M. **(C)** Quantification of the relative cell growth in *TP53* WT PDO5 and *TP53* mutant PDO4 and PDO8 treated with 5-FU+Iri. alone, verteporfin alone or in combination with verteporfin at 0.33 μ M.

To further study the role of YAP1 in CRC patients, we studied the putative prognosis value of YAP1 either by itself or linked to the 28up+8down-felSC signature. Importantly, in the expression data in the studied cohorts only inform on total YAP1 levels, with no indications about the activated form of YAP1, nYAP1. Our results indicated that YAP1 levels do not have prognosis value in the general cohorts (FIGURE R50A) or separating patients by their *TP53* status (FIGURE R50B and C). However, the 28up+8down-felSC signature displayed prognosis value specifically in the group of patients carrying high levels of YAP1, but not in patients with low levels of YAP1, using the Marisa data set (FIGURE R50D and E). However, analysis of TCGA and Jorissen data sets did not reveal any prognosis value of YAP1 in association with the felSC signature (not depicted)

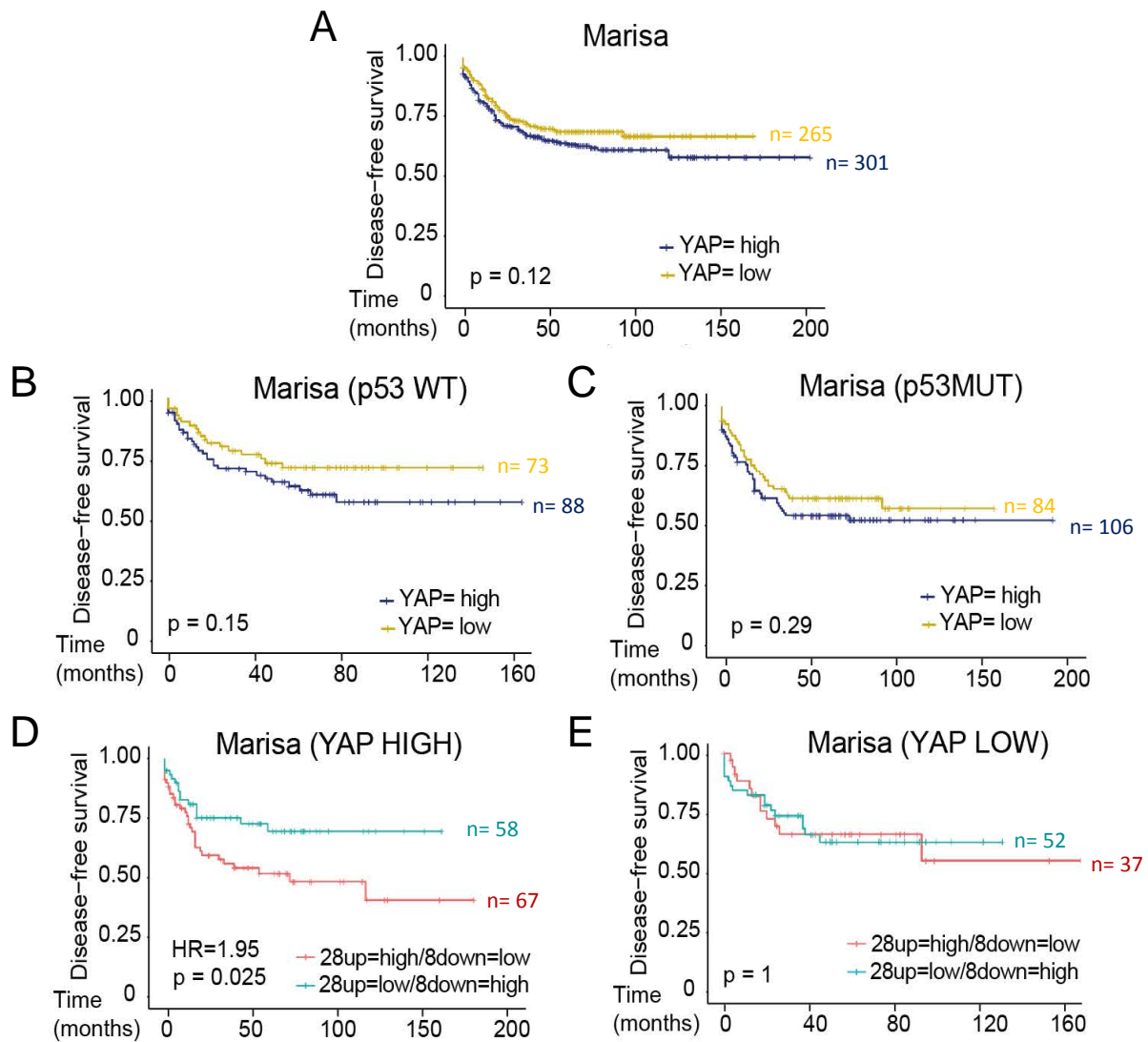


Figure R50. The felSC signature has prognostic value in patients from the Marisa cohort with high YAP1 levels. (A, B, C, D and E) Kaplan-Meier representation of DFS probability over time of Marisa patient's tumours classified by their YAP1 levels **(A)** themselves, previously categorised by *TP53* status as **(B)** WT or **(C)** mutated and **(D and E)** classified by YAP1 levels and then according to their cluster analysis of the 28up+8down-felSC signature.

Finally, we aimed to validate the results with data from our own cohort of patients. We have available samples from a set of 62-paired human gastrointestinal tumours collected at diagnosis (biopsy) and after DNA damaging-based neoadjuvant treatment (surgery). The vast majority of the patients were treated with CT, some of them in combination with targeted therapy, and only six patients with radiotherapy. We had also access to clinical data such as OS and DFS of the patients (see ANNEX 1). We first performed IHC-P analysis of ki67 to determine the proliferation status before and after treatment, to confirm the acquisition of the TQL phenotype in some of the patients. We were able to determine ki67 levels in 56-paired samples. Whereas some

tumours exhibited similar proliferation rates after treatment (type 1; 32.14% of the tumours), we identified a large subset of tumours that displayed reduced proliferation with no morphological evidences of senescence (type 2; 64.29%), such as enlarged nuclei or expression of the senescence marker p16, which are observed in scarce tumours at surgery (type 3; 3.57%) (FIGURE R51A). Classification of the patients by ki67 is indicated in ANNEX 1.

Next, we analysed the DFS probability in the ki67 subgroups of patients, taking into account that we did not have follow-up data from one patient of the 56 included in the ki67 classification. We failed to detect differences in patient prognosis when comparing type 1 and type 2 tumours that are readily observed in patient carrying type 3 tumours (no events of relapse in the follow-up period), although low number of patients did not allow us to significantly affirm that (FIGURE R51B). Thus, TQL phenotype is not particularly of good prognosis, which is in line with the fact that the felSC signature (acquired in TQL cells) in the cohorts of patients is a marker of poor prognosis.

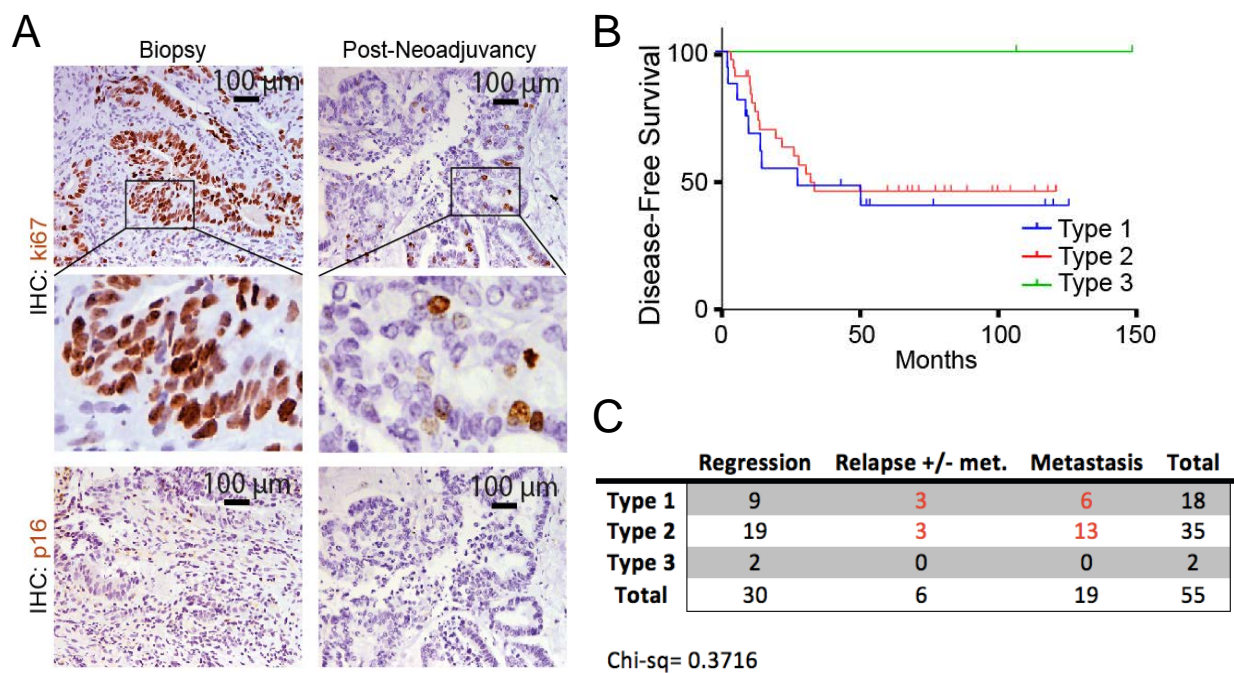


Figure R51. A subgroup of patients displays TQL phenotype acquisition after treatment. (A) IHC-P analysis of ki67 and p16 in representative type 2 CRC tumour samples (Annex 1 #17) from the same patient at diagnosis (biopsy) and after neoadjuvant therapy at the time of surgery (post-neoadjuvancy). **(B)** Kaplan-Meier curves for DFS analysis of patients stratified according to ki67-related tumour type. **(C)** Table showing ki67 classification and outcome of patients. Chi-square test performed with the patients in red.

In addition, as treated PDO5 cells demonstrated to have a slightly high capacity to metastasise (see FIGURES R27 and R28), we grouped patients that presented local relapse (with or without

metastasis), metastasis alone or regression of the tumour. However, when we tested if the number of patients (type 1 and 2) with local relapse and metastasis alone were distributed as expected, we found no significant differences (FIGURE R51C). These results show that TQL cells (type 2 tumours) retain their capacity to produce metastasis, similar to proliferating cells (type 1 tumours).

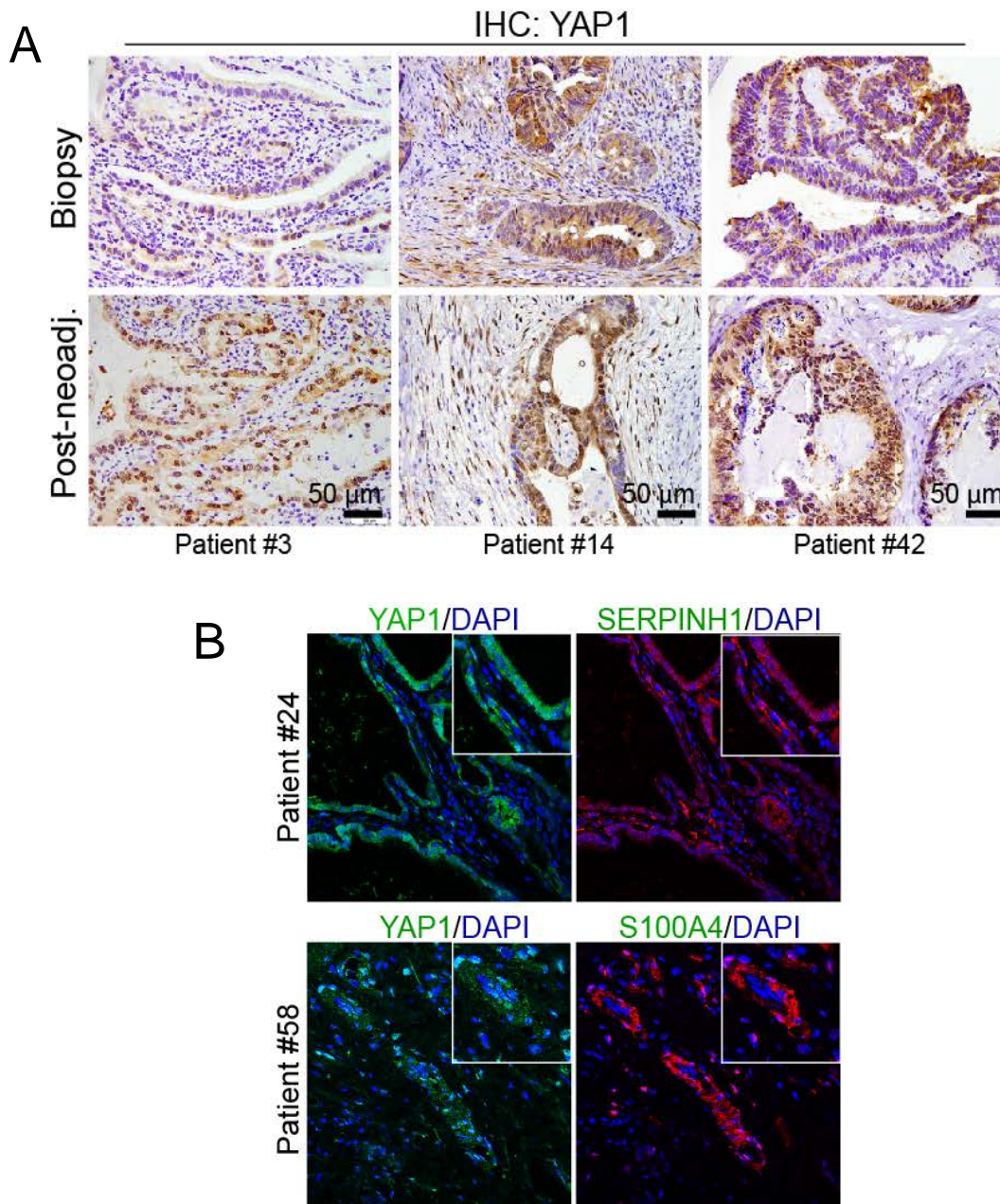


Figure R52. Patients present upregulation of nYAP1 after treatment together with foetal genes. (A) IHC-P analysis of YAP1 in representative type 1 (#14) and type 2 (#3, #42) CRC tumour samples from the same patient at diagnosis (biopsy) and after neoadjuvant therapy at the time of surgery (post-neoadjuvancy). (B) Representative images of YAP1 and the foetal genes SERPINH1 and S100A4 by IF in type 1 (#24) and type 2 (#58) CRC tumour samples (from post-neoadjuvancy).

We next studied YAP1 distribution in these samples. We detected nYAP1 in few epithelial cells of untreated tumours, which was massively increased in neoadjuvant treated tumours (FIGURE R52A and ANNEX 1), mimicking the increase in nYAP1 after CT treatment in PDOs. Presence of nYAP1 was associated with the expression of the fciSC markers S100A4 and SERPINH1, corroborating our hypothesis that the fciSC signature is dependent on YAP1 (FIGURE R52B). Importantly, the increase in nYAP1 found by IHC-P was independent of their proliferation status. Specifically, a 71.43% of the type 1 and a 66.67% of the type 2 patients exhibited at least a 30% of increase in nYAP1 levels after treatment. To note, we could not assess YAP1 levels in all the same samples used for ki67, so we only included 45 patients in this analysis. In this cohort, stratifying patients with increased nYAP1 after treatment (independent of ki67 subtype) showed a tendency of having poor prognosis ($p=0.333$) (FIGURE R53A). We obtained the same results when only analysing the nYAP1 levels after treatment (without considering initial nYAP1 levels) considering the mean value ± 0.6 standard deviations ($p=0.293$) (FIGURE R53B).

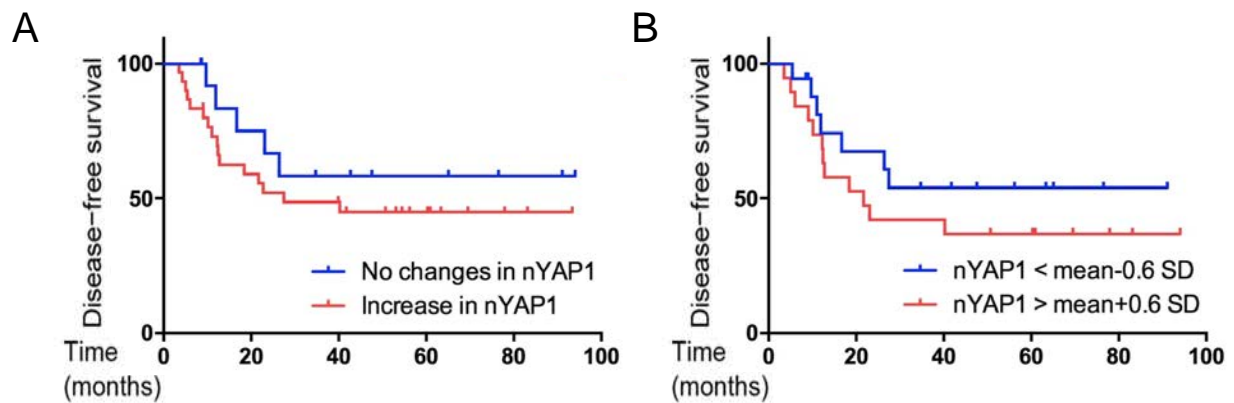


Figure R53. Treated patients of our cohort with higher levels of nYAP1 show a tendency to poor prognosis. (A and B) Kaplan-Meier representation of DFS probability over time of patients classified according to (A) an increase of at least 30% in nYAP1 levels after treatment (increase in nYAP1 $n=30$ and no changes in nYAP1 $n=14$) and (B) nYAP1 levels in treated patients (nYAP1 < mean-0.6 s.d. $n=18$ and nYAP1 > mean+0.6 s.d. $n=19$) of our cohort of patients.

Since the number of samples in the previous studied cohort was insufficient to adequately evaluate the clinical impact of nYAP1 accumulation, we performed IHC-P analysis of YAP1 in a tissue microarray (TMA) containing 194 different human CRC samples in triplicates with available clinical data (ANNEX 2). We determined the H-Score of nYAP1 (as intensity multiplied by percentage of positive tumour cells) in the triplicates and stratified CRC patients accordingly. We calculated the mean value for all the triplicates. Then, considering the mean value ± 0.2 standard deviations of the H-Score, we observed a trend towards poor prognosis in the group

with higher nYAP1 (DFS: $p=0.26$; HR=1.39) that increased when considering mean value ± 0.4 s.d. (DFS: $p=0.12$; HR=1.59). Importantly, nYAP1 levels reached statistical significance when considering the mean value ± 0.6 standard deviations (DFS: $p=0.039$; HR=1.98, OR: $p=0.040$; HR =2.26) (FIGURE R54A and B).

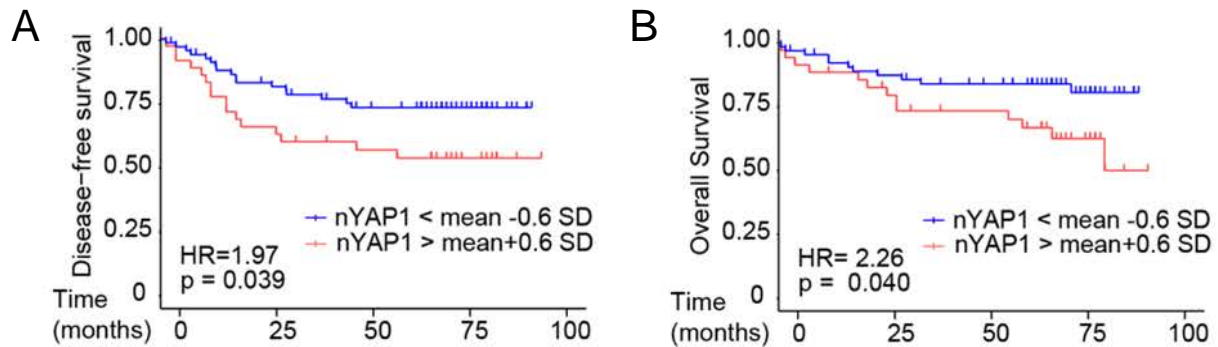


Figure R54. Treated patients of our TMA with higher levels of nYAP1 have poor prognosis. (A and B) Kaplan-Meier representation of (A) DFS and (B) OS probability over time of patients classified according to the H-Score of nYAP1 levels in our TMA of CRC patients (nYAP1<mean-0.6 s.d. n=72 and nYAP1>mean+0.6 s.d. n=39).

R3.6. TQL cells are more resistant to CT treatment, but combination of CT with YAP1 or BRAF inhibitors efficiently kill them

Resistance to treatment is one of the main causes of relapse and death in CRC patients. As the acquisition of the feISC signature is a poor prognosis factor, we wondered if TQL cells were more resistant to CT treatment than untreated cells. We effectively observed in dose-response curves of 5-FU+Iri. that *TP53* WT IC₂₀- and IC₃₀-treated PDO5 displayed more resistance to CT treatment than untreated PDO5. However, *TP53* mutant treated PDOs were not more resistant to subsequent CT (FIGURE R55A). To note, CT-treated PDO4, which did acquire resistance to CT, contained a hypomorphic *TP53* mutation that was permissive for CT-induced activation of several feISC genes (see FIGURE R36A).

Based on the observation that YAP1 inhibition by verteporfin prevented acquisition of the feISC phenotype and imposed cell death in PDO5 alone or in combination with CT (see FIGURE R49C), we anticipated that it could also be effective for reverting CT resistance in TQL cells. Therefore, we first treated PDO5 cells with IC₂₀ doses of CT for 72 h, promoting TQL phenotype acquisition, and after that with CT, verteporfin or combination of both for another 72 h. We found that the increased resistance of TQL cells to subsequent CT treatment was prevented by combination with verteporfin (FIGURE R56A), strongly suggesting that combination of CT plus

YAP1 inhibitors may represent a suitable therapeutic strategy for eradicating CRC tumours showing foetal ISC conversion.

A

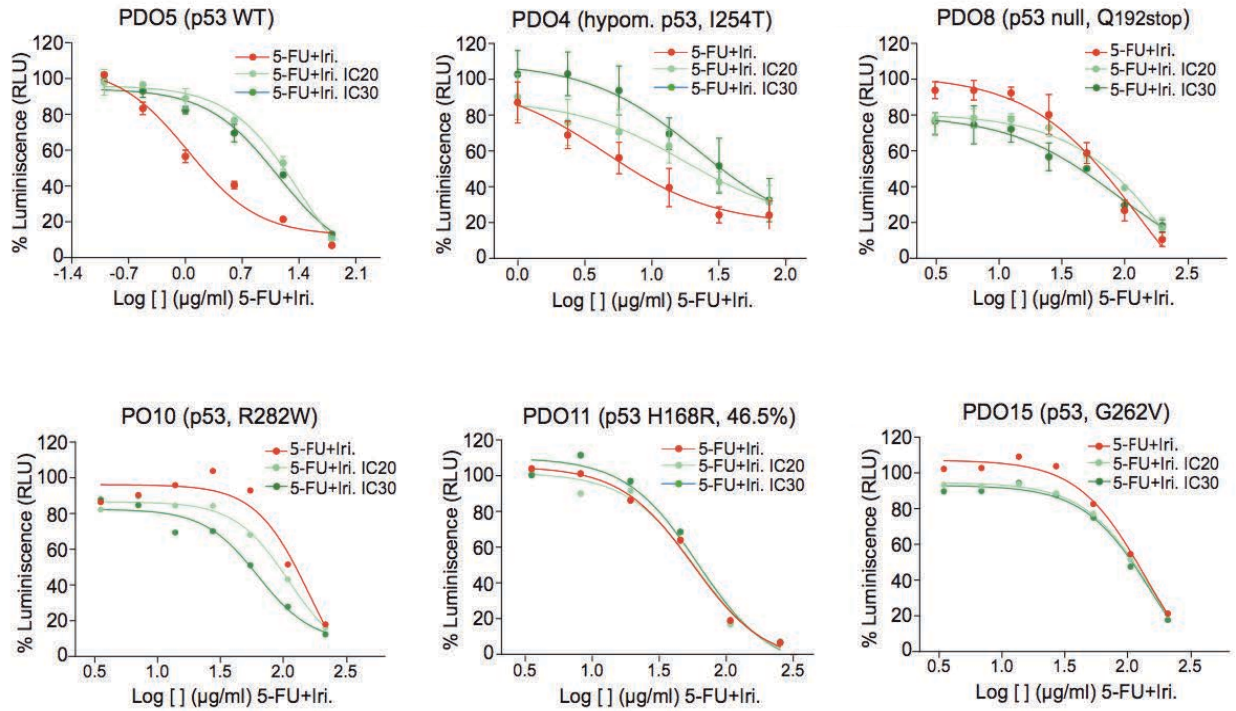


Figure R55. TQL cells display resistance to subsequent CT treatments. (A) Dose-response curves of untreated, IC₂₀- and IC₃₀-pretreated cells next treated for 72 h with 5-FU+Iri., of *TP53* WT and *TP53* mutated PDOs.

A

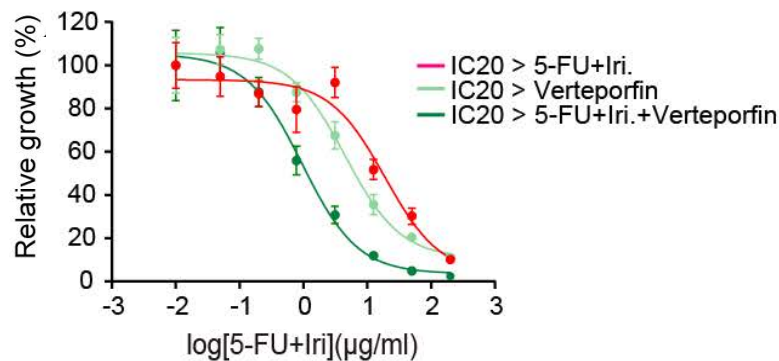


Figure R56. YAP1 inhibitor in combination with CT treatment efficiently kills TQL cells. (A) Dose-response curves of IC₂₀-pretreated PDO5 treated for 72 h with 5-FU+Iri., verteporfin alone or combinations of both.

We wanted to explore other possible drugs or combinations that efficiently eradicate TQL cells. In our lab, we had already demonstrated a synergistic effect of combining CT with BRAF inhibitors for eradication of PDOs, through inhibition of the NHEJ repair pathway³²⁸. Since this NHEJ repair is primarily used by quiescent cells (that includes the TQL cells) to repair DNA-damage, we studied the effectiveness of this combination treatment on TQL cells. We found that combination treatment *in vitro* was more successful than CT alone in promoting cell death of IC₂₀-pretreated PDO5 cells (FIGURE R57A).

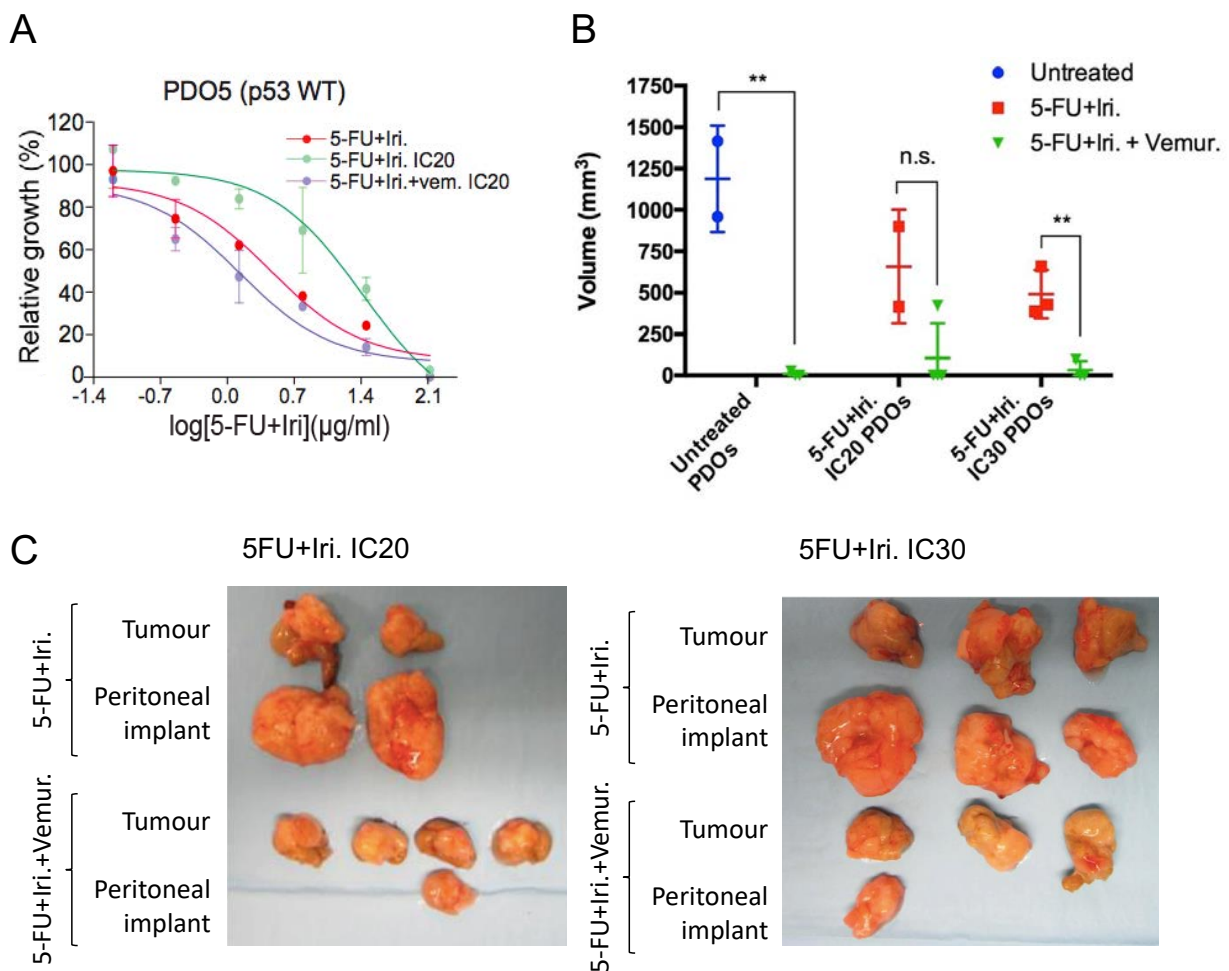


Figure R57. BRAF inhibitor in combination with CT treatment efficiently kills TQL cells. (A) Dose-response curves of untreated and IC₂₀-pretreated PDO5 treated for 72 h with 5-FU+Iri. or in combination with the BRAF inhibitor vemurafenib. **(B and C)** (B) Tumour volume of the peritoneal implants and **(C)** photographs of tumours and peritoneal implants grown after injection of untreated, IC₂₀- and IC₃₀-treated PDO5 cells for 72 h in the cecum of mice, and treated *in vivo* with 5-FU+Iri. or in combination with vemurafenib.

Moreover, *in vivo* treatment of mice injected with untreated, IC₂₀- or IC₃₀-pretreated PDO5 cells indicated that the combination treatment reduced the local tumour volume when compared with 5-FU+Iri. treatment (FIGURE R57C). The more exciting results were that the peritoneal implants, previously reported as growing more and in higher number in the IC₂₀ or IC₃₀ conditions (see FIGURE R28A and B), were almost completely abrogated with the combination treatment (FIGURE R57B and C). Although we cannot confirm that the combination treatment works better against TQL cells compared with tumour cells in general, since the untreated PDO5 control was lacking in these experiments, these results show an alternative therapeutic option for treating tumours carrying the 28up+8down-feISC signature, which we previously found to work in proliferating tumours ³²⁸.

DISCUSSION

D1. PDOs AS A TOOL FOR CANCER RESEARCH

During the progress of this thesis, we have established a **CRC PDOs living biobank**, derived from human CRC tumours displaying different mutations and histological characteristics. Analyses of the PDOs have demonstrated that these cells present mostly an undifferentiated state with a variable proportion of proliferative cells, although we have only analysed few differentiation markers (lysozyme as a marker for Paneth cells and Alcian Blue staining to identify Goblet cells). Since PDOs derive from tumour colonic tissue, we did not expect to observe Paneth cells in these cultures. However, enterocytes and secretory cells could be present depending on the differentiated status of the original tumour. Thus, deeper analysis of differentiation markers or specific analysis of RNA-seq data could be done to extract conclusions². Generation of organoids from normal tissue adjacent to the tumour would be also useful for further comparisons. In addition, since maintenance of the undifferentiated state of PDOs is favoured by 3D culture conditions, specifically designed to preserve stem cells in an undifferentiated and multipotent phenotype¹⁴⁶, analysis of PDOs under the differentiation conditions such as those described by Jung and collaborators¹⁴⁶ or by adding FCS in the culture media¹⁰³ could also be tested.

As previously described by other groups^{138-142,162}, we found that PDOs highly **resemble the original tumours** in terms of mutational profile, with some differences in the percent of mutated cells. Specifically, PDOs carry a higher percentage of cells with the mutations present in the original tumours and some additional mutations that were the likely result of positive selection of rare mutations of the tumour. In one of the PDOs we detected loss of heterogeneity of the *PDGFRA* allele. PDOs also displayed different degrees of drug resistance, which make them a powerful tool for cancer research. Notably, recent publications demonstrated a higher correlation between therapy response of patients' metastases and their corresponding organoids^{139,163}. Thus, we have used PDOs as a model for our research on the effects of sublethal doses of CT.

D2. REVERSIBLE GROWTH ARREST IN WT *TP53* TQL CELLS

CT is the main therapy used for treatment of patients with advanced and metastatic CRC. However, in a percentage of cases tumour cells that escape from death imposed by therapeutic drugs (by efficient drug clearance, effective DNA repair or due to reduced accessibility of the

drugs to specific tumour areas) can acquire a dormant phenotype that provides superior resistance to subsequent DNA damaging-based treatment. In the present study we have shown that **sublethal doses of CT impose a non-senescent and non-proliferating phenotype to cancer cells** (both human CRC PDOs and tumours), in the absence of persistent DNA damage.

Whereas cellular quiescence may be defined as a non-dividing G_0 state from which cells may escape to re-enter the cell cycle in response to physiological stimuli, cellular senescence is traditionally viewed as a permanent form of cell cycle arrest²⁴⁶. This point of view has changed with the demonstration that senescence may be a reversible state depending on the alternative use of p53/p21 (reversible) or p16 (irreversible) and that this senescence-reversibility increases tumour stemness^{208,239,250}. Our observations unequivocally revealed that sublethal CT-treated cells can acquire a quiescent-like state in the absence of a robust senescent phenotype, which is driven by p53 and p21 but not by p16 signalling (only present when treating with higher doses of CT). Most importantly, we demonstrated that this phenotypic transformation imposed by IC₂₀ and IC₃₀ CT treatment **specifically occurs in TP53 wildtype cells**. In contrast, TP53 mutated PDOs exhibited increased apoptosis and accumulation of DNA damage that was not repaired, linked to abrogation of their TIC activity *in vitro*. These findings are in line with the p53/p21 function on the cell cycle regulation and DDR upon DNA damage^{202,204,205}.

Dependency on p53 signalling may also indicate that **the TQL phenotype is reversible**²³⁹. In this sense, we have consistently shown that TQL cancer cells efficiently escape from dormancy following *in vivo* transplantation. In fact, the ortho-xenograft experiments demonstrated a superior capacity of treated-PDOs to escape from the site of implantation and to grow as intraperitoneal implants. This is in agreement with previously studies showing that dormant cell populations of primary human CRC cells retain tumour propagation potential, and specific subpopulations of cancer cells entering a reversible quiescent state exhibit increased tumourigenic potential after CT^{189,223}. Escape from dormancy might be driven by multiple stimuli, including increased Notch signalling²²¹ and MSK1 inactivation²²⁴. We found that tumours formed by treated PDOs accumulate active Notch in the proliferating areas, as shown by ICN1 and Hes1 immunofluorescence. These findings suggest that stimuli from the tumour microenvironment in mice facilitate escape from dormancy, which might be comparable to the mechanisms leading to metastasis and tumour relapse in patients. Because of the relevance of this observation, more experiments should be performed to uncover the elements involved in the re-entry of quiescent cancer cells into cell cycle.

We have here provided proof-of-concept that CT not only eradicates or impose an irreversible senescent state to tumour cells but it can also induce a TQL phenotype with not-yet defined

effects on patients. A number of publications have already indicated that a slow-proliferating state is the main source of DTP cells, but most of them considered this state as an intrinsic characteristic of a specific tumour population rather than a treatment-induced quiescence^{191–194,209,210}. Moreover, since treatment-induced senescence was found to be reversible, these senescent cells are also candidate DTP cells responsible of tumour relapse²⁰⁸. We have consistently shown that the TQL phenotype is a p53-dependent non-senescent state. However, considering that the reversible senescent state and the non-senescent low-proliferating state are both driven by p53 signalling, and they are not completely well differentiated, more research is needed to understand the particularities of both types of proliferation arrest and their functional consequences. Some recent studies uncovering the capacity of tumour cells to switch into a state of growth arrest upon treatment^{197,223,337,338} **have not considered the importance of p53 signalling in the acquisition of the quiescent phenotype**, in contrast to the results obtained by us in the present study.

Whereas our data is all based on sublethal doses of CT, which do not produce remarkable cell death or sustained DNA damage, we speculate that cells that persist after higher doses of CT (without entering into senescence or apoptosis) and are able to repair their DNA might also acquire comparable TQL phenotype. From our data, there is not a clear barrier in terms of doses that define when a cell will acquire the TQL phenotype or it will adopt an irreversible growth arrest, although it is clear that increasing CT dosage will facilitate the accumulation of irreversible damage in cells. Intrinsic characteristics of individual cell including specific mutations or adaptations imposed by the microenvironment might produce different responses in patients.

In addition, our research has been performed by treating PDOs with 5-FU+Iri. and other DNA-damaging agents, such as OX or radiotherapy, that are also used in the clinical practice can impose specific effects⁸⁹. It is of note that we have used the combination of 5-FU+Iri. in all our experiments, which opens the possibility that the TQL phenotype is driven only by one of the two compounds, since they produce DNA damage by different mechanisms: 5-FU inhibits the thymidylate synthetase activity and Iri. inhibits topoisomerase I activity¹⁸⁷. We will investigate the effects of treating PDOs with **single agents** in the future. In this particular, a recent publication indicates that only Iri. induces a quiescent-like state in xenografts tumours, whereas 5-FU and OX (radiotherapy was not tested) did not reduce tumour growth³³⁸, however this results could be tumour-dependent. Our preliminary results indicate that radiotherapy also induces the TQL phenotype, which is of clinical relevance and will be further investigated. Together these data suggest that the TQL phenotype is acquired in response to specific DNA damage agents, thus the mechanisms leading to TQL should be further investigated.

D3. TUMOURAL FOETAL CONVERSION UPON DNA DAMAGE

Transcriptomic analysis revealed that p53 signalling, but also TNF α , IFN γ and EMT associated signalling were upregulated after sublethal CT treatment. In particular, IFN γ signalling has been associated with the conversion of adult into foetal stem cells ⁷⁷. The association of the TQL phenotype with the **shift from an adult to a foetal signature**, as corroborated by GSEA and RT-qPCR analysis, indicated that more profound changes than a simply growth arrest were underlying the response to sublethal CT doses. Since foetal ISC conversion had already been identified as part of the process of tissue regeneration after helminths infection or in the Dextran Sulfate Sodium colitis model ^{77,79}, our results reinforce the concept that tumour response to DNA damage (normally accumulated due to mutations in tumour suppressor and DNA repair genes) is partially mimicking the normal tissue regeneration process. In addition, we have demonstrated the YAP1 dependence of the foetal ISC conversion found in TQL cells, which is in line with the results showing the essential role of YAP1 in ISCs homeostasis and intestinal regeneration ^{78,260-262,266,267}.

The finding that the cancer cells carrying dysfunctional p53 do not acquire the TQL phenotype but display massive amounts of DNA damage may explain the results obtained by Cheung and collaborators indicating that YAP1 activation acts as tumour suppressor in *TP53* depleted tumours ²⁸⁶. Multiple crosstalk between YAP1 and p53 have been already described, showing that YAP1 activation is regulated by p53 ^{280,281,284}, even though we have not been able to demonstrate a direct regulation of YAP1 pathway and the foetal gene signature by p53 in our CHIP-seq data. On the other hand, hyperactivation of YAP1 signalling has consistently been demonstrated as pro-tumorigenic having a role in cancer initiation and progression ^{262,268,277,279}, and has been proposed as a target for cancer treatment ²⁷⁸ in contrast with the results obtained by Cheung and collaborators. In this context, our results are of particular relevance since they clarify the functional **contribution of YAP1 as metastasis driver** in CRC dependent on the p53 status ²⁷⁸.

We propose that functional p53 through p21 upregulation imposes a stop in proliferation in response to CT, associated to a YAP1-dependent foetal conversion, which allow cells to repair the DNA and survive. In contrast, *TP53* mutant cells fail to efficiently repair their DNA thus accumulating irreparable damage leading to apoptotic death or irreversible senescence (FIGURE D1). This cellular response represents, in fact, a double-edge sword whose outcome varies depending on the *TP53* status and the heterogeneity of cancer cells. In this sense, it was demonstrated that 5-FU treatment induced cell dormancy and EMT in lung cancer cells,

associated with p53 accumulation³³⁹. Further experiments genetically deleting YAP1 in *TP53* WT cells, to corroborate the effects observed after verteporfin treatment are required to definitively demonstrate the complete dependence of the fEISC signature acquisition on YAP1.

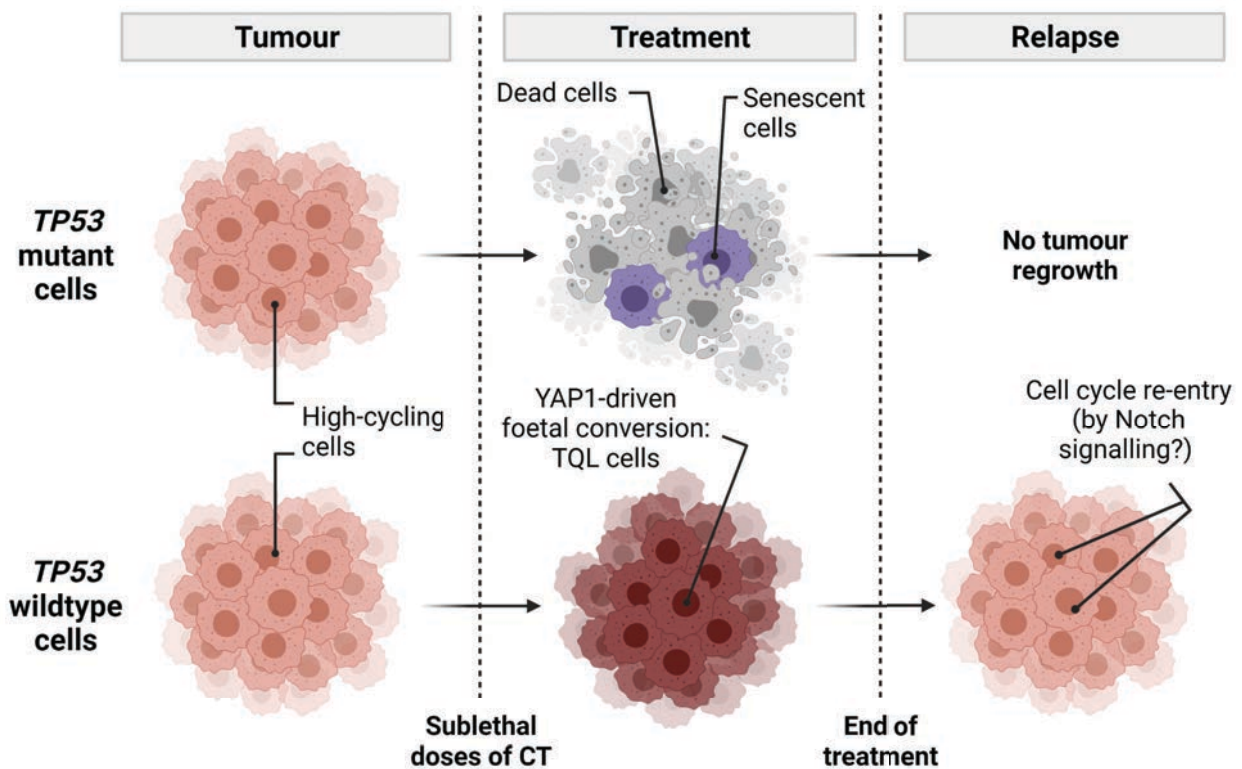


Figure D1. Working model. *TP53* mutant tumour cells are not able to stop cell cycle and acquire a quiescent-like phenotype upon sublethal CT treatment, producing an accumulation of DNA damage that cannot be repaired, which finally leads to cell apoptosis. In contrast, sublethal doses of CT induce a TQL phenotype associated to a YAP1-driven foetal conversion in *TP53* WT tumour cells. TQL cells can be responsible of tumour relapse in patients after cell cycle re-entry, which might be driven by Notch signalling. Created with BioRender.com.

Two recent publications have pointed out that cell dormancy is acquired by tumours to survive CT and that this phenotype resembles the **embryonic diapause state**^{337,338}, which is a reversible period of suspended development in the embryo to overcome unfavourable conditions^{340,341}. In particular, Rehman and colleagues showed that CRC cells are able to acquire a quiescent-like state similar to the one we have here described, maintaining their clonal complexity (by using a barcode library), with a dependency on autophagy associated to reduced mTOR activity³³⁸, as happens in blastocysts³⁴². In the Dhimolea et al. data, very similar results are shown, but they point out to *MYC* inactivation as the main mechanism by

DTP cells to adopt the diapause state³³⁷. However, posterior comparison of our feISC signature with their diapause-like signature revealed low similarities (not shown). Since Dhimolea et al. treat cells with a prolonged exposure to CT and Rehman et al. use maximum tolerated doses, cells might display distinct phenotypes than using sublethal doses for a short exposure as we did in our study. Moreover, while the TQL phenotype is p53 dependent, cells used in Dhimolea et al. were *TP53* mutated and there is no information about the *TP53* status in the other study. Thus, the exact mechanisms inducing TQL or DTP states have to be further explored.

D4. CLINICAL APPLICATIONS OF THE feISC SIGNATURE

Based on the foetal genes that are differentially expressed in CT-treated PDOs, we have here uncovered a restricted **28up+8down feISC signature** with coordinate expression in human CRC tumours that predicts poor prognosis in patients. These results refine the concept that the adult ISC signature, including *Lgr5*³¹⁷, is linked to higher tumour malignancy and in agreement with the recent demonstration that *Lgr5* and other adult ISC markers are temporarily lost from cells seeding metastases, and subsequently recovered (due to cellular plasticity) to allow metastasis establishment¹⁷⁵. Importantly, most data indicating the requirement for adult *Lgr5*⁺ ISCs in metastasis seeding have been obtained on p53-deficient tumour cells^{286,318}. Interestingly, a recent publication from Dr. Batlle's laboratory demonstrated that *Lgr5*⁺ cells differently contribute to cancer initiation in PDOs carrying WT or mutant *TP53* (higher in mutant *TP53*). These results open the possibility that dependence on adult *Lgr5*⁺ ISCs in cancer is linked to *TP53* status, which should be further investigated¹⁰⁵.

The RNA-seq data presented in this study, and used for foetal conversion determination, was obtained from a single PDO (PDO5), but initially validated in other *TP53* WT PDOs by RT-qPCR. To further corroborate foetal conversion in other CT treated-PDOs, we have now performed another RNA-seq from PDO66 (*TP53* WT). Although we currently have only preliminary data (and for this reason, we have not included it in this thesis), the same upregulation of foetal genes and other related pathways upon treatment has been observed. On the other hand, it is worth to mention that not all genes from the feISC signature are equally upregulated in all *TP53* WT PDOs, demonstrating that the signature, rather than expression of single genes, must be used to determine the presence of foetal conversion in cancer. Moreover, in *TP53* mutant PDOs few genes show an upregulated expression upon CT treatment, although increased apoptosis and abrogation of the TIC activity indicates that they are no longer viable after treatment. These results were also observed analysing protein levels of selected foetal

genes in CRC cell lines. Thus, we cannot conclude that the feISC signature is totally dependent on functional p53, but p53 deficient tumours cells, in case of being foetal-converted, accumulate massive amount of DNA damage leading to cell death.

We have used three different data sets from CANCEERTOOL to explore the prognostic value of the feISC signature. Although the feISC signature was firstly obtained from the Marissa data set, we have shown the same potential of the feISC signature to predict poor prognosis in all three cohorts, demonstrating the generality of the signature. Since we did not have the same type of data from all cohorts, we have not been able to perform all the analysis in the three data sets, as discussed in the results section. In addition, including additional selection criteria other than the feISC signature (like p53 status or tumour stages) reduces the number of patients in the analyses, thus refusing the statistical significance of the results.

From a clinical perspective, uncovering genetic signatures that are predictive of recurrence in a group of patients with uncertain projection (stages II and III) represents a powerful tool for diagnosis refinement. In this direction, **we have currently submitted a patent request** for protecting the feISC signature as a diagnosis tool for patient stratification. Even though IHC analyses are the most used technique in the clinics, quantitative analysis of feISC protein levels is limited by the quality of the different antibodies and the non-quantitative nature of IHC data. Thus, we are now setting up the protocols **to design a simple RT-qPCR-based diagnosis kit** (that we term **TUpDo-test**) easy to apply in clinics, in order to classify tumours inside or outside this signature. With this objective, we will extract RNA from retrospective paraffin-embedded stage II, III and IV CRC tumour samples and perform RT-qPCR analysis of genes in our feISC signature. We aim to identify genes inside the 28up+8down signature that better discriminate patients with good/bad prognosis, Next, we will establish a ratio between genes upregulated and genes downregulated in our feISC signature, as previously described^{294,295}, that could facilitate categorising primary human tumours as TUpDo⁺ (displaying the feISC signature) or TUpDo⁻ (FIGURE D2).

To recognise patients with higher probability of recurrence among those of uncertain prognosis (stages II-III) by the analysis of a reduced feISC signature can be clinically relevant. Implementation of this kit should allow a diagnosis/prognosis refinement of this subgroup of patients, which could be translated in the clinical practice into closer follow-up and more aggressive therapeutic strategies (when possible). In addition, we aim to experimentally test the effectiveness of pathway-based therapeutic strategies on human TUpDo⁺ tumours. Since we have demonstrated that PDO cells carrying this signature are resistant to CT (5-FU+Iri.) but highly sensitive to combination treatments of CT plus the YAP1 inhibitor verteporfin, characterisation of CRC patients based on the TUpDo-test will allow not only a better diagnosis

but also the stratification of patients that will benefit from YAP1-inhibitor based therapy, which will be particularly relevant when including patients in clinical trials. However, we have not validated yet the prognosis value of the signature (or simplified versions of the signature) in our own sample collection and whether the anticancer efficacy of CT plus verteporfin (or other YAP1 inhibitors) generally applies to TUpDo⁺ PDOs or CRC patients. Once validated, our findings will open the avenue for further implementation of alternative methodologies to identify foetal conversion of tumours and druggable targets to improve therapeutic protocols to combat resistant cancers.

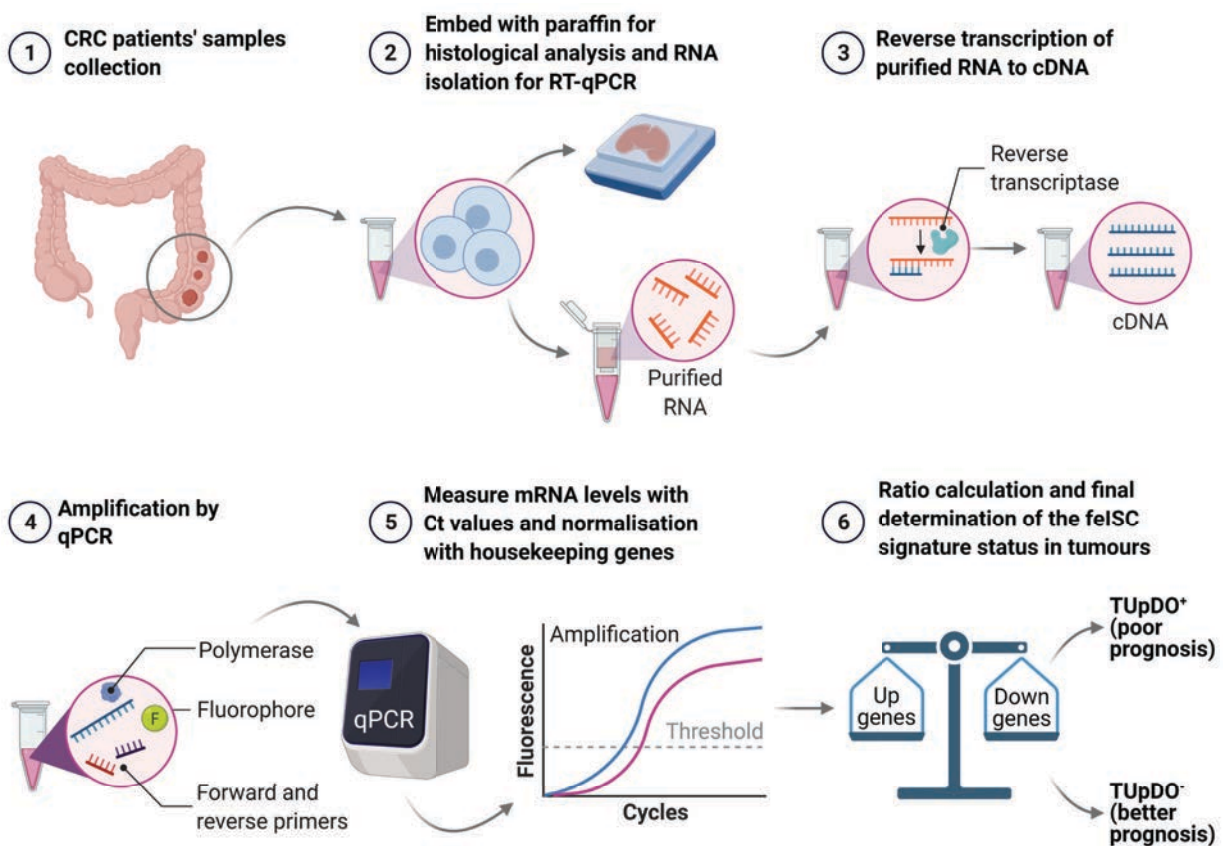


Figure D2. TUpDO test: a RT-qPCR based diagnosis kit. Samples from CRC patients are collected and RNA isolated. Then, cDNA is synthesised, amplified by RT-qPCR and mRNA levels measured and normalised with housekeeping genes. The final ratio of gene expression is calculated by the mean of selected upregulated felSC genes divided by the mean of selected downregulated felSC genes. Patients are classified in TUpDo⁺ or TUpDo⁻ depending on their ratio value. Created with BioRender.com.

D5. CONTRIBUTION OF TUMOUR STROMA TO feISC CONVERSION

Remarkably, we have shown that the sublethal CT-induced **feISC signature is already present in a subset of untreated tumours** at diagnosis in several CRC cohorts. It is tempting to speculate that extrinsic factors or non-cancer cells present in the tumour, such as inflammatory cells, may induce the upstream regulators of this signature (i.e., TGF β signalling) thus leading to the acquisition of TQL traits in the absence of (or previous to) CT treatment. In agreement with this idea, tumours carrying the 28up+8down-feISC signature are primarily included in the poor prognosis CMS4 (74% of the patients) CRC subtype identified by Guinney and collaborators, characterised by stromal infiltration, angiogenesis and **TGF β signalling**⁹⁰. Moreover, we have identified the EMT and TGF β signalling pathways as upregulated in the treated PDOs, both tightly associated with metastasis, which is increased in TQL cells²⁷⁵. Specifically, TGF β signalling can be driven by the tumour microenvironment, which facilitates immune evasion and metastasis initiation^{185,303}. Thus, we speculate that TGF β or additional cytokines derived from the tumour stroma may impose a YAP1-dependent feISC signature, which is in agreement with the previous demonstration that TGF β promotes YAP1 signalling by facilitating the degradation of the negative regulator of the pathway RASSF1A²⁷³. TGF β also promotes YAP1 activation through inducing Zyxin, which stabilises Lats2/Siah2 interaction²⁷⁴. These published data indicates a direct regulation of YAP1 signalling by TGF β stimuli.

To establish the possible contribution of tumour stroma to feISC conversion, further experiments, including the characterisation of stromal populations specifically present in foetal-type tumours and functional validation of cells and factors capable to induce foetal conversion to tumour cells are clearly needed. To accomplish this objective, we will select tumours with high stromal infiltration and perform scRNA-seq analysis of the different cell populations. Analysis of data will allow identifying tumour cells showing foetal conversion and determine the presence of specific non-tumoural populations associated to foetal-type tumours. Then, we will experimentally validate the capacity of these specific populations or associated factors to induce foetal conversion in co-culture or conditioned media assays.

D6. IKK α IN TQL CELLS

DNA damage in quiescent cells is mainly repaired by the NHEJ pathway and, therefore, inhibiting this pathway in treated TQL cells might be a suitable strategy to specifically eliminate them. Our group has recently demonstrated the role in the NHEJ pathway of a phosphorylated form of **IKK α** ³²⁸, which is a constituent of the NF- κ B pathway that is involved in tumour initiation, progression and metastasis of various cancer subtypes^{343–347}. Since this form of IKK α acts downstream of BRAF, the **blockage of NHEJ DNA repair** by using BRAF inhibitors in combination with DNA-damaging agents demonstrated to reduce tumour growth more than single agent treatments³²⁸. In TQL cells, we have shown that this combination treatment reduce their survival in comparison to CT treatment alone. However, the use of BRAF inhibitors in CRC patients have produced largely negative results³⁴⁸, but might be useful in treated tumours displaying a TQL/foetal phenotype. On the other hand, IKK α is also involved in **cell cycle regulation upon DNA damage**, by inducing a downregulation of cyclin D1 expression that leads to cell growth arrest³⁴⁹ and the expression of pro-tumourigenic genes³⁵⁰. Hence, we are currently investigating the role of IKK α in regulating DNA repair and the entrance to quiescence after sublethal CT treatment.

CONCLUSIONS

CONCLUSIONS

PART I: Establishment and characterisation of a CRC PDOs biobank

1. CRC PDOs of our biobank resemble the original tumours and display different drug sensitivity, being a powerful tool for cancer research.

PART II: Characterisation of low-dose chemotherapy treatment effects in CRC PDOs

1. Low-dose treated-PDOs acquire a non-senescent quiescent-like state in the absence of persistent DNA-damage (TQL phenotype), dependent on functional p53.
2. *TP53* mutant treated-PDOs continue proliferating, leading to an accumulation of irreparable damage and apoptotic death.
3. The TQL phenotype is associated with an adult to foetal intestinal stem cell conversion (feISC signature).
4. TQL cells displaying the feISC signature retain their tumour-initiating capacity, which could be associated with increased Notch activation.

PART III: Definition of a feISC signature with prognostic value

1. The feISC signature shows a coordinate expression in human untreated CRC tumours.
2. *TP53* mutant cells do not acquire the TQL phenotype and ultimately enter apoptosis, although partially acquiring the feISC signature.
3. Tumours displaying the feISC signature are mainly classified in the mesenchymal subtype.
4. The feISC signature is predictive of reduced disease-free survival, especially in *TP53* WT CRC tumours.
5. Acquisition of the feISC signature is dependent on YAP1 activation.
6. TQL cells are more resistant to CT treatment, but combination of CT with YAP1 or BRAF inhibitors efficiently eliminate TQL cells.

BIBLIOGRAPHY

BIBLIOGRAPHY

1. Spit, M., Koo, B. K. & Maurice, M. M. Tales from the crypt: Intestinal niche signals in tissue renewal, plasticity and cancer. *Open Biol.* **8**, (2018).
2. Humphries, A. & Wright, N. A. Colonic crypt organization and tumorigenesis. *Nat. Rev. Cancer* **8**, 415–424 (2008).
3. VanDussen, K. L. *et al.* Notch signaling modulates proliferation and differentiation of intestinal crypt base columnar stem cells. *Development* **139**, 488–497 (2012).
4. Kim, T. H. *et al.* Broadly permissive intestinal chromatin underlies lateral inhibition and cell plasticity. *Nature* **506**, 511–515 (2014).
5. Gerbe, F. & Jay, P. Intestinal tuft cells: Epithelial sentinels linking luminal cues to the immune system. *Mucosal Immunol.* **9**, 1353–1359 (2016).
6. Grün, D. *et al.* Single-cell messenger RNA sequencing reveals rare intestinal cell types. *Nature* **525**, 251–255 (2015).
7. Kim, Y. S. & Ho, S. B. Intestinal goblet cells and mucins in health and disease: Recent insights and progress. *Curr. Gastroenterol. Rep.* **12**, 319–330 (2010).
8. Allaire, J. M. *et al.* Frontline defenders: Goblet cell mediators dictate host-microbe interactions in the intestinal tract during health and disease. *Am. J. Physiol. - Gastrointest. Liver Physiol.* **314**, G360–G377 (2018).
9. Ma, J., Rubin, B. K. & Voynow, J. A. Mucins, Mucus, and Goblet Cells. *Chest* **154**, 169–176 (2018).
10. Birchenough, G. M. H., Johansson, M. E. V., Gustafsson, J. K., Bergström, J. H. & Hansson, G. C. New developments in goblet cell mucus secretion and function. *Mucosal Immunology* vol. 8 712–719 (2015).
11. Plovier, H. & Cani, P. D. Enteroendocrine Cells: Metabolic Relays between Microbes and Their Host. *Endocr. Dev.* **32**, 139–164 (2017).
12. Worthington, J. J., Reimann, F. & Gribble, F. M. Enteroendocrine cells-sensory sentinels of the intestinal environment and orchestrators of mucosal immunity. *Mucosal Immunol.* **11**, 3–20 (2018).
13. Beumer, J. *et al.* Enteroendocrine cells switch hormone expression along the crypt-to-villus BMP signalling gradient. *Nat. Cell Biol.* **20**, 909–916 (2018).
14. Beumer, J. *et al.* High-Resolution mRNA and Secretome Atlas of Human Enteroendocrine Cells.

Cell **181**, 1291–1306.e19 (2020).

15. Latorre, R., Sternini, C., De Giorgio, R. & Greenwood-Van Meerveld, B. Enteroendocrine cells: A review of their role in brain-gut communication. *Neurogastroenterol. Motil.* **28**, 620–630 (2016).
16. Gassler, N. Paneth cells in intestinal physiology and pathophysiology. *World J. Gastrointest. Pathophysiol.* **8**, 150–160 (2017).
17. Sato, T. *et al.* Long-term expansion of epithelial organoids from human colon, adenoma, adenocarcinoma, and Barrett's epithelium. *Gastroenterology* **141**, 1762–1772 (2011).
18. Ramasundara, M., Leach, S. T., Lemberg, D. A. & Day, A. S. Defensins and inflammation: The role of defensins in inflammatory bowel disease. *J. Gastroenterol. Hepatol.* **24**, 202–208 (2009).
19. Holly, M. K. & Smith, J. G. Paneth cells during viral infection and pathogenesis. *Viruses* **10**, 17–22 (2018).
20. Formeister, E. J. *et al.* Distinct SOX9 levels differentially mark stem/progenitor populations and enteroendocrine cells of the small intestine epithelium. *Am. J. Physiol. - Gastrointest. Liver Physiol.* **296**, 1108–1118 (2009).
21. Harris, N. The enigmatic tuft cell in immunity. *Science (80-.)*. **351**, 1264–1265 (2016).
22. Howitt, M. R. *et al.* Tuft cells, taste-chemosensory cells, orchestrate parasite type 2 immunity in the gut. *Science (80-.)*. **351**, 1329–1333 (2016).
23. Gerbe, F., Legraverend, C. & Jay, P. The intestinal epithelium tuft cells: Specification and function. *Cell. Mol. Life Sci.* **69**, 2907–2917 (2012).
24. Gerbe, F. *et al.* Intestinal epithelial tuft cells initiate type 2 mucosal immunity to helminth parasites. *Nature* **529**, 226–230 (2016).
25. Shroyer, N. F., Wallis, D., Venken, K. J. T., Bellen, H. J. & Zoghbi, H. Y. Gfi1 functions downstream of Math1 to control intestinal secretory cell subtype allocation and differentiation. *Genes Dev.* **19**, 2412–2417 (2005).
26. McCauley, H. A. & Guasch, G. Three cheers for the goblet cell: Maintaining homeostasis in mucosal epithelia. *Trends Mol. Med.* **21**, 492–503 (2015).
27. Gerbe, F. *et al.* Distinct ATOH1 and Neurog3 requirements define tuft cells as a new secretory cell type in the intestinal epithelium. *J. Cell Biol.* **192**, 767–780 (2011).
28. Sasaki, N. *et al.* Reg4⁺ deep crypt secretory cells function as epithelial niche for Lgr5⁺ stem cells in colon. *Proc. Natl. Acad. Sci. U. S. A.* **113**, E5399–E5407 (2016).
29. Marshman, E., Booth, C. & Potten, C. S. The intestinal epithelial stem cell. *BioEssays* **24**, 91–98

- (2002).
30. Barker, N., Van Oudenaarden, A. & Clevers, H. Identifying the stem cell of the intestinal crypt: Strategies and pitfalls. *Cell Stem Cell* **11**, 452–460 (2012).
 31. Clevers, H. The intestinal crypt, a prototype stem cell compartment. *Cell* **154**, 274 (2013).
 32. Snippert, H. J. *et al.* Intestinal crypt homeostasis results from neutral competition between symmetrically dividing Lgr5 stem cells. *Cell* **143**, 134–144 (2010).
 33. Lopez-Garcia, C., Klein, A. M., Simons, B. D. & Winton, D. J. Intestinal stem cell replacement follows a pattern of neutral drift. *Science (80-.)*. **330**, 822–825 (2010).
 34. Bu, P. *et al.* A miR-34a-Numb Feedforward Loop Triggered by Inflammation Regulates Asymmetric Stem Cell Division in Intestine and Colon Cancer. *Cell Stem Cell* **18**, 189–202 (2016).
 35. Barker, N. Adult intestinal stem cells: Critical drivers of epithelial homeostasis and regeneration. *Nat. Rev. Mol. Cell Biol.* **15**, 19–33 (2014).
 36. Yousefi, M., Li, L. & Lengner, C. J. Hierarchy and Plasticity in the Intestinal Stem Cell Compartment. *Trends Cell Biol.* **27**, 753–764 (2017).
 37. Gehart, H. & Clevers, H. Tales from the crypt: new insights into intestinal stem cells. *Nat. Rev. Gastroenterol. Hepatol.* **16**, 19–34 (2019).
 38. De Lau, W. *et al.* Lgr5 homologues associate with Wnt receptors and mediate R-spondin signalling. *Nature* **476**, 293–297 (2011).
 39. Barker, N. *et al.* Identification of stem cells in small intestine and colon by marker gene Lgr5. *Nature* **449**, 1003–1007 (2007).
 40. Cui, S. & Chang, P. Y. Current understanding concerning intestinal stem cells. *World J. Gastroenterol.* **22**, 7099–7110 (2016).
 41. van der Flier, L. G. *et al.* Transcription Factor Achaete Scute-Like 2 Controls Intestinal Stem Cell Fate. *Cell* **136**, 903–912 (2009).
 42. Barriga, F. M. *et al.* Mex3a Marks a Slowly Dividing Subpopulation of Lgr5+ Intestinal Stem Cells. *Cell Stem Cell* **20**, 801–816.e7 (2017).
 43. Tian, H. *et al.* A reserve stem cell population in small intestine renders Lgr5-positive cells dispensable. *Nature* **478**, 255–259 (2011).
 44. Richmond, C. A., Shah, M. S., Carlone, D. L. & Breault, D. T. An enduring role for quiescent stem cells. *Dev. Dyn.* **245**, 718–726 (2016).
 45. Metcalfe, C., Kljavin, N. M., Ybarra, R. & De Sauvage, F. J. Lgr5+ stem cells are indispensable for

radiation-induced intestinal regeneration. *Cell Stem Cell* **14**, 149–159 (2014).

46. Yan, K. S. *et al.* The intestinal stem cell markers Bmi1 and Lgr5 identify two functionally distinct populations. *Proc. Natl. Acad. Sci. U. S. A.* **109**, 466–471 (2012).
47. Sangiorgi, E. & Capecchi, M. R. Bmi1 is expressed in vivo in intestinal stem cells. *Nat. Genet.* **40**, 915–920 (2008).
48. Suh, H. N. *et al.* Quiescence Exit of Tert⁺ Stem Cells by Wnt/ β -Catenin Is Indispensable for Intestinal Regeneration. *Cell Rep.* **21**, 2571–2584 (2017).
49. Takeda, N. *et al.* Interconversion between intestinal stem cell populations in distinct niches. *Science (80-.).* **334**, 1420–1424 (2011).
50. Wong, V. W. Y. *et al.* Lrig1 controls intestinal stem-cell homeostasis by negative regulation of ErbB signalling. *Nat. Cell Biol.* **14**, 401–408 (2012).
51. Muñoz, J. *et al.* The Lgr5 intestinal stem cell signature: Robust expression of proposed quiescent ' +4' cell markers. *EMBO J.* **31**, 3079–3091 (2012).
52. Itzkovitz, S. *et al.* Single-molecule transcript counting of stem-cell markers in the mouse intestine. *Nat. Cell Biol.* **14**, 106–114 (2012).
53. Kosinski, C. *et al.* Gene expression patterns of human colon tops and basal crypts and BMP antagonists as intestinal stem cell niche factors. *Proc. Natl. Acad. Sci. U. S. A.* **104**, 15418–15423 (2007).
54. Clevers, H. & Nusse, R. Wnt/ β -catenin signaling and disease. *Cell* **149**, 1192–1205 (2012).
55. Battle, E. *et al.* β -catenin and TCF mediate cell positioning in the intestinal epithelium by controlling the expression of EphB/EphrinB. *Cell* **111**, 251–263 (2002).
56. Holmberg, J. *et al.* EphB Receptors Coordinate Migration and Proliferation in the Intestinal Stem Cell Niche. *Cell* **125**, 1151–1163 (2006).
57. Genander, M. *et al.* Dissociation of EphB2 Signaling Pathways Mediating Progenitor Cell Proliferation and Tumor Suppression. *Cell* **139**, 679–692 (2009).
58. Farin, H. F., Van Es, J. H. & Clevers, H. Redundant sources of Wnt regulate intestinal stem cells and promote formation of paneth cells. *Gastroenterology* **143**, 1518–1529.e7 (2012).
59. He, X. C. *et al.* BMP signaling inhibits intestinal stem cell self-renewal through suppression of Wnt- β -catenin signaling. *Nat. Genet.* **36**, 1117–1121 (2004).
60. Thorne, C. A. *et al.* Enteroid Monolayers Reveal an Autonomous WNT and BMP Circuit Controlling Intestinal Epithelial Growth and Organization. *Dev. Cell* **44**, 624–633.e4 (2018).

61. Jiang, H. *et al.* Cytokine/Jak/Stat Signaling Mediates Regeneration and Homeostasis in the *Drosophila* Midgut. *Cell* **137**, 1343–1355 (2009).
62. Carulli, A. J. *et al.* Notch receptor regulation of intestinal stem cell homeostasis and crypt regeneration. *Dev. Biol.* **402**, 98–108 (2015).
63. Guiu, J. *et al.* Hes repressors are essential regulators of hematopoietic stem cell development downstream of notch signaling. *J. Exp. Med.* **210**, 71–84 (2013).
64. Pellegrinet, L. *et al.* Dll1- and Dll4-mediated notch signaling are required for homeostasis of intestinal stem cells. *Gastroenterology* **140**, 1230–1240.e7 (2011).
65. López-Arribillaga, E. *et al.* Bmi1 regulates murine intestinal stem cell proliferation and self-renewal downstream of Notch. *Dev.* **142**, 41–50 (2015).
66. Van Es, J. H. *et al.* Dll1 + secretory progenitor cells revert to stem cells upon crypt damage. *Nat. Cell Biol.* **14**, 1099–1104 (2012).
67. Buczacki, S. J. A. *et al.* Intestinal label-retaining cells are secretory precursors expressing Lgr5. *Nature* **495**, 65–69 (2013).
68. Jadhav, U. *et al.* Dynamic Reorganization of Chromatin Accessibility Signatures during Dedifferentiation of Secretory Precursors into Lgr5+ Intestinal Stem Cells. *Cell Stem Cell* **21**, 65–77.e5 (2017).
69. Tomic, G. *et al.* Phospho-regulation of ATOH1 Is Required for Plasticity of Secretory Progenitors and Tissue Regeneration. *Cell Stem Cell* **23**, 436–443.e7 (2018).
70. Tetteh, P. W. *et al.* Replacement of Lost Lgr5-Positive Stem Cells through Plasticity of Their Enterocyte-Lineage Daughters. *Cell Stem Cell* **18**, 203–213 (2016).
71. Murata, K. *et al.* Ascl2-Dependent Cell Dedifferentiation Drives Regeneration of Ablated Intestinal Stem Cells. *Cell Stem Cell* **26**, 377–390.e6 (2020).
72. Yan, K. S. *et al.* Intestinal Enteroendocrine Lineage Cells Possess Homeostatic and Injury-Inducible Stem Cell Activity. *Cell Stem Cell* **21**, 78–90.e6 (2017).
73. Schneider, C. *et al.* A Metabolite-Triggered Tuft Cell-ILC2 Circuit Drives Small Intestinal Remodeling. *Cell* **174**, 271–284.e14 (2018).
74. Schmitt, M. *et al.* Paneth Cells Respond to Inflammation and Contribute to Tissue Regeneration by Acquiring Stem-like Features through SCF/c-Kit Signaling. *Cell Rep.* **24**, 2312–2328.e7 (2018).
75. Yu, S. *et al.* Paneth Cell Multipotency Induced by Notch Activation following Injury. *Cell Stem Cell* **23**, 46–59.e5 (2018).

76. Pont, A. R. & Yan, K. S. Intestinal Crypts Assume the Fetal Position in Response to Injury. *Cell Stem Cell* **23**, 158–159 (2018).
77. Nusse, Y. M. *et al.* Parasitic helminths induce fetal-like reversion in the intestinal stem cell niche. *Nature* **559**, 109–113 (2018).
78. Yui, S. *et al.* YAP/TAZ-Dependent Reprogramming of Colonic Epithelium Links ECM Remodeling to Tissue Regeneration. *Cell Stem Cell* **22**, 35–49.e7 (2018).
79. Fordham, R. P. *et al.* Transplantation of expanded fetal intestinal progenitors contributes to colon regeneration after injury. *Cell Stem Cell* **13**, 734–744 (2013).
80. Mustata, R. C. *et al.* Identification of Lgr5-Independent Spheroid-Generating Progenitors of the Mouse Fetal Intestinal Epithelium. *Cell Rep.* **5**, 421–432 (2013).
81. Guiu, J. *et al.* Tracing the origin of adult intestinal stem cells. *Nature* **570**, 107–111 (2019).
82. Beyaz, S. *et al.* High fat diet enhances stemness and tumorigenicity of intestinal progenitors. *Nature* **531**, 53–58 (2016).
83. Weitz, J. *et al.* Colorectal cancer. *Lancet* **365**, 153–165 (2005).
84. Farrall, A. L. *et al.* Wnt and BMP signals control intestinal adenoma cell fates. *Int. J. Cancer* **131**, 2242–2252 (2012).
85. Dow, L. E. *et al.* Apc Restoration Promotes Cellular Differentiation and Reestablishes Crypt Homeostasis in Colorectal Cancer. *Cell* **161**, 1539–1552 (2015).
86. Phelps, R. A. *et al.* A Two-Step Model for Colon Adenoma Initiation and Progression Caused by APC Loss. *Cell* **137**, 623–634 (2009).
87. Bakhoun, S. F. & Cantley, L. C. The Multifaceted Role of Chromosomal Instability in Cancer and Its Microenvironment. *Cell* **174**, 1347–1360 (2018).
88. Leslie, A., Carey, F. A., Pratt, N. R. & Steele, R. J. C. The colorectal adenoma-carcinoma sequence. *British Journal of Surgery* vol. 89 845–860 (2002).
89. Brenner, H., Kloor, M. & Pox, C. P. Colorectal cancer. *Lancet* **383**, 1490–1502 (2014).
90. Guinney, J. *et al.* The consensus molecular subtypes of colorectal cancer. *Nat. Med.* **21**, 1350–1356 (2015).
91. Isella, C. *et al.* Selective analysis of cancer-cell intrinsic transcriptional traits defines novel clinically relevant subtypes of colorectal cancer. *Nat. Commun.* **8**, 1–16 (2017).
92. Lee, H. O. *et al.* Lineage-dependent gene expression programs influence the immune landscape of colorectal cancer. *Nat. Genet.* **52**, 594–603 (2020).

93. Marisa, L. *et al.* Gene Expression Classification of Colon Cancer into Molecular Subtypes: Characterization, Validation, and Prognostic Value. *PLoS Med.* **10**, (2013).
94. Dick, J. E. Stem cell concepts renew cancer research. *Blood* **112**, 4793–4807 (2008).
95. Plaks, V., Kong, N. & Werb, Z. The cancer stem cell niche: How essential is the niche in regulating stemness of tumor cells? *Cell Stem Cell* vol. 16 225–238 (2015).
96. Driessens, G., Beck, B., Caauwe, A., Simons, B. D. & Blanpain, C. Defining the mode of tumour growth by clonal analysis. *Nature* **488**, 527–530 (2012).
97. Dalerba, P. *et al.* Phenotypic characterization of human colorectal cancer stem cells. *Proc. Natl. Acad. Sci. U. S. A.* **104**, 10158–10163 (2007).
98. O'Brien, C. A., Pollett, A., Gallinger, S. & Dick, J. E. A human colon cancer cell capable of initiating tumour growth in immunodeficient mice. *Nature* **445**, 106–110 (2007).
99. Ricci-Vitiani, L. *et al.* Identification and expansion of human colon-cancer-initiating cells. *Nature* **445**, 111–115 (2007).
100. Schepers, A. G. *et al.* Lineage tracing reveals Lgr5+ stem cell activity in mouse intestinal adenomas. *Science (80-.)*. **337**, 730–735 (2012).
101. Shimokawa, M. *et al.* Visualization and targeting of LGR5 + human colon cancer stem cells. *Nature* **545**, 187–192 (2017).
102. Cui, G. *et al.* Temporal and spatial changes of cells positive for stem-like markers in different compartments and stages of human colorectal adenoma-carcinoma sequence. *Oncotarget* **8**, 45311–45322 (2017).
103. Vermeulen, L. *et al.* Single-cell cloning of colon cancer stem cells reveals a multi-lineage differentiation capacity. *Proc. Natl. Acad. Sci. U. S. A.* **105**, 13427–13432 (2008).
104. De Sousa E Melo, F. *et al.* A distinct role for Lgr5 + stem cells in primary and metastatic colon cancer. *Nature* **543**, 676–680 (2017).
105. Morral, C. *et al.* Zonation of Ribosomal DNA Transcription Defines a Stem Cell Hierarchy in Colorectal Cancer. *Cell Stem Cell* **26**, 845–861.e12 (2020).
106. Clevers, H. The cancer stem cell: Premises, promises and challenges. *Nat. Med.* **17**, 313–319 (2011).
107. Batlle, E. & Clevers, H. Cancer stem cells revisited. *Nat. Med.* **23**, 1124–1134 (2017).
108. Bartram, I. & Jeschke, J. M. Do cancer stem cells exist? A pilot study combining a systematic review with the hierarchy-of-hypotheses approach. *PLoS One* **14**, 1–12 (2019).

109. Barker, N. *et al.* Crypt stem cells as the cells-of-origin of intestinal cancer. *Nature* **457**, 608–611 (2009).
110. Zhu, L. *et al.* Prominin 1 marks intestinal stem cells that are susceptible to neoplastic transformation. *Nature* **457**, 603–607 (2009).
111. Vermeulen, L. *et al.* Wnt activity defines colon cancer stem cells and is regulated by the microenvironment. *Nat. Cell Biol.* **12**, 468–476 (2010).
112. Schwitalla, S. *et al.* Intestinal tumorigenesis initiated by dedifferentiation and acquisition of stem-cell-like properties. *Cell* **152**, 25–38 (2013).
113. Kreso, A. & Dick, J. E. Evolution of the cancer stem cell model. *Cell Stem Cell* **14**, 275–291 (2014).
114. Hwang, K., Yoon, J. H., Lee, J. H. & Lee, S. Recent advances in monoclonal antibody therapy for colorectal cancers. *Biomedicines* **9**, 1–24 (2021).
115. Van Emburgh, B. O. *et al.* Acquired RAS or EGFR mutations and duration of response to EGFR blockade in colorectal cancer. *Nat. Commun.* **7**, 1–9 (2016).
116. Montagut, C. *et al.* Identification of a mutation in the extracellular domain of the Epidermal Growth Factor Receptor conferring cetuximab resistance in colorectal cancer. *Nat. Med.* **18**, 221–223 (2012).
117. Verissimo, C. S. *et al.* Targeting mutant RAS in patient-derived colorectal cancer organoids by combinatorial drug screening. *Elife* **5**, 1–26 (2016).
118. Drosten, M. & Barbacid, M. Targeting the MAPK Pathway in KRAS-Driven Tumors. *Cancer Cell* **37**, 543–550 (2020).
119. Almeqdadi, M., Mana, M. D., Roper, J. & Yilmaz, Ö. H. Gut organoids: Mini-tissues in culture to study intestinal physiology and disease. *Am. J. Physiol. - Cell Physiol.* **317**, C405–C419 (2019).
120. Sebolt-Leopold, J. S. Development of Preclinical Models to Understand and Treat Colorectal Cancer. *Clin. Colon Rectal Surg.* **31**, 199–204 (2018).
121. Day, C. P., Merlino, G. & Van Dyke, T. Preclinical Mouse Cancer Models: A Maze of Opportunities and Challenges. *Cell* vol. 163 39–53 (2015).
122. Onaciu, A. *et al.* Spontaneous and Induced Animal Models for Cancer Research. *Diagnostics* **10**, 1–36 (2020).
123. Yui, S. *et al.* Functional engraftment of colon epithelium expanded in vitro from a single adult Lgr5 + stem cell. *Nat. Med.* **18**, 618–623 (2012).

124. Fujii, E., Kato, A. & Suzuki, M. Patient-derived xenograft (PDX) models: Characteristics and points to consider for the process of establishment. *J. Toxicol. Pathol.* **33**, 153–160 (2020).
125. Goto, T. Patient-derived tumor xenograft models: Toward the establishment of precision cancer medicine. *J. Pers. Med.* **10**, 1–14 (2020).
126. Evans, D. M. & Teicher, B. A. 3D Cell Culture Models. in 251–275 (2017). doi:10.1007/978-3-319-57424-0_19.
127. Koo, B. K. *et al.* Controlled gene expression in primary Lgr5 organoid cultures. *Nat. Methods* **9**, 81–83 (2012).
128. Nie, J. & Hashino, E. Organoid technologies meet genome engineering. *EMBO Rep.* **18**, 367–376 (2017).
129. Hendriks, D., Clevers, H. & Artegiani, B. CRISPR-Cas Tools and Their Application in Genetic Engineering of Human Stem Cells and Organoids. *Cell Stem Cell* **27**, 705–731 (2020).
130. Clevers, H. Modeling Development and Disease with Organoids. *Cell* **165**, 1586–1597 (2016).
131. Dutta, D., Heo, I. & Clevers, H. Disease Modeling in Stem Cell-Derived 3D Organoid Systems. *Trends Mol. Med.* **23**, 393–410 (2017).
132. Kim, E. *et al.* Creation of bladder assembloids mimicking tissue regeneration and cancer. *Nature* **588**, 664–669 (2020).
133. Gjorevski, N. *et al.* Designer matrices for intestinal stem cell and organoid culture. *Nature* **539**, 560–564 (2016).
134. Bein, A. *et al.* Microfluidic Organ-on-a-Chip Models of Human Intestine. *Cmgh* **5**, 659–668 (2018).
135. Kretschmar, K. & Clevers, H. Organoids: Modeling Development and the Stem Cell Niche in a Dish. *Dev. Cell* **38**, 590–600 (2016).
136. Huch, M. & Koo, B. K. Modeling mouse and human development using organoid cultures. *Dev.* **142**, 3113–3125 (2015).
137. Drakhlis, L. *et al.* Human heart-forming organoids recapitulate early heart and foregut development. *Nat. Biotechnol.* (2021) doi:10.1038/s41587-021-00815-9.
138. Sachs, N. *et al.* A Living Biobank of Breast Cancer Organoids Captures Disease Heterogeneity. *Cell* **172**, 373–386.e10 (2018).
139. Yan, H. H. N. *et al.* A Comprehensive Human Gastric Cancer Organoid Biobank Captures Tumor Subtype Heterogeneity and Enables Therapeutic Screening. *Cell Stem Cell* **23**, 882–897.e11 (2018).

140. Calandrini, C. *et al.* An organoid biobank for childhood kidney cancers that captures disease and tissue heterogeneity. *Nat. Commun.* **11**, (2020).
141. Kawasaki, K. *et al.* An Organoid Biobank of Neuroendocrine Neoplasms Enables Genotype-Phenotype Mapping. *Cell* **183**, 1420–1435.e21 (2020).
142. Jacob, F. *et al.* A Patient-Derived Glioblastoma Organoid Model and Biobank Recapitulates Inter- and Intra-tumoral Heterogeneity. *Cell* **180**, 188–204.e22 (2020).
143. Weeber, F., Ooft, S. N., Dijkstra, K. K. & Voest, E. E. Tumor Organoids as a Pre-clinical Cancer Model for Drug Discovery. *Cell Chem. Biol.* **24**, 1092–1100 (2017).
144. Sato, T. *et al.* Single Lgr5 stem cells build crypt-villus structures in vitro without a mesenchymal niche. *Nature* **459**, 262–265 (2009).
145. Sato, T. & Clevers, H. Growing self-organizing mini-guts from a single intestinal stem cell: Mechanism and applications. *Science (80-)*. **340**, 1190–1194 (2013).
146. Jung, P. *et al.* Isolation and in vitro expansion of human colonic stem cells. *Nat. Med.* **17**, 1225–1227 (2011).
147. Sato, T. *et al.* Supplementary-Long term expansion... *Gastroenterology* **141**, 1762–1772 (2011).
148. Dame, M. K. *et al.* Identification, isolation and characterization of human LGR5-positive colon adenoma cells. *Development (Cambridge)* vol. 145 (2018).
149. Merker, S. R., Weitz, J. & Stange, D. E. Gastrointestinal organoids: How they gut it out. *Dev. Biol.* **420**, 239–250 (2016).
150. Sachs, N., Tsukamoto, Y., Kujala, P., Peters, P. J. & Clevers, H. Intestinal epithelial organoids fuse to form self-organizing tubes in floating collagen gels. *Dev.* **144**, 1107–1112 (2017).
151. Watson, C. L. *et al.* An in vivo model of human small intestine using pluripotent stem cells. *Nat. Med.* **20**, 1310–1314 (2014).
152. Sinagoga, K. L. & Wells, J. M. Generating human intestinal tissues from pluripotent stem cells to study development and disease. *EMBO J.* **34**, 1149–1163 (2015).
153. Kitano, K. *et al.* Bioengineering of functional human induced pluripotent stem cell-derived intestinal grafts. *Nat. Commun.* **8**, (2017).
154. Múnera, J. O. *et al.* Differentiation of Human Pluripotent Stem Cells into Colonic Organoids via Transient Activation of BMP Signaling. *Cell Stem Cell* **21**, 51–64.e6 (2017).
155. Crespo, M. *et al.* Colonic organoids derived from human induced pluripotent stem cells for modeling colorectal cancer and drug testing. *Nat. Med.* **23**, 878–884 (2017).

156. Drost, J. *et al.* Sequential cancer mutations in cultured human intestinal stem cells. *Nature* **521**, 43–47 (2015).
157. Matano, M. *et al.* Modeling colorectal cancer using CRISPR-Cas9-mediated engineering of human intestinal organoids. *Nat. Med.* **21**, 256–262 (2015).
158. Thalheim, T. *et al.* Linking stem cell function and growth pattern of intestinal organoids. *Dev. Biol.* **433**, 254–261 (2018).
159. Li, Y. *et al.* Volumetric Compression Induces Intracellular Crowding to Control Intestinal Organoid Growth via Wnt/ β -Catenin Signaling. *Cell Stem Cell* **28**, 63–78.e7 (2021).
160. Lindeboom, R. G. *et al.* Integrative multi-omics analysis of intestinal organoid differentiation. *Mol. Syst. Biol.* **14**, 1–16 (2018).
161. Jardé, T. *et al.* Mesenchymal Niche-Derived Neuregulin-1 Drives Intestinal Stem Cell Proliferation and Regeneration of Damaged Epithelium. *Cell Stem Cell* **27**, 646–662.e7 (2020).
162. Van De Wetering, M. *et al.* Prospective derivation of a living organoid biobank of colorectal cancer patients. *Cell* **161**, 933–945 (2015).
163. Qureshi-Baig, K., Ullmann, P., Haan, S. & Letellier, E. Tumor-Initiating Cells: A criTICal review of isolation approaches and new challenges in targeting strategies. *Mol. Cancer* **16**, 1–16 (2017).
164. Lugli, N. *et al.* Enhanced Rate of Acquisition of Point Mutations in Mouse Intestinal Adenomas Compared to Normal Tissue. *Cell Rep.* **19**, 2185–2192 (2017).
165. Roerink, S. F. *et al.* Intra-tumour diversification in colorectal cancer at the single-cell level. *Nature* **556**, 437–462 (2018).
166. Bolhaqueiro, A. C. F. *et al.* Ongoing chromosomal instability and karyotype evolution in human colorectal cancer organoids. *Nat. Genet.* **51**, 824–834 (2019).
167. Vlachogiannis, G. *et al.* Patient-derived organoids model treatment response of metastatic gastrointestinal cancers. *Science (80-.)*. **359**, 920–926 (2018).
168. Ramzy, G. M. *et al.* Patient-derived in vitro models for drug discovery in colorectal carcinoma. *Cancers (Basel)*. **12**, 1–21 (2020).
169. Yao, Y. *et al.* Patient-Derived Organoids Predict Chemoradiation Responses of Locally Advanced Rectal Cancer. *Cell Stem Cell* **26**, 17–26.e6 (2020).
170. Battle, E. *et al.* The transcription factor Snail is a repressor of E-cadherin gene expression in epithelial tumour cells. *Nat. Cell Biol.* **2**, 84–89 (2000).
171. Cano, A. *et al.* The transcription factor Snail controls epithelial-mesenchymal transitions by

repressing E-cadherin expression. *Nat. Cell Biol.* **2**, 76–83 (2000).

172. Mani, S. A. *et al.* The Epithelial-Mesenchymal Transition Generates Cells with Properties of Stem Cells. *Cell* **133**, 704–715 (2008).
173. Celià-Terrassa, T. & Kang, Y. Metastatic niche functions and therapeutic opportunities. *Nature Cell Biology* vol. 20 868–877 (2018).
174. Abad, E., Graifer, D. & Lyakhovich, A. DNA damage response and resistance of cancer stem cells. *Cancer Lett.* **474**, 106–117 (2020).
175. Fumagalli, A. *et al.* Plasticity of Lgr5-Negative Cancer Cells Drives Metastasis in Colorectal Cancer. *Cell Stem Cell* **26**, 569–578.e7 (2020).
176. Ganesh, K. *et al.* L1CAM defines the regenerative origin of metastasis-initiating cells in colorectal cancer. *Nat. Cancer* **1**, 28–45 (2020).
177. Todaro, M. *et al.* CD44v6 is a marker of constitutive and reprogrammed cancer stem cells driving colon cancer metastasis. *Cell Stem Cell* **14**, 342–356 (2014).
178. Yin, J. J. *et al.* TGF- β signaling blockade inhibits PTHrP secretion by breast cancer cells and bone metastases development. *J. Clin. Invest.* **103**, 197–206 (1999).
179. Siegel, P. M., Shu, W., Cardiff, R. D., Muller, W. J. & Massagué, J. Transforming growth factor β signaling impairs neu-induced mammary tumorigenesis while promoting pulmonary metastasis. *Proc. Natl. Acad. Sci. U. S. A.* **100**, 8430–8435 (2003).
180. Kang, Y. *et al.* Breast cancer bone metastasis mediated by the Smad tumor suppressor pathway. *Proc. Natl. Acad. Sci. U. S. A.* **102**, 13909–13914 (2005).
181. Massagué, J. & Gomis, R. R. The logic of TGF β signaling. *FEBS Lett.* **580**, 2811–2820 (2006).
182. Padua, D. *et al.* TGF β Primes Breast Tumors for Lung Metastasis Seeding through Angiopoietin-like 4. *Cell* **133**, 66–77 (2008).
183. Scheel, C. *et al.* Paracrine and autocrine signals induce and maintain mesenchymal and stem cell states in the breast. *Cell* **145**, 926–940 (2011).
184. Calon, A. *et al.* Dependency of colorectal cancer on a TGF-beta-driven programme in stromal cells for metastasis initiation. *Cancer Cell* **22**, 571–584 (2012).
185. Tauriello, D. V. F. *et al.* TGF β drives immune evasion in genetically reconstituted colon cancer metastasis. *Nature* **554**, 538–543 (2018).
186. Jackstadt, R. *et al.* Epithelial NOTCH Signaling Rewires the Tumor Microenvironment of Colorectal Cancer to Drive Poor-Prognosis Subtypes and Metastasis. *Cancer Cell* **36**, 319–336.e7

- (2019).
187. Holohan, C., Van Schaeybroeck, S., Longley, D. B. & Johnston, P. G. Cancer drug resistance: An evolving paradigm. *Nat. Rev. Cancer* **13**, 714–726 (2013).
 188. Emmink, B. L. *et al.* Differentiated human colorectal cancer cells protect tumor-initiating cells from irinotecan. *Gastroenterology* **141**, 269–278 (2011).
 189. Kreso, A. *et al.* Variable Clonal Repopulation Dynamics Influence Chemotherapy Response in Colorectal Cancer. *Science* vol. 339 543–8 (2013).
 190. Russo, M. *et al.* Adaptive mutability of colorectal cancers in response to targeted therapies. *Science (80-.)*. **366**, 1473–1480 (2019).
 191. De Angelis, M. L., Francescangeli, F., La Torre, F. & Zeuner, A. Stem cell plasticity and dormancy in the development of cancer therapy resistance. *Front. Oncol.* **9**, 1–14 (2019).
 192. Shen, S., Vagner, S. & Robert, C. Persistent Cancer Cells: The Deadly Survivors. *Cell* **183**, 860–874 (2020).
 193. Kusumbe, A. P. & Bapat, S. A. Cancer stem cells and aneuploid populations within developing tumors are the major determinants of tumor dormancy. *Cancer Res.* **69**, 9245–9253 (2009).
 194. Chen, J. *et al.* A restricted cell population propagates glioblastoma growth after chemotherapy. *Nature* **488**, 522–526 (2012).
 195. Gomis, R. R. & Gawrzak, S. Tumor cell dormancy. *Mol. Oncol.* **11**, 62–78 (2017).
 196. Giancotti, F. G. Mechanisms governing metastatic dormancy and reactivation. *Cell* **155**, 750 (2013).
 197. Recasens, A. & Munoz, L. Targeting Cancer Cell Dormancy. *Trends Pharmacol. Sci.* **40**, 128–141 (2019).
 198. Zeuner, A., Todaro, M., Stassi, G. & De Maria, R. Colorectal cancer stem cells: From the crypt to the clinic. *Cell Stem Cell* **15**, 692–705 (2014).
 199. Gupta, P. B. *et al.* Identification of Selective Inhibitors of Cancer Stem Cells by High-Throughput Screening. *Cell* **138**, 645–659 (2009).
 200. Sachlos, E. *et al.* Identification of drugs including a dopamine receptor antagonist that selectively target cancer stem cells. *Cell* **149**, 1284–1297 (2012).
 201. Saygin, C., Matei, D., Majeti, R., Reizes, O. & Lathia, J. D. Targeting Cancer Stemness in the Clinic: From Hype to Hope. *Cell Stem Cell* **24**, 25–40 (2019).
 202. Blanpain, C., Mohrin, M., Sotiropoulou, P. A. & Passegué, E. DNA-damage response in tissue-

specific and cancer stem cells. *Cell Stem Cell* **8**, 16–29 (2011).

203. Ciccia, A. & Elledge, S. J. The DNA Damage Response: Making It Safe to Play with Knives. *Mol. Cell* **40**, 179–204 (2010).
204. Pitolli, C. *et al.* p53-Mediated Tumor Suppression: DNA-Damage Response and Alternative Mechanisms. *Cancers (Basel)*. **11**, 1983 (2019).
205. Cazzalini, O., Scovassi, A. I., Savio, M., Stivala, L. A. & Prosperi, E. Multiple roles of the cell cycle inhibitor p21CDKN1A in the DNA damage response. *Mutat. Res. - Rev. Mutat. Res.* **704**, 12–20 (2010).
206. Weinberg, R. A. The retinoblastoma protein and cell cycle control. *Cell* **81**, 323–330 (1995).
207. Sherr, C. J. The INK4a/ARF network in tumour suppression. *Nat. Rev. Mol. Cell Biol.* **2**, 731–737 (2001).
208. Saleh, T., Tyutyunyk-Massey, L. & Gewirtz, D. A. Tumor cell escape from therapy-induced senescence as a model of disease recurrence after dormancy. *Cancer Res.* **79**, 1044–1046 (2019).
209. Moore, N., Houghton, J. & Lyle, S. Slow-cycling therapy-resistant cancer cells. *Stem Cells Dev.* **21**, 1822–1830 (2012).
210. Puig, I. *et al.* TET2 controls chemoresistant slow-cycling cancer cell survival and tumor recurrence. *J. Clin. Invest.* **128**, 3887–3905 (2018).
211. Cheung, T. H. & Rando, T. A. Molecular regulation of stem cell quiescence. *Nat. Rev. Mol. Cell Biol.* **14**, 329–340 (2013).
212. Sage, J., Miller, A. L., Pérez-Mancera, P. A., Wysocki, J. M. & Jacks, T. Acute mutation of retinoblastoma gene function is sufficient for cell cycle re-entry. *Nature* **424**, 223–228 (2003).
213. Wesley Overton, K., Spencer, S. L., Noderer, W. L., Meyer, T. & Wang, C. L. Basal p21 controls population heterogeneity in cycling and quiescent cell cycle states. *Proc. Natl. Acad. Sci. U. S. A.* **111**, E4386–E4393 (2014).
214. Kwon, J. S. *et al.* Controlling Depth of Cellular Quiescence by an Rb-E2F Network Switch. *Cell Rep.* **20**, 3223–3235 (2017).
215. Coller, H. A. The paradox of metabolism in quiescent stem cells. *FEBS Lett.* **593**, 2817–2839 (2019).
216. Min, M. & Spencer, S. L. Spontaneously slow-cycling subpopulations of human cells originate from activation of stress-response pathways. *PLoS Biol.* **17**, 1–25 (2019).

217. Arora, M., Moser, J., Phadke, H., Basha, A. A. & Spencer, S. L. Endogenous Replication Stress in Mother Cells Leads to Quiescence of Daughter Cells. *Cell Rep.* **19**, 1351–1364 (2017).
218. Cao, D. Z., Ou, X. L. & Yu, T. The association of p53 expression levels with clinicopathological features and prognosis of patients with colon cancer following surgery. *Oncol. Lett.* **13**, 3538–3546 (2017).
219. Cho, Y. H. *et al.* 5-FU promotes stemness of colorectal cancer via p53-mediated WNT/ β -catenin pathway activation. *Nat. Commun.* **11**, (2020).
220. Sang, L., Coller, H. A. & Roberts, J. M. Control of the reversibility of cellular quiescence by the transcriptional repressor HES1. *Science (80-)*. **321**, 1095–1100 (2008).
221. Oskarsson, T. *et al.* Breast cancer cells produce tenascin C as a metastatic niche component to colonize the lungs. *Nat. Med.* **17**, 867–874 (2011).
222. Malladi, S. *et al.* Metastatic Latency and Immune Evasion through Autocrine Inhibition of WNT. *Cell* **165**, 45–60 (2016).
223. Brown, J. A. *et al.* TGF- β -Induced Quiescence Mediates Chemoresistance of Tumor-Propagating Cells in Squamous Cell Carcinoma. *Cell Stem Cell* **21**, 650–664.e8 (2017).
224. Gawrzak, S. *et al.* MSK1 regulates luminal cell differentiation and metastatic dormancy in ER + breast cancer. *Nat. Cell Biol.* **20**, 211–221 (2018).
225. Gao, H. *et al.* The BMP inhibitor Coco reactivates breast cancer cells at lung metastatic sites. *Cell* **150**, 764–779 (2012).
226. Vicencio, J. M. *et al.* Senescence, apoptosis or autophagy? When a damaged cell must decide its path - A mini-review. *Gerontology* **54**, 92–99 (2008).
227. Feringa, F. M. *et al.* Persistent repair intermediates induce senescence. *Nat. Commun.* **9**, (2018).
228. Serrano, M., Lin, A. W., McCurrach, M. E., Beach, D. & Lowe, S. W. Oncogenic ras provokes premature cell senescence associated with accumulation of p53 and p16(INK4a). *Cell* **88**, 593–602 (1997).
229. Di Micco, R. *et al.* Oncogene-induced senescence is a DNA damage response triggered by DNA hyper-replication. *Nature* **444**, 638–642 (2006).
230. Bartkova, J. *et al.* Oncogene-induced senescence is part of the tumorigenesis barrier imposed by DNA damage checkpoints. *Nature* **444**, 633–637 (2006).
231. Wang, X. *et al.* Evidence of cisplatin-induced senescent-like growth arrest in nasopharyngeal carcinoma cells. *Cancer Res.* **58**, 5019–5022 (1998).

232. Chang, B. D. *et al.* A senescence-like phenotype distinguishes tumor cells that undergo terminal proliferation arrest after exposure to anticancer agents. *Cancer Res.* **59**, 3761–3767 (1999).
233. Hernandez-Segura, A., Nehme, J. & Demaria, M. Hallmarks of Cellular Senescence. *Trends Cell Biol.* **28**, 436–453 (2018).
234. He, S. & Sharpless, N. E. Senescence in Health and Disease. *Cell* vol. 169 1000–1011 (2017).
235. Chang, B. D. *et al.* Role of p53 and p21(waf1/cip1) in senescence-like terminal proliferation arrest induced in human tumor cells by chemotherapeutic drugs. *Oncogene* **18**, 4808–4818 (1999).
236. Narita, M. *et al.* Rb-mediated heterochromatin formation and silencing of E2F target genes during cellular senescence. *Cell* **113**, 703–716 (2003).
237. Lee, S. & Schmitt, C. A. The dynamic nature of senescence in cancer. *Nat. Cell Biol.* **21**, 94–101 (2019).
238. Ryl, T. *et al.* Cell-Cycle Position of Single MYC-Driven Cancer Cells Dictates Their Susceptibility to a Chemotherapeutic Drug. *Cell Syst.* **5**, 237–250.e8 (2017).
239. Beauséjour, C. M. *et al.* Reversal of human cellular senescence: Roles of the p53 and p16 pathways. *EMBO J.* **22**, 4212–4222 (2003).
240. Reyes, J. *et al.* Fluctuations in p53 Signaling Allow Escape from Cell-Cycle Arrest. *Mol. Cell* **71**, 581–591.e5 (2018).
241. Hsu, C. H., Altschuler, S. J. & Wu, L. F. Patterns of Early p21 Dynamics Determine Proliferation-Senescence Cell Fate after Chemotherapy. *Cell* **178**, 361–373.e12 (2019).
242. Lukin, D. J., Carvajal, L. A., Liu, W. J., Resnick-Silverman, L. & Manfredi, J. J. P53 Promotes Cell Survival Due To the Reversibility of Its Cell-Cycle Checkpoints. *Mol. Cancer Res.* **13**, 16–28 (2015).
243. Schmitt, C. A. *et al.* A senescence program controlled by p53 and p16INK4a contributes to the outcome of cancer therapy. *Cell* **109**, 335–346 (2002).
244. Kang, T. W. *et al.* Senescence surveillance of pre-malignant hepatocytes limits liver cancer development. *Nature* **479**, 547–551 (2011).
245. Faget, D. V., Ren, Q. & Stewart, S. A. Unmasking senescence: context-dependent effects of SASP in cancer. *Nat. Rev. Cancer* **19**, 439–453 (2019).
246. Roninson, I. B. Tumor cell senescence in cancer treatment. *Cancer Res.* **63**, 2705–2715 (2003).
247. Mosteiro, L. *et al.* Tissue damage and senescence provide critical signals for cellular reprogramming in vivo. *Science (80-.).* **354**, (2016).

248. Schosserer, M., Grillari, J. & Breitenbach, M. The dual role of cellular senescence in developing tumors and their response to cancer therapy. *Front. Oncol.* **7**, (2017).
249. Angelini, P. D. *et al.* Constitutive HER2 signaling promotes breast cancer metastasis through cellular senescence. *Cancer Res.* **73**, 450–458 (2013).
250. Milanovic, M. *et al.* Senescence-associated reprogramming promotes cancer stemness. *Nature* **553**, 96–100 (2018).
251. Duy, C. *et al.* Chemotherapy induces senescence-like resilient cells capable of initiating AML recurrence. *Cancer Discov.* candisc.1375.2020 (2021) doi:10.1158/2159-8290.cd-20-1375.
252. Dörr, J. R. *et al.* Synthetic lethal metabolic targeting of cellular senescence in cancer therapy. *Nature* **501**, 421–425 (2013).
253. Baell, J. B. *et al.* Inhibitors of histone acetyltransferases KAT6A/B induce senescence and arrest tumour growth. *Nature* **560**, 253–257 (2018).
254. Lee, S. & Lee, J. S. Cellular senescence: A promising strategy for cancer therapy. *BMB Rep.* **52**, 35–41 (2019).
255. Xu, M. *et al.* Senolytics improve physical function and increase lifespan in old age. *Nat. Med.* **24**, 1246–1256 (2018).
256. Short, S., Fielder, E., Miwa, S. & von Zglinicki, T. Senolytics and senostatics as adjuvant tumour therapy. *EBioMedicine* **41**, 683–692 (2019).
257. Stein, C. *et al.* YAP1 Exerts Its Transcriptional Control via TEAD-Mediated Activation of Enhancers. *PLoS Genet.* **11**, 1–28 (2015).
258. Piccolo, S., Dupont, S. & Cordenonsi, M. The biology of YAP/TAZ: Hippo signaling and beyond. *Physiol. Rev.* **94**, 1287–1312 (2014).
259. Cox, A. G. *et al.* Yap regulates glucose utilization and sustains nucleotide synthesis to enable organ growth. *EMBO J.* **37**, 1–16 (2018).
260. Fallah, S. & Beaulieu, J. F. The Hippo Pathway Effector YAP1 Regulates Intestinal Epithelial Cell Differentiation. *Cells* **9**, 1–24 (2020).
261. Li, Q. *et al.* Lats1/2 Sustain Intestinal Stem Cells and Wnt Activation through TEAD-Dependent and Independent Transcription. *Cell Stem Cell* **26**, 675–692.e8 (2020).
262. Cai, J. *et al.* The Hippo signaling pathway restricts the oncogenic potential of an intestinal regeneration program. *Genes Dev.* **24**, 2383–2388 (2010).
263. Taniguchi, K. *et al.* A gp130-Src-YAP module links inflammation to epithelial regeneration. *Nature*

519, 57–62 (2015).

264. Barry, E. R. *et al.* Restriction of intestinal stem cell expansion and the regenerative response by YAP. *Nature* **493**, 106–110 (2013).
265. Gregorieff, A., Liu, Y., Inanlou, M. R., Khomchuk, Y. & Wrana, J. L. Yap-dependent reprogramming of Lgr5+ stem cells drives intestinal regeneration and cancer. *Nature* **526**, 715–718 (2015).
266. Hong, A. W., Meng, Z. & Guan, K. L. The Hippo pathway in intestinal regeneration and disease. *Nat. Rev. Gastroenterol. Hepatol.* **13**, 324–337 (2016).
267. Ayyaz, A. *et al.* Single-cell transcriptomes of the regenerating intestine reveal a revival stem cell. *Nature* **569**, 121–125 (2019).
268. Yu, F. X., Zhao, B. & Guan, K. L. Hippo Pathway in Organ Size Control, Tissue Homeostasis, and Cancer. *Cell* **163**, 811–828 (2015).
269. Moya, I. M. & Halder, G. Hippo–YAP/TAZ signalling in organ regeneration and regenerative medicine. *Nat. Rev. Mol. Cell Biol.* **20**, 211–226 (2019).
270. Cordenonsi, M. *et al.* The hippo transducer TAZ confers cancer stem cell-related traits on breast cancer cells. *Cell* **147**, 759–772 (2011).
271. Rosenbluh, J. *et al.* β -Catenin-driven cancers require a YAP1 transcriptional complex for survival and tumorigenesis. *Cell* **151**, 1457–1473 (2012).
272. Cai, J., Maitra, A., Anders, R. A., Taketo, M. M. & Pan, D. β -catenin destruction complex-independent regulation of Hippo–YAP signaling by APC in intestinal tumorigenesis. *Genes Dev.* **29**, 1493–1506 (2015).
273. Pefani, D. E. *et al.* TGF- β Targets the Hippo Pathway Scaffold RASSF1A to Facilitate YAP/SMAD2 Nuclear Translocation. *Mol. Cell* **63**, 156–166 (2016).
274. Ma, B. *et al.* Zyxin–Siah2–Lats2 axis mediates cooperation between Hippo and TGF- β signalling pathways. *Nat. Commun.* **7**, 1–13 (2016).
275. Shao, D. D. *et al.* KRAS and YAP1 converge to regulate EMT and tumor survival. *Cell* **158**, 171–184 (2014).
276. Harvey, K. F., Zhang, X. & Thomas, D. M. The Hippo pathway and human cancer. *Nat. Rev. Cancer* **13**, 246–257 (2013).
277. Zanconato, F., Cordenonsi, M. & Piccolo, S. YAP/TAZ at the Roots of Cancer. *Cancer Cell* **29**, 783–803 (2016).

278. Warren, J. S. A., Xiao, Y. & Lamar, J. M. YAP/TAZ activation as a target for treating metastatic cancer. *Cancers (Basel)*. **10**, (2018).
279. Boopathy, G. T. K. & Hong, W. Role of Hippo Pathway-YAP/TAZ signaling in angiogenesis. *Front. Cell Dev. Biol.* **7**, 1–12 (2019).
280. Furth, N., Aylon, Y. & Oren, M. P53 shades of Hippo. *Cell Death Differ.* **25**, 81–92 (2018).
281. Raj, N. & Bam, R. Reciprocal Crosstalk Between YAP1/Hippo Pathway and the p53 Family Proteins: Mechanisms and Outcomes in Cancer. *Front. Cell Dev. Biol.* **7**, 1–10 (2019).
282. Touil, Y. *et al.* Colon cancer cells escape 5FU chemotherapy-induced cell death by entering stemness and quiescence associated with the c-Yes/YAP axis. *Clin. Cancer Res.* **20**, 837–846 (2014).
283. Ganem, N. J. *et al.* Cytokinesis failure triggers hippo tumor suppressor pathway activation. *Cell* **158**, 833–848 (2014).
284. Mello, S. S. *et al.* A p53 Super-tumor Suppressor Reveals a Tumor Suppressive p53-Ptpn14-Yap Axis in Pancreatic Cancer. *Cancer Cell* **32**, 460–473.e6 (2017).
285. Kurppa, K. J. *et al.* Treatment-Induced Tumor Dormancy through YAP-Mediated Transcriptional Reprogramming of the Apoptotic Pathway. *Cancer Cell* **37**, 104–122.e12 (2020).
286. Cheung, P. *et al.* Regenerative Reprogramming of the Intestinal Stem Cell State via Hippo Signaling Suppresses Metastatic Colorectal Cancer. *Cell Stem Cell* **27**, 590–604.e9 (2020).
287. Duex, J. E. *et al.* Nuclear CD24 drives tumor growth and is predictive of poor patient prognosis. *Cancer Res.* **77**, 4858–4867 (2017).
288. Zhu, C. Q. *et al.* Prognostic and predictive gene signature for adjuvant chemotherapy in resected non-small-cell lung cancer. *J. Clin. Oncol.* **28**, 4417–4424 (2010).
289. Peng, P. L. *et al.* Identification of a novel gene pairs signature in the prognosis of gastric cancer. *Cancer Med.* **7**, 344–350 (2018).
290. Hu, F., Zeng, W. & Liu, X. A gene signature of survival prediction for kidney renal cell carcinoma by multi-omic data analysis. *Int. J. Mol. Sci.* **20**, (2019).
291. Zuo, S. *et al.* A robust six-gene prognostic signature for prediction of both disease-free and overall survival in non-small cell lung cancer. *J. Transl. Med.* **17**, 1–16 (2019).
292. Glinsky, G. V., Berezovska, O. & Glinskii, A. B. Microarray analysis identifies a death-from-cancer signature predicting therapy failure in patients with multiple types of cancer. *J. Clin. Invest.* **115**, 1503–1521 (2005).

293. Glas, A. M. *et al.* Converting a breast cancer microarray signature into a high-throughput diagnostic test. *BMC Genomics* **7**, 1–10 (2006).
294. Ma, X. J. *et al.* A two-gene expression ratio predicts clinical outcome in breast cancer patients treated with tamoxifen. *Cancer Cell* **5**, 607–616 (2004).
295. Xu, W. *et al.* Yin Yang Gene Expression Ratio Signature for Lung Cancer Prognosis. *PLoS One* **8**, (2013).
296. Jansen, M. P. H. M. *et al.* HOXB13-to-IL17BR expression ratio is related with tumor aggressiveness and response to tamoxifen of recurrent breast cancer: A retrospective study. *J. Clin. Oncol.* **25**, 662–668 (2007).
297. Ma, X. J. *et al.* The HOXB13:IL17BR expression index is a prognostic factor in early-stage breast cancer. *J. Clin. Oncol.* **24**, 4611–4619 (2006).
298. Jerevall, P. L. *et al.* Prognostic utility of HOXB13: IL17BR and molecular grade index in early-stage breast cancer patients from the Stockholm trial. *Br. J. Cancer* **104**, 1762–1769 (2011).
299. Xu, W. *et al.* A 10-Gene Yin Yang Expression Ratio Signature for Stage IA and IB Non-Small Cell Lung Cancer. *J. Thorac. Oncol.* **11**, 2150–2160 (2016).
300. Drost, J. *et al.* Use of CRISPR-modified human stem cell organoids to study the origin of mutational signatures in cancer. *Science (80-.)*. **358**, 234–238 (2017).
301. Lee-Six, H. *et al.* The landscape of somatic mutation in normal colorectal epithelial cells. *Nature* **574**, 532–537 (2019).
302. Perez Villamil, B. *et al.* Colon cancer molecular subtypes identified by expression profiling and associated to stroma, mucinous type and different clinical behavior. *BMC Cancer* **12**, 1 (2012).
303. Calon, A. *et al.* Stromal gene expression defines poor-prognosis subtypes in colorectal cancer. *Nat. Genet.* **47**, 320–329 (2015).
304. Bertucci, F. *et al.* Gene expression profiling of colon cancer by DNA microarrays and correlation with histoclinical parameters. *Oncogene* **23**, 1377–1391 (2004).
305. Lin, Y. H. *et al.* Multiple gene expression classifiers from different array platforms predict poor prognosis of colorectal cancer. *Clin. Cancer Res.* **13**, 498–507 (2007).
306. Anjomshoa, A. *et al.* Reduced expression of a gene proliferation signature is associated with enhanced malignancy in colon cancer. *Br. J. Cancer* **99**, 966–973 (2008).
307. Pesson, M. *et al.* A gene expression and pre-mRNA splicing signature that marks the adenoma-adenocarcinoma progression in colorectal cancer. *PLoS One* **9**, (2014).

308. Barrier, A. *et al.* Stage II colon cancer prognosis prediction by tumor gene expression profiling. *J. Clin. Oncol.* **24**, 4685–4691 (2006).
309. Smith, J. J. *et al.* Experimentally Derived Metastasis Gene Expression Profile Predicts Recurrence and Death in Patients With Colon Cancer. *Gastroenterology* **138**, 958–968 (2010).
310. Salazar, R. *et al.* Gene expression signature to improve prognosis prediction of stage II and III colorectal cancer. *J. Clin. Oncol.* **29**, 17–24 (2011).
311. Laibe, S. *et al.* A seven-gene signature aggregates a subgroup of stage II colon cancers with stage III. *Omi. A J. Integr. Biol.* **16**, 560–565 (2012).
312. Jiang, Y. *et al.* Development of a clinically feasible molecular assay to predict recurrence of Stage II colon cancer. *J. Mol. Diagnostics* **10**, 346–354 (2008).
313. Garman, K. S. *et al.* A genomic approach to colon cancer risk stratification yields biologic insights into therapeutic opportunities. *Proc. Natl. Acad. Sci. U. S. A.* **105**, 19432–19437 (2008).
314. Roepman, P. *et al.* Colorectal cancer intrinsic subtypes predict chemotherapy benefit, deficient mismatch repair and epithelial-to-mesenchymal transition. *Int. J. Cancer* **134**, 552–562 (2014).
315. Tsuji, S. *et al.* Potential responders to FOLFOX therapy for colorectal cancer by Random Forests analysis. *Br. J. Cancer* **106**, 126–132 (2012).
316. Oh, H. J. *et al.* p53 expression status is associated with cancer-specific survival in stage III and high-risk stage II colorectal cancer patients treated with oxaliplatin-based adjuvant chemotherapy. *Br. J. Cancer* **120**, 797–805 (2019).
317. Merlos-Suárez, A. *et al.* The intestinal stem cell signature identifies colorectal cancer stem cells and predicts disease relapse. *Cell Stem Cell* **8**, 511–524 (2011).
318. De Sousa E Melo, F. *et al.* Methylation of cancer-stem-cell-associated wnt target genes predicts poor prognosis in colorectal cancer patients. *Cell Stem Cell* **9**, 476–485 (2011).
319. Akhtar-Zaidi, B. *et al.* Epigenomic enhancer profiling defines a signature of colon cancer. *Science (80-.)*. **336**, 736–739 (2012).
320. Kim, D. *et al.* TopHat2: Accurate alignment of transcriptomes in the presence of insertions, deletions and gene fusions. *Genome Biol.* **14**, R36 (2013).
321. Anders, S., Pyl, P. T. & Huber, W. HTSeq-A Python framework to work with high-throughput sequencing data. *Bioinformatics* **31**, 166–169 (2015).
322. Love, M. I., Huber, W. & Anders, S. Moderated estimation of fold change and dispersion for RNA-seq data with DESeq2. *Genome Biol.* **15**, 1–21 (2014).

323. Galili, T., O'Callaghan, A., Sidi, J. & Sievert, C. Heatmaply: An R package for creating interactive cluster heatmaps for online publishing. *Bioinformatics* **34**, 1600–1602 (2018).
324. Krueger, B. *et al.* Different evolutionary modifications as a guide to rewire two-component systems. *Bioinform. Biol. Insights* **6**, 97–128 (2012).
325. Langmead, B. & Salzberg, S. L. Fast gapped-read alignment with Bowtie 2. *Nat. Methods* **9**, 357–359 (2012).
326. Zhang, Y. *et al.* Model-based analysis of ChIP-Seq (MACS). *Genome Biol.* **9**, (2008).
327. Yu, G., Wang, L. G. & He, Q. Y. ChIP seeker: An R/Bioconductor package for ChIP peak annotation, comparison and visualization. *Bioinformatics* **31**, 2382–2383 (2015).
328. Colomer, C. *et al.* IKK α Kinase Regulates the DNA Damage Response and Drives Chemoresistance in Cancer. *Mol. Cell* **75**, 669–682.e5 (2019).
329. Kagoya, Y. *et al.* Positive feedback between NF- κ B and TNF- α promotes leukemia-initiating cell capacity. *J. Clin. Invest.* **124**, 528–542 (2014).
330. Liu, M. *et al.* The canonical NF- κ B pathway governs mammary tumorigenesis in transgenic mice and tumor stem cell expansion. *Cancer Res.* **70**, 10464–10473 (2010).
331. Rajasekhar, V. K., Studer, L., Gerald, W., Socci, N. D. & Scher, H. I. Tumour-initiating stem-like cells in human prostate cancer exhibit increased NF- κ B signalling. *Nat. Commun.* **2**, 113–166 (2011).
332. Tacutu, R. *et al.* Human Ageing Genomic Resources: New and updated databases. *Nucleic Acids Res.* **46**, D1083–D1090 (2018).
333. Fischer, M. Census and evaluation of p53 target genes. *Oncogene* **36**, 3943–3956 (2017).
334. Cortazar, A. R. *et al.* Cancertool: A visualization and representation interface to exploit cancer datasets. *Cancer Res.* **78**, 6320–6328 (2018).
335. Kemper, K. *et al.* Mutations in the Ras-Raf axis underlie the prognostic value of CD133 in colorectal cancer. *Clin. Cancer Res.* **18**, 3132–3141 (2012).
336. Jorissen, R. N. *et al.* Metastasis-associated gene expression changes predict poor outcomes in patients with Dukes stage B and C colorectal cancer. *Clin. Cancer Res.* **15**, 7642–7651 (2009).
337. Dhimolea, E. *et al.* An Embryonic Diapause-like Adaptation with Suppressed Myc Activity Enables Tumor Treatment Persistence. *Cancer Cell* **39**, 240–256.e11 (2021).
338. Rehman, S. K. *et al.* Colorectal Cancer Cells Enter a Diapause-like DTP State to Survive Chemotherapy. *Cell* **184**, 226–242.e21 (2021).

339. Dai, Y. *et al.* Activation of anaphase-promoting complex by p53 induces a state of dormancy in cancer cells against chemotherapeutic stress. *Oncotarget* (2016) doi:10.18632/oncotarget.8172.
340. Boroviak, T. *et al.* Lineage-Specific Profiling Delineates the Emergence and Progression of Naive Pluripotency in Mammalian Embryogenesis. *Dev. Cell* **35**, 366–382 (2015).
341. Lin, Y. H. & Zhu, H. A Malignant Case of Arrested Development: Cancer Cell Dormancy Mimics Embryonic Diapause. *Cancer Cell* **39**, 142–144 (2021).
342. Bulut-Karslioglu, A. *et al.* Inhibition of mTOR induces a paused pluripotent state. *Nature* **540**, 119–123 (2016).
343. Colomer, C. *et al.* IKK α is required in the intestinal epithelial cells for tumour stemness. *Br. J. Cancer* **118**, 839–846 (2018).
344. Margalef, P. *et al.* A Truncated Form of IKK α Is Responsible for Specific Nuclear IKK Activity in Colorectal Cancer. *Cell Rep.* **2**, 840–854 (2012).
345. Fernández-Majada, V. *et al.* Nuclear IKK activity leads to dysregulated Notch-dependent gene expression in colorectal cancer. *Proc. Natl. Acad. Sci. U. S. A.* **104**, 276–281 (2007).
346. Vreka, M. *et al.* Europe PMC Funders Group I κ B kinase α is required for development and progression of KRAS -mutant lung adenocarcinoma. **78**, 2939–2951 (2019).
347. Luo, J. L. *et al.* Nuclear cytokine-activated IKK α controls prostate cancer metastasis by repressing Maspin. *Nature* **446**, 690–694 (2007).
348. Sundar, R. Targeting BRAF Mutant Colorectal Cancer: Progress in Combination Strategies. *Cancer Discov.* **63**, 1–18 (2014).
349. Song, L. *et al.* A novel role of IKK α in the mediation of UVB-induced G0/G1 cell cycle arrest response by suppressing Cyclin D1 expression. *Biochim. Biophys. Acta - Mol. Cell Res.* **1803**, 323–332 (2010).
350. Kwak, Y. T. *et al.* Cells lacking IKK α show nuclear cyclin D1 overexpression and a neoplastic phenotype: Role of IKK α as a tumor suppressor. *Mol. Cancer Res.* **9**, 341–349 (2011).

ANNEX

ANNEX 1

Clinical data from the paired patient samples with gastrointestinal tumours (at biopsy and after neoadjuvancy) used in this project. ki67 subtype classification: 1. No changes in ki67 levels, 2. Decrease in ki67 levels, 3. Decrease in ki67 levels displaying giant nuclei.

Patient n°	Tumour Location	Clinical TNM	Treatment	ki67% postQ	ki67% biopsy	ki67 subtype	nYAP1 % postQ	nYAP1% biopsy	OS (mo)	DFS (mo)
1	Gastric	T4N1M1	Chemotherapy	20	40	2	30	0	7.13	5.40
2	Colorectal	T3N1M1	Chemotherapy + Targeted therapy	1	55	3	N/A	N/A	115.23	115.23
3	Gastric	T3N1	Chemotherapy	10	70	2	90	5	60.90	60.90
4	Colorectal	T3N1M1	Radiotherapy	5	70	2	N/A	N/A	17.33	9.50
5	Gastric	T3N1M0	Chemotherapy	5	60	2	80	5	26.73	12.23
6	Colorectal	T3N0	Chemotherapy	30	70	2	50	2	53.10	53.10
7	Gastric	T3N1M1	Chemotherapy	70	90	2	90	80	41.10	23.07
8	Gastric	T3N1M1	Chemotherapy + Targeted therapy	10	5	1	70	0	89.83	40.23
9	Colorectal	T3N1	Chemotherapy	15	75	2	N/A	N/A	94.23	94.23
10	Gastric	T3N0M0	Chemotherapy	85	95	1	5	10	91.10	91.10
11	Gastric	T2-3N1M0	Chemotherapy	90	90	1	N/A	N/A	93.37	93.37
12	Gastric	T3N1M0	Chemotherapy	80	90	1	N/A	N/A	97.70	97.70
13	Gastric	T3N0M0	Chemotherapy	20	70	2	0	0	25.23	9.67
14	Colorectal	T4N1	Chemotherapy	80	60	1	95	20	38.17	12.43
15	Gastric	T3N1M1	Chemotherapy + Targeted therapy	70	85	1	50	15	93.37	93.37
16	Colorectal	T3N1	Chemotherapy + Targeted therapy	10	80	2	90	0	42.67	21.67
17	Colorectal	T4N1M0	Chemotherapy	20	95	2	60	20	39.90	39.90
18	Colorectal	T3N0M0	Chemotherapy	40	90	2	N/A	N/A	81.53	81.53
19	Colorectal	T2N1M0	Chemotherapy	5	25	3	90	3	83.13	83.13
20	Colorectal	T4N1M0	Chemotherapy	20	60	2	70	60	94.03	94.03
21	Colorectal	T3N1M0	Chemotherapy	25	80	2	N/A	30	91.90	91.90
22	Colorectal	T3N1M0	Chemotherapy	1	95	2	N/A	N/A	88.30	88.30
23	Colorectal	T3N2bM0	Chemotherapy	1	90	2	30	30	76.53	76.53
24	Gastric	T3N1M0	Chemotherapy	20	20	1	90	0	29.87	12.77
25	Colorectal	T3N1M0	Chemotherapy	N/A	N/A	N/A	N/A	N/A	79.77	N/A
26	Colorectal	T3N0M0	Chemotherapy	N/A	N/A	N/A	N/A	N/A	53.63	N/A
27	Colorectal	T3N0M0	Chemotherapy	1	55	2	5	10	8.53	8.53
28	Colorectal	T3N1M0	Chemotherapy + Targeted therapy	40	65	2	30	1	121.23	27.47
29	Colorectal	T3N1M0	Chemotherapy	N/A	N/A	N/A	N/A	N/A	33.90	20.83
30	Colorectal	T3N0	Chemotherapy	20	10	1	70	3	60.30	60.30
31	Gastric	T3N0	Chemotherapy	20	30	1	100	0	12.17	9.10
32	Gastric	T3N1	Chemotherapy	30	40	1	N/A	N/A	16.53	8.40

33	Gastric	T3N0M0	Chemotherapy	30	70	2	80	5	77.93	77.93
34	Colorectal	T3N1M1	Chemotherapy + Targeted therapy	5	80	2	90	0	N/A	N/A
35	Colorectal	T3N1M0	Radiotherapy	1	60	2	100	15	69.50	69.50
36	Gastric	T3N1M0	Chemotherapy	25	N/A	N/A	N/A	N/A	39.37	39.37
37	Gastric	T3N1M0	Chemotherapy	20	55	2	2	2	65.10	65.10
38	Gastric	T3N1M0	Chemotherapy	10	20	1	60	20	39.23	22.73
39	Pancreas	T4N0M0	Chemotherapy	0	N/A	N/A	N/A	N/A	45.63	15.63
40	Colorectal	T3N1M1	Chemotherapy	25	30	1	90	10	18.23	6.00
41	Colorectal	T3N0M0	Radiotherapy	25	40	1	30	0	41.77	41.77
42	Colorectal	T3N0M1	Chemotherapy + Targeted therapy	40	90	2	90	0	22.50	10.13
43	Colorectal	T4N1M0	Chemotherapy	0	65	2	0	5	45.60	11.90
44	Colorectal	T3N1	Chemotherapy	5	15	1	0	5	8.70	8.70
45	Colorectal	T3N0M0	Chemotherapy	1	70	2	N/A	N/A	62.73	25.00
46	Colorectal	T3N1M1	Chemotherapy + Targeted therapy	5	50	2	80	0	33.47	18.43
47	Colorectal	T3N2M0	Chemotherapy	60	95	2	0	2	59.63	26.40
48	Colorectal	T3N1M0	Chemotherapy	20	60	2	30	0	56.20	56.20
49	Gastric	T4N0M0	Chemotherapy	50	60	1	50	50	42.70	42.70
50	Colorectal	T3N0M0	Chemotherapy	10	70	2	5	0	47.60	47.60
51	Gastric	T2N1M0	Chemotherapy	15	75	2	2	0	38.73	16.70
52	Colorectal	T3N0M0	Chemotherapy	5	25	2	30	0	63.37	63.37
53	Colorectal	T3N1M0	Chemotherapy	20	95	2	30	0	9.00	9.00
54	Gastric	T3N3M0	Chemotherapy	15	60	2	30	0	11.93	11.03
55	Colorectal	T4N1M0	Radiotherapy	20	30	1	15	0	34.73	34.73
56	Colorectal	T2N1M0	Chemotherapy	N/A	N/A	N/A	N/A	N/A	53.27	N/A
57	Colorectal	T3N1M0	Chemotherapy	45	85	2	50	5	54.47	54.47
58	Colorectal	T3N0M0	Chemotherapy	70	90	2	90	20	50.67	50.67
59	Colorectal	T3N0M0	Chemotherapy	45	80	2	70	25	12.23	5.00
60	Colorectal	T4N2M0	Chemotherapy	75	95	2	40	0	22.47	4.27
61	Colorectal	T3Nx (sigma)+ T2N0M1 (rectum)	Radiotherapy	65	65	1	N/A	N/A	36.47	3.27
62	Colorectal	T3N0 (rectum) +T4Nx (bladder) M1	Radiotherapy	80	95	1	80	5	5.37	3.53

ANNEX 2

Clinical data from the CRC patient samples (TMA) used in the present thesis. Nuclear YAP1 H-Score calculated as the mean of three replicates.

Patient n°	Tumour Location	Clinical TNM	Treatment	nYAP1 Hscore	OS (mo)	DFS (mo)
1	Sigma	T3N0	Surgery	8.3	42.6	42.6
2	Rectum-Sigma	T3N2M1 lung	Chemotherapy + Targeted therapy	135.0	47.8	47.8
3	Sigma	T4N2	Chemotherapy	126.7	77.0	77.0
4	Right colon	T3N1	Chemotherapy	160.0	27.3	27.3
5	Splenic angle	T4N2	Surgery	240.0	6.0	6.0
6	Right colon	T2N0	Chemotherapy	40.0	75.0	75.0
7	Sigma	T3N1	Surgery	70.0	58.9	58.9
8	Sigma	T3N1	Chemotherapy	20.0	69.0	69.0
9	Sigma	T3N1	Chemotherapy	63.3	74.0	74.0
10	Sigma	N/A	Surgery	46.7	67.9	67.9
11	Right colon	T4N1	Surgery	0.0	20.3	15.2
12	Sigma	T3N2	Surgery	190.0	56.9	23.3
13	Sigma	T3N0	Surgery	43.3	61.8	61.8
14	Rectum	T2N2	Chemotherapy+Radiotherapy	66.7	70.0	32.5
15	Sigma	T3NX	Chemotherapy	60.0	12.2	35.6
16	Sigma	T3N0	Surgery	3.3	7.1	7.1
17	Sigma	T3N0	Surgery	0.0	74.0	74.0
18	Rectum	T3N0	Surgery	40.0	23.4	8.2
19	Sigma	T3N0	Surgery	33.3	36.5	36.5
20	Right colon	T3N0	Surgery	6.7	51.8	51.8
21	Sigma	T3N0	Surgery	3.3	67.0	67.0
22	Sigma	T3N0	Surgery	0.0	74.1	74.1
23	Ascending colon	T3N2	Chemotherapy	30.0	30.4	30.4
24	Sigma	T3N0	Surgery	73.3	72.0	72.0
25	Right colon	T3N2	Chemotherapy	93.3	67.0	67.0
26	Right colon	T3N0	Surgery	3.3	60.9	32.5
27	Sigma	T3N2	Chemotherapy+Targeted therapy	93.3	24.3	10.1
28	Right colon	T3N0	Surgery	53.3	63.9	63.9
29	Right colon	T4N0	Chemotherapy	53.3	64.9	64.9
30	Sigma	T4N0	Chemotherapy	5.0	26.4	26.4
31	Right colon	T4N0	Surgery	0.0	2.0	2.0
32	Sigma	T3N0	Surgery	6.7	26.4	26.4
33	Descendent colon	T4N0	N/A	25.0	29.4	25.3
34	Rectum-Sigma	T3N0	Surgery	46.7	67.9	67.9
35	Rectum-Sigma	T3N0	Surgery	130.0	67.9	67.9
36	Sigma	T3N1	Chemotherapy+Radiotherapy	0.0	46.7	5.1
37	Right colon	T4N1	Surgery	100.0	22.3	13.2
38	Sigma	T4N1	Surgery	40.0	28.4	28.4
39	Sigma	T3N1	Chemotherapy	N/A	62.9	62.9
40	Rectum	T3N0	Chemotherapy+Radiotherapy	146.7	64.9	64.9

41	Rectum-Sigma	T2N0	Chemotherapy+Radiotherapy	96.7	67.9	67.9
42	Right colon	T2N1	Chemotherapy	12.5	70.0	70.0
43	Sigma	T4N1	Chemotherapy	0.0	63.9	63.9
44	Splenic angle	T4N1	Surgery	103.3	21.3	9.1
45	Right colon	T3N0	N/A	120.0	33.5	33.5
46	Right colon	T3N1	Surgery	20.0	5.0	5.0
47	Right colon	T4N2	Surgery	0.0	5.1	3.0
48	Right colon	T3N0	Surgery	5.0	65.0	65.0
49	Sigma	T4N0	Chemotherapy	0.0	64.9	64.9
50	Right colon	T3N2	Chemotherapy	3.3	15.2	11.2
51	Sigma	T4N1	Chemotherapy	22.5	66.9	66.9
52	Sigma	T4N1	Chemotherapy+Targeted therapy	12.5	29.4	14.2
53	Descendent colon	T2N1	Surgery	20.0	65.9	65.9
54	Sigma	T3N2	Surgery	10.0	10.1	6.0
55	Sigma	T4N2	Surgery	48.3	60.9	18.2
56	Right colon	T3N0	Surgery	45.0	71.0	71.0
57	Sigma	T3N0	Surgery	2.5	75.1	75.1
58	Sigma	T3N1	Surgery	0.0	55.8	55.8
59	Hepatic angle	T3N0	Surgery	0.0	66.0	66.0
60	Rectum-Sigma	T3N0	Surgery	N/A	28.4	28.4
61	Right colon	T3N0	Surgery	6.7	62.9	62.9
62	Right colon	T3N2	Chemotherapy	73.3	68.0	68.0
63	Right colon	T3N0	Surgery	65.0	1.0	1.0
64	Right colon	T3N1	Chemotherapy	27.5	52.8	52.8
65	Sigma	T3N0	Surgery	0.0	74.0	22.4
66	Right colon	T3N1	Chemotherapy	45.0	72.0	18.3
67	Right colon	T3N0	Surgery	1.7	72.0	72.0
68	Rectum-Sigma	T4N2	Chemotherapy+Radiotherapy	160.0	16.3	15.2
69	Rectum	T3N0	Surgery	66.7	70.0	70.0
70	Sigma	T3N2	Chemotherapy	60.0	70.0	70.0
71	Right colon	T3N0	Surgery	75.0	65.9	65.9
72	Splenic angle	T3N0	Surgery	160.0	10.1	10.1
73	Sigma	T3N0	Surgery	3.3	39.5	39.5
74	Rectum	T4N0	Chemotherapy+Radiotherapy	37.5	63.9	63.9
75	Right colon	T3N1	Chemotherapy+Targeted therapy	43.3	70.0	70.0
76	Sigma	T3N1	Chemotherapy	63.3	75.0	75.0
77	Rectum	T4N1	No treatment	0.0	14.2	11.1
78	Right colon	T3N0	Surgery	23.3	41.6	13.2
79	Right colon	T4N2	Surgery	N/A	37.5	33.5
80	Descendent colon	T3N2	Chemotherapy	3.3	68.0	68.0
81	Sigma	T4N0	Chemotherapy	18.3	60.9	60.9
82	Sigma	T4N1	Chemotherapy	3.3	65.9	37.6
83	Sigma	T4N0	Chemotherapy	33.3	62.9	62.9
84	Right colon	T3N0	Surgery	0.0	67.0	67.0
85	Right colon	T4N0	Surgery	20.0	30.4	8.1
86	Descendent colon	T4N1	Chemotherapy	16.7	63.9	63.9
87	Rectum	T3N1	Chemotherapy+Radiotherapy	166.7	67.9	39.6
88	Sigma	T3N1	Chemotherapy	26.7	59.8	59.8

89	Right colon	T3N0	Surgery	3.3	0.0	0.0
90	Descendent colon	T3N1	Chemotherapy	26.7	50.7	50.7
91	Descendent colon	T3N1	Chemotherapy	3.3	71.0	71.0
92	Sigma	T3N0	Surgery	3.3	65.9	65.9
93	Right colon	T3N0	Surgery	36.7	72.1	72.1
94	Right colon	T3N0	Surgery	6.7	25.4	25.4
95	Right colon	T3N0	Chemotherapy+Radiotherapy	23.3	52.8	32.5
96	Right colon	T3N0	Chemotherapy	3.3	61.9	61.9
97	Right colon	T3N0	Surgery	100.0	64.9	64.9
98	Sigma	T3N0	Surgery	1.0	10.1	10.1
99	Sigma	T3N0	Surgery	2.5	60.9	60.9
100	Right colon	T3N1	Chemotherapy	0.0	61.9	61.9
101	Rectum-Sigma	T3N0	Surgery	2.5	62.9	62.9
102	Sigma	T3N0	Surgery	13.3	60.9	60.9
103	Sigma	T3N2	Chemotherapy+Targeted therapy	100.0	63.9	3.0
104	Sigma	T3N1	Chemotherapy	106.7	24.3	24.3
105	Sigma	T4N1	Chemotherapy	58.3	64.9	64.9
106	Right colon	T3N1	Chemotherapy	86.7	3.0	3.0
107	Right colon	T3N1	Chemotherapy	40.0	61.9	61.9
108	Right colon	T3N0	N/A	6.7	33.5	33.5
109	Transverse colon	T3N0	Surgery	3.3	67.0	67.0
110	Right colon	T3N0	Surgery	63.3	32.5	13.2
111	Right colon	T3N0	Surgery	66.7	59.8	59.8
112	Splenic angle	T3N0	Surgery	5.0	64.9	64.9
113	Sigma	T3N0	Surgery	80.0	50.7	8.2
114	Sigma	T3N0	Surgery	63.3	52.8	52.8
115	Hepatic angle	T3N0	Surgery	30.0	58.8	58.8
116	Right colon	T3N0	Surgery	45.0	54.8	54.8
117	Rectum-Sigma	T3N0	Chemotherapy+Radiotherapy	140.0	60.9	60.9
118	Rectum	T2N1	Chemotherapy+Radiotherapy	40.0	63.9	63.9
119	Sigma	T3N0	Surgery	40.0	53.8	53.8
120	Descendent colon	T3N0	Surgery	140.0	54.8	54.8
121	Right colon	T4N2	Chemotherapy	83.3	18.2	10.1
122	Splenic angle	T3N1	Surgery	46.7	61.8	61.8
123	Rectum-Sigma	T3N0	Chemotherapy	103.3	60.9	60.9
124	Sigma	T3N1	Chemotherapy	10.0	59.8	59.8
125	Sigma	T3N2	Chemotherapy+Targeted therapy	41.7	42.6	14.1
126	Rectum-Sigma	T4N0	Surgery	20.0	31.5	23.3
127	Right colon	T3N0	Surgery	18.3	58.8	58.8
128	Right colon	T4N0	Surgery	10.7	55.8	55.8
129	Descendent colon	T3N0	Surgery	0.0	56.8	9.1
130	Rectum	T3N0	Chemotherapy+Radiotherapy	16.7	56.8	56.8
131	Descendent colon	T3N0	Surgery	23.3	51.7	51.7
132	Rectum-Sigma	T2N0	Chemotherapy+Radiotherapy	0.0	48.7	48.7
133	Right colon	T3N0	Surgery	33.3	67.0	67.0
134	Right colon	T3N0	Surgery	50.0	49.7	49.7
135	Splenic angle	T4N0	Surgery	4.0	58.8	58.8
136	Rectum	T2N0	Chemotherapy+Radiotherapy	N/A	19.3	19.3

137	Rectum-Sigma	T1N0	Chemotherapy+Radiotherapy	110.0	54.8	54.8
138	Rectum-Sigma	T2N0	Chemotherapy+Radiotherapy	15.0	54.8	54.8
139	Right colon	T3N1	Chemotherapy	50.0	58.8	58.8
140	Sigma	T4N2	Surgery	160.0	0.0	0.0
141	Ascending colon	T3N0	Surgery	56.7	58.8	58.8
142	Sigma	T3N0	Surgery	15.0	35.5	35.5
143	Rectum-Sigma	T3N1	Chemotherapy+Radiotherapy	50.0	28.5	11.2
144	Right colon	T3N2	Chemotherapy	20.0	52.8	52.8
145	Right colon	T4N2	Chemotherapy	8.3	53.8	53.8
146	Descendent colon	T4N1	Chemotherapy	35.0	58.8	30.5
147	Right colon	T4N1	Surgery	0.0	54.8	54.8
148	Rectum-Sigma	T3N1	Chemotherapy	93.3	58.8	58.8
149	Sigma	T1N1	Chemotherapy	1.7	57.8	57.8
150	Sigma	T3N2	Chemotherapy	8.3	56.8	56.8
151	Right colon	T4N1	Surgery	0.0	52.8	52.8
152	Right colon	T4N1	Chemotherapy	160.0	54.7	54.7
153	Descendent colon	T3N1	Chemotherapy	1.7	56.8	15.2
154	Sigma	T3N2	Surgery	100.0	66.0	16.2
155	Sigma	T3N1	Chemotherapy	90.0	57.8	57.8
156	Sigma	T1N0	Chemotherapy	5.0	20.3	20.3
157	Caecum	T3N2	Chemotherapy	21.7	56.8	56.8
158	Right colon	T2N1	Chemotherapy	50.0	63.8	63.8
159	Right colon	T3N0	Surgery	0.0	52.7	52.7
160	Right colon	T3N0	Surgery	17.0	13.2	7.1
161	Sigma	T3N0	Surgery	60.0	51.8	51.8
162	Sigma	T3N0	Surgery	12.5	59.8	59.8
163	Descendent colon	T3N0	Surgery	6.7	57.8	57.8
164	Rectum-Sigma	T2N0	Radiotherapy	110.0	55.8	55.8
165	Descendent colon	T3N2	Chemotherapy+Radiotherapy	63.3	41.6	41.6
166	Rectum-Sigma	T3N2	Chemotherapy	6.7	48.7	48.7
167	Sigma	T4N2	Chemotherapy	153.3	58.8	58.8
168	Sigma	T4N0	Chemotherapy	26.7	60.9	60.9
169	Right colon	T2N1	Chemotherapy	8.3	55.8	55.8
170	Right colon	T3N1	Chemotherapy	0.0	52.7	52.7
171	Sigma	T3N1	Surgery	11.7	56.9	56.9
172	Ascending colon	T4N1	Chemotherapy	36.7	58.8	58.8
173	Right colon	T3N0	Surgery	0.0	55.8	55.8
174	Transverse colon	T4N1	Chemotherapy	106.7	59.8	59.8
175	Right colon	T3N1	Chemotherapy	6.7	61.9	38.6
176	Sigma	T4N2	Chemotherapy	N/A	62.9	33.5
177	Sigma	T3N0	Surgery	50.0	56.8	56.8
178	Right colon	T4N0	Chemotherapy	60.0	57.8	57.8
179	Splenic angle	T3N0	Surgery	1.7	61.9	61.9
180	Descendent colon	T3N0	Chemotherapy	0.0	62.8	62.8
181	Sigma	T3N2	Surgery	86.7	1.0	1.0
182	Rectum-Sigma	T3N2	Chemotherapy	63.3	49.6	49.6
183	Sigma	T4N0	Chemotherapy	56.7	60.9	60.9
184	Ascending colon	T3N0	Surgery	4.0	52.7	52.7

185	Rectum-Sigma	T3N1	Chemotherapy	0.0	64.9	25.3
186	Right colon	T3N0	Surgery	N/A	25.4	14.2
187	Descendent colon	T3N0	Chemotherapy	66.7	68.0	68.0
188	Sigma	T4N0	Chemotherapy	110.0	51.7	13.2
189	Right colon	T4N0	Surgery	0.0	54.8	54.8
190	Sigma	T2N1	Chemotherapy	5.0	52.7	52.7
191	Right colon	T3N0	Surgery	26.7	53.8	53.8
192	Rectum-Sigma	T3N1	Surgery	0.0	1.0	1.0
193	Right colon	T3N0	Surgery	21.7	0.0	0.0
194	Right colon	T3N0	Surgery	33.3	61.9	61.9